



SCUOLA INTERNAZIONALE SUPERIORE DI STUDI AVANZATI

Dust in hydrodynamic and semi-analytic galaxy evolution simulations

Author:
MASSIMILIANO PARENTE

Supervisors:
DR. CINTHIA RAGONE-FIGUEROA
DR. GIAN LUIGI GRANATO
PROF. ANDREA LAPI

*A thesis submitted in fulfillment of the requirements
for the degree of Philosophiae Doctor*

in

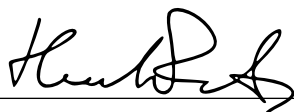
ASTROPHYSICS AND COSMOLOGY

October 2024

Declaration of Authorship

- This work was done wholly or mainly while in candidature for a research degree at this University.
- Where any part of this thesis has previously been submitted for a degree or any other qualification at this University or any other institution, this has been clearly stated.
- Where I have consulted the published work of others, this is always clearly attributed.
- Where I have quoted from the work of others, the source is always given. With the exception of such quotations, this thesis is entirely my own work.
- I have acknowledged all main sources of help.
- Where the thesis is based on work done by myself jointly with others, I have made clear exactly what was done by others and what I have contributed myself.

Signed:

A handwritten signature in black ink, appearing to be 'Hendrik', written over a horizontal line.

Date:

15 oct 2024

Massimiliano Parente

Abstract

Dust grains are fundamental components of the galaxies of our Universe, affecting both the physical processes of galaxy evolution and their observability. Therefore, incorporating dust physics into galaxy evolution simulations is essential. This Thesis investigates various aspects of dust within galaxy evolution using a state-of-the-art dust model integrated into two commonly adopted tools: hydrodynamic simulations and semi-analytic models (SAMs). The dust model includes both stellar production of dust and the growth/destruction of grains in the gaseous phase, allowing to track the dust content and, in an approximate manner, the size and chemical composition of grains. This model, originally developed in previous hydrodynamic simulations, was integrated into a SAM as part of the work done in this Thesis.

The dust model in cosmological hydrodynamic simulations is exploited to study the size and chemical properties of grains across different galaxies, alongside with some other basic predictions concerning the simulated galaxy population. The key result is that grains features depend on the evolutionary history of galaxies. Massive galaxies tend to have a population of silicate-rich and smaller grains compared to less massive galaxies. This difference is attributed to the larger relevance of grain growth in the interstellar medium (ISM) of massive galaxies, driven by the large amount of dense gas, compared to dust production by stars.

The SAM equipped with the dust model is used to explore various topics, including the evolution of cosmic dust abundance across redshift. Observations suggest a decrease in galactic dust abundance from $z \sim 1$ to $z = 0$. Predictions from the model presented here are in keeping with this trend, suggesting that the decrease may not be due to intrinsic dust-related processes but rather the adopted galaxy evolution framework. Specifically, the growth of supermassive black holes (SMBHs) during disc instabilities (DIs) is critical for reproducing the observed drop within the context of this model.

The SAM-based model is employed also to investigate the star formation rate (SFR) and dust content of local galaxies within different regions of the cosmic web. An analysis using SDSS and GAMA data shows that galaxies in less dense environments (such as voids and walls) tend to be more star-forming and dust-rich up to a certain mass ($\sim 10^5 - 10^8 M_\odot$), beyond which environmental differences reduce. The model is in agreement with these observations, attributing the reduced environmental impact in massive galaxies to the *in situ* growth of SMBHs driven by DIs, which makes galaxy quenching less sensitive to the environment where galaxies reside.

Finally, the galaxy catalog produced by the SAM is post-processed with a Radiative Transfer (RT) code to predict observable galaxy properties taking into account dust absorption and emission. The analysis reported here focuses on the sub-mm emission of galaxies in the local Green Valley (GV), i.e. the transition region between the blue cloud and red sequence of the color-mass diagram. In keeping with GAMA and H -ATLAS observations, the model predicts significant sub-mm emission in GV galaxies due to their substantial dust content, which declines more slowly compared to the SFR, resulting in their optical green color. Conversely, rejuvenating systems in the GV exhibit low sub-mm emission due to insufficient time for significant dust growth after a quenched period.

Acknowledgements

This Thesis is the result of a four years long effort, an extremely productive, and, often, funny period. A scientific document of ~170 pages, like this one, could not have been produced by myself without the support of many colleagues, especially more experienced ones. Therefore, I find it necessary to acknowledge those who have played a significant role in this work, as I have had the privilege to learn something from each of them.

Undoubtedly, my supervisors are at the top of this list. Cinthia and Gian Luigi have been the key figures in terms of scientific collaboration. I owe much of what I learned during this time to them, especially about doing and, most importantly, approaching science. The most important thing I learned from them is to think independently and without bias, skill that constitutes half of a scientist's work. For all this — their constant support, their availability, for the immense (perhaps too much) trust in me, and the time we spent together both inside and outside of the office — I am deeply grateful. I fully realize how incredibly lucky I have been to meet two such people and friends.

I thank Andrea, who has been a key figure for me, a reference point for any student, always available for advice and great for having (often enlightening) conversations.

I would like to thank some other people that I had the pleasure to collaborate with and to discuss about (not only) science in the Trieste area: Sandro Bressan, Laura Silva, Stefano Borgani, Giuseppe Murante, Milena Valentini. A special thanks goes to my PhD and Post-Doc colleagues at SISSA and INAF for their constant support (and assistance in many cases), in particular Lumen Boco, Tommy Ronconi, Meriem Behiri, Alice Damiano, and Roberta Tripodi. And of course, to my dear office mates, Mavi, Cristiano, and Francesco.

I want to thank all the people of the L-Galaxies crew, in particular Robert Yates, Reza Ayromlou and Aswin Vijayan, for including me in their community and for their full availability to discuss about science at any time.

As well, a special acknowledgments is needed to my Argentinian collaborators: Julian Martínez, Valeria Coenda, Pablo Lopez, Andres Ruiz, Facundo Rodriguez, Laura Ceccarelli, Hernán Muriel. This acknowledgement is extended to all my IATE friends, especially Selene and Facundo, who made me feel at home during my time in Cordoba.

I want to mention and thank all the people that I had the pleasure to meet, interact with, discuss and collaborate with during these years: Cedric Lacey, Carlton Baugh, Carlos Frenk, Francesco Calura, Francesca Pozzi, Alberto Traina, Jakob Nadolny, Darko Donevski.

Lastly, I want to thank SISSA for the opportunity to travel and meet people, and the whole SISSA community (especially the canteen staff!), who made my time here really great.

A quick mention to all the friends and people that I have had the pleasure of spending time with over these years in Trieste. The biggest thanks go to this environment and to everyone who made it possible. More or less in chronological order, my flatmates (including Andrea and Mavi) from a house that we will hardly forget. The companions of the first Sundays, Mavi and Cristiano. The Buongiorno group, whose trick was to combine Andrea's dangerous madness with Giovanni's *seraficità* (only moral, not in tone of voice), all mixed with copious amounts of Campari and Prosecco. The wonderful duo Delpo&Diego, who could order a glass of *mieru* in any place in Salento, united, albeit for different reasons, by being night visitors of Via Machiavelli (but I'll also remember them at the table: Diego's pizzas, the mirto, Diego's castagne, the mirto, Diego's risottos, the mirto). A friend from France, Stéphane, to whom I owe many beautiful moments, both in front of a *parmigiana* and on top of a mountain. And to repay him, I introduced him to the cult of San Giseppu. Many of these moments came from the mind, always too active, of Fabiana, whom I prefer to remember for our lunches on the *Molo Audace*. My dear friend of Adriatic Sea crossings and his house,

Giua, who is truly *serafico* in everything. Even when accompanying me and Morgy in our WhatsApp group. And the less *serafico* Diego(2), also holder of the title of Mr. Luna Pork and the largest quantity of *ricotta scante* consumed in one single night. Alice, who has many qualities, but none as great as bringing a contagious joy *meridionale* that we often forget is so important. And then the poet (of rare sensitivity), Flavio, the (albeit brief) companion of daily life, Elisa, the companion of *calamari* and thoughts, Davide, the splendidi Valentina, Giulio, and Fragarosi.

In concluding this list, which comes with the conclusion of my time as an academic student, it is impossible to me not mentioning Vania, who shared with me the whole 9 years long journey, and many many many daily life, happy and sad, moments.

I hope you haven't all been shooting stars, but rather comets that we look forward to seeing again, somewhere.

It is worth mentioning, and also a pleasure for me, all my *radici* that have supported me over the years. Closest to me are my cousins Giorgio and Alessandra from Staranzano, and our unforgettable Christmas. There's the Venice Queen Bettina, the guide for many (but never too many) *bakari tours*. My Friulian run-bro Giulio who has been following my academic journey for 8 years and now prefers frico over *munaceddhre*, and my *racchettoni*-sister Marta, who now is closer thanks to him.

I also want to acknowledge those who, although not nearby, have had the pleasure of tasting my Triestine experience. Angelo, who Trieste (as well as the nord-est, Vienna, and Sicily) will rarely forget, an extension of the Buongiorno group in Florence. And the unforgettable Miss Altea, sometimes my best male friend. The recurring (but never enough) Matteo, and Massi, one of the few people with whom I share too many things (including the name), and the evergreen Giuseppe Rossi.

And to anyone from Salento (and not only) who has been close to me, especially in these days, Emanuele and Cristina, my first *socio* Ludovico and the other *socio* Piergiacomo with Yly, my dear old flatmate Sara, Giuseppe di Massi, H and Barbara, and all the others who are here with the thought, Antonio, Giordano, CIM and the *Casu Nighters*...I can not list all.

It is impossible not to mention my family. Not only because it's nice to have something solid outside of this often uncertain work, but also because it is far from trivial to know that I am the source of such pride. This thesis is also yours.

Lastly, I must mention all the music¹ that has accompanied me throughout these years in this work. Music has that beautiful quality of adapting to all moments of life and often pushing us to adapt our lives to its rhythm. And this is the most beautiful superpower I know. The most heartfelt thanks go to her.

¹And I apologize for having shared it publicly often accompanied by my not-always perfectly tuned sweet voice.

Contents

| | |
|--|------------|
| Declaration of Authorship | iii |
| Abstract | vi |
| Acknowledgements | vii |
| List of Abbreviations | xv |
| List of Publications | xvi |
| | |
| I Background and Methods | 1 |
| 1 Introduction | 3 |
| 1.1 Structure of the Thesis | 6 |
| 2 Simulating galaxy evolution | 9 |
| 2.1 General background | 9 |
| 2.1.1 The cosmological model | 9 |
| 2.1.2 DM halos | 10 |
| 2.1.3 Overview of the main astrophysical processes | 14 |
| 2.2 SAMs and hydrodynamic simulations | 14 |
| 2.2.1 Gravity | 17 |
| 2.2.2 Hydrodynamical modeling | 18 |
| 2.2.3 Thermal energy and gas cooling | 18 |
| 2.2.4 Astrophysical modeling | 19 |
| 2.3 The L-GALAXIES SAM | 23 |
| 2.3.1 DM merger trees | 23 |
| 2.3.2 Gas infall and cooling | 23 |
| 2.3.3 The cold disc and star formation | 24 |
| 2.3.4 Chemical and energetic feedback from stars | 25 |
| 2.3.5 Disc Instabilities and Mergers | 25 |
| 2.3.6 Black hole physics | 26 |
| 2.3.7 Environmental processes | 27 |
| 2.4 Hydrodynamic simulations with MUPPI | 27 |
| 2.4.1 Multiphase gas: partitioning and evolution | 27 |
| 2.4.2 Cooling and star formation | 29 |
| 2.4.3 Stellar feedback | 30 |
| 2.4.4 Black hole physics | 31 |
| 3 Modeling dust in galaxy evolution simulations | 33 |
| 3.1 Dust life-cycle | 35 |

| | | |
|-----------|--|-----------|
| 3.2 | Chemical evolution models | 36 |
| 3.3 | Numerical simulations | 38 |
| 3.3.1 | Modeling dust processes in the SA and hydrodynamic framework | 39 |
| 3.3.2 | Key results from numerical simulations | 43 |
| 3.3.3 | Future prospects for dusty simulations | 51 |
| 3.4 | The dust model in L-GALAXIES and MUPPI | 55 |
| 3.4.1 | Stellar production | 58 |
| 3.4.2 | Shattering and coagulation | 59 |
| 3.4.3 | Grains accretion | 60 |
| 3.4.4 | Grains destruction in SNe shocks | 60 |
| 3.4.5 | Grains sputtering | 61 |
| 3.4.6 | Dust cooling | 62 |
| II | Results | 63 |
| 4 | Dust evolution with MUPPI in cosmological volumes | 65 |
| 4.1 | Numerical Simulations | 66 |
| 4.1.1 | Galaxies identification | 67 |
| 4.2 | General properties of the galaxy population | 67 |
| 4.2.1 | Galaxy Main Sequence | 70 |
| 4.2.2 | Stellar Mass Function | 70 |
| 4.2.3 | SMBH-bulge relation | 70 |
| 4.2.4 | Cosmic Star Formation Rate | 71 |
| 4.3 | Main properties of MWHM galaxies | 74 |
| 4.4 | Dust inside galaxies | 76 |
| 4.4.1 | Dust Mass Function | 76 |
| 4.4.2 | Dust, Stellar Mass and SFR | 78 |
| 4.4.3 | Dust and Metallicity | 78 |
| 4.4.4 | Size and chemical composition of grains | 82 |
| 4.5 | Dust outside galaxies | 85 |
| 4.5.1 | Dust profile around galaxies | 85 |
| 4.5.2 | Redshift evolution of dust profiles | 86 |
| 4.6 | Summary and Discussion | 90 |
| 5 | The $z \lesssim 1$ drop of cosmic dust abundance | 93 |
| 5.1 | Observing the cosmic dust abundance | 93 |
| 5.2 | The SAM simulations | 94 |
| 5.2.1 | A new treatment for Disc Instabilities | 95 |
| 5.2.2 | Bulge sizes | 96 |
| 5.3 | General Properties of the Galaxy Population | 98 |
| 5.3.1 | Mass Functions and Cosmic SFRD | 98 |
| 5.3.2 | Galaxy morphology and star formation | 98 |
| 5.3.3 | Bulge sizes and Bulge-BH relation | 101 |
| 5.4 | Dust properties | 103 |
| 5.4.1 | Dust Mass Function | 103 |
| 5.4.2 | Dust, stars and metallicity | 104 |
| 5.4.3 | Grain sizes | 107 |
| 5.4.4 | Dust profiles | 107 |
| 5.5 | The Cosmic Dust Abundance | 107 |
| 5.5.1 | Galactic dust budget | 107 |

| | | |
|----------------------------------|--|------------|
| 5.5.2 | Extra-galactic dust budget | 113 |
| 5.5.3 | Total dust budget | 117 |
| 5.6 | Conclusions | 117 |
| 6 | Star Formation and Dust in the Cosmic Web | 121 |
| 6.1 | Galaxies in the Cosmic Web: Observations and Models so far | 122 |
| 6.2 | The simulated and observed samples | 123 |
| 6.2.1 | The SAM catalog | 123 |
| 6.2.2 | Observational data | 124 |
| 6.3 | Identifying Cosmic Web Environments | 124 |
| 6.3.1 | Cosmic web segmentation: NEXUS+ | 124 |
| 6.3.2 | Spherical voids identification | 125 |
| 6.3.3 | Filaments and groups identification | 125 |
| 6.4 | Properties of galaxies across cosmic environments | 126 |
| 6.4.1 | Environments Stellar Mass Function and satellites fraction | 128 |
| 6.4.2 | Star Formation and Dust | 129 |
| 6.4.3 | Galaxy evolution across environments | 130 |
| 6.4.4 | The impact of in situ SMBH growth on isolated galaxies evolution | 132 |
| 6.4.5 | Convergence mass and SMBH growth | 135 |
| 6.5 | Comparison with observations | 136 |
| 6.5.1 | Star formation | 137 |
| 6.5.2 | Dust mass | 139 |
| 6.6 | Summary and conclusions | 141 |
| 7 | Dust sub-mm emission in Green Valley galaxies | 145 |
| 7.1 | The simulated catalog | 146 |
| 7.1.1 | The SAM catalog | 146 |
| 7.1.2 | Radiative Transfer with GRASIL | 146 |
| Stars and ISM geometry | 146 | |
| Stellar emission | 147 | |
| Radiative Transfer | 147 | |
| 7.2 | Observational data | 148 |
| 7.3 | The color-mass diagram | 148 |
| 7.4 | Defining the GV | 149 |
| 7.5 | The impact of dust attenuation | 153 |
| 7.6 | The sub-mm $250\mu\text{m}$ emission | 154 |
| 7.7 | Evolution in the color- $S_{250\mu\text{m}}$ diagram | 158 |
| 7.7.1 | Model GV redshift evolution | 158 |
| 7.7.2 | A red galaxy case study | 159 |
| 7.7.3 | A red statistical sample | 160 |
| 7.7.4 | The color- $S_{250\mu\text{m}}$ diagram | 161 |
| 7.8 | Rejuvenating systems | 163 |
| 7.9 | Summary and Conclusions | 163 |
| III | Conclusions | 165 |
| 8 | Closing remarks and perspectives | 167 |
| 8.1 | Results summary | 167 |
| 8.2 | Other projects and perspectives | 169 |
| | Bibliography | 171 |

List of Figures

| | | |
|------|--|-----|
| 1.1 | Example SED of a galaxy with the contribution of stars and interstellar dust. | 4 |
| 2.1 | Example of DM halos merger tree. | 10 |
| 2.2 | Theoretical HMF compared to the observed SMF | 11 |
| 2.3 | Illustration of the huge range of scales involved in galaxy evolution. | 13 |
| 2.4 | Basic working scheme of a SAM. | 15 |
| 2.5 | Basic working scheme of a hydrodynamic simulation. | 16 |
| 2.6 | IMFs comparison. | 21 |
| 3.1 | Schematic sketch depicting the dust life-cycle in galaxies | 34 |
| 3.2 | DTG and DTM versus gas metallicity Z at $z \simeq 0$ | 44 |
| 3.3 | Cosmic rate of ISM grain growth and ISM grains destruction. | 45 |
| 3.4 | DMF at $z \sim 0, 1, 2, 4$ | 47 |
| 3.5 | $\Omega_{\text{dust}}^{\text{ISM}}$ as a function of redshift. | 48 |
| 3.6 | Dust inside and outside galaxies at $z \sim 0.5$ | 50 |
| 3.7 | The dust model adopted in this Thesis. | 56 |
| 4.1 | Map of stars, gas, and dust in the simulation | 66 |
| 4.2 | Main Sequence | 68 |
| 4.3 | Stellar Mass Function | 69 |
| 4.4 | Main sequence and SMBH-Bulge relation | 71 |
| 4.5 | Cosmic Star Formation Rate Density | 72 |
| 4.6 | Bulge-to-Total ratio | 74 |
| 4.7 | Gas fraction | 75 |
| 4.8 | Mass-Metallicity relation | 75 |
| 4.9 | Dust Mass Function | 77 |
| 4.10 | Dust-stellar mass relation | 79 |
| 4.11 | DTG and DTM ratio versus the ISM gas phase metallicity Z | 80 |
| 4.12 | DTG and DTM ratio versus the ISM gas phase metallicity Z - dust parameters | 81 |
| 4.13 | DTG and DTM ratio versus the ISM gas phase metallicity Z - SF efficiency | 81 |
| 4.14 | Small-to-Large grains ratio – $z = 0$ | 83 |
| 4.15 | Small-to-Large grains ratio – $z = 1.25$ | 83 |
| 4.16 | Silicate-to-Carbon grains ratio | 83 |
| 4.17 | Small-to-Large and Silicate-to-Carbon grains ratio evolution | 84 |
| 4.18 | Dust surface density profile | 88 |
| 4.19 | Radial profiles of dust-related quantities | 89 |
| 4.20 | Gas temperature profile | 90 |
| 5.1 | Stellar, gas, molecular mass function | 99 |
| 5.2 | Cosmic Star Formation Rate Density | 100 |
| 5.3 | Morphology and specific SFR | 101 |
| 5.4 | Specific SFR distribution | 102 |
| 5.5 | Stellar half-mass radius | 103 |

| | | |
|------|--|-----|
| 5.6 | BH-bulge mass relation | 104 |
| 5.7 | Dust Mass Function | 105 |
| 5.8 | Dust Mass Function – morphology | 106 |
| 5.9 | Dust-stellar mass relation | 108 |
| 5.10 | Evolution of $M_{\text{dust}}/M_{\text{stars}}$ and production/destruction rates | 109 |
| 5.11 | DTG-metallicity relation | 110 |
| 5.12 | Small-to-Large grains ratio | 111 |
| 5.13 | Small-to-Large grains ratio profile | 112 |
| 5.14 | Cosmic ISM dust abundance across redshift | 113 |
| 5.15 | Rates of dust-related processes across redshift | 114 |
| 5.16 | Galactic dust evolution – dust processes | 114 |
| 5.17 | Dust abundance outside galaxies | 116 |
| 5.18 | CGM dust versus stellar mass | 116 |
| 5.19 | Total dust budget across redshift | 118 |
| | | |
| 6.1 | Cosmic Web environments | 127 |
| 6.2 | SMF and satellites in cosmic environments | 128 |
| 6.3 | Specific SFR and dust in cosmic environments | 130 |
| 6.4 | Stellar age in cosmic environments | 131 |
| 6.5 | Galaxy evolution in cosmic environments | 133 |
| 6.6 | Stellar mass assembly time | 134 |
| 6.7 | Mergers and ex situ fraction in cosmic environments | 135 |
| 6.8 | Disc instability driven SMBH growth impact on convergence mass | 136 |
| 6.9 | Specific SFR distribution in the cosmic web | 138 |
| 6.10 | Passive galaxies and specific SFR in the cosmic web | 139 |
| 6.11 | Dust-stellar mass relation in the cosmic web | 140 |
| | | |
| 7.1 | Color-mass diagram | 149 |
| 7.2 | Algorithm for GV identification | 150 |
| 7.3 | Color-mass diagram with GV identification | 151 |
| 7.4 | Dust attenuation impact on the color-mass diagram | 153 |
| 7.5 | Color distribution with different $S_{250\mu\text{m}}$ thresholds | 154 |
| 7.6 | Color distribution with different $S_{250\mu\text{m}}$ thresholds – mass bins | 155 |
| 7.7 | Fraction of $250\mu\text{m}$ emitters | 156 |
| 7.8 | GV evolution with redshift | 158 |
| 7.9 | Evolution of a red galaxy | 159 |
| 7.10 | Evolution of a sample of red galaxies | 160 |
| 7.11 | Average $S_{250\mu\text{m}}$ during different phases of the color-mass diagram | 161 |
| 7.12 | Color- $S_{250\mu\text{m}}$ diagram | 162 |
| 7.13 | $250\mu\text{m}$ emission in rejuvenating galaxies | 162 |

List of Tables

| | | |
|-----|---|----|
| 3.1 | Dust processes adopted in cosmological simulations published so far | 54 |
| 3.2 | Dust processes in the dust model adopted in this Thesis | 57 |

| | | |
|-----|---|-----|
| 4.1 | Varying dust parameters in hydrodynamic simulations | 78 |
| 6.1 | Number of galaxies in cosmic web environments | 126 |
| 6.2 | Characteristic mass in different environments | 129 |
| 6.3 | Environment classification in the observed sample | 137 |

List of Abbreviations

| | |
|-----------------|--|
| AGB | A symptotic G iant B ranch |
| AGN | A ctive G alactic N ucleus |
| ALMA | A tacama L arge M illimeter/submillimeter A rray |
| BC | B lue C loud |
| BH | B lack H ole |
| B-to-T | B ulge- t o- T otal |
| CMB | C osmic M icrowave B ackground |
| CGM | C ircum G alactic M edium |
| DI | D isc I nstability |
| DM | D ark M atter |
| DMF | D ust M ass F unction |
| DTG | D ust- T o- G as |
| DTM | D ust- T o- M etals |
| FOF | F riends- O f- F riends |
| FOF | G rain- S ize- D istribution |
| GV | G reen V alley |
| HMF | H alo M ass F unction |
| IGM | I nter G alactic M edium |
| IMF | I nitial M ass F unction |
| IR | I nfra R ed |
| ISM | I nter S tellar M edium |
| MC | M olecular C loud |
| MP | M ulti P hase |
| MS | M ain S equence |
| MW | M ilky W ay |
| NFW | N avarro F renk W hite |
| QSO | Q uasi S tellar O bject |
| RS | R ed S equence |
| RT | R adiative T ransfer |
| SDSS | S loan D igital S ky S urvey |
| SED | S pectral E nergy D istribution |
| SFH | S tar F ormation H istory |
| SFR | S tar F ormation R ate |
| SFRD | S tar F ormation R ate D ensity |
| Sil-to-C | S ilicate- t o- C arbonaceous |
| SMBH | S uper M assive B lack H ole |
| SMF | S tellar M ass F unction |
| SN | S uper N ova |
| SPH | S moothed P article H ydrodynamics |
| S-to-L | S mall- t o- L arge |
| UV | U ltra V iolet |

List of Publications

The research carried out during my Ph.D. has resulted in several papers, both published in refereed journals and under revision, which form the basis of this Thesis:

- **Dust evolution with MUPPI in cosmological volumes** [Chapter 4]
Parente, M.; Ragone-Figueroa, C.; Granato, G. L.; Borgani, S.; Murante, G.; Valentini, M.; Bressan, A.; Lapi, A.
Monthly Notices of the Royal Astronomical Society, Volume 515, Issue 2, pp.2053-2071, September 2022
- **The $z \lesssim 1$ drop of cosmic dust abundance in a semi-analytic framework** [Chapter 5]
Parente, M.; Ragone-Figueroa, C.; Granato, G. L.; Lapi, A.
Monthly Notices of the Royal Astronomical Society, Volume 521, Issue 4, pp.6105-6123, June 2023
- **Star Formation and Dust in the Cosmic Web** [Chapter 6]
Parente, M.; Ragone-Figueroa, C.; López, P.; Martínez, H. J.; Ruiz, A. N.; Ceccarelli, L.; Coenda, V.; Rodriguez, F.; Granato, G. L.; Lapi, A.; van de Weygaert, R.
The Astrophysical Journal, Volume 966, Issue 2, id.154, 17 pp., May 2024
- **Sub-mm dust emission in Green Valley galaxies** [Chapter 7]
Parente, M.; Ragone-Figueroa, C.; Granato G. L.; Silva, L.; Coenda V.; Martínez, H. J.; Muriel H.; Lapi, A.
submitted to A&A, arXiv:2410.05385

I have also contributed to the following papers, which are not the main topic of this Thesis.

- **The fate of the interstellar medium in early-type galaxies. IV. The impact of stellar feedback, mergers, and black holes on the cold ISM in simulated galaxies**
 Nadolny, J.; Michałowski, M. J.; **Parente, M.**; Hjorth, J.; Gall, C.; Leśniewska, A.; Solar, M.; Nowaczyk, P.; Ryzhov, O.
accepted for publication in Astronomy & Astrophysics, arXiv:2406.16533, 2024
- **Intertwined Formation of H_2 , Dust, and Stars in Cosmological Simulations**
 Ragone-Figueroa, C.; Granato, G. L.; **Parente, M.**; Murante, G.; Valentini, M.; Borgani, S.; Maio, U.
accepted for publication in Astronomy & Astrophysics, arXiv:2407.06269, 2024
- **A^3 COSMOS: the dust mass function and dust mass density at $0.5 < z < 6$**
 Traina, A.; Magnelli, B.; Gruppioni, C.; Delvecchio, I.; **Parente, M.**; Calura, F.; Bisigello, L.; Feltre, A.; Pozzi, F.; Vallini, L.
accepted for publication in Astronomy & Astrophysics, arXiv:2407.09607, 2024

*Perché dovremmo studiare questo problema
se non ci divertiamo a risolverlo?*

—

*Why should we study this problem
if we don't enjoy solving it?*

Nicola Cabibbo

Part I

Background and Methods

1

Introduction

Although luminous matter in our Universe makes up just a ridiculously small fraction ($\lesssim 5\%$) of the total mass-energy budget, it provides most of our knowledge of how everything works. Astronomers typically refer to it as *baryonic* matter, which is essentially composed of gas and stars. These components, especially the stars, are organised into larger structures known as galaxies. Often called the building blocks of the Universe, galaxies are of particular interest to astronomers for two main reasons. First, they are complex systems that host a variety of poorly understood physical processes that rule the formation and evolution of galaxies, including our own. Second, due to their abundance, galaxies can be used as tracers of the structure of the Universe. These characteristics make the study of galaxy formation and evolution an extremely stimulating field for a wide range of diverse interests.

Extra-galactic astrophysics has become one of the major fields of astrophysics and cosmology since its foundation, which dates back about a century. Although galaxies were observed as early as the 18th century, their true nature was not understood until the 1920s. Astronomers initially believed that these *nebulae* were objects within our own galaxy. This view was supported by Harlow Shapley, who opposed Heber Curtis's position during the 'Great Debate' held at the Smithsonian Museum of Natural History in 1920. Curtis argued that these nebulae were actually other galaxies, existing on extra-galactic scales. This idea was ultimately confirmed a few years later by Edwin Hubble (Hubble, 1925), who used Cepheid stars to measure the distances of some of these nebulae, thereby confirming their extra-galactic nature.

Since then, extra-galactic astronomy has advanced significantly. Galaxies have been observed in a diverse range of morphologies, luminosities, and sizes, and more recently, their composition, large-scale environment, and redshift distribution have been extensively studied. In particular, the fact that light travels at a finite speed is invaluable in astronomy, as it allows us to observe galaxies at different stages of their evolution. The advancement of telescopes enabled astronomers to observe the electromagnetic spectrum of galaxies, known as their Spectral Energy Distribution (SED), up to high redshift. This has provided crucial insights into the components of galaxies, especially concerning the characteristics of stars and the Interstellar Medium (ISM) they contain. The radiation observed primarily originates from stars, but it is heavily modified by the interaction with the surrounding ISM. Consequently, the SED that we observe is influenced not only by the stars features like age and chemical composition but also by the composition and geometry of the ISM.

Among the various components of the galactic ISM, dust plays a particularly crucial role, at least within the context of this Thesis. Dust grains are small solid particles ranging in size from $\sim \text{\AA}$ to $\sim 0.1 \mu\text{m}$, composed of heavy elements such as carbon, oxygen, magnesium, silicon, and iron. Despite constituting a tiny fraction of the galaxies mass, dust is critically important for both the detectability and evolution of these systems.

As for detectability, grains significantly obscure light emitted by stars and Active Galactic Nuclei (AGN), making it necessary to take dust into account when interpreting observations.

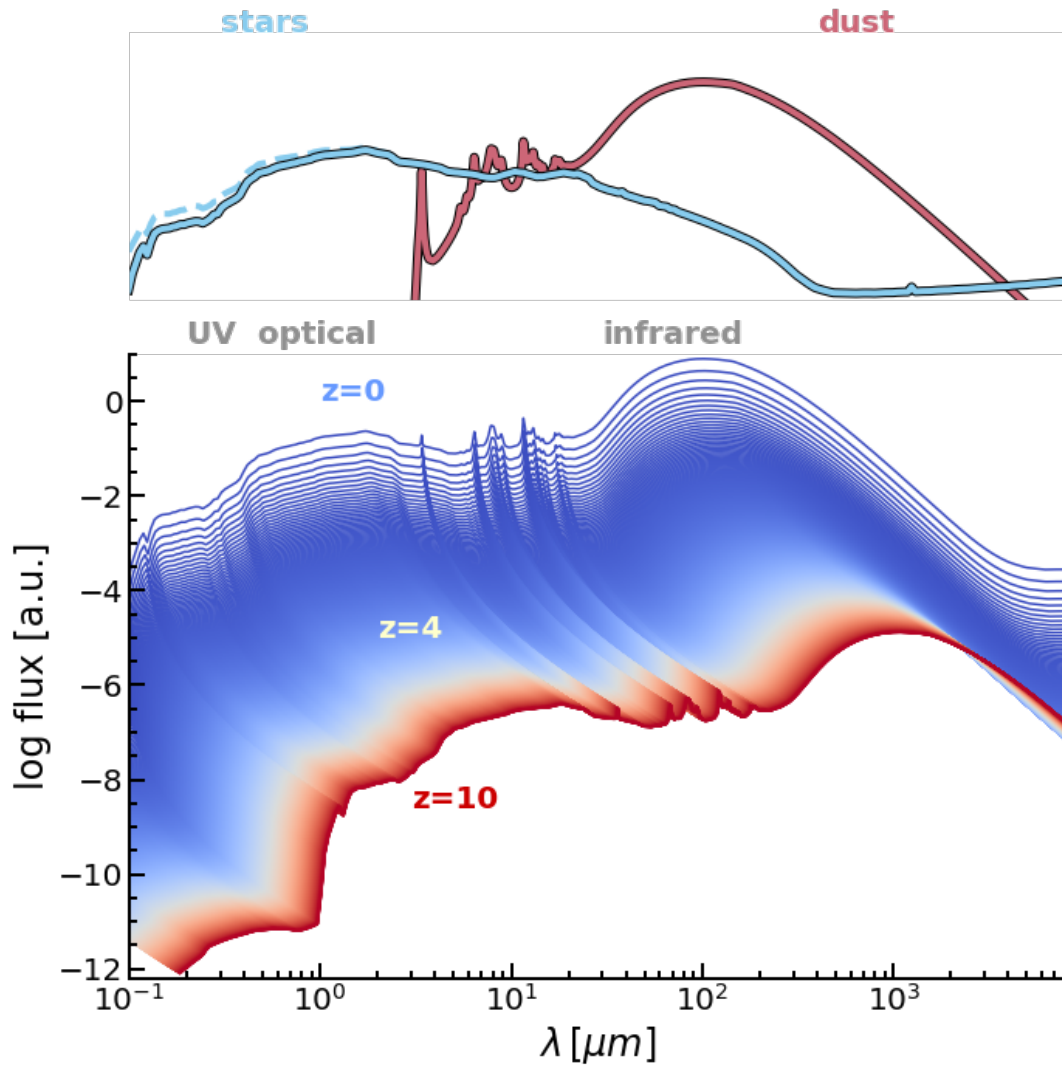


FIGURE 1.1: Example SED of a galaxy with the contribution of stars and interstellar dust. The flux is in arbitrary units. Different lines refer to the same SED observed as it were at different redshifts, from $z = 0$ (blue) to $z = 10$ (red). The top figure schematize the contribution of stars (blue) and dust (red) to the $z = 0$ observable SED. Also, the stellar emission without the contribution of dust obscuration (unextincted) is shown as dashed line.

This insight dates back a century ago to [Trumpler \(1930\)](#) study on light absorption in our galaxy, which linked it to the presence of "fine cosmic dust particles of various sizes". The author also noted the non-uniform distribution of these particles within the galaxy. Dust grains absorb radiation in the optical-UV spectrum, subsequently re-emitting it in the infrared (IR) region. This is explicitly shown in the pedagogic example reported in [Figure 1.1](#), which presents a typical galactic SED observed with contribution from both stars and interstellar dust¹. Note that dust IR emission, which shifts to longer wavelengths at higher redshift, contributes a substantial fraction to the total panchromatic emission of the galaxy.

Detecting this IR emission became a primary objective for numerous facilities developed since the 1980s, such as the Infrared Astronomical Satellite (IRAS) and the Infrared Space Observatory (ISO), which operated within the wavelength range of ~ 10 to $250 \mu\text{m}$. These instruments confirmed the great potential of observing the sky in the IR wavelength regime, where dust-obscured galaxies or regions become visible. In more recent times, we have a multitude of instruments able to detect dust emission across (observed) IR and longer wavelengths (sub-millimeter, radio), like the *Herschel* Space Observatory and the Atacama Large Millimeter/submillimeter Array (ALMA), extending our ability to observe galaxies even at high redshifts. These advancements, coupled with multi-wavelength imaging from other facilities, have significantly enhanced our understanding of galaxy evolution and the role of dust in shaping their observable properties.

However, the interaction between radiation and dust depends on numerous uncertain factors, including the relative star-dust geometry² and the microscopic properties of dust grains, such as their size and chemical composition. Therefore, it is essential to study the nature of astrophysical grains. Many different approaches have been taken to link observed radiation with grain properties, based on physical models of the interaction between these small particles and light. Examples include observing dust in stellar envelopes or ejecta, where dust grains are thought to form (e.g. [Matsuura et al., 2011](#)), or examining the UV extinction (e.g. [Fitzpatrick & Massa, 2007](#)). Additionally, understanding the chemical composition of dust is possible by studying the depletion of metals missing from the ISM gas phase (e.g. [Jenkins, 2009](#)) and examining meteorites (e.g. [Lewis et al., 1987](#); [Bernatowicz et al., 1987](#)). However, such detailed studies on dust are only available in the Milky Way (MW) and, to some extent, in nearby galaxies, making the interpretation of the observations of dusty galaxies at high redshift even more uncertain.

Besides affecting the radiation we observe from galaxies, dust grains play a significant role in the physical processes that shape galaxy evolution. They contribute to the cooling of hot gas: when ions collide with dust grains, thermal energy is transferred to the grains, which then radiate this energy in the infrared, thus easily losing it from the system (e.g. [Burke & Silk, 1974](#); [Dwek & Werner, 1981](#); [Montier & Giard, 2004](#)). On the other hand, metals removed from the gas by dust grains would serve as effective coolants in their gaseous form. Dust grain surfaces also catalyze the formation of H_2 molecules, along with other reactions (see review by [Wakelam et al., 2017](#)). Consequently, dust promotes the formation of molecular clouds, which are the sites of star formation, and shields them from stellar light. The presence of dust in the ISM can enhance the effectiveness of radiation pressure by orders of magnitude, stimulating the onset of galactic winds (e.g. [Murray et al., 2005](#)). Dust can also help in creating a reservoir of low angular momentum gas in galaxies, providing accretion fuel for their supermassive black holes (SMBHs, e.g. [Granato et al., 2004](#)).

¹Note that this SED neglects some important features that could significantly influence its shape, such as gas emission lines and the AGN contribution.

²In this context, the term geometry refers to the relative spatial distribution of stars and the dusty medium, which affect the total outgoing SED of a galaxy.

In summary, dust is a crucial ingredient of galaxies, and understanding its formation and evolution is necessary for interpreting observations and modelling galaxy evolution. This is the scientific motivation behind this Thesis, which aims to study various aspects of dust in galaxy evolution, mainly from a theoretical perspective. I will utilize the most advanced tools available, specifically numerical simulations of galaxy formation and evolution. These state-of-the-art simulations are integrated with physically motivated models that predict the abundance and properties of dust grains throughout galaxy evolution. Together, these tools are invaluable to the astrophysical community, as demonstrated by the growing interest in this topic over the past decade.

1.1 Structure of the Thesis

Given the broad range of topics this Thesis aims to cover, the next two chapters are dedicated to introducing them from both a technical and, to some extent, historical perspective. Specifically, Chapter 2 provides an overview of galaxy evolution simulations in a cosmological context, which is the essential backbone of this work. It introduces the main physical processes driving galaxy evolution and provides a detailed description of the two methods utilized in this Thesis: Semi-Analytic Models (SAMs) and hydrodynamic simulations. Additionally, the chapter includes a technical description of the specific simulation codes used in this work. After discussing the framework for simulating galaxy evolution, Chapter 3 focuses on the modeling of dust grains formation and evolution within these simulations. It begins with a brief overview of the physical processes ruling the abundance and properties of dust grains in an astrophysical context. The chapter then reviews the main methods adopted in literature to incorporate these processes into galaxy evolution simulations, as well as the key results obtained over the past decade. It is worth noting that some results presented in this Thesis will be discussed in advance in this chapter to contextualize them within existing simulations. The chapter concludes with a technical description of the dust model employed in this Thesis and its implementation within the two galaxy evolution frameworks used.

The remaining chapters present the original results obtained in this work. Chapter 4 exploits the dust model in hydrodynamic simulations. It discusses various issues of the simulations and focuses on the predicted chemical and geometrical properties of dust grains both within and outside galaxies, as well as their relation to different galaxy evolution histories.

Chapter 5 studies the total dust budget in the Universe, comparing and discussing SAM predictions with recent observational estimates of cosmic dust at $z \lesssim 4$. Historically, simulations with dust have struggled to reproduce the observed trends, and in particular the drop of the galactic dust budget at $z \lesssim 1$. This chapter proposes a solution and discusses other sources of discrepancies when comparing galactic and extra-galactic dust budgets derived from simulations and observations.

Chapter 6 focuses on the star formation and dust content of galaxies in different environments within the large-scale structure of the local Universe. For the first time, this work derives observationally based estimates of dust content in various regions of the cosmic web and compares them with predictions from the SAM adopted here. This comparison is highly informative for constraining aspects of galaxy evolution as modeled in our simulations.

Chapter 7 explores the impact of dust on the observable properties of galaxies as predicted by the SAM when coupled with a Radiative Transfer pipeline. Specifically, it studies the sub-mm emission of dust in the (optical) Green Valley galaxies, achieving a successful comparison with observations. Additionally, the sub-mm emission of these galaxies provides important insights into their potential rejuvenating nature.

Finally, Chapter 8 concludes the Thesis by summarizing the results and discussing potential future directions for this research.

2

Simulating galaxy evolution

Given the current wealth and variety of observations, developing advanced theoretical models to accurately interpret extra-galactic data has become essential. Although various methods have been devised for this purpose, this Thesis will concentrate on two: semi-analytic models (SAMs) and hydrodynamic simulations. Both approaches aim to describe the properties and evolution of galaxies within a cosmological framework by modeling several key physical processes which are believed to shape galaxy evolution.

This Chapter is structured as follows. First, I will provide a fundamental overview of the cosmological and astrophysical background on which these theoretical tools are typically based (Section 2.1). Then, I will explain the typical *modus operandi* of these two methods (Section 2.2) and introduce the specific SAM and hydrodynamic simulations used in this study (Section 2.3 and 2.4).

CONTENTS

| | |
|---|----|
| 2.1 General background | 9 |
| 2.2 SAMs and hydrodynamic simulations | 14 |
| 2.3 The L-GALAXIES SAM | 23 |
| 2.4 Hydrodynamic simulations with MUPPI | 27 |

2.1 General background

This Section provides a basic introduction to the minimal background relevant to galaxy evolution, namely the cosmological framework, the theory of DM halos and the astrophysical processes occurring within them.

2.1.1 The cosmological model

Simulating galaxy evolution in a cosmological context first requires adopting certain assumptions about a cosmological model. Among the various proposed models for the evolution of the Universe, the most widely accepted is the Λ CDM (Λ Cold Dark Matter). This model is based on the cosmological principle, which states that the Universe is isotropic and homogeneous on large scales, and on Einstein's General Relativity, which describes the evolution of space-time. The key features of this model are cold dark matter (CDM) and dark energy (DE), the latter represented by the cosmological constant Λ . These components make up approximately 25% and 70% of the Universe mass-energy density, respectively. Their nature is *dark* because we lack a precise physical description of them in terms of fundamental particles. DM is a type of non-relativistic (cold) matter that interacts only gravitationally and does not emit electromagnetic radiation, while DE is a form of energy required to explain the observed accelerating expansion of the Universe. The remaining $\sim 5\%$ consists of baryonic

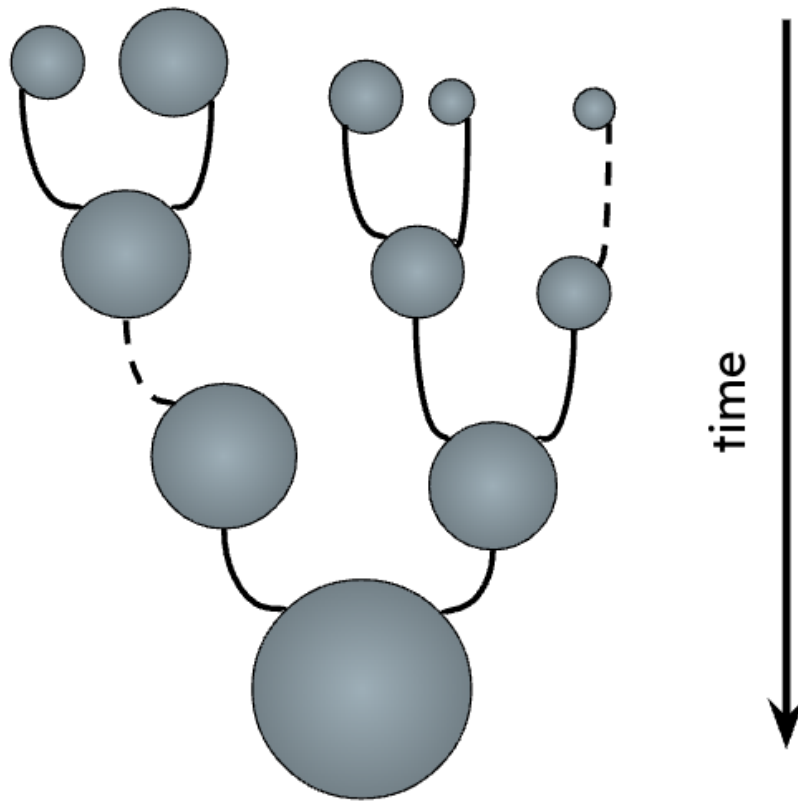


FIGURE 2.1: Example of DM halos merger tree. The bottom DM halos resulted from the mergers of smaller halos (solid lines) and accretion of matter (dashed line) at previous times. The size of circles represents the halo mass.

matter¹ and $\lesssim 10^{-5}\%$ is in the form of radiation. These components are well described by the standard model of particle physics.

Despite the unclear details of the dark components of the Λ CMD model, it provides an extremely accurate description of the observable Universe. Some key observables that this model is able to reproduce include the temperature anisotropies of the Cosmic Microwave Background (CMB; e.g. [de Bernardis et al. 2000](#)) and the large-scale distribution of galaxies (e.g. [Percival et al. 2001](#)). These and other observables have allowed for the constraint of the model parameters, such as the mass-energy fraction of each component, which regulate the Universe evolution.

2.1.2 DM halos

For the purposes of understanding galaxy evolution, one of the most important predictions of the cosmological model is the formation of structures. These structures emerge from the gravitational instability of small primordial perturbations in the DM density field, eventually leading to the creation of gravitationally bound entities, commonly referred to as DM halos, which decouple from the expansion of the Universe. These virialized halos have masses

¹This fraction includes not only baryons but also all non-relativistic particles (e.g., mesons, leptons).

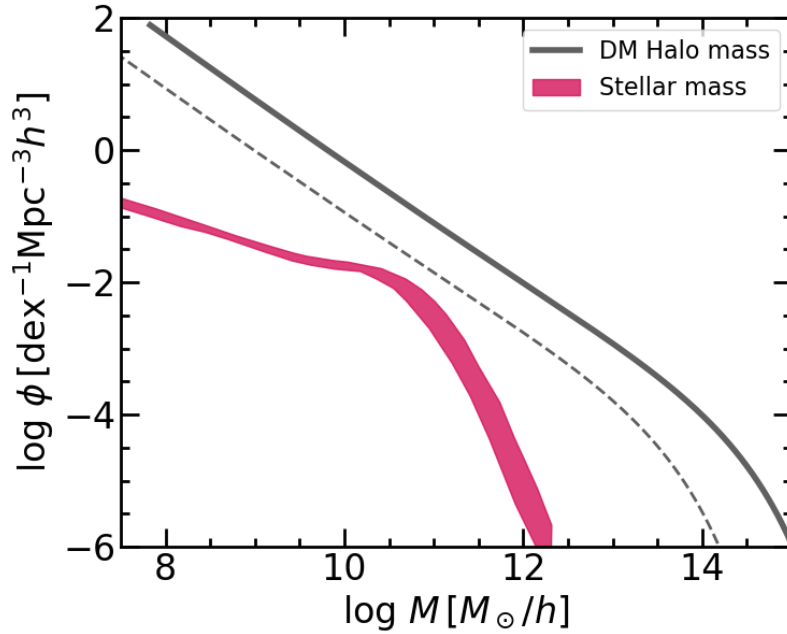


FIGURE 2.2: HMF (gray solid line) compared to the observed SMF (red filled region, [Rodríguez-Puebla et al. 2020](#)). The dashed line represent the HMF rescaled by a factor 0.15, to emulate the cosmic baryonic fraction $f_{\text{bar}} \approx 15\%$. The HMF has been obtained with the `hmf` Python package ([Murray et al., 2013](#)), assuming a standard Planck cosmology ([Planck Collaboration et al., 2016](#)).

$$M_{\text{vir}} = \frac{4\pi}{3} \Delta \rho_m R_{\text{vir}}^3, \quad (2.1)$$

where $\Delta \rho_m$ is the halo mass density, expressed as an overdensity parameter Δ times the background matter density ρ_m . The overdensity parameter is somewhat conventional and represents the overdensity expected for a virialized object that has undergone spherical collapse (e.g. [Bryan & Norman, 1998](#)). A commonly adopted value is $\Delta \sim 200$, although it can sometimes vary with redshift. The virial radius R_{vir} is associated with the virial mass once an overdensity is assumed. Subsequently, the virial velocity of the halo is defined as

$$V_{\text{vir}} := \sqrt{\frac{GM_{\text{vir}}}{R_{\text{vir}}}}. \quad (2.2)$$

To provide some context, our Milky Way (MW) is expected to have a DM halo with $M_{\text{vir}} \sim 10^{12} M_{\odot}$, the largest galaxy clusters have $M_{\text{vir}} \sim 10^{15} M_{\odot}$, and dwarf galaxies have $M_{\text{vir}} \sim 10^9 M_{\odot}$.

The first attempt to quantify the abundance of gravitationally bound structures given an initial perturbation power spectrum was by [Press & Schechter \(1974\)](#). Their theory started with a Gaussian density contrast, evolved in the linear regime (i.e. when overdensities $|\delta| \ll 1$). The field is smoothed on different scales R , which is the radius of the spherical top-hat windows. When a spherical region exceeds a critical density, it is considered a DM halo. This framework links the abundance per unit volume and mass of virialized halos $n(M, z)$ with the variance of the linearly extrapolated density fields. The Press-Schechter formalism has been further extended and improved (e.g., [Bond et al. 1991](#); [Sheth, Mo & Tormen 2001](#);

see also [Zentner 2007](#)). These analytic tools provide highly accurate predictions of $n(M, z)$ compared to results from numerical N -body simulations (e.g. [Efstathiou et al., 1988](#); [Lacey & Cole, 1994](#)).

Besides confirming analytic results, N -body simulations were fundamental to study the internal structure of DM halos (e.g. [Dubinski & Carlberg, 1991](#); [Navarro et al., 1996](#)). [Navarro, Frenk & White \(1997\)](#) proposed an universal shape of the DM profile within halos:

$$\rho(r) = \frac{4\rho_{-2}}{\left(\frac{r}{r_{-2}}\right)\left(1 + \frac{r}{r_{-2}}\right)^2}, \quad (2.3)$$

known as the Navarro-Frenk-White (NFW) profile. In this formula, the subscript -2 denotes the radius at which the logarithmic slope of the profile is -2 . The profile is typically described using the concentration parameter $c = R_{\text{vir}}/r_{-2}$. Given c and M_{vir} , the profile is fully specified. This concentration parameter depends on both redshift and halo mass, with some scatter (e.g., [Jing 2000](#), [Bullock et al. 2001](#)). Although the NFW profile is widely used today, a three-parameter Einasto profile often performs better (e.g. [Gao et al., 2008](#)).

DM halos are not smooth entities. They can host numerous smaller halos known as subhalos or substructures, as demonstrated by high-resolution numerical simulations (e.g., [Ghigna et al. 1998](#)). When a smaller halo enters the virial radius of a larger system, it becomes a satellite halo orbiting the larger halo. The dense cores of subhalos typically survive within the larger structure, although they can lose significant mass through interactions and tidal stripping, and their orbital velocities can change.

Both mergers of smaller structures and accretion of surrounding matter – known as diffuse accretion – contribute to the growth of DM halos. This process, known as hierarchical assembly, is a bottom-up process where smaller structures collapse first and eventually merge to form larger ones. This growth process is often depicted using a merger tree, as shown in [Figure 2.1](#).

Studies focused on DM halos are crucial for understanding galaxy formation and evolution, as these halos are (believed to be) the sites where galaxies form and evolve. In other words, DM halos constitute the gravitational wells where all the baryonic processes that lead to galaxy formation occur. Predictions from both analytic calculations and numerical simulations have provided a solid foundation on which to build our models of galaxy evolution. However, the connection between DM halos and galaxies is complex. For instance, suppose that each DM halo with mass M_{DM} contains a fixed fraction of baryons $M_{\text{bar}} = M_{\text{DM}} \times f_{\text{bar}}$, where $f_{\text{bar}} \approx 15\%$ is the cosmic ratio between baryonic and dark matter. If a fraction of the baryonic matter ϵ_* has been converted into stars, we can convert the distribution of DM halo masses to the distribution of galaxy stellar masses. These distributions are referred to as the Halo Mass Function (HMF) and the Stellar Mass Function (SMF), respectively. An example of HMF and SMF (solid and dashed gray lines) derived in this way is reported in [Figure 2.2](#), naively assuming $\epsilon_* = 1$. However, when comparing the so obtained SMF with the observed one (red filled regions) it becomes apparent that the two distributions have profoundly different shapes. The efficiency of a DM halo in accreting baryonic matter and forming stars is highly mass dependent, with halos of $\sim 10^{12} M_{\odot}/h$ showing the highest efficiency. Unfortunately, the precise functional form of the ratio between DM and stellar mass is complex and strongly depends on various baryonic processes, which are discussed in the following Section.

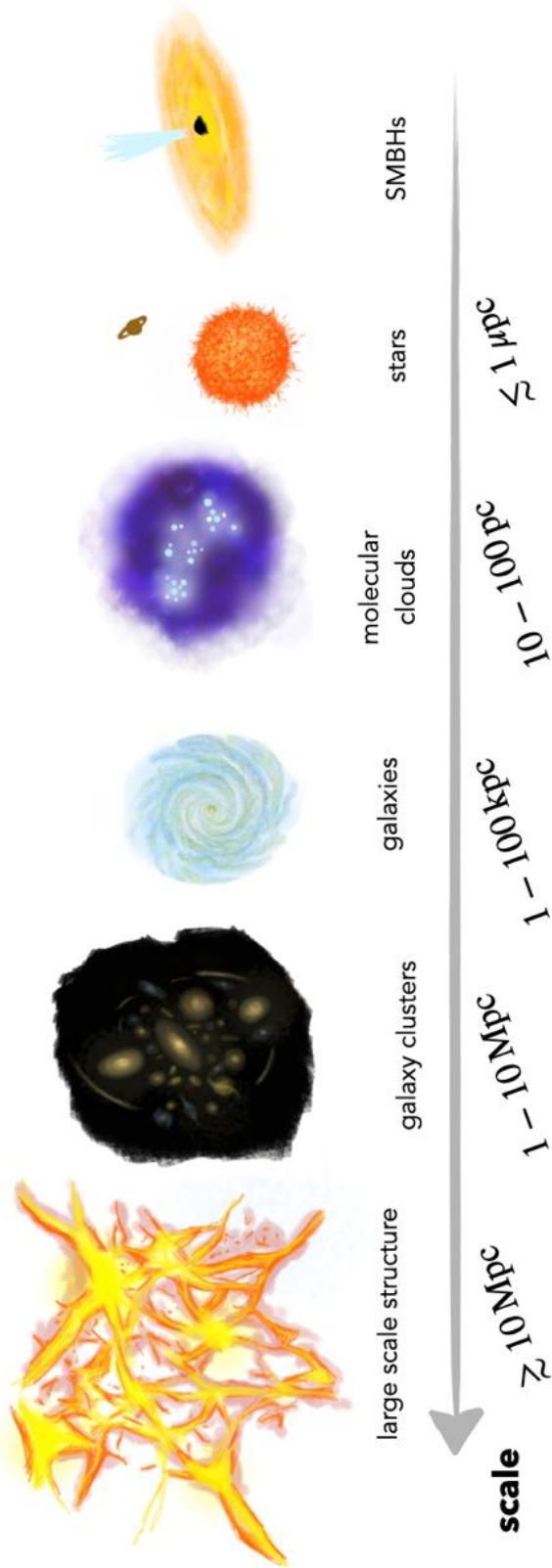


FIGURE 2.3: Illustration of the huge range of scales involved in galaxy evolution. Galaxies reside within the web-like large-scale structure of the Universe, where they form clusters, the largest known virialized objects. On sub-galactic scales, molecular clouds serve as star factories. Lastly, the small yet massive SMBHs at galaxy centers exert powerful energetic feedback.

2.1.3 Overview of the main astrophysical processes

While the formation of structures is well understood thanks to gravity, the physics driving the evolution of baryonic matter is much more complex and challenging to understand. In particular, it spans a huge range of spatial, time, and energetic scales (see e.g. illustration in Figure 2.3). Unlike DM, baryons can radiate away their energy, allowing them to cool, which is a crucial process for galaxy formation. As DM halos form, baryonic gas falls into them and is heated by shocks. This gas can then cool through various processes to form a self-gravitating structure at the center of the halo. This cooling process depends on several factors, including the properties of the DM halo and the cooling capabilities of the gas, which are influenced by its thermodynamics and chemical composition. This cold gas serves as the fuel for star formation.

Stars form in the densest regions of cold gas, typically within molecular clouds, where cooling is effective enough to promote gas collapse to densities needed to ignite nuclear fusion. The physics of star formation is a field of extensive investigation, but many details remain poorly understood. The cooling and fragmentation of gas during star formation episodes lead to a range of stellar masses, from low ($\lesssim 1 M_{\odot}$) to high ($\gtrsim 50 - 100 M_{\odot}$). The mass distribution of newly formed stars, known as the Initial Mass Function (IMF), depends on the physical properties of the star-forming gas and significantly impacts galaxy evolution. This is because stellar evolution and feedback processes are closely tied to the initial stellar mass. In addition to enriching the ISM with chemical elements, stellar feedback – particularly from Supernovae (SNe) – injects energy into the gas phase, potentially driving outflows and suppressing the star formation of the galaxy.

In addition to stars, Supermassive Black Holes (SMBHs) play a significant role in galaxy evolution. These objects, whose formation and growth are still not well understood theoretically, are found at the centers of many galaxies. Feedback from SMBHs can drive galactic-scale winds and heat substantial amounts of gas. These processes impact the amount of gas in DM halos and its cooling, eventually reducing star formation².

2.2 SAMs and hydrodynamic simulations

A robust galaxy formation and evolution simulation should incorporate at least all the aforementioned physics, albeit with a simplified treatment. Both SAMs and hydrodynamic simulations attempt to achieve this. The primary difference between these two methods lies in the smallest scale they can resolve.

SAMs operate on top of DM halo merger trees, associating each halo with a galaxy. As DM halos evolve over time, various astrophysical processes occurring within them are modeled to determine the abundance of different components of each galaxy (e.g., gas, stars). Thus, SAMs resolve processes up to the galactic scale, sometimes attempting to provide a simplified distribution of matter within the galaxy (e.g., bulge component, disc profiles).

Hydrodynamic simulations offer better mass and space resolution by dividing a volume – typically a box – into numerous elements. When these represent mass elements they are commonly referred to as particles. These units represent dark and baryonic matter that interact via gravity and hydrodynamics, allowing the structure of galaxies to be resolved to some extent. Processes occurring within these elements are below the resolution of the simulation and are therefore treated in an approximate manner.

The strategy of modeling physical processes occurring below a certain resolution (in mass or space) is commonly referred to as sub-grid modeling. The rest of this Section details the most common strategies for building SAMs and hydrodynamic simulations, with

²Sometimes the effect of AGNs may result into *positive feedback*, in which the pressurization of the surrounding material stimulates star formation.

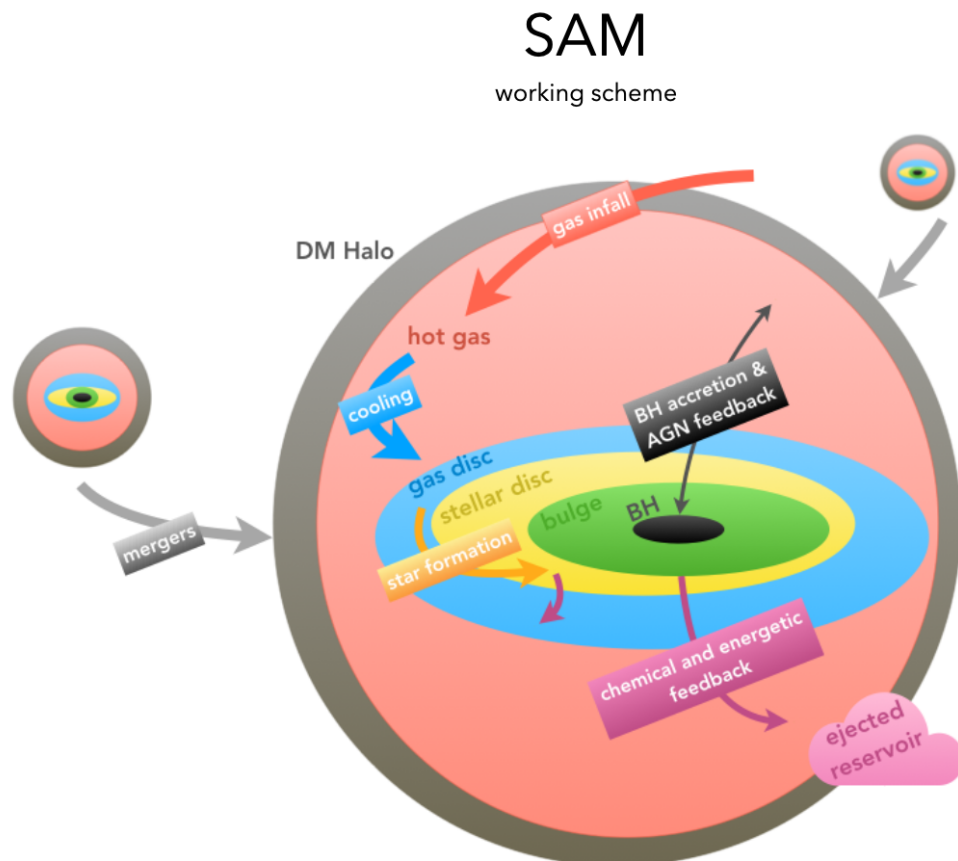


FIGURE 2.4: Basic working scheme of a SAM. Galaxies are associated with DM halos, in turn extracted from N -body simulations or generated with Monte Carlo techniques. Gas is assumed to infall into halos, being shock heated and becoming hot gas. This can cool to form a rotationally supported cold disc, where stars can form. Bulges are assumed to form during disc instabilities or mergers, which are tracked by the DM merger tree. Stars return chemical and energetic feedback to the surrounding gas, which can prevent the hot gas to cool further (ejected reservoir). The SMBH accretes typically during mergers and instabilities, and exerts feedback on the gas.

SPH hydrodynamic simulation

working scheme

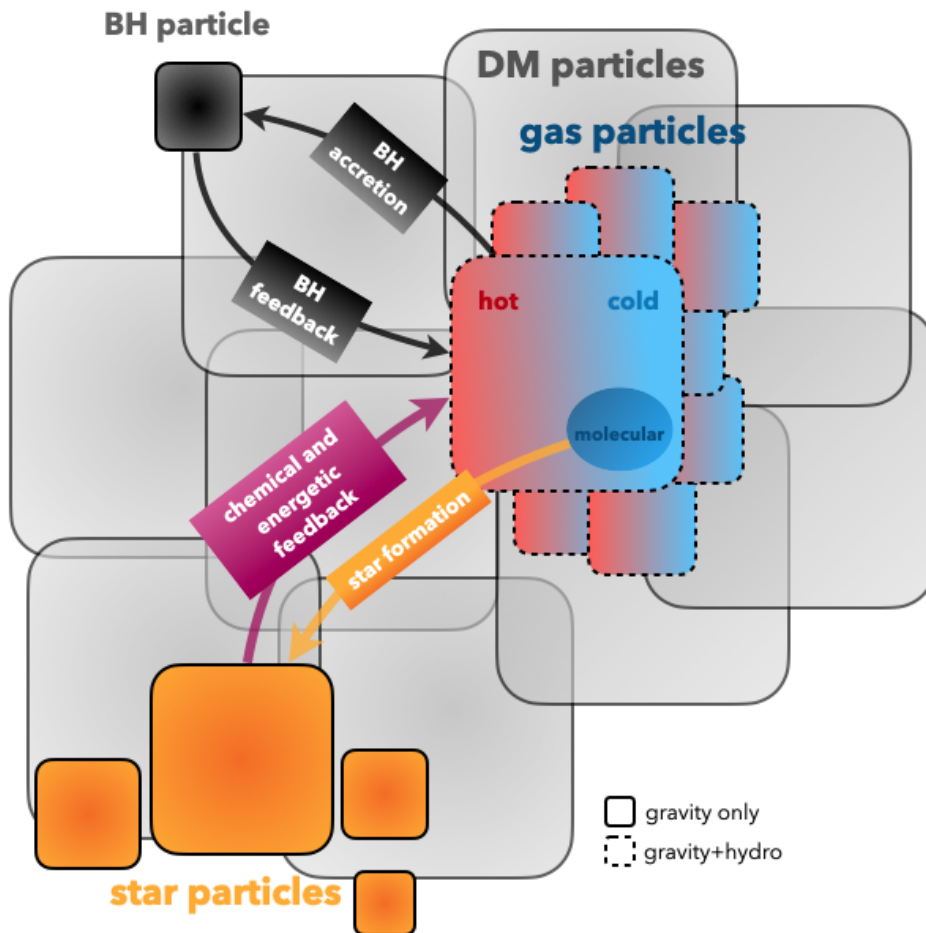


FIGURE 2.5: Basic working scheme of a SPH-based hydrodynamic simulation. Gas, stars, BHs and DM are sampled with particles. All of them interact gravitationally, while only gas particles follow hydrodynamic equations. The latter sample the baryonic gas in the Universe, and in particular the ISM. Hence they are the sites where star formation occurs, i.e. they generate star particles. In turn, stars enrich the gas particles with chemical elements and provide them with energy coming essentially from SNe feedback. Finally, gas particles are also assumed to feed the growth of BH particles, which in turn exert energetic feedback on them.

a particular focus on the sub-grid modeled physics. For an excellent review on the topic, refer to [Somerville & Davé \(2015\)](#). A schematic sketch of the structure of both SAMs and hydrodynamic simulations is provided in, respectively, Figures 2.4 and 2.5.

Before we discuss the details, it is important to note that the better mass and space resolution of hydrodynamic simulations comes at the cost of significantly higher computational demands, whereas SAMs are much less expensive. This is the main limitation of hydrodynamic simulations, as their high computational demands make it impractical to explore many sub-grid recipes. Conversely, SAMs are limited by their mass resolution, as almost all processes occurring on sub-galactic scales must be included using sub-grid recipes. Therefore, these two methods can be seen as conceptually similar in many aspects but not mutually exclusive. Hydrodynamic simulations are particularly suitable for investigating small-scale processes and their impact on overall galaxy evolution (such as outflows, metal spreading, star forming regions). Conversely, SAMs allow for the simulation of much larger volumes and the exploration of a wider range of parameter space, which can, in turn, inform and complement hydrodynamic simulations.

2.2.1 Gravity

The initial step in simulating galaxies is modeling the formation of structures under the influence of gravitational attraction. Generally, N -body techniques are employed to simulate the evolution of a matter field from its initial conditions under the influence of Newtonian gravity (e.g. [Dehnen & Read, 2011](#)). This method involves discretizing the volume of interest into various mass elements (particles) and solving the Poisson equation considering all the relative forces. In practice, various methods are adopted to speed up the computation. One such technique is the tree approach ([Barnes & Hut, 1986](#)), in which the gravitational potential from nearby particles is calculated precisely, while the influence of distant particles is approximated using multipole expansions. Another widely adopted method is the Particle Mesh (PM) approach ([Hockney & Eastwood, 1988](#)), which involves dividing the volume into a grid, solving the Poisson equation in Fourier space for each grid cell, interpolating over the grid, and then evolving the position of each particle accordingly. Hybrid methods are also common. For example, the tree and PM methods are often combined into the tree-PM approach, where gravitational forces are computed via the tree method on small scales and the PM approach on large scales, preserving the accuracy of the former and the computational efficiency of the latter.

N -body simulations have historically been used to simulate the evolution of collisionless DM in an expanding universe, leading to significant achievements such as the discovery of the web-like structure of the Universe and insights into the abundance and properties of DM halos (see Section 2.1.2). However, identifying halos is not straightforward, and various algorithms and strategies have been proposed (see e.g., [Knebe et al. 2011](#) for a comparison). The simplest algorithm is the spherical overdensity method, which identifies halos as regions where the density exceeds a certain threshold relative to the background density (see Equation 2.1). Another well-known algorithm is the Friends-of-Friends (FOF, [Davis et al., 1985](#)), which groups DM particles closer than a fraction (usually $\approx 0.1 - 0.2$) of the mean inter-particle distance as part of the same structure.

Hydrodynamic simulations follow the evolution of DM particles under the Poisson equation and the collisionless Boltzmann equation, requiring halo finder algorithms to identify bound halos (and galaxies) both on-the-fly and in post-processing. In contrast, SAMs are based on merger trees. Although these can be obtained semi-analytically (e.g., [Kauffmann et al., 1993](#); [Cole et al., 1994](#); [Parkinson et al., 2008](#)), it is now common to derive them from N -body gravity only simulations. Merger trees provide crucial information (such as mass,

position, velocity, concentration, and angular momentum) on the evolution of DM halos, constituting the basis for sub-grid physics modeling in SAMs.

2.2.2 Hydrodynamical modeling

Beside from the ability of hydrodynamic simulations to resolve scales smaller than those of galaxies (or their macro components, e.g. bulge, disc), the main difference between SAMs and hydrodynamic simulations is that the latter directly models the hydrodynamics of baryonic gas. While DM and stars are considered collisionless and influenced only by gravity, gas particles are evolved by solving both the Poisson and Euler equations for an ideal fluid³. These equations describe the evolution of the density, velocity, and internal energy of the gas, along with an (ideal) equation of state.

Two main approaches are generally adopted to solve hydrodynamic equations. The Eulerian approach discretizes the fluid spatially, evaluating gas properties at grid points. Sometimes, an adaptive mesh refinement (AMR) is used to enhance grid resolution when necessary. Examples of Eulerian codes are ZEUS (Stone & Norman, 1992), ENZO (Bryan et al., 2014), and RAMSES (Teyssier, 2002). These codes perform well in studying shocks and fluid discontinuities, and can achieve high resolution in fluid dynamics using AMR.

The alternative approach, known as the Lagrangian method, discretizes the fluid mass into individual particles. This is the method employed in the simulations presented in this Thesis. This method is particularly advantageous for galaxy evolution problems, in which it is important to follow the mass assembly and to achieve better resolution in regions where mass is more concentrated⁴. The most popular Lagrangian method in cosmological simulations is Smoothed Particle Hydrodynamics (SPH; Lucy 1977; Gingold & Monaghan 1977; see Monaghan 1992 for a review). SPH evaluates any (scalar or vector) field F of the fluid⁵ at a position \mathbf{x} as follows:

$$F(\mathbf{x}) = \sum_{i=1}^N m_i \frac{F_i}{\rho_i} W(\mathbf{x} - \mathbf{x}_i; h), \quad (2.4)$$

where the summation i is over neighboring gas particles with values of the field F_i and density ρ_i . The kernel function $W(\mathbf{x}; h)$ has a characteristic length h , which may vary according to the fluid particle density to ensure uniform sampling accuracy. The kernel function is symmetric, isotropic, twice differentiable, and vanishes at $|\mathbf{x} - \mathbf{x}_i| > h\eta \sim O(h)$. Here η is a parameter that determines the size of the region over which the kernel has a significant effect, so the summation extends to the nearest N neighbor particles.

In essence, SPH statistically samples fluid quantities by considering the (weighted) contributions of particles near a given position \mathbf{x} . This technique has been widely used in cosmological simulations, e.g. GADGET (Springel et al., 2001; Springel, 2005), GASOLINE (Wadsley et al., 2004, 2017), PHANTOM (Price et al., 2017). Lastly, it is worth mentioning hybrid methods that combine the benefits of mesh-based approaches and SPH (e.g., AREPO; Springel 2010).

2.2.3 Thermal energy and gas cooling

Baryonic gas possesses thermal energy and, importantly, can cool through radiative processes such as bremsstrahlung, recombination, and radiative de-excitation. These processes are accounted for in galaxy evolution simulations with different levels of accuracy.

³Ideal fluids lack viscosity. However, it is common practice to introduce an explicit viscosity term (Artificial Viscosity; AV) to handle phenomena like shocks (e.g. Monaghan, 1992).

⁴Actually, this is true also for the aforementioned AMR approach.

⁵A similar strategy is used to estimate fluid derivatives.

In most hydrodynamic simulations, gas particles radiate their internal energy according to a temperature- and metallicity-dependent cooling function $\Lambda(T, Z)$ (e.g., [Sutherland & Dopita, 1993](#); [Wiersma et al., 2009](#)). This function considers cooling from hydrogen, helium, and metals, operating at temperatures $T \gtrsim 10^4 - 10^5$ K. The thermal evolution and cooling of warm-hot gas are thus consistently modeled in hydrodynamic simulations. Below these temperatures, cooling by ions fine structure and molecular lines (see e.g., [Maio et al., 2007](#)) becomes significant and must be considered, with gas density playing a crucial role. Collisional de-excitation can overcome radiative processes in these regimes, inhibiting cooling. However, typical cosmological simulations cannot resolve the cold phase ($T \lesssim 10^4$ K) directly and instead model it using sub-grid methods.

Hydrodynamic simulations also incorporate photoionization heating. An extragalactic ultraviolet background (UVB), dependent on redshift and generated by stars and quasars (QSOs), is commonly assumed (e.g., [Haardt & Madau, 2012](#)) in the post Epoch of Reionization (EoR) ($z \lesssim 6$), when the gas is presumed to be fully ionized. During and prior to the EoR, when hydrogen remains partially neutral, detailed radiative transfer calculations are required for an accurate modeling of photoheating.

In contrast, SAMs employ a more complex cooling scheme, since gas hydrodynamics is not explicitly tracked. Gas is assumed to infall into DM halos, typically assuming a cosmic baryon fraction $\Omega_{\text{bar}}/\Omega_{\text{m}}$, and simultaneously undergo shock heating to the virial temperature $T_{\text{vir}} = 35.9 (V_{\text{vir}}/(\text{km/s}))^2$ [K]. This heated gas, often referred to as hot gas, is commonly assumed to follow an isothermal distribution ($\rho \propto r^{-2}$), or in some cases, it is assumed to follow an NFW profile or a β model (e.g., [Cavaliere & Fusco-Femiano, 1976](#)). While this hot gas can cool down via the aforementioned cooling function, the temperature of the hot gas remains unchanged, with cooling leading to the accumulation of cold gas. This cold gas is typically assumed to form a self-gravitating, rotating disc that inherits angular momentum from the halo. The amount of gas cooling into the disc is determined by comparing the cooling timescale

$$t_{\text{cool}} = \frac{E_{\text{therm}}^{\text{hot gas}}(T)}{\rho(r)\Lambda(T, Z)} \quad (2.5)$$

with a typical timescale associated with the halo, such as the dynamical time $t_{\text{dyn}} = R_{\text{vir}}/V_{\text{vir}}$. Here, $E_{\text{therm}}^{\text{hot gas}}(T)$ is the internal energy of the gas, and $\rho(r)$ represents the radial density distribution. A common approach is to distinguish between regimes dominated by cooling or infall. The former (latter) occurs when the cooling time is longer (shorter) than the dynamical time, resulting in gas transitioning from the hot to the cold phase over different timescales (e.g., [White & Frenk, 1991](#); [De Lucia et al., 2004](#)). This simplified model performs well when compared to results from hydrodynamic simulations (e.g., [Monaco et al., 2014](#)).

Finally, SAMs also account for the UVB, albeit in a more pragmatic way. Ionizing photons from stars are expected to heat gas, preventing it from cooling. Therefore, the amount of gas infalling into small halos is adjusted according to redshift- and mass-dependent functions inspired by results of hydrodynamic simulations (e.g., [Gnedin, 2000](#)).

2.2.4 Astrophysical modeling

Most of the astrophysical processes of relevance for galaxy evolution occur well below the resolution of current cosmological simulations. This Section provides an overview of the most common strategies to implement these processes as sub-grid physics in both SAMs and hydrodynamic simulations.

- **Star Formation**

So far, the physics of DM and gas has been discussed. However, a fundamental component of galaxies are stars, which not only serve as the primary sources of observable luminous radiation but also provide essential chemical and energetic feedback crucial for the evolution of the ISM and CGM.

Gas transform into stars within dense and cold giant molecular clouds (GMCs, or MCs), typically with a relatively low efficiency (around $\sim 1\%$, e.g., [Bigiel et al. 2008](#)). GMCs are characterized by high densities ($n \gtrsim 1 - 100 \text{ cm}^{-3}$), typically exceeding the resolution capabilities of cosmological simulations. Therefore, empirical relationships are commonly employed to model their formation. Molecular hydrogen (H_2) is the main component of GMCs. This molecule forms on the surfaces of dust grains (in non-primordial environments; e.g., [Wakelam et al. 2017](#)) and is susceptible to dissociation by Lyman-Werner radiation. In simulations that distinguish between atomic and molecular gas, these physical processes are typically incorporated through empirically derived relations linking H_2 abundance with ISM metallicity or mid-plane pressure of the disc (e.g., [Blitz & Rosolowsky, 2006](#); [Krumholz et al., 2009](#)).

To simulate star formation, which is quantified by the star formation rate (SFR), both SAMs and hydrodynamic simulations adopt equations similar to the Schmidt-Kennicutt law (e.g., [Schmidt, 1959](#); [Kennicutt, 1998](#)).

$$\text{SFR} = \epsilon \frac{M_{\text{fuel}}}{\tau_{\text{SF}}}. \quad (2.6)$$

Here, ϵ represents an efficiency parameter (typically around $\sim 1 - 10\%$) that determines how effectively the star formation *fuel* converts into stars over a characteristic timescale τ_{SF} . Various approaches have been used to compute the terms in the equation above. One approach involves considering the star formation fuel as cold gas, often with a specified density (and sometimes temperature) threshold (e.g., [Springel & Hernquist, 2003](#); [Somerville et al., 2008](#)), either on a hydrodynamic particle level or within the context of SAMs. Alternatively, when employing sub-grid models to distinguish between atomic and molecular gas, the fuel is typically assumed to be the mass of gas in molecular form (e.g. [Davé et al., 2019](#); [Henriques et al., 2020](#)). In this context, it is worth mentioning [Ragone-Figueroa et al. \(2024\)](#), who were the first to model star formation based on the abundance of molecular gas derived from dust in hydrodynamic simulations.

In hydrodynamic simulations, the star formation timescale τ_{SF} is usually linked to the free-fall time of the gas, resulting in $\tau_{\text{SF}} \propto \rho^{-1/2}$. In SAMs, this timescale is often associated with the dynamical timescale of the halo or disc, $\propto R/V$.

SAMs employ additional strategies to model star formation. While the aforementioned methods describe standard star formation occurring in the cold gas disc, starbursts may be triggered by galaxy mergers or disc instabilities. In such cases, star formation rates are linked to parameters such as the mass ratio and gas content of merging galaxies (e.g., [Somerville et al., 2001](#)), or to a short timescale associated with spheroidal components resulting from disc instabilities (e.g., [Lacey et al., 2016](#)). These events, including dry mergers, are assumed to contribute to the build-up of the spheroidal component of galaxies.

The ultimate outcome of star formation includes the creation of stars (in hydrodynamic simulations) and the formation of a stellar disc (and possibly a bulge) in SAMs. These components represent stellar populations (not individual stars) formed according to an assumed IMF. Figure 2.6 shows three commonly adopted IMFs: [Salpeter \(1955\)](#), [Kroupa et al. \(1993\)](#), and [Chabrier \(2003\)](#). The IMF (by mass) $\phi(m)$ represents the distribution of stellar masses at birth per unit mass interval. In this Thesis, both the [Kroupa et al. \(1993](#), in hydrodynamic simulations) and [Chabrier \(2003](#), in the SAM) are adopted. Note the different slope of these

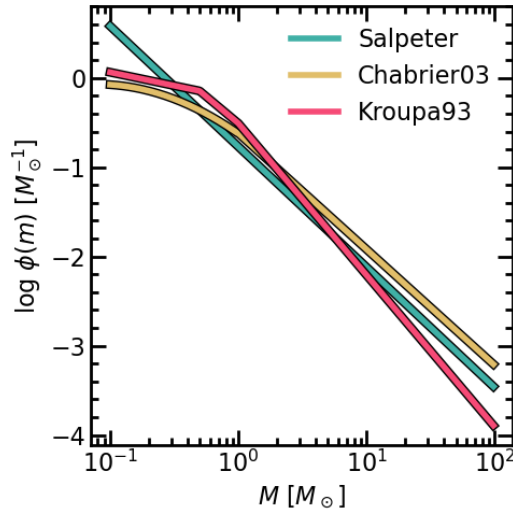


FIGURE 2.6: Three different IMFs widely adopted in literature: **Salpeter** (1955, green), **Chabrier** (2003, yellow) and **Kroupa et al.** (1993, red). All the IMFs are by mass and normalized in the mass range $[0.1, 100]M_{\odot}$.

two in the massive end.

- **Chemical and Energetic Stellar Feedback**

Galaxy evolution simulations enable the study of chemical and energetic feedback from stars. In the first works, stars were assumed to release metals into surrounding gas immediately upon formation, following the Instantaneous Recycling Approximation (IRA). However, more recent progresses have introduced refined chemical evolution models in both hydrodynamic simulations and SAMs (e.g., **Tornatore et al.**, 2007; **Yates et al.**, 2013). These models can track the Star Formation History (SFH) of each stellar component (such as individual particles or disc/bulge structures), accounting for delayed chemical enrichment from various sources like Type II supernovae (SNII), Type Ia supernovae (SNIa), and asymptotic giant branch stars (AGBs) based on assumed stellar lifetimes. They also incorporate detailed element-by-element yields, weighted by the assumed IMF. However, uncertainties remain regarding these yields derived from stellar evolution studies.

Stars, particularly SNe, significantly impact the ISM thermodynamics by releasing substantial energy (approximately $\sim 10^{51} - 10^{53}$ erg per event) during their explosions. This energy heats the gas and drives galactic-scale outflows, a crucial ingredient in galaxy evolution simulations.

In hydrodynamic simulations, this energetic feedback is modeled injecting energy from stellar particles (or star forming particles) directly into neighboring gas particles. However, early studies highlighted the inefficiency of this method in driving galactic outflows, primarily due to rapid cooling processes (e.g., **Katz et al.**, 1996). To address this, various techniques have been developed to stimulate outflows. Some simulations temporarily disable gas cooling following heating events (e.g., **Stinson et al.**, 2006), while others inject kinetic energy to stimulate outflows (e.g., **Springel & Hernquist**, 2003). An alternative method, as proposed by **Dalla Vecchia & Schaye** (2012), involves stochastic thermal energy injection to sufficiently heat gas particles and prevent rapid cooling, thereby promoting outflows.

Since the first seminal works like **White & Frenk** (1991), SAMs have employed tailored sub-grid approximations to simulate galactic outflows. Specifically, the outflow rate is typically

tied to the SFR through parameters that often correlate with halo properties. This approach enhances feedback efficiency in less massive halos with shallower potential wells. These outflows primarily transfer gas from the cold phase to a hot phase, assumed to be at virial temperature. Some models also incorporate an additional reservoir known as the ejected reservoir (e.g. [De Lucia et al., 2004](#); [Croton et al., 2006](#)). This reservoir accumulates material enriched by SN explosions, where the energy released overcomes that required to expel cold gas into the hot halo, resulting in an excess energy budget. Unlike hot gas, ejected material can not cool, although it remains available for potential reincorporation into the hot gas.

- **Black Hole Growth and Feedback**

While initial studies typically neglected them, current simulations commonly incorporate the physics of SMBHs, which is crucial for the evolution of massive galaxies. This includes modeling both the accretion of SMBHs and the associated feedback processes. These feedback mechanisms are typically categorized into quasar and radio modes (e.g., [Fabian, 2012](#)). The quasar mode corresponds to periods of high SMBH accretion rates, leading to the development of AGN winds. In contrast, the radio mode, which operates inefficiently in terms of radiation, produces jets and hot bubbles around massive galaxies during low-power SMBH accretion.

In hydrodynamic simulations, SMBHs are often represented by individual collisionless particles. The origin of the seed BHs, from which SMBHs grow, remains a topic of ongoing debate (e.g., [Volonteri, 2010](#)). In simulations, seeds are typically agnostically introduced once halos reach a certain mass threshold, sometimes with additional constraints on the mass of stars and gas. These seeds can grow by accreting surrounding gas, commonly modeled using the [Bondi \(1952\)](#) formula, where the SMBH accretion rate scales with ρM_{BH}^2 , with ρ representing the surrounding gas density. This accretion is often (upper-)bounded by the Eddington rate and may be further limited by the non-zero angular momentum of the gas (e.g., [Rosas-Guevara et al., 2015](#)). Eventually, two SMBHs merge when they approach each other within a specific distance, typically of the order of the softening length. Additionally, a criterion based on relative velocity can be adopted (e.g., [Di Matteo et al., 2005](#); [Davé et al., 2019](#)).

The single-particle representation of SMBHs in simulations is not trivial due to the statistical nature of N -body simulations. As a consequence of two-body interactions between SMBHs and surrounding particles, the motion of SMBH particles can become heated (e.g., [Tremmel et al., 2015](#)), potentially causing them to migrate or scatter outside the central regions of their host halos. In order to keep SMBHs at the centers of halos (or subhaloes) various ad-hoc strategies are employed, such as repositioning the center in the particle with minimum potential, adjusting the BH dynamical masses, or introducing effects like dynamical friction (e.g., [Springel et al., 2005a](#); [Debuhr et al., 2011](#); [Hirschmann et al., 2014](#); [Damiano et al., 2024](#)).

SMBH feedback is typically implemented by converting the SMBH accretion rate into a bolometric luminosity. A fraction of this luminosity, known as the radiative efficiency ($\approx 1 - 20\%$), is assumed to thermally couple with surrounding gas, heating it. In one of the pioneering studies on this topic, [Sijacki et al. \(2007\)](#) also incorporated radio mode feedback, active when the SMBH accretion rate is low, generating specialized hot gas bubbles.

In contrast, SAMs do not require detailed modeling of SMBH dynamics as they are assumed to form and remain at the centers of galaxies. Occasionally, seeding procedures are employed in these models. SMBH growth can occur during galaxy mergers (e.g., [Kauffmann & Haehnelt, 2000](#)) and disc instabilities (e.g., [Croton et al., 2016](#)), which are known to funnel

significant amounts of cold gas towards the galactic center. Cold gas accretion is often dependent on halo properties such as circular velocity. Additionally, accretion from the hot halo is considered and is typically modeled using phenomenological prescriptions. SMBHs eventually merge when their host galaxies merge.

In SAMs, SMBH feedback is treated in a simplified manner. Nearly all SAMs incorporate radio mode feedback, which is linked to low-rate hot gas accretion. This feedback injects energy into the hot gas medium, heating it and preventing excessive cooling (e.g., [Croton et al., 2006](#)). Quasar mode feedback, associated with cold gas accretion, is typically modeled by assuming that the ejection rate of cold gas into the hot halo is proportional to the SMBH accretion rate, adjusted for efficiency and halo properties (e.g., [Somerville et al., 2008](#)). However, in many cases, the quasar mode feedback is not explicitly implemented, justified by the concurrent occurrence of events like mergers and disc instabilities, which trigger starbursts which produce stellar feedback. In any case, this type of feedback is modeled using 1 – 2 free parameters that control the efficiency of energy coupling with the ISM. These parameters are difficult to constrain and are typically adjusted to reproduce key observables of the galaxy population.

2.3 The L-GALAXIES SAM

The SAM adopted in this work is the last public⁶ release of the Munich model, L-GALAXIES. A complete and detailed description of the model can be found in [Henriques et al. \(2020\)](#), as well as in the supplementary material available online at https://lgalaxiespublicrelease.github.io/Hen20_doc.pdf. While referring the reader to the aforementioned material, the main features of the model will be introduced in the following sections.

2.3.1 DM merger trees

L-GALAXIES has been originally designed to run on DM merger trees extracted from the MILLENNIUM and MILLENNIUM-II simulations ([Springel et al. 2005b](#); [Boylan-Kolchin et al. 2009](#)). The trees are constructed with the SUBFIND algorithm ([Springel et al., 2001](#); [Dolag et al., 2009](#)), and constitutes the backbone on top of which the baryonic processes are implemented. The time between the snapshots of the simulation, which is of the order of $\sim 30 - 500$ Myr, is divided into 20 equally spaced time-steps in order to model baryonic physics on a finer time grid. The SAM distinguishes between central, satellite, and orphan galaxies based on the DM halos they belong to. Central and satellite galaxies are associated with DM halos and satellite subhalos, respectively. Orphan galaxies are satellite that have lost their DM halo, either due to merging or falling below the resolution of the simulation, and are in the process of merging with the galaxy associated with the central (sub-)halo.

2.3.2 Gas infall and cooling

The starting point is assigning some gas to each DM halo, that is simulating the infall. The gas fraction, in the form of hot gas at the virial temperature T_{vir} of the halo, is assumed to be equal to the cosmic baryonic fraction $f_{\text{bar}} = 0.155$. At each time-step of the simulation, the total baryonic fraction of the halo is computed and the amount of hot gas is adjusted in order to ensure that f_{bar} is met. The effect of the UVB, which prevents infall into low-mass, high- z halos, is as well taken into account by considering a redshift- and DM halo mass-dependent f_{bar} ([Gnedin, 2000](#)).

⁶The source code is available at https://github.com/LGalaxiesPublicRelease/LGalaxies_PublicRepository/releases/tag/Henriques2020.

The hot gas M_{hot} , which is assumed to follow an isothermal distribution within the gravitational potential of the halo ($\rho_{\text{hot}} \propto r^{-2}$), is allowed to cool according to a time-scale:

$$t_{\text{cool}}(r) = \frac{3\mu m_{\text{H}} k_{\text{B}} T_{\text{vir}}}{2\rho_{\text{hot}}(r)\Lambda(T_{\text{vir}}, Z_{\text{hot}})}, \quad (2.7)$$

where $\Lambda(T_{\text{vir}}, Z_{\text{hot}})$ is the temperature- and metallicity-dependent cooling function of [Sutherland & Dopita \(1993\)](#).

From the cooling time-scale a cooling radius can be defined as the radius where the cooling time equals the halo dynamical time $t_{\text{dyn,h}} = R_{\text{vir}}/V_{\text{vir}}$:

$$r_{\text{cool}} = \left(\frac{t_{\text{dyn,h}} M_{\text{hot}} \Lambda(T_{\text{vir}}, Z_{\text{hot}})}{6\pi\mu m_{\text{H}} k_{\text{B}} T_{\text{vir}} R_{\text{vir}}} \right)^{0.5}. \quad (2.8)$$

If this radius is smaller than the virial radius, gas is in the *cooling flow regime* and cools at a rate

$$\dot{M}_{\text{cooling}} = M_{\text{hot}} \frac{r_{\text{cool}}}{R_{\text{vir}}} \frac{1}{t_{\text{dyn,h}}}, \quad (2.9)$$

otherwise, when $r_{\text{cool}} > R_{\text{vir}}$, gas is in the *fast accretion regime*:

$$\dot{M}_{\text{cooling}} = M_{\text{hot}} \frac{1}{t_{\text{dyn,h}}}. \quad (2.10)$$

2.3.3 The cold disc and star formation

The result of cooling is the formation (or accretion, if already existing) of the cold gas disc in the center of the halo, assumed to be rotationally supported. In this SAM, cold disc is divided in 12 concentric annuli with radii $r_i = 0.01 \cdot 2^i h^{-1}$ kpc ($i = 0, \dots, 11$; [Fu et al. 2013](#)). The gas within the disc is assumed to be distributed according to an exponential profile with scale-length r_{infall} . This is determined assuming the angular momentum of the cooling gas is conserved, i.e.

$$r_{\text{infall}} = \frac{j_{\text{DM,halo}}}{2V_{\text{max}}} \quad (2.11)$$

being $j_{\text{DM,halo}}$ and V_{max} , respectively, the specific angular momentum and the maximum circular velocity of the DM halo. A simple model for gas inflow within the disc due to the loss of angular momentum (assumed to be proportional to the angular momentum itself) is as well included.

The baryonic physics of the cold disc is modelled relying on this ring-based structure. Star formation is assumed to occur in molecular clouds within the disc. The molecular abundance is derived following the [Krumholz et al. \(2009\)](#) prescription (see also [McKee & Krumholz 2010](#)), which links the molecular-to-atomic ratio to the metallicity and surface density of the gas. This gives a molecular abundance for each gas ring, from which the SFR is derived according to:

$$\Sigma_{\text{SFR}} = \alpha_{\text{H}_2} \frac{\Sigma_{\text{H}_2}}{t_{\text{dyn}}}, \quad (2.12)$$

where t_{dyn} is the dynamical time of the cold gas disc (the ratio between the disc radius and the circular velocity assumed to be V_{max}) and α_{H_2} a free parameter of the model.

2.3.4 Chemical and energetic feedback from stars

The newly formed stars constitute the stellar disc, which is also divided into annuli. Feedback from these stellar populations is also modeled at the ring level.

The chemical feedback is modelled according to Yates et al. (2013), and it is capable to follow the time-dependent mass and elements return from AGB stars, SNIa and SNII to both the cold and hot medium. The model follows 11 elements, namely H, He, C, N, O, Ne, Mg, Si, S, Ca and Fe. This detailed implementation requires the tracking of SFHs in each ring (Shamshiri et al., 2015).

These stars will of course produce energetic feedback as well, which is modelled as follows. A certain amount of energy from SNe explosions is assumed to be returned to the gas component:

$$\Delta E_{\text{SN}} = \epsilon_{\text{halo}} \Delta M_{*,\text{ret}} \eta_{\text{SN}} E_{\text{SN}}, \quad (2.13)$$

where $\Delta M_{*,\text{ret}}$ is the mass returned from stellar evolution, η_{SN} the number of expected SNe per mass returned to the ISM, $E_{\text{SN}} = 10^{51}$ erg the energy of each SN event and $\epsilon_{\text{halo}} = \epsilon_{\text{halo}}(V_{\text{max}})$ a free parameter of the model. Some of this energy is used to re-heat the cold gas component, which is transferred to the hot gas atmosphere. The re-heated mass is $\Delta M_{\text{reheat}} = \epsilon_{\text{disc}} \Delta M_{*,\text{ret}}$, where $\epsilon_{\text{disc}} = \epsilon_{\text{disc}}(V_{\text{max}})$ is another free parameter of the model. The reheating thus requires an energy

$$\Delta E_{\text{reheat}} = \frac{1}{2} \Delta M_{\text{reheat}} V_{\text{vir}}^2, \quad (2.14)$$

which is of course limited by the total amount of ΔE_{SN} available. Should $\Delta E_{\text{SN}} > \Delta E_{\text{reheat}}$ there is still some energy $\Delta E_{\text{eject}} = \Delta E_{\text{SN}} - \Delta E_{\text{reheat}}$ available. This is used to eject material from the hot halo into another reservoir, called the ejected reservoir. The ejected mass is computed as

$$\Delta E_{\text{eject}} = \frac{1}{2} \Delta M_{\text{eject}} V_{\text{vir}}^2. \quad (2.15)$$

This material represents hot gas which is not able to cool, and it has been historically introduced in SAMs to avoid the overabundance of low mass galaxies. This material can be reincorporated into the hot gas atmosphere (therefore being again able to cool) assuming a reincorporation timescale which is a free parameter of the model and proportional to $\propto M_{\text{vir}}^{-1}$, so that it is more stringent for less massive objects.

2.3.5 Disc Instabilities and Mergers

While the stellar disc originates from the *canonical* star formation, a stellar bulge can form during disc instabilities and mergers. As for the former, they occur when the centrifugal force of the disc is not enough to counteract its gravity, giving origin to instabilities (e.g. bar formation). This is modelled by transferring some material from the stellar disc to the stellar bulge when some condition is met. In this Thesis, the implementation of disc instabilities has been substantially changed from the original L-GALAXIES formulation, and therefore will be discussed in detail in Section 5.2.1.

Mergers of DM halos can as well affect the stellar component, and star formation, of a galaxy. When DM halos merge, their associated galaxies (i.e. all their components) merge as well, with some delay. This delay, due to dynamical friction, is associated with a time

scale which depends, among other factors, on the ratio of the satellite and the central galaxy (Binney & Tremaine, 1987).

Mergers trigger starbursts, modelled according to the collisional starburst (SB) recipe introduced by Somerville et al. (2001):

$$M_{*,\text{SB}} = \alpha_{\text{SB}} \left(\frac{M_1}{M_2} \right)^{\beta_{\text{SB}}} M_{\text{cold}}. \quad (2.16)$$

In the above formula, $M_1/M_2 < 1$ is the baryonic ratio of the two galaxies, M_{cold} is the cold gas mass in each of the rings resulting from the merger, and α_{SB} and β_{SB} free parameters of the model.

The outcome of a merger event depends as well on the total baryonic mass ratio of the two galaxies. If it is > 0.1 the merger is dubbed major, the stellar discs of the two galaxies are destroyed and transferred to a bulge component⁷. Also, stars formed in the SB event are transferred to the bulge. In a minor merger (baryonic mass ratio < 0.1), the stars of the smaller galaxy are transferred to the bulge component of the larger one. However, the disc of the latter can survive and host any stars formed during the SB.

The stellar bulge is also divided into concentric rings, and the mass distribution is assumed to follow a Jaffe (1983) profile. The characteristic scale-length of the latter is obtained from energy conservation arguments. Updates introduced in this Thesis about bulge sizes are described in detail in Section 5.2.2.

2.3.6 Black hole physics

BHs in L-GALAXIES are assumed to grow in a twofold way, namely by accretion of cold and hot gas, as well as during mergers of BHs, which are associated with galaxy mergers.

Cold gas accretion, often referred to as quasar mode, is assumed to occur during mergers. If no BH is present, this is the way to form a BH in this model. The mass of gas transferred to the new or existing BH during a merger whose *total* cold gas mass is M_{cold} reads:

$$\Delta M_{\text{BH}} = \frac{f_{\text{BH}}(M_1/M_2)M_{\text{cold}}}{1 + (V_{\text{BH}}/V_{\text{vir}})^2}, \quad (2.17)$$

where f_{BH} and V_{BH} are free parameters of the model. This merger-driven channel is the most important for BH growth, albeit it is not associated with any form of feedback. A commonly invoked justification for this lack is that, during mergers, the feedback associated with the starburst already ejects some cold gas from the ISM.

The other growth mode⁸ of BHs is the radio-mode, during which BHs accrete material from the hot gas, according to the phenomenological description introduced by Croton et al. (2006):

$$\dot{M}_{\text{BH}} = k_{\text{AGN}} \left(\frac{M_{\text{hot}}}{10^{11} M_{\odot}} \frac{M_{\text{BH}}}{10^8 M_{\odot}} \right), \quad (2.18)$$

with k_{AGN} a free parameter of the model. This channel is associated with feedback. Namely, a fraction of the accreting energy is radiated away and coupled to the hot gas according to an efficiency $\eta = 0.1$:

$$\dot{E}_{\text{AGN}} = \eta \dot{M}_{\text{BH}} c^2. \quad (2.19)$$

⁷Also pre-existing bulges, if any, are added to the new bulge.

⁸This channel can not create a BH. Therefore, a BH must be already in place to be effective.

This input energy is thought to limit the hot gas cooling into the cold gas disc. Specifically, the cooling rate discussed in Section 2.3.2 is reduced by an amount of $2\dot{E}_{\text{AGN}}/V_{\text{vir}}^2$. If the latter overcomes the cooling rate, cooling is completely stopped. Therefore, this process is able to quench star formation by *preventing* cooling of the hot gas.

Finally, in this Thesis a new channel for BH formation and growth has been introduced. This is essentially the same as in mergers, but assuming to occur during disc instabilities. It will be discussed at length in Section 5.2.1.

2.3.7 Environmental processes

DM merger trees are able to follow the relative position and mergers of DM halos, thus processes occurring on inter-galactic scales can be modelled as well.

One of these processes is tidal stripping, occurring when a DM halo enters the virial radius of a larger one. In this case gas infall is stopped, and the hot gas is removed (stripped) in the same proportion of the DM mass. When the DM halo is completely destroyed (or, equivalently, falls below the resolution of the simulation), its hot gas atmosphere has been completely removed as well. In the context of this SAM, these galaxies are dubbed *orphan*.

Similarly, ram pressure stripping is assumed to occur in satellites systems of large halos ($M_{\text{DM,halo}} \geq 10^{14} M_{\odot}$) and depends on the virial velocities of the two halos. It only affects the hot gas atmosphere, and not the cold gas disc.

Finally, tidal disruption of orphan galaxies is assumed to occur when the baryonic density of these galaxies is lower than the DM density of the host halo within the satellite orbit. In this case, the stars and the cold gas of the satellite are transferred, respectively, to the IntraCluster Light (ICL) and hot atmosphere of the central DM halo.

2.4 Hydrodynamic simulations with MUPPI

The hydrodynamic simulations conducted in this Thesis adopt the GADGET3 code, which evolved from its precursor GADGET2 (Springel, 2005). It is able to follow the evolution of both collisionless (DM, stars) and ideal fluid (gas) particles. Gravitational forces are computed with the TreePM algorithm, while the SPH scheme is the one introduced by Beck et al. (2016).

The modeling of unresolved physics relies on the MUPPI (MULTI Phase Particle Integrator) algorithm. It is adopted to model the processes already introduced in Section 2.2, i.e. gas cooling, star formation, feedback. For more information on the model, I refer the reader to Murante et al. (2010, 2015), as well as to Valentini et al. (2020) for a detailed description of the version adopted here. In this section, I will sketch its main features, which are essential to understand the dust model implementation within the context of hydrodynamic simulations adopted in this work.

2.4.1 Multiphase gas: partitioning and evolution

The fundamental unit of the MUPPI model is the multiphase (MP) gas particle, which represents a piece of multiphase ISM. It hosts both a hot and a cold phase coexisting at pressure equilibrium, as well as a *virtual* stellar component. These components have mass, respectively, M_h , M_c , and M_* . The total mass of the MP particle M_{MP} is the sum of the three components.

The hot and cold phases have number density n and temperature T such that they are at pressure equilibrium, which means

$$n_c T_c = n_h T_h. \quad (2.20)$$

While the cold gas temperature is assumed to be fixed⁹ $T_c = 300$ K, the other quantities are determined in the following way. At the beginning, gas particles are not MP. They become MP particles when the density and temperature become, respectively, larger and lower than a certain threshold. In the current implementation, these conditions read $n \geq n_{\text{thresh}} = 0.01 \text{ cm}^{-3}$ and $T \leq T_{\text{thresh}} = 5 \cdot 10^4$ K. When these conditions are met, the MP particle is made entirely of hot gas, whose temperature T_h is the temperature of the gas particle derived from the hydrodynamic scheme. The hot gas is allowed to cool, according to the prescriptions by [Wiersma et al. \(2009\)](#). This prescription links the cooling rate to the metals element abundance of each MP particle. Moreover, gas is assumed to be optically thin and exposed to a UVB ([Haardt & Madau, 2001](#)). In summary, the cooling rate of each MP particle will depend on the density, temperature, and redshift. When cooling is on, some hot gas mass becomes cold gas, with temperature $T_c = 300$ K. At this point, the mass fraction of the hot and cold gas, F_h and F_c , are related to the volume filling factor f_h and $f_c = 1 - f_h$ by

$$f_h = \frac{1}{1 + \frac{F_c \mu_h T_c}{F_h \mu_c T_h}}, \quad (2.21)$$

where $\mu_h = 0.6$ and $\mu_c = 1.2$ are the mean atomic weights of the hot and cold phase, obtained assuming a ionized and neutral gas, respectively.

Once the filling factor is known, deriving the number density of the hot (and consequently of the cold) component of the MP particle is straightforward:

$$n_h = \frac{F_h}{f_h \mu_h m_H} \rho, \quad (2.22)$$

with m_H the proton mass and ρ the gas particle density as estimated by the SPH algorithm.

The thermodynamic properties of the MP components are well specified (the stellar component of the MP particle is completely specified by its mass M_*). The ordinary differential equations which regulates the exchange of mass and energy between these components are:

$$\dot{M}_h = -\dot{M}_{\text{cool}} + \dot{M}_{\text{ev}} + \dot{M}_{\text{c} \rightarrow \text{h}}^{\text{AGN}}, \quad (2.23)$$

$$\dot{M}_c = \dot{M}_{\text{cool}} - \dot{M}_{\text{sf}} - \dot{M}_{\text{ev}} - \dot{M}_{\text{c} \rightarrow \text{h}}^{\text{AGN}}, \quad (2.24)$$

$$\dot{M}_* = \dot{M}_{\text{sf}}, \quad (2.25)$$

$$\dot{E}_h = \dot{E}_{\text{fb, local}} - \dot{E}_{\text{cool}} + \dot{E}_{\text{hydro}} + \dot{E}_{\text{c} \rightarrow \text{h}}^{\text{AGN}} + \dot{E}_h^{\text{AGN}}, \quad (2.26)$$

$$\dot{E}_{\text{c, used}}^{\text{AGN}} = \dot{E}_{\text{c} \rightarrow \text{h}}^{\text{AGN}} \quad (2.27)$$

The first three equations regulate the exchange of mass between the MP particle components, while the fourth equation determines the energy (and temperature) evolution of the hot gas component¹⁰. The last equation describes the AGN feedback energy used to evaporate the cold gas. Let us analyse each of the terms appearing in these equations.

⁹Keeping the cold gas temperature fixed is needed because the cooling of the gas is not followed below $< 10^4$ K. The chosen value is a free parameter of the model which essentially regulates the duration of the MP stage (see [Murante et al. 2010](#)).

¹⁰Please remember that the cold gas component is assumed to be at fixed temperature $T_c = 300$ K.

2.4.2 Cooling and star formation

The hot mass gas evolution (Eq. 2.23) depends on the cooling, which transfers mass from the hot to the cold phase at a rate:

$$\dot{M}_{\text{cool}} = \frac{M_{\text{hot}}}{t_{\text{cool}}}, \quad (2.28)$$

with t_{cool} the cooling time. Hot gas mass is also enriched by some material coming from the molecular clouds, which is thought to evaporate as a result of the feedback from newly born massive stars. This process, called *evaporation*, is modelled linking the evaporating mass to the SFR of the particle \dot{M}_{sf}

$$\dot{M}_{\text{ev}} = f_{\text{ev}} \cdot \dot{M}_{\text{sf}}, \quad (2.29)$$

where f_{ev} is a parameter of the model.

The cold gas mass (Eq. 2.24) is affected by the same processes (with reversed signs), in addition to star formation. The latter is assumed to occur in molecular clouds, which are well below the resolution of the MP particles. The cold phase is assumed to host a certain fraction of mass f_{mol} which is in the form of molecular clouds¹¹. The molecular fraction is computed following the empirical prescription of [Blitz & Rosolowsky \(2006\)](#), which has been derived from observations and links f_{mol} to the pressure P of the gas particle:

$$f_{\text{mol}} = \frac{1}{1 + \frac{P_0}{P}}, \quad (2.30)$$

with $P_0 = 2 \cdot 10^4 k_B \text{ K cm}^{-3}$ is the pressure of the ISM at which $f_{\text{mol}} = 0.5$ and it is derived from observations (see [Blitz & Rosolowsky, 2006](#)).

Once the molecular mass is specified, the SFR of the MP particle is computed as

$$\dot{M}_{\text{sf}} = f_* \frac{f_{\text{mol}} M_c}{t_{\text{dyn,c}}}, \quad (2.31)$$

where f_* is the star formation efficiency set to 0.02, and

$$t_{\text{dyn,c}} = \sqrt{\frac{3\pi}{32G\rho_c}} \quad (2.32)$$

is the dynamical time associated with the cold phase of the MP particle.

The MP particle SFR is used to spawn star particles according to the model of [Springel & Hernquist \(2003\)](#). In brief, given an MP particle of mass M_{MP} which has converted some gas into stars ΔM_* during a time-step (Eq. 2.25) it has a probability

$$p = \frac{M_{\text{MP}}}{M_{*,\text{init}}} \left[1 - \exp\left(-\frac{\Delta M_*}{M_{\text{MP}}}\right) \right] \quad (2.33)$$

to generate a star particle with mass $M_{*,\text{init}}$. Operationally, the star particle is generated if p exceeds a random number $\in [0, 1]$. In star formation episodes, a number $N_* = 4$ stellar particles are generated¹², each with mass $M_{*,\text{init}} = M_{\text{MP}}/N_*$.

¹¹Of course, thermodynamic properties of the molecular clouds are not the same as the ones of the cold phase.

¹²When a stellar particle is created, $M_{*,\text{init}}$ is subtracted from the virtual stellar reservoir. If the reservoir does not have enough mass, then the required mass is taken from the cold phase.

2.4.3 Stellar feedback

The thermal energy of the hot gas is regulated by Equation 2.26. In the hypothesis of ideal gas and assuming a polytropic EOS with adiabatic index $\gamma = 5/3$, this determines the hot gas temperature

$$T_h = \frac{E_h}{M_h} \frac{(\gamma - 1)\mu_h m_H}{k_B}. \quad (2.34)$$

Energy (and temperature) are affected by two processes, that is feedback (from stars and AGN) and cooling. Feedback from stars is taken into account into the $\dot{E}_{\text{fb, local}}$ and \dot{E}_{hydro} terms¹³. The first describes the thermal energy feedback coming from SN explosions occurring in molecular clouds within the same MP particle (i.e. locally). This is

$$\dot{E}_{\text{fb, local}} = f_{\text{fb, local}} E_{\text{SN}} R_{\text{SNII}}, \quad (2.35)$$

where R_{SN} is the IMF- and SFR-dependent SNII rate, $E_{\text{SN}} = 10^{51}$ erg is the energy assumed to be released by each SN event, and $f_{\text{fb, local}} = 0.02$ is a free parameter of the model.

In addition to the feedback coming from the local star formation, also neighboring particles are able to exert a form of feedback. In particular, star forming particles are able to transfer a certain amount of thermal energy to their surrounding particles. For each neighboring star forming particle, this energy is essentially the same as before, but with a different parameter $f_{\text{fb, therm}} = 0.2$. This means that, in a time-step, each star forming particle is able to donate an amount of energy

$$\Delta E_{\text{fb, therm}} = f_{\text{fb, therm}} E_{\text{SN}} N_{\text{SNII}}, \quad (2.36)$$

with N_{SNII} the IMF- and SFR-dependent number of SNII formed.

This energy is shared among particles within a cone with opening angle $2\theta = 60^\circ$ aligned as (minus) the particle density gradient. Each particle in the cone receive energy weighted by the SPH kernel (see [Valentini et al. 2017](#) for details).

Also kinetic feedback is implemented. When a particle exits the MP ($\rho < 0.2\rho_{\text{thresh}}$ or it spent a time $t_{\text{clock}} = t_{\text{dyn, c}}$ in this stage) it can be eligible to become a wind particle. This is essentially a particle which can receive kinetic feedback from surrounding particles. The probability of becoming a wind particle $P_{\text{wind}} = 0.05$ is a free parameter of the model, as well as the time during which the wind particle is decoupled from the others particle ($t_{\text{wind}} = 20 - t_{\text{clock}}$ [Myr])¹⁴. Each star forming MP particle can deliver an amount of kinetic energy in a given time-step

$$\Delta E_{\text{kin}} = f_{\text{fb, kin}} E_{\text{SN}} N_{\text{SNII}}, \quad (2.37)$$

with $f_{\text{fb, kin}} = 0.26$ a free parameter of the model. Following a similar approach to the thermal energy distribution, this energy is distributed among wind particles within the aforementioned cone and its smoothing length.

Finally, chemical feedback from star particles is taken into account. The chemical enrichment model, which follows 15 elements (H, He, C, N, O, Ne, Na, Mg, Al, Si, S, Ar, Ca, Fe, and Ni), relies on the work of [Tornatore et al. \(2007\)](#). Each star particle, which represents a co-eval stellar population, has the chemical composition of the gas from which it originated. Assuming the IMF and mass-dependent lifetimes, the contribution of AGB, SNIa and SNII

¹³The latter also includes the hydrodynamic heating and cooling, that is due to the gravitational compression and expansion of the gas.

¹⁴The particle can also exits the wind stage if its density falls below $0.3\rho_{\text{thresh}}$, which would indicate the particle went out from the star forming region from which it is receiving feedback.

to the chemical yields is taken into account at each time-step of the simulation. Consistently, the SNIa rate of each star particle is used to include their contribution to the energy feedback in Equation 2.26. The ejected metals are distributed among neighbouring gas particles.

2.4.4 Black hole physics

The MUPPI version adopted here includes a treatment for BH physics, i.e. growth and feedback (Valentini et al., 2020). BHs are represented by sink collisionless particles. When a DM halo exceeds a threshold of $M_{\text{DM, thresh}} = 1.7 \cdot 10^{10} M_{\odot}$ and has a stellar mass fraction of $\geq 2\%$, a BH of mass $M_{\text{BH, seed}} = 1.1 \cdot 10^5 M_{\odot}$ is seeded in its center^{15,16}. BHs can grow by accreting surrounding gas following the Bondi accretion rate:

$$\dot{M}_{\text{BH}} = \frac{4\pi G^2 M_{\text{BH}}^2 \langle \rho \rangle}{(\langle c_s \rangle^2 + \langle v \rangle^2)^{3/2}}, \quad (2.38)$$

where ρ is the gas density, c_s the speed of sound and v the relative gas-BH velocity. These quantities are averaged over particles within the BH smoothing length. Both cold and hot gas accretion is considered, and their sum can not exceed the Eddington limit. In addition, BHs accretion is limited by the angular momentum of the gas, so that only gas with low angular momentum (i.e. non rotationally supported) can be accreted into the BH. Operationally, the accretion is implemented by allowing surrounding gas particle to be swallowed by the BH. The other BHs accretion channel available is merging, which is assumed to occur when two BH particles are within twice the softening length, and their relative velocity is lower than half the speed of sound in the surrounding gas.

Accretion of gas into BHs translates into feedback, an important process which modifies the thermodynamic properties of the gas. The energy associated with accretion is assumed to be

$$\dot{E}_{\text{fb}}^{\text{AGN}} = \epsilon_r \epsilon_f \dot{M}_{\text{BH}} c^2, \quad (2.39)$$

where ϵ_r and ϵ_f are two parameters representing, respectively, the fraction of energy radiated away and the coupling efficiency with the surrounding gas. This energy is distributed among gas particles within the smoothing kernel. If a gas particle is *not* MP, this amount of energy simply enters into the hydrodynamic equation that regulates the internal energy.

For MP particles, a more careful approach is adopted to distribute the energy between the cold and hot phase. Namely, a fraction \mathcal{A}_c is used to heat the cold phase, and the remaining fraction $\mathcal{A}_h = 1 - \mathcal{A}_c$ is coupled to the hot phase. In brief, the energy to the hot phase is used to increase the hot gas temperature (\dot{E}_h^{AGN} in Equation 2.26). Contrarily, being the cold phase at a fixed temperature $T_c = 300$ K, the feedback to the cold phase translates into the evaporation of cold gas to the hot phase. At each time-step, the evaporating mass is computed, represented by the term $\dot{M}_{c \rightarrow h}^{\text{AGN}}$ in Equations 2.23 and 2.24. The corresponding AGN energy used is $\dot{E}_{c \rightarrow h}^{\text{AGN}}$ and it also contributes to increase the hot gas temperature (Equation 2.26).

Note that $\dot{E}_{c \rightarrow h}^{\text{AGN}}$ does not necessarily corresponds to the available AGN feedback energy, since the evaporating mass is limited by the actual amount of the cold gas. For this reason, the amount of energy coupled to the cold phase which is actually used (Equation 2.27) is $\leq \mathcal{A}_c \dot{E}_{\text{fb}}^{\text{AGN}}$. Should remain some available energy not consumed to evaporate cold gas, it is coupled to the hot gas.

¹⁵These values are possibly scaled with the resolution of the simulation.

¹⁶In order to avoid spurious numerical effects, it is re-positioned in the position of minimum gravitational potential of the halo at each time-step of the simulation.

3

Modeling dust in galaxy evolution simulations

Being dust grains an essential ingredient of galaxies, it is highly desirable to model its production and evolution within galaxy evolution simulations. This has at least three different and well motivated aims. First, it helps us understand the role of various processes that influence the abundance of observed dust in both local and high-redshift galaxies. Second, it is a necessary step for our simulations to properly predict observable quantities, which are of course affected by both dust obscuration and emission. Lastly, since dust grains actively participate to the physics of galaxy evolution, modeling dust is essential to incorporate a number of processes that improve the accuracy of our simulations.

In this context, a dust model is a physical model designed to predict the abundance and properties of dust throughout the galaxy evolution simulation. This model is fully integrated into the simulation, meaning it both is based on and influences the simulation predictions. In this Thesis, I will not discuss dust models working in post-processing.

Most of this Chapter is devoted to describe the development and historical evolution of dust models in literature. First, I will depict the life-cycle of dust grains in galactic environments, which represents the physical foundation of any dust model. Next, I will review the pioneering dust models used in galactic chemical evolution studies. Following this, I will introduce and discuss the dust models recently adopted in both SAMs and hydrodynamic simulations, highlighting the key results achieved by these studies. Finally, I will detail the dust model which is at the core of this Thesis.

CONTENTS

| | |
|--|----|
| 3.1 Dust life-cycle | 35 |
| 3.2 Chemical evolution models | 36 |
| 3.3 Numerical Simulations | 43 |
| 3.4 The dust model in L-GALAXIES and MUPPI | 55 |

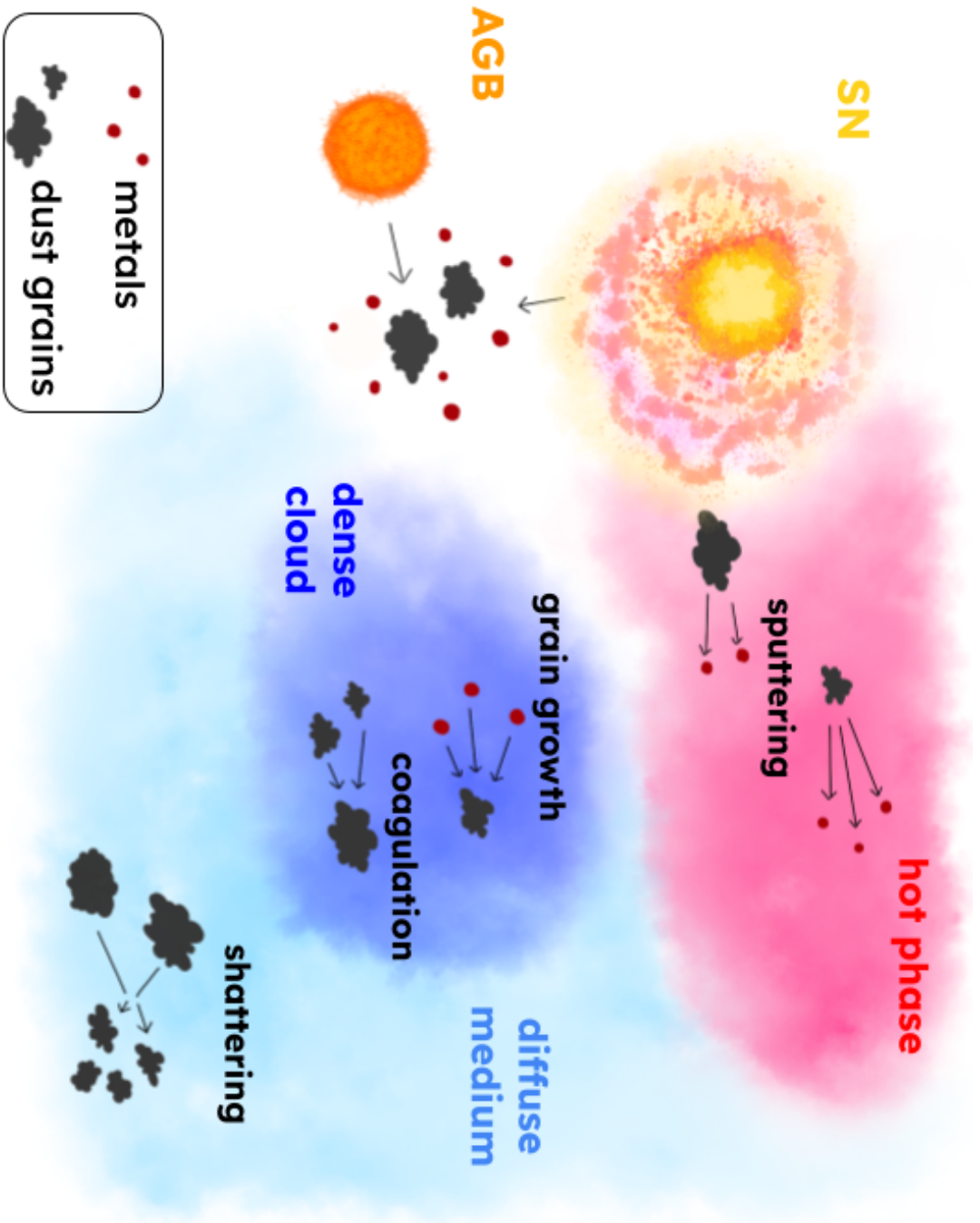


Figure 3.1: Schematic sketch depicting the dust life-cycle in galaxies. Grains form in AGB winds and SNe ejecta, and are thus injected into the ISM. Here, accordingly to the physical conditions of the medium, different processes may affect grains evolution. Shattering in the diffuse and turbulent medium, coagulation of small grains and accretion of gas phase metals in dense and cold clouds, sputtering in the hot medium. See text for details on the processes.

3.1 Dust life-cycle

To model the evolution of dust grains within the broader galactic context, it is essential to understand their life-cycle and how various astrophysical processes influence their abundance and properties. A schematic illustration of the main processes described below is provided in Figure 3.1.

Dust grains are produced in the final stages of stellar evolution. As suggested by IR observations of circumstellar material (e.g. Gehrz & Woolf, 1971), high density winds associated with late stellar phases, in particular the AGB one, of low-to-intermediate mass stars ($1 \lesssim M/M_{\odot} \lesssim 8$) are suitable sites for the condensation of solid grains. The composition of these grains depends on the chemical composition of the outflowing material (e.g. Ferrarotti & Gail, 2006; Gail et al., 2009; Di Criscienzo et al., 2013; Nanni et al., 2013, 2014; Dell’Agli et al., 2017). Grains produced in AGB winds are expected to be relatively large, with sizes $\gtrsim 0.1 \mu\text{m}$ (e.g. Winters et al., 1997; Ventura et al., 2012).

The other relevant channel of grains production are SNe ejecta. Far-IR observations of the SN1987A event have clearly demonstrated this (Moseley et al., 1989; Kozasa et al., 1989; Wooden et al., 1993). Models based on the nucleation theory (Feder et al., 1966) provided estimates of the amount and properties of grains formed in ejecta of core collapse SNe, predicting large amount of dust formed ($\approx 0.1 - 1 M_{\odot}$ per event; e.g. Todini & Ferrara 2001; Nozawa et al. 2003). However, the survival of these grains during the explosion-driven reverse shock is uncertain (e.g. Nozawa et al., 2007; Bianchi & Schneider, 2007; Bocchio et al., 2014). The reverse shock is also expected to skew the distribution of grains towards large sizes, since small grains are destroyed more easily (e.g. Nozawa et al., 2007).

Once ejected into the ISM, various processes can influence the evolution of dust grains. Collisions between grains can affect the grain size distribution. In dense and cold molecular clouds, low-speed collisions promote the sticking of grains, known as *coagulation*, resulting in the formation of larger particles (e.g. Ormel et al., 2009; Hirashita & Voshchinnikov, 2014). In contrast, in the diffuse and turbulent medium, collisions can lead to the fragmentation, or *shattering*, of grains (e.g. Yan et al., 2004; Hirashita & Yan, 2009), which significantly shift the distribution towards smaller sizes.

Dust grains can also change their mass during their journey into the ISM. In dense and cold clouds, gas-phase metals can stick on the surfaces on dust grains, increasing their mass (e.g. Liffman & Clayton, 1989; Dwek, 1998; Hirashita, 1999b). This process is often referred to as *grain growth* or (*metals*) *accretion*. It is of course favoured by the metals content of the cloud, and it also depends on the grain size distribution. Indeed, this is a surface process and it is more likely to occur on small dust grains, whose surface-to-volume ratio is larger (e.g. Hirashita & Kuo, 2011).

In hostile environments, collisions between gas and grains can cause grains to lose mass by returning gas-phase metals to the ISM, a process known as *sputtering*. The most destructive environment for this process is the shock generated by a SN explosion, where conditions for both thermal and non-thermal sputtering are met, such as high velocities $\gtrsim 100 \text{ km s}^{-1}$ and high temperatures $\gtrsim 10^6 \text{ K}$ (e.g. Dwek & Scalo, 1980; McKee, 1989; Nozawa et al., 2006; Hu et al., 2019). In this work, this process will be referred to as *SN destruction* to differentiate it from *pure* thermal sputtering, which occurs in the hot gaseous galactic and circum-galactic phases. This occurs in the high-temperature ($T \gtrsim 10^6 \text{ K}$) plasma as a result of ions-grains collisions which eventually leads to grains erosion (e.g. Barlow, 1978; Tsai & Mathews, 1995). Another (minor) destruction process at work for dust grains is photo-evaporation, which occurs in the presence of strong radiation fields (e.g. Nanni et al., 2024).

To conclude, it is important to mention some additional properties of grains that influence their life-cycle in the ISM. Grains typically possess a non-zero electric charge, which can affect their interactions with ions (and thus grain growth), their dynamics, and their interactions with photons (e.g. [Zhukovska et al., 2018](#); [Melzer, 2019](#); [Glatzle et al., 2022](#)). Another characteristic that can impact grain evolution in the ISM is porosity, as it alters the total surface area (e.g. [Hirashita, 2022](#)). In this Thesis, as well as in the large majority of galaxy evolution simulations which include dust, neither electric charge nor porosity are considered.

3.2 Chemical evolution models

Historically, the first tools adopted by theoreticians to model dust formation and evolution in a galactic context were chemical evolution models (e.g. [Tinsley 1980](#); see also [Matteucci 2003](#) and references therein). These are typically one-zone and one-phase models. The former means that they lack spatial resolution (i.e. same properties in the whole disc, or disc+bulge in the case of two-zones models), while the latter that the model averages gas ISM properties over the cold, warm and hot phase. In the most simple cases, a set of coupled non-linear integro-differential equations are used to model gas infall, star formation, and chemical enrichment, eventually adopting different prescriptions for different types of galaxies (e.g. [Matteucci & Tornambe, 1987](#); [Bradamante et al., 1998](#); [Chiappini et al., 2001](#)).

Due to the chemically-oriented nature of these models, their use for studying galactic dust was a natural choice. The first pioneering attempts to include dust within basic models can be traced back to the 1980s ([Dwek & Scalo, 1980](#); [Liffman & Clayton, 1989](#); [Liffman, 1990](#); [Wang, 1991](#)). These early studies mainly aimed to explain depletion patterns or the chemical composition of grains in the solar neighborhood. They provided valuable insights for future, more complex models. For example, they suggested the importance of SNe as grains factories¹, as well as the need of grain growth in molecular clouds, which was not always included at that time.

[Dwek \(1998\)](#) was the first to include a dust model in a proper chemo-dynamical, two-zones chemical evolution model. The equation describing dust evolution is of the type²:

$$\dot{M}_{\text{dust}} = \dot{M}_{\text{dust}}^{\text{stars}}(t) - \frac{M_{\text{dust}}}{M_{\text{gas}}}\psi + \dot{M}_{\text{dust}}^{\text{growth}}(\tau_{\text{gg}}) - \dot{M}_{\text{dust}}^{\text{SN des}}(\tau_{\text{SN des}}) - \dot{M}_{\text{dust}}^{\text{outflow}}. \quad (3.1)$$

This equation essentially relates the ISM dust mass variation to the time-dependent stellar production of grains $\dot{M}_{\text{dust}}^{\text{stars}}(t)$, the mass of dust re-embedded into stars (commonly referred to as *astration*) proportional to the SFR ψ , the growth of grains in molecular clouds ($\dot{M}_{\text{dust}}^{\text{growth}}$, dependent on some timescale τ_{gg}), the destruction of grains in SN shocks ($\dot{M}_{\text{dust}}^{\text{SN des}}$, dependent on some timescale $\tau_{\text{SN des}}$), and the mass of dust removed by outflows $\dot{M}_{\text{dust}}^{\text{outflow}}$. These processes are identified as the fundamental ones in all the future dust models which aim at following the amount of dust³, even in the case of more complex, numerical simulations. The main differences among various dust models stand in the assumptions (e.g. dust yields, time-scales functional forms) that determine the terms in the above equation, along with possible adjustments in multi-phase models.

¹In [Dwek & Scalo \(1980\)](#), a number of sources were assumed to produce grains: planetary nebulae, winds of red giant stars, proto-stellar nebulae, novae and supernovae. As they report in a note added in proof, there was an observational claim of dust condensation in SN ejecta. The future clear SN1987a detection was just the confirm of the relevance of the SN channel.

²Actually, in the original [Dwek \(1998\)](#) model dust densities are considered instead of dust masses.

³Models that additionally describe the evolution of grain sizes should also take into account other processes, such as shattering and coagulation.

The seminal work by [Dwek \(1998\)](#) was focused on galactic dust, in particular on depletion patterns. The model essentially confirmed the dominance of SNII (and SNIa, for iron dust) as dust sources, as well as of the grain growth in molecular clouds.

Thanks to the advance in observations, and in particular to the *IRAS* satellite and SCUBA camera operating in the IR, it became also possible to study dust beyond our Galaxy. A particularly intriguing relation that emerged was that between the dust-to-gas ratio (DTG) and gas phase metallicity Z (e.g. [Issa et al., 1990](#); [Schmidt & Boller, 1993](#)). Chemical models constituted a powerful tool to investigate this relation, in both dwarf and spiral local galaxies ([Lisenfeld & Ferrara, 1998](#); [Dwek, 1998](#); [Hirashita, 1999a,b](#); [Edmunds, 2001](#); [Inoue, 2003](#); [Galliano et al., 2008](#); [Mattsson & Andersen, 2012](#); [Kuo et al., 2013](#); [Feldmann, 2015](#); [Schneider et al., 2016](#)). In the low metallicity range, dwarfs exhibit a flatter and more scattered pattern in the observed DTG– Z relationship, whereas spiral galaxies display an inclining slope. It became apparent that, while the relation in dwarf galaxies is well reproduced thanks to the stellar production channel and some stochasticity to ensure the observed scatter, the growth in clouds is necessary for explaining the DTG in more metal enriched galaxies ([Hirashita, 1999a,b](#)). [Inoue \(2011\)](#) and [Asano et al. \(2013a\)](#) introduced the concept of *critical metallicity*, above which ISM grain growth becomes the dominant process. This is set by the competition between the efficiency of grain growth and destruction (or dust-free inflows, see [Feldmann 2015](#)).

Other extra-galactic observations (e.g. [Lilly et al., 1999](#); [Eales et al., 2000](#)) made it necessary to expand the study of dust evolution in galaxies different from our MW. A step in this direction was moved by [Calura et al. \(2008\)](#). Adopting a formalism similar to that of [Dwek \(1998\)](#), they formulated a treatment of the evolution of dust in spirals, ellipticals and irregular galaxies, assuming different prescriptions for grain growth in each of these categories. Also, they included ejection of dust by outflows, pointing out that large dust masses may be found in the hot CGM/IGM, although they were missing a model for the destruction in this hostile medium by thermal sputtering.

Starting from the [Calura et al. \(2008\)](#) model, [Gioannini et al. \(2017\)](#) tried to overcome the lack of cosmological context of chemical models. The different prescriptions for dust evolution in different galaxy types are coupled with some assumptions on the abundance of spiral, elliptical and irregular galaxies across cosmic time. In this way, the authors were able to predict the cosmic dust mass density, Ω_{dust} , which was in good agreement with the observations available at that time. This is the first time that a model has been compared with this quantity, which will be widely discussed by the forthcoming cosmological models with dust in the subsequent years.

One on the main ingredients of these models was also the most uncertain, that is the stellar production of grains. The first detailed studies, based on the nucleation theory, provided predictions on the effective grains production by different stellar sources (AGBs: [Ferrarotti & Gail 2006](#); and SNe [Todini & Ferrara 2001](#); [Nozawa et al. 2006](#); [Bianchi & Schneider 2007](#)). [Zhukovska et al. \(2008\)](#) were the first to implement detailed mass and metallicity dependent dust yields from AGB stars in a chemical evolution model.

The focus on dust sources was further motivated by high- z observations, thanks to which emerged a picture in which a consistent abundance of dust was in place already in the first $\lesssim 1$ Gyr of the Universe lifetime. This is the case of the SDSS1048+46 quasar at $z = 6.2$ ([Maiolino et al., 2004b](#)), which challenged the models of the time ([Maiolino et al., 2004a](#); [Dwek et al., 2007](#)), who supported a picture in which SN production has to dominate in these early epochs, although with some extreme assumptions. The model by [Valiante et al. \(2009\)](#), based on detailed dust yields, suggested that stellar sources could account for the observed dust, and also that the AGB contribution is not negligible at that early times. However,

in their model they neglect grains accretion in MCs. Studying $z \gtrsim 6$ FIR-detected QSOs, [Calura et al. \(2014\)](#) claimed the need for a strong efficiency of grain growth (or alternatively a strong star formation efficiency or a top-heavy IMF; see also [Rowlands et al. 2014](#)). A similar conclusion was reached by [Valiante et al. \(2011\)](#) and [Mancini et al. \(2015\)](#), with a semi-numerical⁴ chemical model.

Another crucial ingredient that were often missing in many chemical evolution models was the treatment of the grains size distribution. Some seminal works studied the variations of the latter in different processes, such as sputtering, grains growth, shattering and coagulation (e.g. [Liffman & Clayton, 1989](#); [O'Donnell & Mathis, 1997](#); [Hirashita et al., 2010](#); [Hirashita, 2010](#)). However, the first work including a treatment of the processes affecting dust sizes in a galactic context is the one by [Asano et al. \(2013b\)](#). Stars produce large ($\sim 0.1 \mu\text{m}$) grains, whose size may evolve by shattering and coagulation, modelled in a simplified way. Also, ISM processes like growth and destruction are size-dependent. The result is that the grain size distribution evolves with the galaxy age, from a large-grains to a small-grains dominated one. Moreover, also the dust abundance is affected by the processes: shattering plays a relevant role to produce small grains and to boost up the grain growth process, which is more effective on small sized particles.

Cheaper treatments of the grain size distributions introduced in the context of chemical models are also the two-size approximation ([Hirashita, 2015](#)) and the method of moments⁵ ([Mattsson, 2016](#)).

At more recent times, although chemical evolution models were replaced by the advent of more detailed and complex numerical simulations, they are still adopted to study the dust budget and scaling relations of galaxies (e.g. [Clark et al., 2015](#); [Ginolfi et al., 2017](#); [De Vis et al., 2017](#); [De Vis et al., 2019](#); [Nanni et al., 2020](#); [Galliano et al., 2021](#); [Calura et al., 2023](#)). Also, one-zone dust-focused⁶ models are adopted to explore dust-related processes still not included in galaxy evolution models. Examples are dust grains aromatization ([Hirashita & Murga, 2020](#)), the treatment and impact of grain porosity ([Hirashita & Il'in, 2022](#)), the evolution of small carbonaceous grains ([Hirashita, 2022](#)), molecules formation on grains ([Hirashita, 2023](#)).

In summary, chemical evolution models provided a valuable tool for the pioneering exploration of dust evolution in galactic contexts. They obtained key results, such as a physical explanation of the DTG–Z relation and the evolution of the grain size distribution. Moreover, these models developed analytical prescriptions for dust-related processes which served as foundation of the forthcoming numerical simulations.

3.3 Numerical simulations

Both SAMs and hydrodynamic simulations allow us to study dust evolution in a cosmological context, as well as on (sub-)galactic scales. The importance of these tools has to be understood in light of the large amount of observations now available. Nowadays instruments and facilities (e.g. *Herschel*, ALMA) made it possible to make a detailed census of dusty galaxies

⁴Here semi-numerical means that the chemical model has been applied to a set of merger trees obtained with the extended Press-Schechter algorithm.

⁵The method of moments is a statistical technique that involves tracking (some of the) moments of the mass and size distribution of grains. Using this approach, the size distribution is approximated and reconstructed from a truncated hierarchy of moments.

⁶This means their goal is to study the dust evolution of galaxies based on certain assumptions about key features, such as the star formation history.

up to very high redshifts, as well as to study dust distribution in resolved, nearby galaxies. Numerical simulations allowed our community to compare with these data and to test our dust models against them.

As most of the physics considered, given the limited resolution of both SAMs and hydrodynamic simulations, dust-related processes have to be implemented in a *sub-grid* fashion, relying on approximated relations. Drawing from more than 20 years of experience with chemical evolution models has been fundamental in developing these recipes, which only required adaptation to fit the new numerical frameworks. The next Section is devoted to detail this practical aspect.

3.3.1 Modeling dust processes in the SA and hydrodynamic framework

The dust model recipes are tailored to align with the basic working scheme of SAMs and hydrodynamic simulations (Section 2.2), which defines the fundamental *discretization units* of these frameworks. I will resume the main concepts adopted by most of the simulations to regulate the exchange and the evolution of dust grains in these *units*. A comprehensive summary of the processes modeled in various published simulations is reported in Table 3.3.3.

- **Stellar production**

The starting point of dust life-cycle is the stellar production of grains, and their subsequent ejection in the gaseous medium. This process closely resemble those of metals production (by stellar sources) and spreading. As a result, a part of the ejected metals are labeled as *condensed* in the solid phase, that is they are in dust grains. These will enrich the gaseous component of a semi-analytic galaxy (e.g. the gaseous disc, the hot halo), or the gas close to stars in the hydrodynamic simulation. In most cases, numerical simulations are provided with detailed chemical models which are able to associate to each stellar population a specific SFH, thus they are able to follow the delayed chemical (and dust) enrichment by different stellar sources (e.g. SNII, AGBs, SNIa).

The fraction of metals *condensed* into dust grains is the first important assumption that any dust model has to do. Inspired by chemical evolution models, different options are available. In the most simplistic cases, a fixed fraction δ of the metals yields is assumed to be in the solid phase (e.g. Aoyama et al., 2017, for SNII only). A more sophisticated still simple approach is the one of Dwek (1998), widely adopted by both SAMs and hydrodynamical simulations (e.g. Bekki, 2013; Popping et al., 2017; McKinnon et al., 2016). In this case the condensed fraction δ_i^j (in the broad range $\sim 0.05 - 1$) is different for each stellar source (i ; AGBs, SNII, and SNIa) and it refers to each single element assumed to be part of dust grains (j ; typically C, O, Mg, Si, Fe, but also Al, S, Ca, Ti). Another solution is to adopt a condensation fraction which depends on the assumed chemical composition of dust grains. This method, often referred to as *key element* and first introduced by Zhukovska et al. (2008), consist in identifying, for each dust compounds, the element whose abundance is such that it constitutes a bottleneck for the formation of the compound with given stoichiometric ratios. In other words, the key element is the one for which the ratio between the available number of atoms and the number of atoms in a given compound N/N_{comp} is minimum.

A minority of simulations (e.g. McKinnon et al., 2018; Graziani et al., 2020) uses instead a more detailed treatment of dust production, by adopting mass- and metallicity-dependent yields for AGB stars and SNe. However, these yields are based on a number of assumptions, such as the micro-physics and the thermodynamics of the ejected material, which makes model prediction unavoidably uncertain.

- **Dust spreading in the ISM**

Newly produced dust grains are subsequently spread in the gaseous medium. However, the dynamics of dust grains is not necessarily the same of the gas.

All the SAMs discussed here assume that dust is simply a component of the various gaseous units (e.g. disc, halo). It is then implicitly assumed that dust is perfectly coupled with gas. This is somehow forced to be in SAMs, due to their lack of spatial resolution. However, it is noteworthy that certain recent SAMs (Parente et al., 2023; Yates et al., 2024) which incorporate dust feature coarse spatial resolution of galaxy discs and a simplified treatment of gaseous inflows resulting from angular momentum loss. Therefore, there is an opportunity to introduce a basic model for gas-dust drag interactions. Employing a distinct inflow mechanism for dust could provide a straightforward way of representing this phenomenon.

As well, the large majority of the hydrodynamic simulations mentioned here include dust as an ingredient, or a property, of gas particles. Some exceptions are the work by Bekki (2015); McKinnon et al. (2018); Li et al. (2021), in which dust grains are represented by independent *live* particles⁷. These are coupled to the gas via the modelling of a gas-dust drag force which depends on the gas properties. This method is particularly suitable for studying dynamical dust processes (e.g. radiation pressure; see Bekki 2015). Also, these experiments demonstrated that the widely adopted strong coupling between gas and dust is a reasonable assumption (McKinnon et al., 2018).

- **Grains accretion in dense medium**

The treatment of dust grains accretion in simulations is generally inspired by some of the aforementioned analytical works (e.g. Dwek, 1998; Zhukovska et al., 2008; Asano et al., 2013a), although the practical implementation greatly vary. A commonly adopted functional form for the accretion time-scale is

$$\tau_{\text{acc}} \propto n^{-1} T^{-1/2} Z^{-1}, \quad (3.2)$$

where n , T , and Z are the density, temperature and metallicity of the gas. This formulation takes into account that gaseous medium with higher densities, lower temperatures and higher metal abundances favour the collision and subsequent sticking between gas-phase metals and grains. This process is of course allowed to occur in the cold gas which is expected to host dense medium. However, it is worth reminding that this dense medium, namely molecular clouds, is far below the resolution of our current cosmological simulations. As a result, different approaches are adopted to compute the above quantities. In the semi-analytic approach, only the cold disc is considered, and the density and temperature of the gas are assumed to be fixed (e.g. Popping et al., 2017). In the hydrodynamic approach, these quantities may be evaluated on a particle-by-particle basis, relying on the predictions of the hydrodynamic solver (e.g. McKinnon et al., 2016; Li et al., 2019; Graziani et al., 2020). In some other cases, being molecular dense clouds below the resolution of typical cosmological simulations, a fixed n and T is assumed (e.g. Granato et al., 2021).

The dependence on the dense medium is sometimes explicitly considered, for example rescaling the timescale by the molecular fraction in the cold gas. This is assumed to be fixed (e.g. Aoyama et al. 2017) or computed by mean of sub-grid recipes (e.g. Granato et al., 2021; Parente et al., 2023). Alternatively, Vijayan et al. (2019) and Yates et al. (2024) model an exchange of dust between dense and diffuse medium (Zhukovska, 2014).

⁷The expression *live particles* has been introduced by Bekki (2015). In these cases, the gas properties (e.g. thermodynamical, metallicity, SN rates; see later) needed to evaluate the efficiency of dust processes, are evaluated by smoothing the properties of the neighboring gas particles of each *live* dust particle.

In both the semi-analytic and hydrodynamic approach, the metallicity of the gas Z is self-consistently computed by the simulation. However, we point out that some other dependences are sometimes adopted (e.g. the mass of dust in molecular clouds [Vijayan et al. 2019](#); [Yates et al. 2024](#)).

Eventually, some models incorporate a more sophisticated approach which consider some extra-dependence on grains properties (e.g. [McKinnon et al., 2018](#); [Granato et al., 2021](#); [Li et al., 2021](#)). For example, accretion depends on both the chemical composition (which regulates the mass density) and the size of grains. When dust properties are not considered (e.g. [Li et al., 2019](#); [Triani et al., 2020](#)), representative values are chosen (e.g. a size of $\sim 0.01 \mu\text{m}$ and material density $\sim 2 - 3 \text{ g cm}^{-3}$). When a the simulation follows the chemical composition and size of grains, appropriate values are used to compute τ_{acc} . The size of the grains significantly influences the process, with smaller grains being more efficiently accreted ($\tau_{\text{acc}} \propto \text{size}$, e.g. [Hirashita & Kuo 2011](#)).

- **Grains destruction in SN shocks**

There are relatively few variations in the modeling of dust grain destruction in SN shocks across different simulations. While the practical implementation may differ, most models are based on the work of [McKee \(1989\)](#), according to which grains within the sweeping radius of a SN explosion are destroyed. This is conveniently quantified as a swept mass of gas M_{sw} , which depends on the energy of the SN explosion and the shock velocity, assumed to be fixed values (of the order of $\sim 10^{51} \text{ erg}$ and $\sim 200 \text{ km s}^{-1}$). In both SAMs and hydrodynamic simulations, the resulting destruction timescale reads as:

$$\tau_{\text{des,SN}} \propto \frac{1}{R_{\text{SN}} M_{\text{sw}} \epsilon}, \quad (3.3)$$

where R_{SN} is the SN rate which is consistently derived from the simulation, and ϵ a parameter quantifying the dust destruction efficiency of the order of $\sim 10\%$ (e.g. [McKee, 1989](#); [Nozawa et al., 2006](#)). In some cases, different kind of SNe are associated with different destruction efficiencies ([Graziani et al., 2020](#)).

The impact of SN explosions on the surrounding medium also depends on the properties of that medium. As demonstrated by [Yamasawa et al. \(2011\)](#), see also [Nozawa et al. 2006](#), the swept mass decreases with increasing metallicity and density of the surrounding medium, as more efficient cooling leads to easier shock deceleration. This has led various simulators to adopt the fitting formula provided by [Yamasawa et al. \(2011\)](#) to account for the density (in hydrodynamic simulations) and metallicity dependence of the SN destruction efficiency ($M_{\text{sw}} \propto n^{-0.202} Z^{-0.298}$; e.g., [McKinnon et al. 2018](#), [Triani et al. 2020](#), [Parente et al. 2023](#), [Yates et al. 2024](#)). Additionally, [Hu et al. \(2019\)](#) noted that silicate grains are more easily destroyed than carbonaceous grains. This has been incorporated into some models that track the chemical evolution of dust (e.g., [Yates et al., 2024](#); [Dubois et al., 2024](#)).

Lastly, models accounting for grain size distribution often take into account the larger efficiency of grains destruction on smaller grains, which may be easily eroded by the intervening shock (e.g. [McKinnon et al., 2018](#); [Aoyama et al., 2020](#); [Dubois et al., 2024](#)).

- **Grain size evolution: shattering and coagulation**

Another crucial property of the grains population is its size distribution, as it also affects the rates of various processes. Among the simulations that account for this, two common

strategies are used. The first, a coarse and computationally inexpensive method, is the two-size approximation (Hirashita, 2015). This approach considers only two representative sizes of grains (e.g., $a \sim 0.005 \mu\text{m}$ and $\sim 0.1 \mu\text{m}$), and it is able to reproduce the main features of full calculations of grain size distribution. The distinction between small and large grains is determined noting that, when the full size distribution is considered, different processes generate two peaks in the distribution, with the boundary located at $\sim 0.03 \mu\text{m}$ (see Figure 6 in Asano et al. 2013b). Stars produce large grains, accretion acts on small grains, and eventually destruction processes have different efficiencies based on the assumed grains size ratio. In more sophisticated approaches (e.g. McKinnon et al., 2018; Aoyama et al., 2020; Li et al., 2021), each dust grains population is represented by a N -bins size distribution.

The processes that regulate the exchange between small and large grains, reshuffling the grain size distribution (GSD) without changing the total dust mass, are shattering and coagulation. These are collisional processes where grains, depending on their relative velocity, either fragment into smaller particles (shattering) or stick together to form larger grains (coagulation). The relative velocity of grains is modeled based on the properties of the gas. Shattering typically occurs in diffuse medium (gas with $n < 1 \text{ cm}^{-3}$), while coagulation is effective in dense, unresolved molecular clouds. Therefore, similar to the approach adopted for accretion, coagulation efficiency is often linked to the fraction of dense gas assumed by the model (e.g., Aoyama et al., 2017; Granato et al., 2021). Typical grain velocities are assumed to be approximately $\sim 10 \text{ km s}^{-1}$ in diffuse gas and $\sim 0.1 \text{ km s}^{-1}$ in dense gas. However, more complex size- and density-dependent functional forms are used when N -bin distributions are considered (e.g., McKinnon et al., 2018; Aoyama et al., 2020).

Lastly, it is worth mentioning the SAM by Parente et al. (2023), which will be discussed extensively throughout this Thesis. It is the only semi-analytic approach that follows two size distributions⁸. Given the limitations of the semi-analytic approach, the treatment of shattering and coagulation is simplified, relying on the fraction of molecular gas in the cold gas disc to distinguish between the diffuse and dense components of the ISM.

• Grains sputtering in the hot medium

In the hot medium ($T \gtrsim 10^5 - 10^6 \text{ K}$), grains are eroded by the collisions with energetic particles. The prescription introduced by Tsai & Mathews (1995) is by far the most widely adopted to model thermal sputtering in galaxy evolution simulation. It suggests a dependence on the density n and temperature T of the hot gas, as well as on the grain radius a :

$$\tau_{\text{sput}} \propto \frac{a}{n} \left[\left(\frac{T_0}{T} \right)^\omega + 1 \right]. \quad (3.4)$$

This is an outcome of theoretical computation (Tielens et al. (1994), but see also Nozawa et al. 2006), which essentially predict a rapidly ($\omega = 2.5$) increasing sputtering efficiency with temperature T up to T_0 , temperature above which it is nearly constant. This is trivially implemented in simulations. In SAMs, density and temperature are typically computed assuming a hot, virialized gas in the DM halo, extending up to the virial radius. The hot gas is at the virial temperature and at some average density, dependent on the assumed density profile (e.g., uniform density, β model; e.g., Yates et al. 2024). In hydrodynamic simulations, sputtering is computed on a particle-by-particle basis, with the hot gas having density and temperature predicted by the hydrodynamic scheme.

• Astration, inflows, mergers, outflows

⁸I also mention the work by Makiya & Hirashita (2022), who studied the size distribution by post-processing the galaxies catalog of a SAM.

It is worth mentioning some processes that re-locate dust within the gas and stellar phases of the simulations. Astaration, the process by which grains are embedded again into newly formed stars, acts to reduce the amount of dust into the ISM. In both the semi-analytic and hydrodynamic approach, this is trivially modelled by reducing the amount of dust in the SF gas⁹, typically assuming a constant DTG. A constant DTG is typically assumed also in the case of inflows, outflows, and mergers in SAMs, in which during this process a certain amount of dust is transferred from a reservoir to another (e.g. from cold disc to hot halo, in the case of outflows). In hydrodynamic simulations, these processes naturally emerge from the dynamics and transformation of gas particles. Consequently, dust does not deserve a specific treatment. However, we note that [Li et al. \(2019\)](#) destroy dust in wind gas particles, which represent outflows generated by stellar feedback.

3.3.2 Key results from numerical simulations

Galaxy evolution simulations with dust allowed to produce theoretical predictions for a number of different observables, as well as to study the different contribution of the dust processes to the total dust budget. In this Section some of the key results obtained by dusty simulations of the last decade are presented. Also, some comparisons are performed and discussed. Some of the results obtained in this Thesis will be included in this review process. However, they will be extensively discussed in the next chapters.

- **The DTG-Z relation**

A key diagnostic relation for dust models already discussed in the chemical evolution framework is the DTG (and DTM)-Z relation. Also simulations extensively compared with it, at both low and high redshift. The result is that models are able to broadly match the observations up to $z \approx 5$, but not at all redshifts simultaneously. ([Popping & Péroux 2022](#), but see also [Yates et al. 2024](#)). Here I focus on the $z \approx 0$ relation, which is reported in [Figure 3.2](#) for various cosmological simulations, compared to observations by [Rémy-Ruyer et al. \(2014\)](#) and [De Vis et al. \(2019\)](#).

At low metallicity, DTG and DTM are mainly determined by the stellar production channel, that is the condensation efficiency or the adopted stellar yields. There is a huge variation (~ 2 dex) in models predictions in this regime. For example, in the study by [Hou et al. \(2019\)](#) low Z galaxies feature large DTG and DTM ratios, suggesting that their assumed 10% metals condensation fraction in SNII ejecta is too large (or equivalently, the SN-driven destruction is not efficient). A similar conclusion may be drawn for the [Triani et al. \(2020\)](#) model.

Grain growth is the main driver of the peculiar s -shape of the increasing relation between DTG (and DTM) and Z , (e.g. [Popping et al., 2017](#); [Li et al., 2019](#); [Parente et al., 2022](#)). This shape highlights the critical metallicity Z_{crit} , above which grain growth becomes more efficient than stellar production. The different prescriptions adopted for dust growth, dust production and dust destruction may substantially affect the outcomes, as well as the other sub-grid recipes adopted by the models. Also in this case, a huge variation is observed in models predictions for $Z_{\text{crit}} \sim 10^{-2} - 1 Z_{\odot}$. [Parente et al. \(2022\)](#) have shown explicitly that the grain growth efficiency regulates Z_{crit} . However, [Popping & Péroux \(2022\)](#) pointed out that different predictions about Z_{crit} may inform about more profound differences among various simulations, such as different star formation timescales ([Asano et al., 2013a](#); [Zhukovska, 2014](#); [Feldmann, 2015](#)). They also suggested that the [Yamasawa et al. \(2011\)](#) Z -dependent prescription for dust destruction in SN shocks may be inadequate, since the [Triani et al. \(2020\)](#) model – which incorporates

⁹Or according to the neighboring gas particles in the case of *live* dust particles, (e.g. [Li et al., 2021](#)). However, in some cases astration is not included at all ([McKinnon et al., 2018](#)).

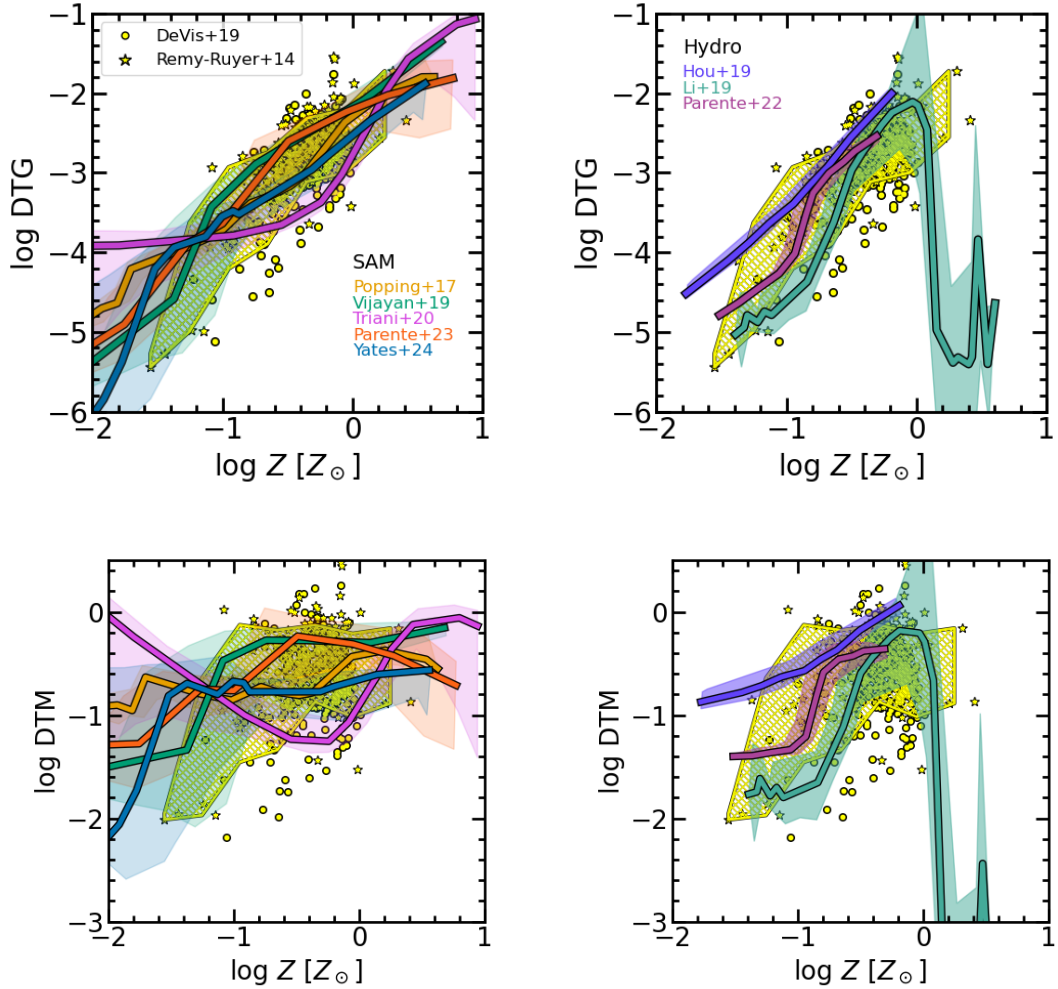


FIGURE 3.2: Relation between DTG (top panels) and DTM (bottom panels) versus gas metallicity Z at $z \approx 0$. Predictions from both SAMs (left panels; Popping et al. (2017), yellow; Vijayan et al. (2019), green; Triani et al. (2020), magenta; Parente et al. (2023), orange; Yates et al. (2024), their binary stars model, blue) and hydrodynamic simulations (right panels; Hou et al. (2019), purple; Li et al. (2019), green; Parente et al. (2022), dark red) are shown. Median trends and dispersions are reported as solid lines and shaded areas. Observational determinations from Rémy-Ruyer et al. (2014) and De Vis et al. (2019) are reported in each panel, respectively as filled circles and stars. The 16 – 84th percentiles dispersion of observational data is reported as a yellow region.

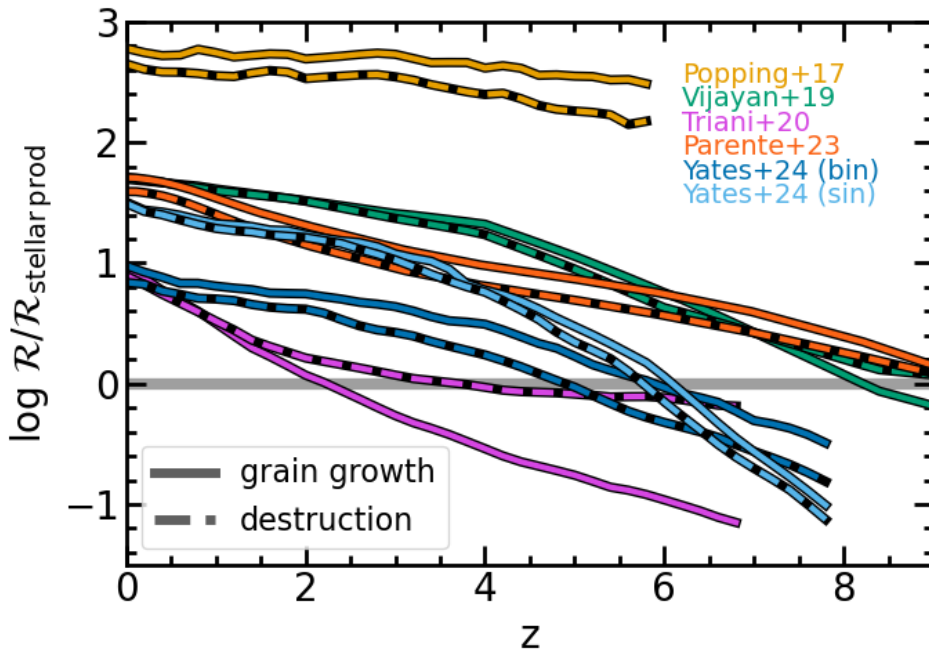


FIGURE 3.3: Cosmic rate of ISM grain growth (solid lines) and ISM grains destruction (dashed lines) as predicted by different SAMs: [Popping et al. \(2017, yellow\)](#), [Vijayan et al. \(2019, green\)](#), [Triani et al. \(2020, pink\)](#), [Parente et al. \(2023, orange\)](#), [Yates et al. \(2024, dark and light blue for the model with single and binary stars, respectively\)](#). Grains destruction refers to only SN destruction in the case of [Triani et al. \(2020\)](#). The horizontal gray line marks the rates normalization, i.e. the dust stellar production rate (= 1 in this scale).

this prescription – predicts a (decreasing up to $Z \sim Z_{\odot}$) DTM- Z relation inconsistent with observations. However, the same Z -dependent prescription is adopted in [Parente et al. \(2023\)](#), which predicts a DTM- Z relation in keeping with observational data. The [Triani et al. \(2020\)](#) inconsistency may result from a too low grain growth efficiency at relatively high Z , which makes the destruction channel dominant. This would agree with the quite high $Z_{\text{crit}} \sim Z_{\odot}$ featured by this model.

As for the high Z regime, here the saturation of the grain growth is reached, hence a \sim constant DTM is retrieved. This is not the case of the [Li et al. \(2019\)](#) model, which predicts a strongly decreasing DTG and DTM in this region of the diagram. This behaviour is attributed to the AGN feedback, which induces gas heating and consequently enhances dust destruction through thermal sputtering.

• The role of dust-related processes

What processes contribute to the dust budget of galaxies, and to what extent do they do so? Simulations offer some insight into this question. Predictions from various SAMs over a broad redshift range are shown in Figure 3.3. The rate of grain growth and destruction in the ISM is summed over the whole galaxy population and normalized to the dust production rate by stellar sources. This normalization procedure is needed to highlight the relative importance of the ISM processes. All the simulations agree on the increasing dominance of the grain growth channel over the stellar production channel as z decreases. The latter only dominates

in the early phases of galaxy evolution, although there is no consensus on the redshift at which this *transition* occurs. This transition redshift is very high ($z \gtrsim 6$) for 5 out of the 6 models reported, while [Triani et al. \(2020\)](#) predicts an unusually low one ($z \simeq 2$). It appears that grain growth is limited in this model¹⁰ (see also discussion of the DTG- and DTM-Z relation).

Also, there is a huge difference in the predictions of the relative importance of grain growth over stellar production, being it ~ 10 in [Triani et al. \(2020\)](#) and [Yates et al. \(2024\)](#), their model with binary stars) and $\sim 10^3$ in [Popping et al. \(2017\)](#) at $z \sim 0$. Although the adopted grain growth prescriptions are different (see Table 3.3.3), it is worth noting that these variations might originate from the substantial differences on the underlying galaxy evolution and chemical models. These affect both the star formation, metallicity and molecular fraction, which are all relevant in determining the timescales for dust processes. Interestingly, the SAM by [Yates et al. \(2024\)](#), in which the effect of chemical enrichment by binary stars has been investigated, found two similar *transition* redshifts ($z \simeq 6.5$) when adopting the chemical yields from both single and binary stars.

The clear result that should be emphasized is the relative similarity of the grain growth and destruction rate (but at $z \gtrsim 2$ in [Triani et al. \(2020\)](#), which supports the hypothesis of limited grain growth in this SAM). This means that the metals recycling is quite fast: grains destroyed in SN shocks produce gas phase metals which are quickly re-locked again into grains by grain growth. As a result, large differences in rates (~ 2 order of magnitudes) does not necessarily reflect into large differences in dust masses (see discussion later).

Finally, note that quantities discussed here have been summed over the whole galaxy population, but it should be kept in mind that the efficiency of the various processes vary from galaxy to galaxy. For example, [Popping et al. \(2017\)](#) pointed out that grain growth dominates the dust production budget only in relatively massive galaxies ($\log M_{\text{stars}}/M_{\odot} \gtrsim 8$).

- **High- z**

The role of various processes is more controversial at high redshift. While the hydrodynamic simulation by [Graziani et al. \(2020\)](#) confirmed the importance of the grains growth in the ISM to reproduce the dust abundance of $4 < z < 8$ ALMA detected galaxies, [Dayal et al. \(2022\)](#) claimed recently a negligible role of this process to explain the mass of dust in REBELS $z \simeq 7$ galaxies.

Caution is needed when performing this comparisons, given the large uncertainty of dust temperature in these objects, whose dust emission spectral region is not always well sampled. Dust temperature is degenerate with dust mass, thus large uncertainties are expected. This was recently pointed out by [Choban et al. \(2024a\)](#), who conducted a series of zoom-in cosmological simulations. They concluded that although grain growth in the ISM is the dominant channel for dust production at $z \gtrsim 5$, their model still under predicts observed dust masses at such high redshifts.

- **The Dust Mass Function and Cosmic Dust Budget**

Simulating galaxy evolution in a cosmological context made it possible the comparison with IR-to-submm surveys, from which dust mass functions (DMFs) and information on the redshift evolution of cosmic dust abundance are inferred. Figure 3.4 reports DMF predictions by various SAMs and hydrodynamic simulations at $z \sim 0, 1, 2, 4$, compared with a compilation of observations (see caption for details). It is worth noting several aspects of this comparison. Firstly, the predicted DMF exhibits a Schechter-like shape in SAMs, whereas it

¹⁰Note that in their model a single size of grains is assumed, namely $0.1 \mu\text{m}$. Smaller sizes could enhance grains growth.

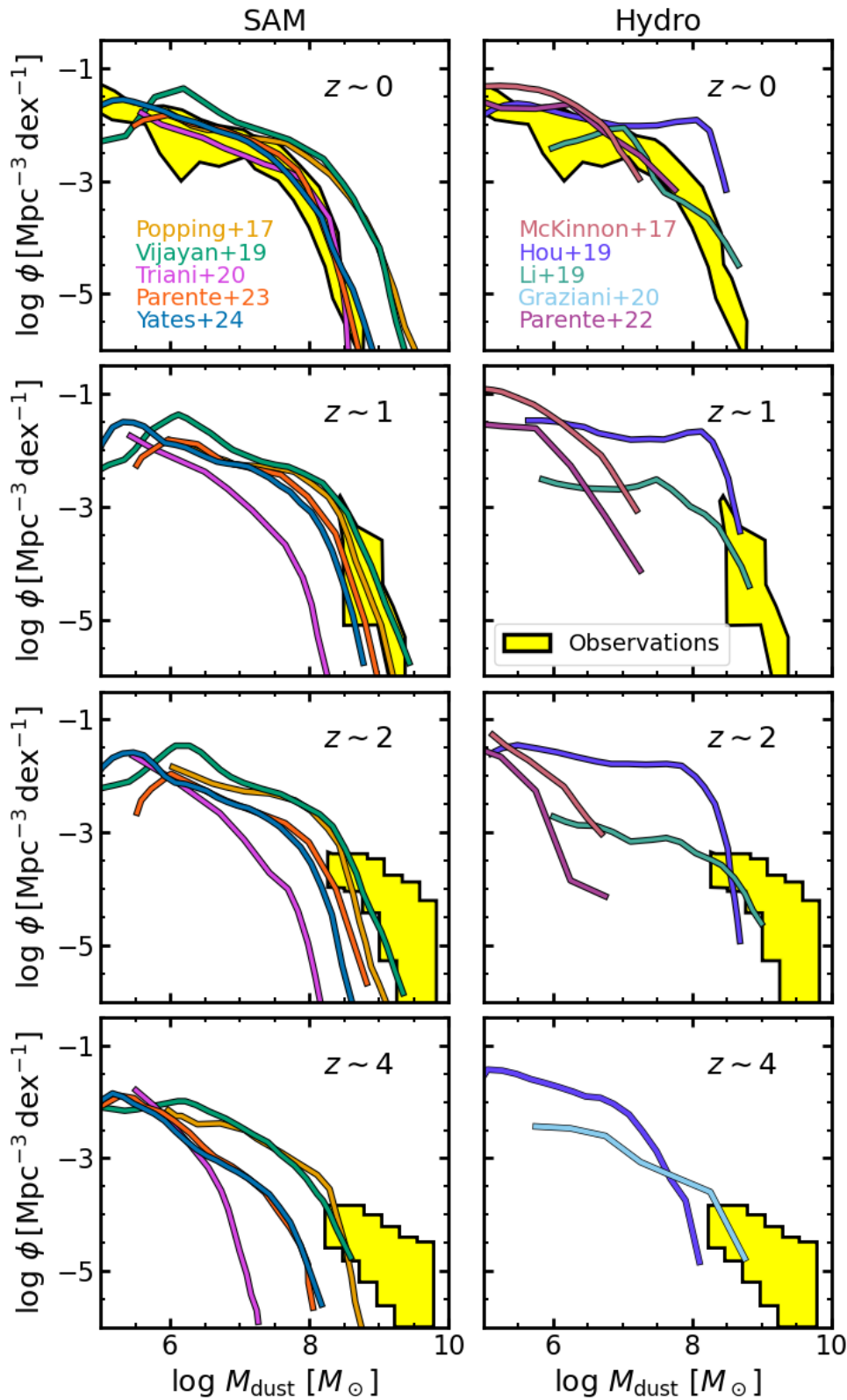


FIGURE 3.4: DMF at $z \sim 0, 1, 2, 4$ as predicted by SAMs (Popping et al., 2017; Vijayan et al., 2019; Triani et al., 2020; Parente et al., 2023; Yates et al., 2024, left panels) and hydrodynamic simulations (McKinnon et al., 2017; Hou et al., 2019; Li et al., 2019; Graziani et al., 2020; Parente et al., 2022, right panels). Yellow regions represent compilations of observational data taken from Vlahakis et al. (2005); Dunne et al. (2011); Beeston et al. (2018) at $z \sim 0$, Pozzi et al. (2020, $z \sim 1$ and ~ 2), Dunne et al. (2003, $z \sim 2$), and Traina et al. (2024, $z \sim 1, \sim 2$, and ~ 4).

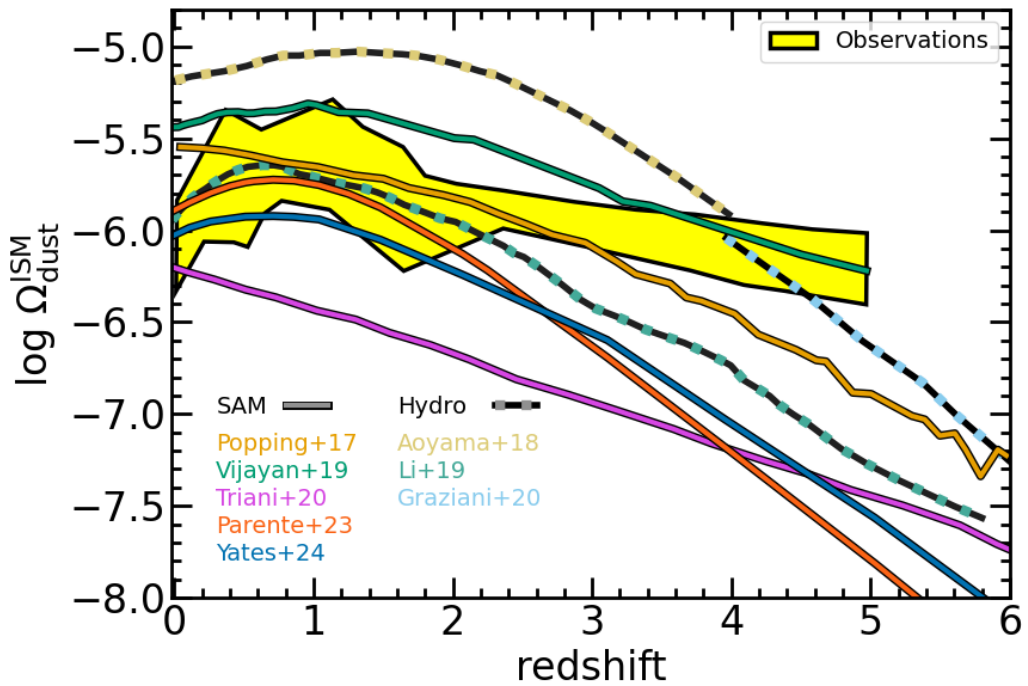


FIGURE 3.5: Cosmic ISM dust parameter $\Omega_{\text{dust}}^{\text{ISM}}$ as a function of redshift. Model predictions from both SAMs (Popping et al., 2017; Vijayan et al., 2019; Triani et al., 2020; Parente et al., 2023; Yates et al., 2024) and hydrodynamic simulations (Aoyama et al., 2018; Li et al., 2019; Graziani et al., 2020) are shown as solid and dotted lines. The yellow shaded region includes a number of observational derivation of $\Omega_{\text{dust}}^{\text{ISM}}$ obtained by integrating the DMF (Vlahakis et al., 2005; Dunne et al., 2011; Beeston et al., 2018; Driver et al., 2018; Dudzevičiūtė et al., 2020; Pozzi et al., 2020; Traina et al., 2024).

appears more irregular in hydrodynamic simulations. It is crucial to bear in mind that SAMs typically yield a better agreement with the observed SMF than hydrodynamic simulations, largely due to the simplicity of running and tuning SAMs. Additionally, hydrodynamic simulations are often conducted on smaller volumes, which may result in inadequate sampling of the most massive objects. Both these factors are likely to influence the shape of the DMF.

The observed high- z DMF is typically much more difficult to match with respect to the $z \sim 0$ one. [Graziani et al. \(2020\)](#) perform the best at $z \sim 4$, but a larger simulated volume (their box size is $30h^{-1}$ cMpc) would be needed to better constrain the high mass end. At such high redshifts all the other models under predict the observed dust masses. A similar tendency is found at $z \sim 2$. Here some SAMs ([Popping et al., 2017](#); [Vijayan et al., 2019](#)) and hydrodynamic simulations ([Hou et al., 2019](#); [Li et al., 2019](#)) broadly matches, still underestimating, the high mass end of the observed DMF. However, it is worth noting that predictions by these models typically worsen at $z \sim 0$. On the contrary, models that exhibit a good agreement with the $z \sim 0$ mass function, tend to (heavily) underestimate the observed DMF at $z \sim 1 - 2$ ([Triani et al., 2020](#); [McKinnon et al., 2017](#); [Parente et al., 2022](#); [Yates et al., 2024](#)). In conclusion, none of the shown models is able to reproduce both the high- z and low- z observed DMFs.

A similar issue arises when examining the cosmic dust density ρ_{dust} , or Ω_{dust} ¹¹. Here the focus is on galactic dust, hence $\Omega_{\text{dust}} = \Omega_{\text{dust}}^{\text{ISM}}$. Predictions from both SAMs and hydrodynamic cosmological simulations are shown in [Figure 3.5](#). None of the models can adequately reproduce both the shape, characterized by a decline at $z \lesssim 1$, and the normalization of the observed $\Omega_{\text{dust}}^{\text{ISM}}$. In particular, as already noted for the DMF, models struggle to reproduce both the high- and low- z observed dust abundance. Reasons behind this discrepancy may be multiple and, importantly, not necessarily related to differences in the dust model. This has been noted recently by [Parente et al. \(2023\)](#), who showed that a different prescription for SMBH growth (i.e. galaxy quenching) can improve the $z \lesssim 1$ drop prediction¹². Indeed, these simulations typically predict very different key quantities, such as SFR density or metals content, which profoundly affect the dust assembly, and consequently $\Omega_{\text{dust}}^{\text{ISM}}$.

As a final remark, it is important to highlight that $\Omega_{\text{dust}}^{\text{ISM}}$ may not serve as an ideal quantity for comparison with observations, where it is computed¹³ by integrating the observed DMF. The bulk of this integral ($\gtrsim 95\%$) arises from the contribution of galaxies with $M_{\text{dust}} \lesssim 10^8 M_{\odot}$, a mass range that is largely unconstrained by observations, necessitating the use of DMF Schechter-like extrapolation to estimate its contribution. Such extrapolations can potentially lead to misleading comparisons. As an explicit example, take the DMF and $\Omega_{\text{dust}}^{\text{ISM}}$ at $z \sim 2$. While various models may align well with the observed $\Omega_{\text{dust}}^{\text{ISM}}$, none of them can accurately reproduce the high-mass end of the observed DMF. This highlights the importance of preferring comparisons based on the latter rather than on $\Omega_{\text{dust}}^{\text{ISM}}$.

- **Dust on sub-galactic scales**

Hydrodynamical simulations and spatially resolved SAMs allowed to study the dust distribution and properties on sub-galactic scales. Dust (as well as DTG and DTM) profiles have been investigated, and compared with the few available observational results coming from nearby galaxies (e.g. [Casasola et al., 2017](#); [Relaño et al., 2020](#); [Chiang et al., 2021](#)).

Simulations recover a slowly decreasing dust, DTG and DTM profiles, in broad agreement with observations ([Granato et al., 2021](#); [Yates et al., 2024](#)). However, the normalization often

¹¹The cosmic dust parameter is related to the cosmic dust density by $\Omega_{\text{dust}}(z) = \frac{\rho_{\text{dust}}(z)}{\rho_0}$, with $\rho_{c,0} = 2.775 h^2 \times 10^{11} M_{\odot}/\text{Mpc}^3$ the critical density of the Universe today. Note the common *bad practice* in this definition, which is at odds with the standard meaning of the density parameters Ω in cosmology, where densities are normalized to the critical density at a given redshift $\Omega(z) = \frac{\rho(z)}{\rho_{\text{crit}}(z)}$.

¹²This will be discussed at length in [Chapter 5](#).

¹³At least in the examples considered here.

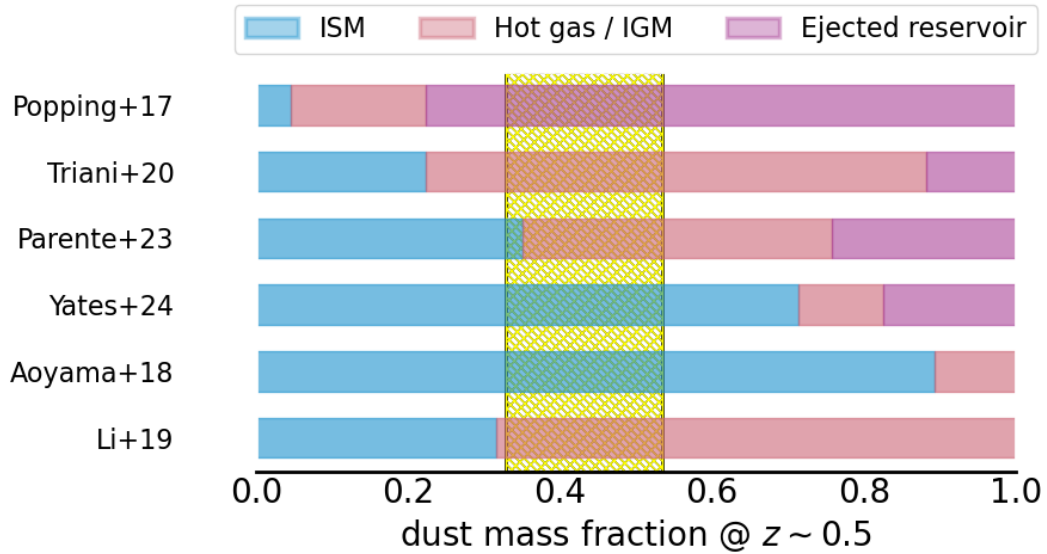


FIGURE 3.6: Fraction of dust in and outside galaxies at $z \sim 0.5$ as predicted by different simulations (SAMs: Popping et al. (2017); Triani et al. (2020); Parente et al. (2023); Yates et al. (2024); hydrodynamic simulations: Aoyama et al. (2018); Li et al. (2019)). Blue refers to dust in the ISM (or, equivalently, in galaxies), red to dust in the hot gas of SAMs or the IGM (i.e. outside galaxies) of hydrodynamic simulations, purple to dust in the ejected reservoir in SAM galaxies. The hatched yellow region represents a naive estimate of the ISM dust fraction at $z \sim 0.5$ by combining data from Ménard et al. (2010); Ménard & Fukugita (2012) (for extra-galactic dust) and Driver et al. (2018); Pozzi et al. (2020) (for galactic dust).

exhibits discrepancies, as indicated by offsets in various studies (e.g., Aoyama et al., 2017; Parente et al., 2022; Choban et al., 2022; Romano et al., 2022). The drop of DTM is particularly clear at outer radii. Yates et al. (2024) noted that this is also influenced by the efficiency of dust destruction in the hot CGM, which supplies dust to the peripheral regions of the galactic disc where dust production is less efficient. Romano et al. (2022) highlighted the importance of dust diffusion in determining the profiles. Diffusion of large grains towards the outer regions of the galaxy makes the DTM profile shallower and dropping at larger radii than those obtained when neglecting diffusion.

As for the grain size distribution, most numerical models predict a nearly flat or smoothly increasing profile of the ratio between small and large grains mass (Aoyama et al., 2017; Granato et al., 2021; Parente et al., 2022; Romano et al., 2022; Parente et al., 2023), as observations do (Relaño et al., 2020). This suggests the balance between shattering and coagulation of grains on galactic scales.

- **Dust on extra-galactic scales**

Cosmological simulations allow to follow the evolution of the hot CGM and IGM, hence the dust distribution in these extra-galactic environments. Figure 3.6 reports predictions from simulations for what concerns the fraction of dust inside and outside galaxies. Dust inside galaxies is labeled as ISM dust, and it corresponds to dust in the cold gas of SAM galaxies and to dust bound in identified structures in hydrodynamic simulations. Dust outside galaxies is identified as dust not belonging to structures in hydrodynamic simulations (IGM), or belonging to both the hot and ejected reservoir in SAM galaxies. A naive estimation of the

observed fraction of dust inside galaxies at $z \sim 0.5$ has been obtained by combining results from [Ménard et al. \(2010\)](#); [Ménard & Fukugita \(2012\)](#) for extra-galactic dust and from [Driver et al. \(2013, 2018\)](#) for galactic dust. It is reported for comparison. It should be kept in mind that this is an upper limit of the real galactic dust fraction, since a considerable part of the extra-galactic one may be missing.

The variation of model predictions is huge, with the extra-galactic dust fraction ranging from $\sim 10\%$ to $\sim 95\%$, whereas observations suggest a more balanced distribution between intra- and extragalactic dust (around $\sim 60\%$ and $\sim 40\%$, respectively). Since dust is only produced inside galaxies, key processes that regulate the amount of extra-galactic dust are thermal sputtering in the hot medium and galactic winds. Differences in the predictions of hydrodynamic simulations may stem from AGN feedback, which is implemented in [Li et al. \(2019\)](#) but not in [Aoyama et al. \(2018\)](#). Notably, the latter tends to overestimate the stellar and dust mass function at $z = 0$, whereas a process like AGN feedback may aid in reconciling these discrepancies with observations¹⁴, also helping in ejecting dust and increasing the extra-galactic dust budget.

As for SAMs, the ones predicting a larger amount of extra-galactic dust ([Popping et al., 2017](#); [Triani et al., 2020](#)) are the only ones having an implementation of AGN feedback capable to eject dust (and gas) from galaxies. However, the discrepancy with observations suggests the need to introduce a mechanism for dust destruction within such ejecta. The two remaining models ([Parente et al., 2023](#); [Yates et al., 2024](#)) are based on the same SAM ([Henriques et al., 2020](#)), but feature a factor of ~ 2 difference in the predictions of the ISM dust mass fraction. This is likely due to the fact that [Parente et al. \(2023\)](#) adopts a smaller efficiency (by a factor of 10) of the sputtering timescale¹⁵. A reduced efficiency was previously suggested by simulations examining the dust content of the intra-cluster medium ([Gjergo et al., 2018](#); [Vogelsberger et al., 2019](#)), and in this case allows the model to well match the observed ISM dust fraction.

Numerical simulations have also investigated extragalactic dust profiles, extending up to approximately $\simeq 1$ Mpc from the centers of galaxies ([McKinnon et al., 2017](#); [Aoyama et al., 2018](#); [Parente et al., 2022](#), refer to Figure 4.18). Despite differences in the treatment of dust evolution and prescriptions for feedback and galactic winds, all of these simulations observe a similar slope of profiles ($\Sigma_{\text{dust}} \propto r^{-0.8}$), broadly consistent with observations ([Ménard et al., 2010](#)).

3.3.3 Future prospects for dusty simulations

So far, dusty galaxy evolution simulations have clarified many aspects of our understanding of the dust life-cycle inside and outside galaxies. These simulations (and the next ones as well) have the unique opportunity to exploit dust to improve our galaxy evolution studies. This can be achieved in different ways.

- **Realistic mock catalogs**

¹⁴This aspect has been addressed in [Hou et al. \(2019\)](#), although they do not specifically discuss the abundance of extra-galactic dust.

¹⁵Also the hot gas density is computed in a different way (isotropic distribution is assumed in [Parente et al. 2023](#), while a β model is adopted in [Yates et al. 2024](#)).

The first, and perhaps most obvious, improvement is to use dust to produce mock observational catalogs¹⁶ (as done in [Triani et al. 2023](#)). This method allows for a more coherent comparison with observations, as the observables become genuine predictions of the simulations, eliminating the need to rely on empirical relations to convert fluxes to physical quantities (e.g., dust mass from IR luminosity). This approach is particularly crucial at high redshifts, where observations are poor and the conversion from observed data to physical quantities is highly uncertain.

The other intriguing way to exploit dust is to include it actively in the physics of galaxy evolution. Indeed, so far most of the simulations include dust as a passive ingredient of the gas phase of galaxy. One notable exception is the inclusion of dust grain cooling in a few hydrodynamic simulations ([Gjergo et al., 2018](#); [Vogelsberger et al., 2019](#)).

Some natural extensions of the dust models would include:

- **Molecules formation on grains surfaces**

In a metal enriched Universe, grains are the main channel for molecule formation, in particular H_2 , the most abundant molecule in the Universe (e.g. [Wakelam et al., 2017](#)). Since star formation in simulations is typically linked to H_2 , incorporating this aspect represents a significant improvement for current simulations. The work by [Ragone-Figueroa et al. \(2024\)](#) is the first to explore this direction in a cosmological context.

- **Radiative transfer**

Due to their interaction with energetic photons, dust grains significantly influence the physics of the ISM. For instance, dust shielding can affect the thermal properties of gas, thereby facilitating star formation. Also, in the presence of radiation fields from stellar sources or AGNs, radiation pressure must be considered, especially for the dusty medium. Radiation pressure on dusty gas can drive galactic outflows, which are crucial in the current galaxy evolution paradigm. Therefore, a proper dust-based model for this process is highly desirable. A first step in this direction, that is the inclusion of radiation in dusty simulations, has been done in the THESAN project ([Kannan et al., 2022](#)).

¹⁶In the literature, there are several examples of simulations that have been post-processed to produce mock catalogs (e.g. [Lacey et al., 2016](#); [Vijayan et al., 2021](#); [Shen et al., 2022](#)). However, in these cases, dust abundance is not consistently tracked by the simulation. Instead, it is typically linked to the ISM metals content by assuming a certain DTM ratio.

| reference | scheme | chemical composition | grain sizes | dust production | grains accretion | SN destruction | thermal sputtering |
|--|--------|------------------------|-------------|--|--|--|---|
| Bekki (2013) Bekki (2015) | hydro | – | – | δ^{fixed} (SNII, SNIa, AGB) | fixed | fixed | – |
| McKinnon et al. (2016) McKinnon et al. (2017) Vogelsberger et al. (2019) | hydro | Sil, Car | – | δ^{fixed} (SNII, SNIa, AGB) | $n_{\text{gas}}, T_{\text{gas}}, Z_{\text{gas}}$ | fixed | $n_{\text{gas}}, T_{\text{gas}}$ |
| Popping et al. (2017) | SAM | Sil, Car | – | δ^{fixed} (SNII, SNIa, AGB) | $n_{\text{gas}}, \text{H}_2$ | chem | $n_{\text{gas}}, T_{\text{gas}}$ |
| Aoyama et al. (2017) Aoyama et al. (2018) | hydro | – | 2 | δ^{fixed} (SNII) | $n_{\text{gas}}, \text{size}, \text{H}_2$ | n_{gas} | $n_{\text{gas}}, \text{size}$ |
| Hou et al. (2017) Hou et al. (2019) | hydro | Sil, Car | 2 | δ^{fixed} (SNII, SNIa, AGB) | $n_{\text{gas}}, T_{\text{gas}}$ size, chem | fixed | $n_{\text{gas}}, \text{size}$ |
| McKinnon et al. (2018) | hydro | – | N | dust yields tables (SNII, SNIa, AGB) | $n_{\text{gas}}, T_{\text{gas}}, Z_{\text{gas}}$ size | $n_{\text{gas}}, Z_{\text{gas}}$ size | $n_{\text{gas}}, T_{\text{gas}}, \text{size}$ |
| Gjergo et al. (2018) Granato et al. (2021) Parente et al. (2022) | hydro | Sil, Car | 2 | δ^{fixed} (SNII, SNIa, AGB) | Z_{gas} size, chem | fixed | $n_{\text{gas}}, T_{\text{gas}}, \text{size}$ |
| Vijayan et al. (2019) | SAM | Sil, Car, SiC, Iron | – | dust yields tables (AGB) $\delta^{\text{key element}}$ (SNII, SNIa) | M_{dust} chem | fixed | – |
| Li et al. (2019) | hydro | – | – | δ^{fixed} (SNII, AGB) | $n_{\text{gas}}, T_{\text{gas}}, Z_{\text{gas}}$ | fixed | $n_{\text{gas}}, T_{\text{gas}}$ |
| Graziani et al. (2020) | hydro | – | – | dust yields tables (PISN, SNII, AGB) | $n_{\text{gas}}, T_{\text{gas}}, Z_{\text{gas}}$ | fixed | $n_{\text{gas}}, T_{\text{gas}}$ |
| Triani et al. (2020) | SAM | – | – | δ^{fixed} (SNII, AGB) | $Z_{\text{gas}}, \text{H}_2$ | Z_{gas} | $n_{\text{gas}}, T_{\text{gas}}$ |
| Aoyama et al. (2020) Romano et al. (2022) | hydro | – | N | δ^{fixed} (SNII, SNIa, AGB) | $n_{\text{gas}}, T_{\text{gas}}, Z_{\text{gas}}$ size | size | $n_{\text{gas}}, T_{\text{gas}}, \text{size}$ |
| Li et al. (2021) | hydro | – | N | δ^{fixed} (SNII, AGB) | $n_{\text{gas}}, T_{\text{gas}}, Z_{\text{gas}}$ size | size | $n_{\text{gas}}, T_{\text{gas}}, \text{size}$ |
| Dayal et al. (2022) | SAM | – | – | fixed mass per SNII | Z_{gas} | fixed | – |

| | | | | | | | |
|-----------------------|-------|------------------------|---|---|--|------------------|--|
| Choban et al. (2022) | hydro | Sil, Car SiC, Iron | – | dust yields tables (AGB), $\delta_{\text{key element}}$ (SNII, SNIa) | $n_{\text{gas}}, T_{\text{gas}}, \text{H}_2$, chem | n_{gas} | $n_{\text{gas}}, T_{\text{gas}}$ |
| Choban et al. (2024b) | | | | | | | |
| Parente et al. (2023) | SAM | Sil, Car | 2 | $\delta_{\text{key element}}$ (SNII, AGB) | $Z_{\text{gas}}, \text{H}_2$, chem, size | Z_{gas} | $n_{\text{gas}}, T_{\text{gas}}, \text{size}$ |
| Yates et al. (2024) | SAM | Sil, Car, SiC, Iron | – | dust yields tables (AGB) $\delta_{\text{key element}}$ (SNII, SNIa) | $M_{\text{dust}}, \text{H}_2$, chem | chem | $n_{\text{gas}}, T_{\text{gas}}$ |
| Dubois et al. (2024) | hydro | Sil, Car | 2 | $\delta_{\text{key element}}$ (SNII, SNIa, AGB) | $n_{\text{gas}}, T_{\text{gas}}, Z_{\text{gas}}$, size, chem | size, chem | $n_{\text{gas}}, T_{\text{gas}}$ size, chem |

TABLE 3.1: Schematic summary of the main processes ruling dust formation and evolution as implemented in different galaxy evolution simulations. Similar works, belonging to the same group, are organized together in the same row. The description of the processes is a summary of the works, or refer to the most updated, fiducial version. For each entry it is reported: *(i)* **Main references.** *(ii)* **Galaxy evolution scheme** SAM or hydrodynamic. *(iii)* **Chemical composition of grains** Silicates (Sil), Carbonaceous (Car), SiC and Iron dust. Reported only when it is explicitly followed during both dust production and evolution. *(iv)* **Number of grain sizes assumed** 2 stands for the two-size approximation, N is when a $N(> 2)$ -bins distribution is adopted. Note that the treatment of the grain size distribution implies the treatment of shattering and coagulation processes. *(v)* **Dust production channels** δ_{fixed} means that a fixed fraction of the metals (not necessarily the same for each metal) is assumed to condense into grains, $\delta_{\text{key element}}$ refers to the adoption of the key element strategy to respect stoichiometric ratios in the composition of produced dust, while dust yields tables means that pre-computed results are exploited. The stellar sources of dust are also reported. *(vi)* **Physical dependences of the grains accretion process** These may include gas density (n_{gas}), temperature (T_{gas}), metals composition of the gas Z_{gas} , molecular gas content (H_2), grain size and chemical properties of grains. *(vii)* **Physical dependences of the SN destruction process** These may include $n_{\text{gas}}, Z_{\text{gas}}$, grain size and chemical properties of grains. These dependencies refer to the assumed mass swept of gas by a single SN and to the grain destruction efficiency. Fixed means that these quantities are constant in the simulation (but a dependence on the SN rate is always assumed). *(viii)* **Physical dependences of the thermal sputtering process** These may include $n_{\text{gas}}, T_{\text{gas}}$, grains size and chemical composition.

3.4 The dust model in L-GALAXIES and MUPPI

The work presented in this Thesis is based on a dust model incorporated into two numerical frameworks used for galaxy evolution simulations in a cosmological context. These frameworks are the L-GALAXIES SAM (Henriques et al., 2020) and the MUPPI model for sub-resolution physics used in hydrodynamic simulations (Valentini et al., 2020). The main features of these models have been thoroughly described in Sections 2.3 and 2.4. This Section focuses on the implementation of the dust model within these two contexts.

The dust model was initially introduced by our group in Gjergo et al. (2018) within the context of galaxy cluster hydrodynamic simulations. It was later refined and integrated with MUPPI¹⁷ in Granato et al. (2021) for zoom-in simulations of isolated MW-like galaxies, and then further adjusted in Parente et al. (2022), who explored its application in a cosmological volume. More recently, as a relevant part of the work presented in this Thesis, the dust model was incorporated into the L-GALAXIES SAM framework (Parente et al., 2023).

The dust formation and evolution model tracks the mass evolution of two grain populations of different sizes, referred to as *large* and *small* grains. It utilizes the two-size approximation proposed by Hirashita (2015), which has been shown to be a computationally efficient method for accurately capturing the effects of various processes in dust evolution models, including grain size distribution. This method has been further validated by Aoyama et al. (2020). Additionally, the dust model independently tracks carbonaceous (C) and silicate dust grains, specifically olivine (MgFeSiO₄).

The model takes into account the most important processes capable to affect both the mass and size of grains within a galactic context (Section 3.1). These are:

- Dust production by stellar sources;
- Grains accretion in dense molecular clouds;
- Grains destruction in SN shocks;
- Shattering and coagulation;
- Sputtering in the hot medium.

Before delving into the specifics of each process and its relative implementation, I give a brief overview here of the model. Large grains are produced by stellar populations and injected into the surrounding gas medium, in the same manner as gas-phase metals. Once in the diffuse medium, large grains may shatter to produce small grains. On the contrary, in the dense medium, small grains can coagulate into large grains. The two latter processes do not affect the total amount of dust, but only the size distribution (small ↔ large). Small grains can accrete gas phase metals in the dense molecular clouds of the ISM, hence increasing the dust mass. Also, both small and large grains may be destroyed in presence of SN shocks and sputtered in the hot gas. The two latter processes act to decrease the dust content. A diagram illustrating how these processes regulate the exchange between the various dust and gas-phase metals components is provided in Figure 3.7, while a schematic description of their implementation in both the SAM and hydrodynamic framework adopted in this work is reported in Table 3.2.

In both the SAM and hydrodynamic implementations, dust grains are a component of the gas. Specifically, dust grains reside in the cold gas disc, hot atmosphere, and ejected reservoir

¹⁷Note that the dust model in Gjergo et al. (2018) was implemented on top of a different star formation and feedback model.

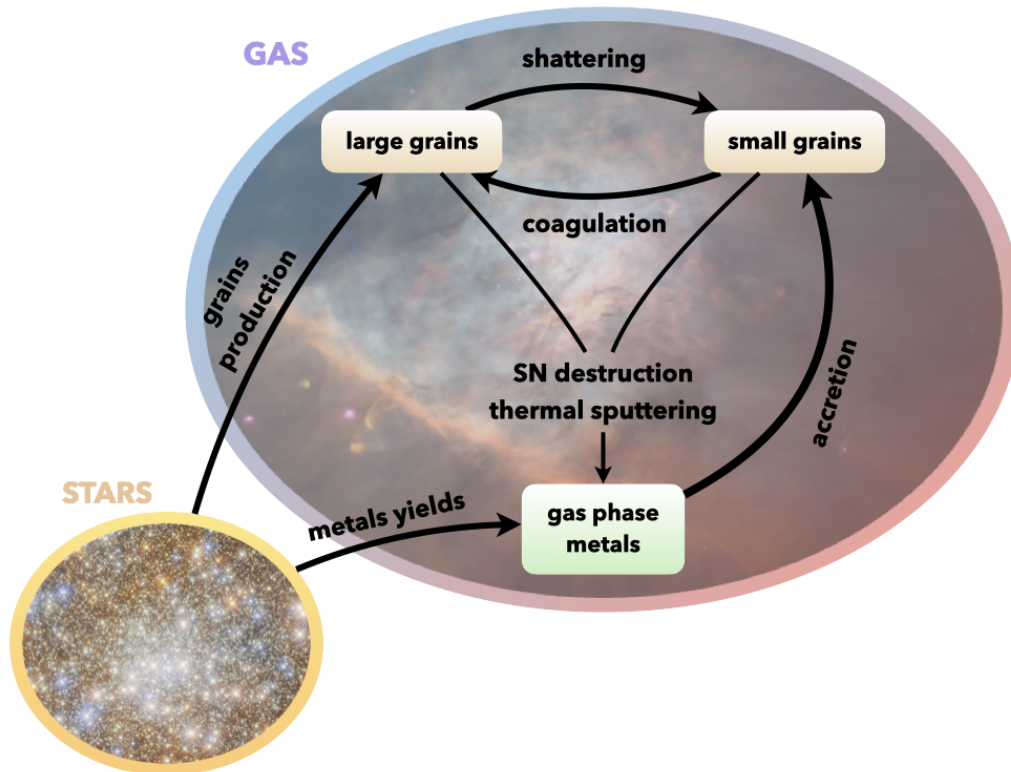


FIGURE 3.7: This schematic diagram illustrates the processes included in the dust model within both the SAM and hydrodynamic simulations discussed in this Thesis (refer to Table 3.2). Dust grains are categorized into two representative sizes (large and small) and are associated with the gaseous components of the simulations. In the hydrodynamic simulation, this corresponds to gas particles, whereas in the SAM framework, it corresponds to the cold gas disc, the hot gas atmosphere, and the ejected reservoir. Stellar populations enrich the gaseous medium with gas phase metal elements and large dust grains. Various processes in the gaseous medium regulate the exchange of mass between large grains, small grains, and gas phase metals. Shattering and coagulation transfer mass between small and large grains without affecting the total dust content. Gas phase metals can accrete onto small grains, increasing their mass. Additionally, both large and small grains can be destroyed in SN shocks and energetic collisions with ions (thermal sputtering), converting them back into gas phase metals. Another process that can reduce dust amounts is astration, which involves the incorporation of grains into newly formed stars. This process, which also affects gas phase metals, is not depicted in the diagram as it is simply a consequence of the transformation of some gas (along with the dust and metals it contains) into stars.

| Physical Process | Where? SAM | Hydro | Net effect |
|---------------------------|---|---------------------------------|--------------------|
| Production by stars | stellar disc, bulge and ICL to cold disc and hot halo | star particles to gas particles | + large |
| Shattering | cold gas disc | gas particles | large → small |
| Coagulation | cold gas disc (dense phase) | MP particles (dense phase) | small → large |
| Accretion | cold gas disc (dense phase) | MP particles (dense phase) | + small |
| Destruction in SNe shocks | cold gas disc | MP particles | – small – large |
| Thermal sputtering | hot gas and ejected reservoir | hot gas phase | – small – large |

TABLE 3.2: List of the processes included in the dust model adopted in this work (see also Figure 3.7). The second and third columns schematically indicate the component of the SAM or hydrodynamic simulations in which each process is effective. The last column reports the net effect of each process in terms of the mass variation of small and large grains. See the text for details.

in the SAM, and in the gas particles of the hydrodynamic simulation. Based on the properties of the gas as modeled in the two frameworks, the dust mass evolution of both small and large grains (M_S , M_L) is computed according to the following equations:

- **SAM**

$$\dot{M}_L^{\text{cold}} = \dot{M}_*^{\text{cold}} + \dot{M}_{\text{coag}} - \dot{M}_{\text{shat}} - \dot{M}_{\text{astr}} - \dot{M}_{\text{SN}}; \quad (3.5)$$

$$\dot{M}_S^{\text{cold}} = \dot{M}_{\text{acc}} - \dot{M}_{\text{coag}} + \dot{M}_{\text{shat}} - \dot{M}_{\text{astr}} - \dot{M}_{\text{SN}}; \quad (3.6)$$

$$\dot{M}_L^{\text{hot}} = \dot{M}_*^{\text{hot}} - \dot{M}_{\text{spu}}; \quad (3.7)$$

$$\dot{M}_S^{\text{hot}} = -\dot{M}_{\text{spu}}; \quad (3.8)$$

$$\dot{M}_{L,S}^{\text{ej}} = -\dot{M}_{\text{spu}}. \quad (3.9)$$

- **Hydro**

$$\dot{M}_L^{\text{gas}} = \dot{M}_* + \dot{M}_{\text{coag}} - \dot{M}_{\text{shat}} - \dot{M}_{\text{astr}} - \dot{M}_{\text{SN}} - \dot{M}_{\text{spu}}; \quad (3.10)$$

$$\dot{M}_S^{\text{gas}} = \dot{M}_{\text{acc}} - \dot{M}_{\text{coag}} + \dot{M}_{\text{shat}} - \dot{M}_{\text{astr}} - \dot{M}_{\text{SN}} - \dot{M}_{\text{spu}}. \quad (3.11)$$

$$(3.12)$$

In the equations above, \dot{M}_* represents the dust produced by stars (large grains), while \dot{M}_{acc} denotes the dust grown through metal accretion, affecting only small grains. The terms \dot{M}_{shat} and \dot{M}_{coag} describe the processes of shattering and coagulation, respectively. \dot{M}_{astr} represents the dust removed from the gas phase during star formation (astration), and \dot{M}_{SN} is the dust destroyed in SN shocks. \dot{M}_{spu} describes thermal sputtering. Below, I provide

a detailed description of these processes. Most are modeled by computing an associated timescale τ_{process} , from which the mass rate is derived:

$$\dot{M}_{\text{S,L}} = \frac{M_{\text{S,L}}}{\tau_{\text{process}}}. \quad (3.13)$$

The following sections will detail how these timescales are computed.

3.4.1 Stellar production

The model for grain production takes advantage of the detailed chemical evolution models provided by L-GALAXIES and MUPPI (Yates et al. 2013 and Tornatore et al. 2007, respectively), both capable of tracking chemical enrichment element by element.

Stellar populations enrich their surrounding medium with gas-phase metals and large dust grains. Specifically, winds from AGB stars and SN ejecta are considered the sources of grain production. It is assumed that a certain fraction of these elements, as detailed below, condenses into dust grains. In our model, grains are produced by AGB stars and SNII ejecta. Although dust production from SNIa sources can be trivially computed, it has been neglected in our last works, with our results being largely insensitive to this choice (see also e.g., [Giannini et al. 2017](#); [Li et al. 2019](#)).

AGB stars are assumed to produce either carbonaceous or silicate grains, depending on the C/O ratio in their ejecta. Due to microscopic mixing in the ejecta, the maximum amount of CO forms before grain condensation, leaving only the remaining C or O atoms available for other compounds (e.g., [Dwek, 1998](#)). When $C/O > 1$, AGB stars generate carbon dust by utilizing the C atoms that are not bound in CO:

$$M_{\text{C dust}} = \max [\delta_{\text{AGB,C}} (M_{\text{C ej}} - 0.75M_{\text{O ej}}), 0], \quad (3.14)$$

where $M_{\text{X ej}}$ is the ejected mass of the X element and 0.75 is the ratio between O and C atomic weights. The condensation efficiency $\delta_{\text{AGB,C}} = 0.1$.

AGB stars produce silicates when $C/O < 1$. In the model, the key element technique is adopted to determine the amount of silicate dust produced, once the chemical composition of silicate grains is assumed. The key element minimizes the ratio between the number of ejected atoms and the number of atoms required to form the compound, thus determining the maximum units of silicate compounds N_{sil} that can potentially form in the ejecta. The mass of the element X belonging to the compound and condensed into dust is then

$$M_{\text{X dust}} = N_{\text{sil}} \mu_{\text{X}} N_{\text{ato}}^{\text{X}}, \quad (3.15)$$

where μ_{X} is the atomic weight of the element and $N_{\text{ato}}^{\text{X}}$ the number of X atoms in the compound.

In the model we assume that silicates have the chemical composition of Olivine, i.e. $\text{Mg}_{2-x}\text{Fe}_{2-x}\text{SiO}_4$ (here $x = 1$ is taken). The key element is identified by computing

$$N_{\text{sil}} = \delta_{\text{AGB,sil}} \min_{\text{X} \in [\text{Mg, Fe, Si, O}]} \left(\frac{M_{\text{X ej}}}{\mu_{\text{X}} N_{\text{ato}}^{\text{X}}} \right), \quad (3.16)$$

and taking $\delta_{\text{AGB,sil}} = 0.1$.

Differently from AGB stars, in SNII ejecta the formation of carbon and silicate dust grains is not mutually exclusive due to the lack of microscopic mixing in their ejecta. Therefore, we determine the mass that condenses into dust grains in SNII ejecta as

$$M_{\text{C dust}} = \delta_{\text{SNII,C}} M_{\text{C ej}} \quad (3.17)$$

for carbon grains and

$$M_{X \text{ dust}} = N_{\text{sil}} \mu_X N_{\text{ato}}^X. \quad (3.18)$$

for silicates, being $X \in [\text{Mg}, \text{Fe}, \text{Si}, \text{O}]$. In the above expressions, $M_{X \text{ ej}}$ is the mass of the X element ejected by SNII, and N_{sil} is computed as in Equation 3.16, adopting $\delta_{\text{SNII}, \text{C}} = \delta_{\text{SNII}, \text{sil}} = 0.1$.

In concluding this Section, it is important to note that the condensation efficiency parameters used in this study and their impact on model predictions will be further discussed within the context of the hydrodynamic simulations described in Chapter 4.

3.4.2 Shattering and coagulation

In the context of the two-size approximation used here, shattering simply transfers mass from large to small grains, and conversely, coagulation does the opposite.

Shattering occurs in the diffuse medium where typical velocities are relatively high. The corresponding timescale in our model is calculated as:

$$\tau_{\text{sh}} = \begin{cases} \tau_{\text{sh},0} \left(\frac{0.01}{\text{DTG}_{\text{L}}} \right) \frac{\text{cm}^{-3}}{n_{\text{gas}}} & n_{\text{gas}} < 1 \text{ cm}^{-3}, \\ \tau_{\text{sh},0} \left(\frac{0.01}{\text{DTG}_{\text{L}}} \right) \frac{\text{cm}^{-3}}{n_{\text{gas}}} \left(\frac{n_{\text{gas}}}{\text{cm}^{-3}} \right)^{2/3} & 1 \text{ cm}^{-3} \leq n_{\text{gas}} < 10^3 \text{ cm}^{-3}, \end{cases} \quad (3.19)$$

where $\tau_{\text{sh},0} = 5.41 \cdot 10^7$ yr (assuming a grain size of $0.1 \mu\text{m}$ and material density of 3 g cm^{-3} ; [Aoyama et al., 2017](#)), DTG_{L} represents the dust-to-gas ratio considering only large grains, and n_{gas} denotes the gas density. Differently from [Aoyama et al. \(2017\)](#), the smooth scaling of the shattering time-scale adopted here at $n_{\text{gas}} \geq 1 \text{ cm}^{-3}$ has been introduced in [Granato et al. \(2021\)](#) and resulted to be significant for the production of substantial amounts of small grains.

In the MUPPI context, the gas density of the particle is used to evaluate n_{gas} , except when the particle is in the MP state, in which case the cold gas density is employed. Shattering in the hot phase is neglected because the hot phase constitutes a typically insignificant fraction of the gas mass, and grains in the this phase are rapidly destroyed.

Clearly, in the SAM some assumption is needed to use a proper gas density in the above formula. In the fiducial model, n_{gas} is computed in each cold gas ring from:

$$\rho_{\text{gas}} = \frac{\Sigma_{\text{cold gas}}}{0.1 R_{\text{cold gas}}}, \quad (3.20)$$

where $\Sigma_{\text{cold gas}}$ is the surface density of the cold gas in a ring, and $R_{\text{cold gas}}$ the radius of the cold gas disc (i.e. we assume the height of the disc to be 0.1 its radius). Assuming $\mu = 1.2$, n_{gas} is derived from the above formula. The reasons for the choice of this prescription instead of, for example, a fixed n_{gas} will be briefly discussed in Section 5.4.4.

By converse, in the densest phases of the ISM (molecular clouds), small grains have relative velocities low enough to allow them to aggregate into large grains. The adopted coagulation timescale is ([Aoyama et al. 2017](#); see also [Granato et al. 2021](#)):

$$\tau_{\text{coa}} = \tau_{\text{co},0} \left(\frac{0.01}{\text{DTG}_{\text{S}}} \right) \left(\frac{0.1 \cdot \text{km s}^{-1}}{v_{\text{coa}}} \right) \frac{1}{F_{\text{dense}}}. \quad (3.21)$$

In the above expression, $\tau_{\text{coa},0} = 2.71 \cdot 10^5 \text{ yr}$ (obtained assuming a grain size of $0.005 \mu\text{m}$ and material density of 3 g cm^{-3}), $v_{\text{coa}} = 0.2 \text{ km s}^{-1}$, DTG_S is the dust-to-gas ratio considering only small grains, and F_{dense} is the dense gas fraction.

In MUPPI, coagulation is assumed to take place exclusively in MP particles. The fraction of dense gas, F_{dense} , is determined using the molecular gas partitioning provided by MUPPI (see Section 2.4.2), specifically calculated as $F_{\text{dense}} = f_{\text{mol}} \cdot f_{\text{cold}}$, where f_{cold} denotes the mass fraction of the gas particle in cold gas.

In the SAM, coagulation is able to affect only small grains in the cold gas disc, and $F_{\text{dense}} = f_{\text{mol}}$, where the molecular fraction is computed self-consistently by the model for each ring (Section 2.3.3).

3.4.3 Grains accretion

The process of grains accretion, or *grain growth*, is effective within molecular clouds. Therefore, it operates in MP gas particles in the MUPPI based hydrodynamic simulations and within each cold gas disc ring in SAM when the molecular gas fraction is non-zero. The accretion timescale is modeled for each element X according to [Hirashita & Kuo \(2011\)](#):

$$\tau_{\text{acc},X} = \frac{a f_X s \mu_X}{3 n Z_X \bar{\mu} S} \left(\frac{2\pi}{m_X k T} \right)^{0.5} \frac{1}{F_{\text{dense}}}. \quad (3.22)$$

In the above expression, $S = 0.3$ is the sticking efficiency, $T = 50 \text{ K}$ and $n = 10^3 \text{ cm}^{-3}$ the temperature and the density assumed for molecular clouds, μ_X and m_X the atomic weight and mass of the element, $\bar{\mu}$ the mean molecular weight, f_X the mass fraction of the element in the grain, and Z_X the gas phase mass fraction of the element. The material density s is assumed to be $s = 2.2 \text{ g cm}^{-3}$ and $s = 3.3 \text{ g cm}^{-3}$ for carbonaceous and silicate grains. F_{dense} represents the fraction of dense gas where the accretion process occurs (similar to coagulation), and a denotes the grain radius. According to [Hirashita \(2015\)](#), this surface process is assumed to exclusively affect small grains due to their larger surface-to-mass ratio. A representative radius of $a = 0.005 \mu\text{m}$ for small grains is employed in the previous equation.

The accretion timescale is computed for each chemical element that contributes to the dust composition, within each MUPPI MP gas particle and within each L-GALAXIES cold gas ring. The timescale derived from Equation 3.22 is straightforwardly applied to carbon grains. For the elements composing silicate grains (O, Si, Mg, and Fe), the accretion timescale of the element that maximizes it is used. This approach ensures the preservation of the olivine-like chemical composition adopted in this model.

3.4.4 Grains destruction in SNe shocks

The implementation of small and large grain destruction in SN shocks differs between the MUPPI and L-GALAXIES contexts. However, conceptually, both models relate the number of exploded SNe to the rate of grain destruction, with some assumptions about the efficiency of this process.

In the hydrodynamic simulations, the SN destruction timescale due to the explosion of N_{SN} SNe (both SNII and SNIa) during a time-step Δt is written as ([Aoyama et al., 2017](#)):

$$\tau_{\text{des},\text{SN}} = \frac{\Delta t}{1 - (1 - \eta)^{N_{\text{SN}}}}, \quad (3.23)$$

where

$$\eta = \epsilon_{\text{SN}} \min \left(\frac{M_{\text{sw}}}{M_{\text{g}}} \right), \quad (3.24)$$

being $\epsilon_{\text{SN}} = 0.1$ the destruction efficiency and M_{sw} the swept mass per SN event (which is always much smaller than the mass of the gas particle M_{g}). The swept mass is computed following [McKee \(1989\)](#) as

$$M_{\text{sw}} = 6800 M_{\odot} \left(\frac{E_{\text{SN}}}{10^{51} \text{erg}} \right) \left(\frac{v_{\text{s}}}{100 \text{km s}^{-1}} \right)^{-2}, \quad (3.25)$$

where $E_{\text{SN}} = 10^{51}$ erg is the energy assumed to be associated with each SN event and $v_{\text{s}} = 200 \text{km s}^{-1}$ the shock velocity.

In the SAM, the timescale of the process is evaluated for each cold gas ring, when the rate R_{SN} of the associated stellar disc ring is non zero:

$$\tau_{\text{des, SN}} = \frac{M_{\text{cold}}}{\epsilon_{\text{SN}} M_{\text{sw}} R_{\text{SN}}}, \quad (3.26)$$

where M_{cold} is the mass of the gas ring, M_{sw} is the gas mass swept by a SN event, R_{SN} is the SN rate and $\epsilon_{\text{SN}} = 0.1$ is the dust destruction efficiency. Following [Asano et al. \(2013a\)](#), see also [Yamasawa et al. 2011](#)) the swept mass is evaluated as:

$$M_{\text{swept}} = 1535 \left(\frac{Z}{Z_{\odot}} + 0.039 \right)^{-0.289} M_{\odot}, \quad (3.27)$$

being Z the gas metallicity of the ring. The SN rate is computed self-consistently by the SAM, without differentiating between SNII and SNIa, so that $R_{\text{SN}} = R_{\text{SNII}} + R_{\text{SNIa}}$.

3.4.5 Grains sputtering

Sputtering is assumed to take place in the hot phase of gas particles within hydrodynamic simulations and in the hot atmosphere of SAM halos.

The timescale for this process is obtained following [Tsai & Mathews \(1995\)](#):

$$\tau_{\text{spu}} = \tau_{\text{spu},0} \frac{a_{0.1} \mu\text{m}}{\rho_{10^{-27} \text{g cm}^{-3}}^{\text{gas,hot}}} \left[\left(\frac{T_{\text{spu},0}}{\min(T_{\text{gas,hot}}, 3 \cdot 10^7 \text{K})} \right)^{\omega} + 1 \right], \quad (3.28)$$

where $T_{\text{spu},0} = 2 \cdot 10^6$ K, $\omega = 2.5$, $a_{0.1} \mu\text{m}$ is the grain radius in $0.1 \mu\text{m}$ units, $\rho_{10^{-27} \text{g cm}^{-3}}^{\text{gas,hot}}$ the hot gas density in $10^{-27} \text{g cm}^{-3}$ units, and $T_{\text{gas,hot}}$ the hot gas temperature. The representative grain radii assumed for large and small grains are, respectively, $a_{\text{L}} = 0.05 \mu\text{m}$ and $a_{\text{S}} = 0.005 \mu\text{m}$.

The hot gas density in the hydrodynamic simulation is determined either by considering the gas density of the particle or solely the density of the hot gas phase in the case of MP particles. A fully ionized medium with a molecular weight of $\mu = 0.59$ is assumed. Similarly, the temperature corresponds to that of the gas particle or the temperature of the hot phase.

In the SAM, the hot gas density is determined by averaging its value assuming it fills the DM halo up to the virial radius. The temperature of the hot gas is set to the virial temperature $T_{\text{vir}} = \frac{\mu m_{\text{p}}}{2k} V_{\text{vir}}^2$, so that:

$$\rho^{\text{gas,hot}} = \frac{M_{\text{gas,hot}}}{4\pi R_{\text{vir}}^3/3} \quad \text{and} \quad T_{\text{gas,hot}} = 35.9 \cdot \left(\frac{V_{\text{vir}}}{\text{km/s}} \right)^2 \quad [\text{K}], \quad (3.29)$$

where R_{vir} and V_{vir} are the virial radius and virial velocity of the halo for central galaxies, or these quantities at infall for satellites.

The same prescription is adopted for dust in the ejected reservoir of SAM galaxies.

In the hydrodynamic simulations, the normalization constant for thermal sputtering is $\tau_{\text{sput},0} = 2.7 \cdot 10^8$ yr. However, in the SAM, this constant is doubled to $\tau_{\text{sput},0} = 5.4 \cdot 10^8$ yr in order to obtain a less efficient sputtering process. The rationale for reducing the sputtering efficiency has been discussed in previous studies of galaxy clusters by [Gjergo et al. \(2018\)](#) and [Vogelsberger et al. \(2019\)](#). In the SAM context, this reduction is further implemented to better match the cosmic abundance of dust in the CGM (see Section 5.5.2).

3.4.6 Dust cooling

In hydrodynamic simulations, the contribution of dust infrared (IR) emission to gas cooling in the hot phase is considered, whereas this effect is not included in the SAM implementation.

The heating rate of dust grains within gas particles is expressed as a function of the grain size, gas temperature T_{gas} and electron number density n_e ([Dwek & Werner, 1981](#)):

$$H(a, T) = \begin{cases} 5.38 \cdot 10^{-18} n_e a^2 T_{\text{gas}}^{1.5} & x > 4.5, \\ 3.37 \cdot 10^{-13} n_e a^{2.41} T_{\text{gas}}^{0.88} & 1.5 < x \leq 4.5, \\ 6.48 \cdot 10^{-6} n_e a^3 & 1.5 \leq x, \end{cases} \quad (3.30)$$

with $x = 2.71 \cdot 10^8 a^{2/3} T_{\text{gas}}^{-1}$. From the above expression, the cooling rate Λ_{dust} due to large and small ($a = 0.05 \mu\text{m}$ and $0.005 \mu\text{m}$) is derived as:

$$\Lambda_{\text{dust}}(a) = n_{\text{dust}}(a) H(a, T_{\text{gas}}, n_e). \quad (3.31)$$

This contribution is summed to the one coming from the metallicity- and temperature-dependent standard gas cooling function.

Part II

Results

4

Dust evolution with MUPPI in cosmological volumes

The admittedly complex and uncertain dust processes are incorporated into cosmological galaxy formation and evolution simulations in a non-systematic way (Section 3.3). Moreover, dust properties are often neglected in these simulations, which are able to track only the mass of dust and not, e.g., the size distribution and/or chemical composition of grains (see Table 3.3.3 for a summary of other cosmological simulations). In this Chapter, we¹ analyze a cosmological box simulated with the sub-resolution model MUPPI (see Murante et al., 2015; Valentini et al., 2020, and references therein; see also Section 2.4), and including the state-of-the-art dust model introduced in Gjergeric et al. 2018; Granato et al. 2021 (see also Section 3.4).

The present study is the first one in which the evolution of the chemical composition of dust and its size distribution are tracked simultaneously and independently for two dust species in a cosmological volume. Moreover, for the first time, the general performances of the most recent version of MUPPI, with included AGN physics, are tested on cosmological volumes. MUPPI has been developed, refined and calibrated in a series of papers on zoom-in cosmological simulations of Milky Way (MW) like galaxies. For this reason, in the present work, the MUPPI parameters and setup are taken as given, and particular attention is devoted to the properties of the simulated galaxies hosted by DM halos featuring a mass within a factor ~ 3 from that of MW. In this Chapter, these objects are referred to as MWHM (Milky Way Halo Mass) galaxies. However, the results of MUPPI when compared with observations related to the general galaxy populations are critically discussed, and a few possible modifications of the model are discussed in order to improve its performances. The MW halo total mass² adopted is $M_{200} \approx 10^{12} M_{\odot}$ (for a recent compilation of estimates see Callingham et al., 2019).

The Chapter is structured as follows. The simulations setup is introduced in Section 4.1. Sections 4.2 and 4.3 discuss how the simulated galaxy population matches the available observational constraints, focusing on general properties independent of dust. Then we will discuss the ISM dust properties of galaxies in Section 4.4, including the DMF, dust scaling relations and grains properties. Section 4.5 focuses on extra-galactic dust. Finally, Section 4.6 presents a summary, some discussion and future developments.

¹This Chapter is based on a published work done in collaboration with Cinthia Ragone-Figueroa, Gian Luigi Granato, Stefano Borgani, Giuseppe Murante, Milena Valentini, Alessandro Bressan, and Andrea Lapi (Parente et al., 2022).

² M_{200} is the mass enclosed within a sphere whose mean density is 200 times the critical density at the considered redshift. The radius of this sphere is dubbed R_{200} .

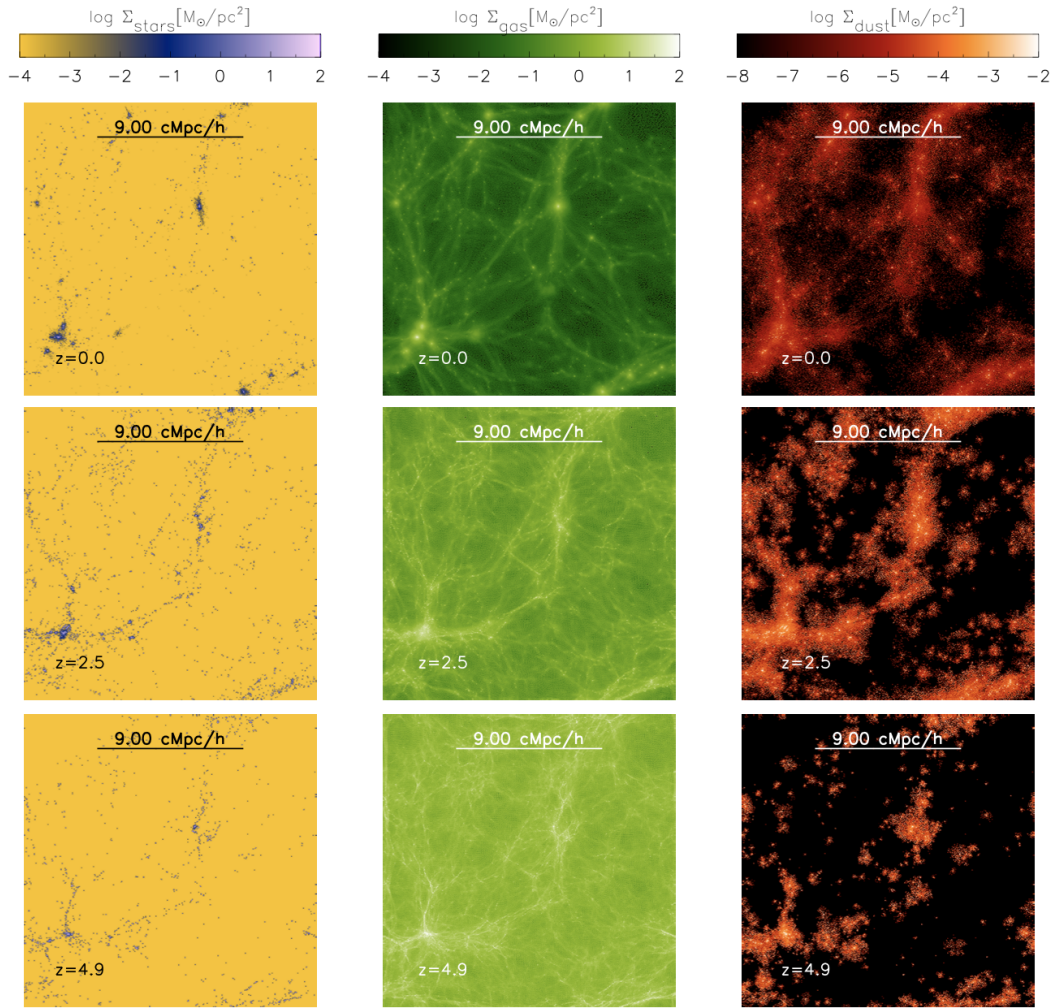


FIGURE 4.1: Maps of stars, gas, and dust in the largest simulated box at $z = 0.0, 2.5,$ and 4.9 . These distributions correspond to slices of the box with a depth of $5 \text{ Mpc}/h$.

CONTENTS

| | |
|---|----|
| 3.1 Numerical Simulations | 66 |
| 3.2 General properties of the galaxy population | 67 |
| 3.3 Main properties of the MWHM galaxies | 74 |
| 3.4 Dust inside galaxies | 76 |
| 3.5 Dust outside galaxies | 85 |
| 3.6 Summary and Discussion | 90 |

4.1 Numerical Simulations

The hydrodynamic simulations are performed with our branch of the GADGET3 code, which is a non-public evolution of GADGET2 (Springel, 2005). The hydrodynamics is treated with the improved SPH by Beck et al. (2016).

The same cosmological parameters as the IllustrisTNG simulation³ are used here, which in turn were selected in accordance with [Planck Collaboration et al. \(2016\)](#). Thus $\Omega_m = \Omega_{\text{DM}} + \Omega_b = 0.3089$, $\Omega_b = 0.0486$, $\Omega_\Lambda = 0.6911$, $h = 0.6774$, adopting a power spectrum with primordial index $n_s = 0.9667$ and normalization $\sigma_8 = 0.8159$. The main simulated box has a size of 26 cMpc from initial conditions (ICs) obtained at $z = 99$. Maps of the stellar, gas and dust component of this box are shown in [Figure 4.1](#). To improve the statistic, and to test quickly the effects of model variations, 4 boxes of size 13 cMpc each were also run. The initial conditions have been generated with the public code N-GenIC⁴.

The mass resolution of DM particles is $M_{\text{DM}} \simeq 3.75 \cdot 10^7 M_\odot$, while the gas particles have initially a mass $M_{\text{gas}} \simeq 7 \cdot 10^6 M_\odot$. However, the masses of gas particles undergo modifications due to star formation and chemical feedback (i.e. enriched gas restitution due to stellar evolution processes) from neighbouring stellar particles, which are spawned from the former ones during the evolution of the system ([Section 2.4.2](#)). The gravitational force is softened with a Plummer-equivalent softening length of 740 pc, constant in comoving units at $z > 2$, and constant in physical units at lower redshift. The resolution adopted here is very similar to that of the AqC6 initial conditions, which have been extensively studied in [Granato et al. \(2021\)](#), as well as in several previous MUPPI works not related to dust. However, as discussed in [Murante et al. \(2015\)](#), MUPPI is weakly resolution dependent, as long as molecular cloud masses are not resolved (see also [Figure 13 in Granato et al., 2021](#)).

This work relies on the MUPPI model for unresolved processes, namely star formation, feedback, chemical enrichment ([Section 2.4](#)) with parameters as in [Valentini et al. \(2020\)](#). The dust evolution model is the one outlined in [Section 3.4](#). The adopted IMF is that by [Kroupa et al. \(1993\)](#).

4.1.1 Galaxies identification

The Friends-of-Friends (FoF) algorithm is used to arrange particles in groups with a linking length of 0.16 the mean interparticle separation. Then the gravitationally bound sub-structures of the identified halos are detected by applying the Subfind algorithm ([Springel et al., 2001](#); [Dolag et al., 2009](#)). Throughout this paper only central galaxies are analysed, which are associated with the main subhalo of a FoF halo, i.e. the subhalo which hosts the most gravitationally bound particle of the group.

The quantities of each galaxy (e.g. stellar mass, metallicity, dust mass) are computed considering gas and stellar particles within a 3D aperture with radius $R_{\text{gal}} = 0.1R_{200}$, including only particles belonging to the corresponding subhalo. This refer to R_{gal} as the radius of the galaxy. In our analysis we consider only galaxies with stellar mass $M_{\text{stars}} \gtrsim 10^8 M_\odot$, which corresponds to $\gtrsim 100$ stellar particles.

4.2 General properties of the galaxy population

This Section discusses how our fiducial simulation aligns with several fundamental observational quantities associated with the stellar component of the galaxy population. Nevertheless, we emphasize that the goal of this work is to evaluate our dust evolution modeling on a relatively large sample of simulated galaxies, specifically targeting those with masses similar to that of the MW, for which MUPPI has been previously tailored, rather than to modify MUPPI

³<https://www.tng-project.org>

⁴<https://www.h-its.org/2014/11/05/ngenic-code>

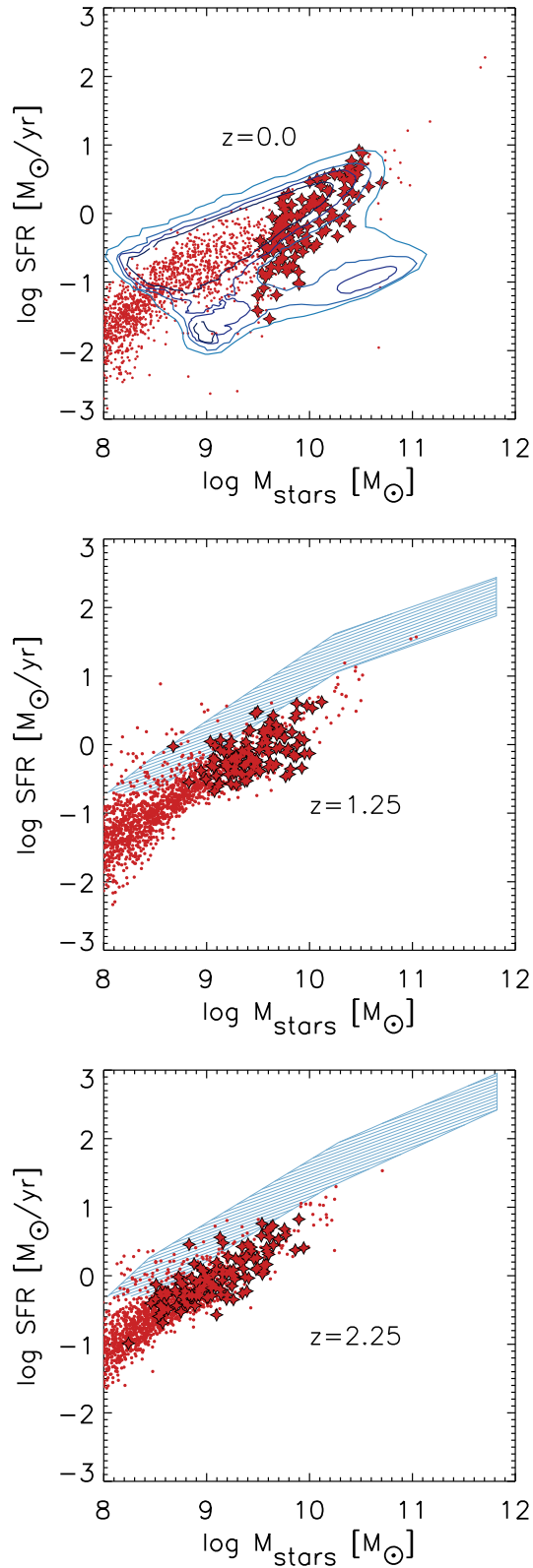


FIGURE 4.2: Main Sequence of the set of fiducial runs at different redshifts. Star symbols refer to MWHM galaxies and their progenitors. At $z = 0.0$ we compare our results with [Renzini & Peng \(2015\)](#). Four contour levels from their Figure 4 are shown. From lighter to darker blue they correspond to number density of $\approx 4, 8, 11, 13 \cdot 10^4$. At higher redshift we show with shaded regions the distribution of Main Sequence galaxies from [Leja et al. \(2019\)](#).

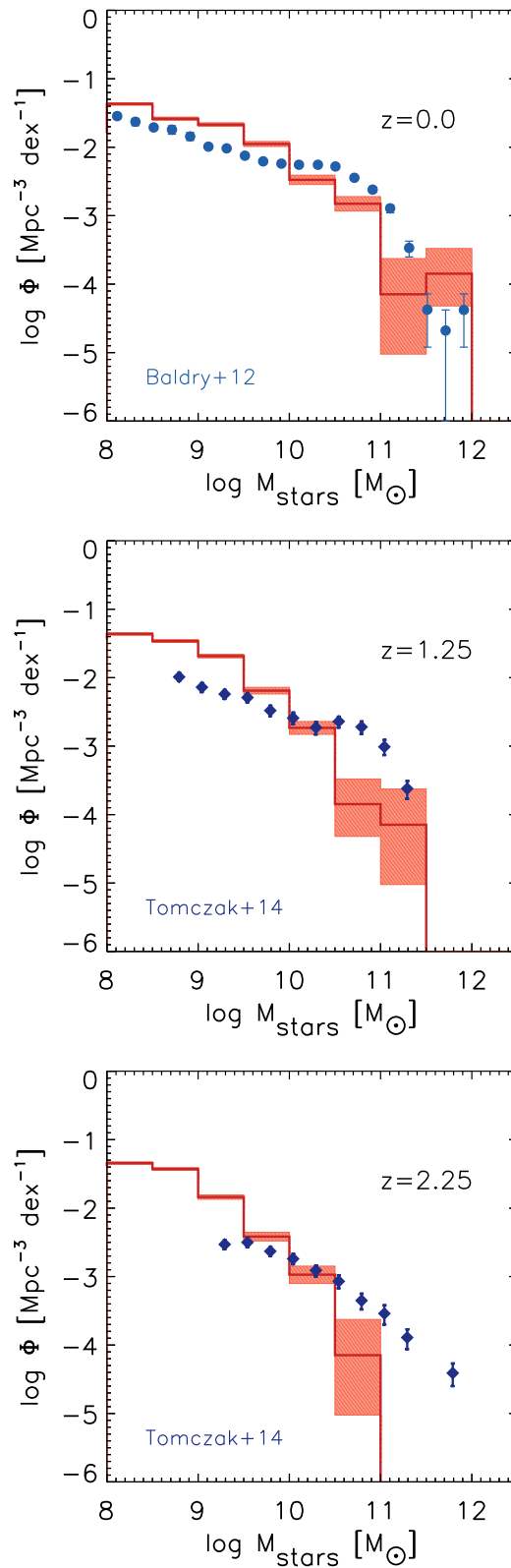


FIGURE 4.3: Stellar Mass Function of the set of fiducial runs at different redshifts; the shaded area is the Poissonian error. The local determination of Baldry et al. (2012) is shown, while we compare with Tomczak et al. (2014) data in the $z = 1.25$ and $z = 2.25$ panels.

to fit the general galaxy population in the sample. Unsurprisingly, achieving this outcome required several model adjustments, as we detailed in [Ragone-Figueroa et al. \(2024\)](#).

4.2.1 Galaxy Main Sequence

It is well established that galaxies concentrate in specific regions on the star formation-stellar mass plane (see [Renzini & Peng, 2015](#), and references therein). Star-forming galaxies delineate the so-called main sequence (MS), as these two quantities are strongly correlated. The MS represents the most populated region of the plane in terms of number, whereas the mass budget in the local Universe is dominated by quenched galaxies, which exhibit a SFR roughly an order of magnitude below the MS.

In [Figure 4.2](#), we present the distribution of simulated galaxies on the M_{stars} -SFR plane across three redshift snapshots, along with a selection of recent observational data. At $z = 0$, we overlay four density contours from [Figure 4](#) of [Renzini & Peng \(2015\)](#). Their spectroscopic sample, which is drawn from the Sloan Digital Sky Survey DR7 release, includes approximately 240,000 galaxies.

At $z = 1.25$ and 2.25 , we show the recent observational determinations of the MS of star-forming galaxies by [Leja et al. \(2019\)](#) for the redshift ranges $1.0 < z < 1.5$ and $2.0 < z < 2.5$, respectively. To accurately compare our results with observational data, we convert the observational estimates of SFRs and stellar masses to our adopted IMF ([Kroupa et al., 1993](#))⁵. [Figure 4.2](#) shows a reasonable qualitative agreement at $z = 0$ between the distribution of our simulated galaxies and the observed MS in the M_{stars} -SFR plane. However, our simulation exhibits a shortage of quenched galaxies, particularly at $z = 0$. We found that this issue could be mitigated by increasing the SMBH growth and related AGN feedback, compared to the setup used in [Valentini et al. \(2020\)](#) ([Section 4.2.3](#)).

At higher redshifts, the simulated galaxies show a deficiency in SFR by a factor of ~ 3 at a given stellar mass, consistent with the under-prediction of the SFRD discussed in [Section 4.2.4](#).

4.2.2 Stellar Mass Function

The predicted SMFs at the same three cosmic epochs are shown in [Figure 4.3](#), alongside several observational estimates. At $z = 0$, the agreement is reasonably good, although there is a tendency to overproduce galaxies with $M_{\text{stars}} < 10^{10} M_{\odot}$ and under-produce those above this mass. This issue becomes more clear at higher redshifts. However, the statistical significance at high masses is limited by the size of the simulated sample. It is noteworthy that achieving a good match with observed SMFs in state-of-the-art cosmological simulations often requires complex and somewhat ad-hoc adjustments to galactic wind velocities and/or efficiencies, which may vary with galaxy properties such as metallicity, mass, and redshift (e.g., [Pillepich et al., 2018](#)).

4.2.3 SMBH-bulge relation

Here we briefly explore the impact of modifying the SMBH growth and feedback scheme in our fiducial model ([Section 2.4.4](#)). The model dubbed FID-moreBH was obtained from the

⁵For SFRs, we use the coefficients reported in [Table 1](#) of [Driver et al. \(2013\)](#). The conversion of stellar masses is more uncertain as it depends on the region of the SED used to estimate the stellar mass and on the star formation and metal enrichment histories. Throughout this work, when comparing our predictions with observed stellar masses, we use the results by [Portinari et al. \(2004\)](#), who provide the $M/L_{\text{I band}}$ ratios for different IMFs. Specifically, we scale the observed stellar masses by a factor $(M/L_{\text{I,K93}})/(M/L_{\text{I,IMF}})$, where the subscripts K93 and IMF refer to the [Kroupa et al. \(1993\)](#) IMF (used in this work) and the generic IMF used to derive the observed stellar masses, respectively. For the metallicity values investigated by [Portinari et al. \(2004\)](#), the correction is approximately 1.1 for a [Chabrier \(2003\)](#) IMF and 1.4 for a [Salpeter \(1955\)](#) IMF.

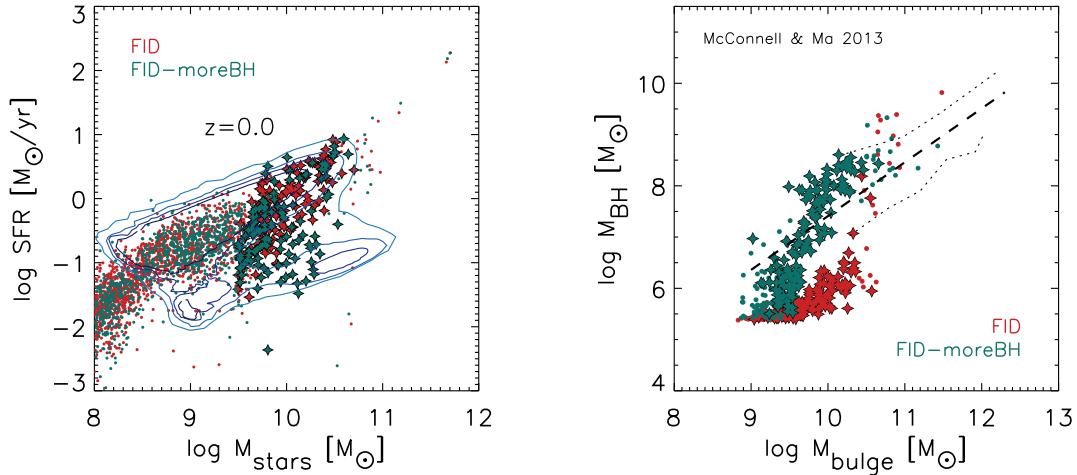


FIGURE 4.4: *Left panel:* Same as $z = 0.0$ panel of Figure 4.2 for our fiducial run and the run with enhanced BH feedback (see text). MWHM galaxies are marked with star symbols. *Right panel:* $M_{\text{bulge}} - M_{\text{BH}}$ at $z = 0.0$ for fiducial run and the run with enhanced BH feedback. MWHM galaxies are marked with star symbols. The fit by [McConnell & Ma \(2013\)](#) is shown.

fiducial one by increasing the feedback efficiency ϵ_f , from the value 0.01 used by [Valentini et al. \(2020\)](#) (see their Equation 19 and 25, and their Table 2) to 0.05, and by switching off the angular momentum limiter described in their Section 3.3. As it is clear from the figure, this modification produces a population of more quenched galaxies at low redshift, and yields a correlation between the SMBH and spheroidal stellar component⁶ in better agreement with the observations. However, since the results discussed here on dust are largely unaffected, we stick to the setup of [Valentini et al. \(2020\)](#) for the fiducial run.

4.2.4 Cosmic Star Formation Rate

Figure 4.5 illustrates the redshift evolution of the total cosmic SFRD from our simulations, together with some observational determinations. Unfortunately, the SFRD predicted by our fiducial run (FID) significantly deviates from observational estimates, exhibiting a broad peak at too high redshifts (around $z \sim 4$) and low values at lower redshifts. The largest discrepancy occurs at redshifts around $\sim 2 - 3$, where we under-predict the SFRD by a factor of ~ 3 .

It is important to note that numerous studies have explored the consistency between the histories of the SFRD and the cosmic stellar mass density (SMD). In many cases, it has been found that the former needs to be revised downward to align better with the latter, particularly around $z \sim 2$. This discrepancy could arise from various factors that might lead to an underestimate of the SMD or an overestimate of the SFRD (see [Yu & Wang, 2016](#), and references therein). If the SFRD were adjusted downward, it could better align with our fiducial simulation.

Indeed, as discussed in Section 4.2.2, the predicted SMF in the local universe matches reasonably well with observations. Consequently, the final stellar mass density is well reproduced. The integral of the observed and simulated SMFs differs by a modest ~ 0.1 dex.

Setting aside the aforementioned considerations about potential observational tensions, we dedicated some effort to investigate an enhancement to our model, exploiting our treatment

⁶See the definition of bulge stars in Section 4.3.

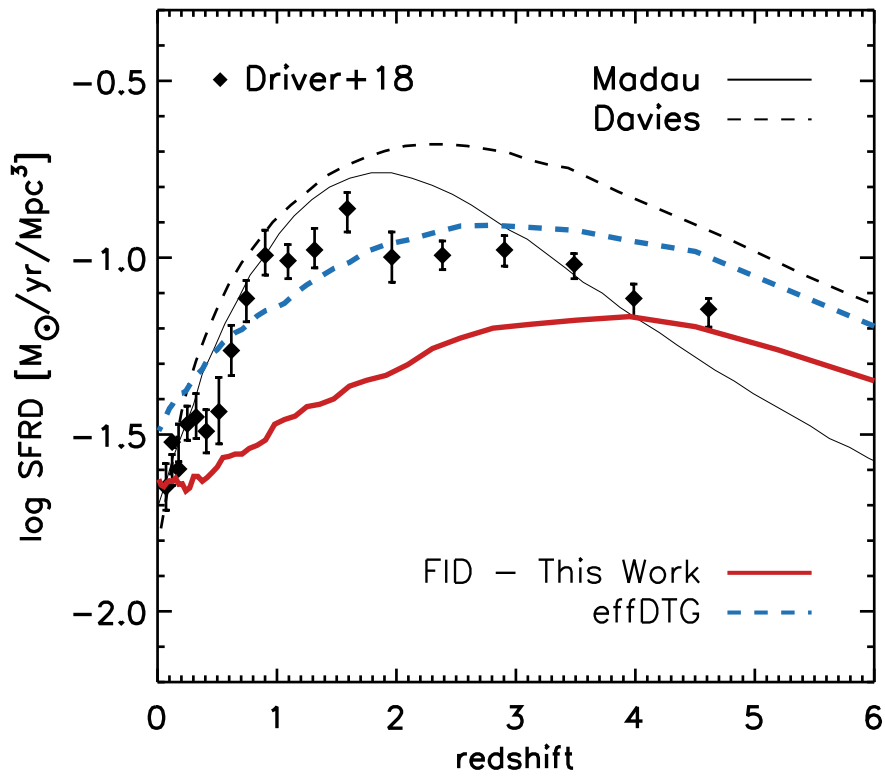


FIGURE 4.5: Median SFRD of the boxes used in this study (FID; red), alongside a potential enhancement discussed in Section 4.2.4 (effDTG; blue). We overlay various determinations of SFRD(z) from the literature: the *solid* and *dashed* black lines represent fits to the cosmic SFRD by Madau & Dickinson (2014) and Davies et al. (2016), respectively, while the *black points* denote the measurements by Driver et al. (2018). All these data have been recalibrated to match our IMF (Kroupa et al., 1993) using the coefficients provided in Table 1 of Driver et al. (2013).

of ISM dust. A better alignment with the SFRD can be achieved if the star formation efficiency increases with cosmic time. A plausible hypothesis is that this efficiency rises with the DTG ratio of the gas particles in our simulation. It is conceivable that an ISM enriched with dust enhances star formation through mechanisms not fully resolved at our simulation's level. Star formation occurs within cold, dense, and dusty molecular clouds, whose masses and sizes are far below our current resolution. Dust plays a pivotal role in these regions by influencing the amount of star-forming gas. It promotes processes such as the formation of H_2 molecules and shields gas from the UV interstellar radiation field. It is well established that catalytic reactions on the surfaces of interstellar grains become the primary channel for H_2 formation whenever dust is present (for a recent review, see [Wakelam et al., 2017](#)). Furthermore, it has been proposed that dust shielding might be even more critical than H_2 presence in facilitating star formation within gas clouds (e.g., [Krumholz et al., 2011](#); [Glover & Clark, 2012](#); [Byrne et al., 2019](#)). In conclusion, molecular clouds with higher DTG ratios could potentially convert a larger fraction of their mass into stars before eventual destruction, benefiting from enhanced shielding and increased capability to produce new H_2 molecules.

Motivated by these insights, we decided to explore a star formation efficiency that depends on the DTG⁷, as detailed in the following.

The DTG-dependent star formation efficiency we adopt is (effDTG model in [Figure 4.5](#)):

$$\dot{M}_{\text{sf}} = f_*(\text{DTG}) \cdot \frac{f_{\text{mol}} M_{\text{c}}}{t_{\text{dyn,c}}}. \quad (4.1)$$

Here M_{c} is the cold mass of the MP particle, f_{mol} its molecular fraction, and $t_{\text{dyn,c}}$ is the cold gas dynamical time. The factor $f_*(\text{DTG})$ represents the star formation efficiency of the molecular clouds. In our fiducial model (as well as in previous MUPPI works), the same equation is used setting a constant and quite low value for $f_* = 0.02$. The dependence on the DTG ratio of the particle is adopted instead in the effDTG model:

$$f_*(\text{DTG}) = \left(\alpha + \frac{\beta - \alpha}{1 + \left(\frac{\text{DTG}}{\text{DTG}_{\text{crit}}} \right)^\gamma} \right)^{-1}. \quad (4.2)$$

A good match with the observed SFRD can be obtained by setting $\beta = 50$, $\alpha = 12$, $\text{DTG}_{\text{crit}} = 2 \cdot 10^{-5}$ and $\gamma = 0.8$. With these values, the star formation efficiency increases smoothly with DTG, ranging from 0.02, when there is no dust, to ≈ 0.08 , when $\text{DTG} \gg \text{DTG}_{\text{crit}}$. We remark that [Equation 4.2](#) simply aims at describing an increasing star formation efficiency with DTG, with a smooth functional form covering reasonable star formation efficiency values (e.g. [Kim et al. 2021](#)).

Despite the promising results regarding SFRD predictions with the effDTG model, we have not pursued this solution. We recognize that further modifications to the code would be necessary to align the statistical results with observations and to recover the findings from MUPPI zoom-in simulations of MW-like galaxies. Consequently, this work has been deferred to [Ragone-Figueroa et al. \(2024\)](#), where we aimed to address these goals by adjusting the model and incorporating a dust-promoted H_2 component to model the SFR.

To summarize the results of this [Section 4.2](#), our current model struggles to accurately reproduce the cosmic SFRD, although the local SMF shows acceptable agreement with observational data, especially for galaxies with stellar masses within approximately an order

⁷We utilize our dust model and consider the DTG of SPH gas particles hosting star formation. However, due to the DTG-Z correlation (see [Section 4.4.3](#)), a metallicity-dependent star formation efficiency might also yield similar outcomes.

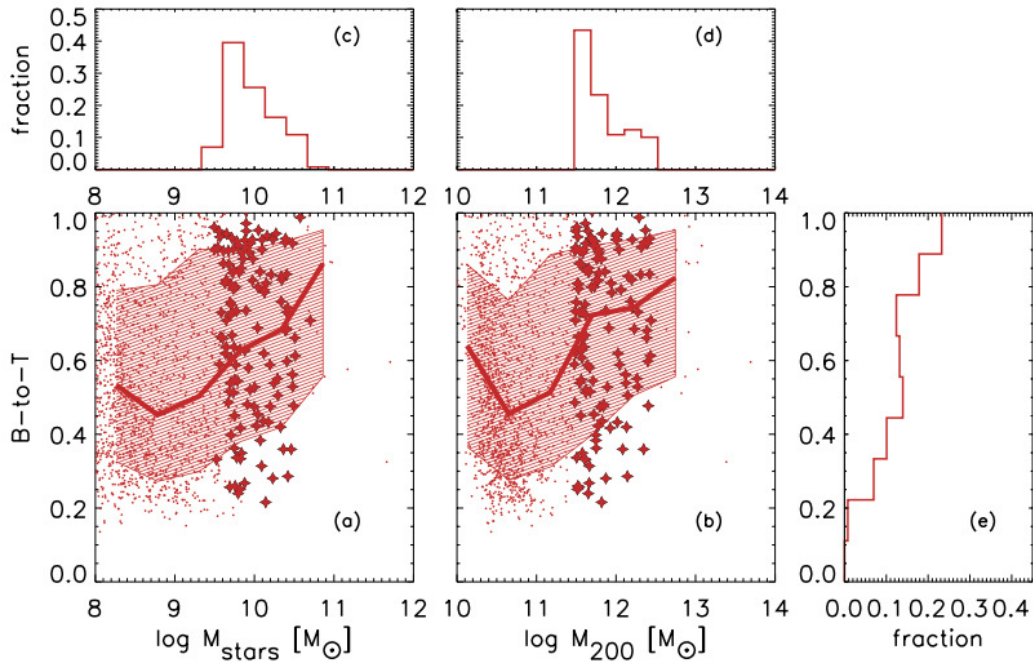


FIGURE 4.6: Bulge-to-Total ratio as a function of the stellar mass (a) and halo mass (b) at $z = 0.0$. We show the full sample of our simulated galaxies, and mark MWHM galaxies with a star symbol. In small panels we show the distribution of M_{stars} (c), M_{200} (d) and B-to-T (e) restricted to MWHM galaxies. The solid line marks the median of all galaxies, while the shaded region encloses the 25-75th percentiles.

of magnitude of the MW mass. This alignment is consistent with MUPPI calibration on this particular galaxy mass scale.

Therefore, we focus particular attention on galaxies forming in halos with final masses M_{200} ranging from $3 \cdot 10^{11}$ to $3 \cdot 10^{12} M_{\odot}$, which spans one dex around the estimated mass of the MW halo ($10^{12} M_{\odot}$) (see Callingham et al., 2019, and references therein). These galaxies, referred to as MWHM galaxies hereafter, are where MUPPI is believed to capture the essential characteristics of unresolved star formation and feedback processes.

4.3 Main properties of MWHM galaxies

We now discuss some properties, not directly related to dust, of the simulated galaxies formed in DM halos whose mass is within a factor ~ 3 that of the MW (MWHM galaxies).

Figure 4.6 shows 1D and 2D distributions of the bulge over total mass ratio B/T as a function of stellar and halo mass. The B/T is estimated from the star particles 6D phase space information, following Murante et al. (2015). We compute the orbital circularity $\epsilon_j = J_{\hat{z},j}/J_{\text{circ},j}$ of stellar particles within R_{gal} . Here, \hat{z} is the net spin axis of the galaxy, $J_{\hat{z},j}$ is the z component of the particle j specific angular momentum and $J_{\text{circ},j}$ is its specific angular momentum if the particle had a circular orbit with the same energy. The bulge mass is obtained by summing the mass of the stellar particles with $\epsilon_j < 0$, and multiplying it by 2, under the hypothesis that the bulge is supported by velocity dispersion and the number of co- and counter-rotating stars is equal.

The resulting distribution of B/T for MWHM galaxies is quite broad, featuring a median of 0.68 and an inter-quartile range 0.47-0.83. This is in broad agreement with observational

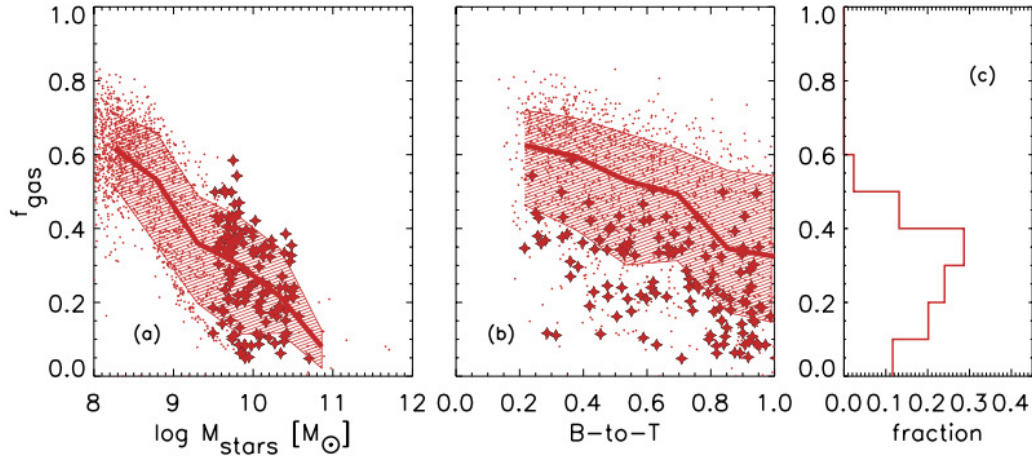


FIGURE 4.7: Gas fraction $f_{\text{gas}} = M_{\text{gas,MP}} / (M_{\text{gas,MP}} + M_{\text{stars}})$ as a function of the stellar mass (a) and Bulge-to-Total ratio (b) at $z = 0.0$. We show the full sample of our simulated galaxies, and mark MWHM galaxies with a star symbol. In the right small panel (c) the distribution of f_{gas} of the MWHM galaxies is shown. The solid line marks the median of all galaxies, while the shaded region encloses the 25-75th percentiles.

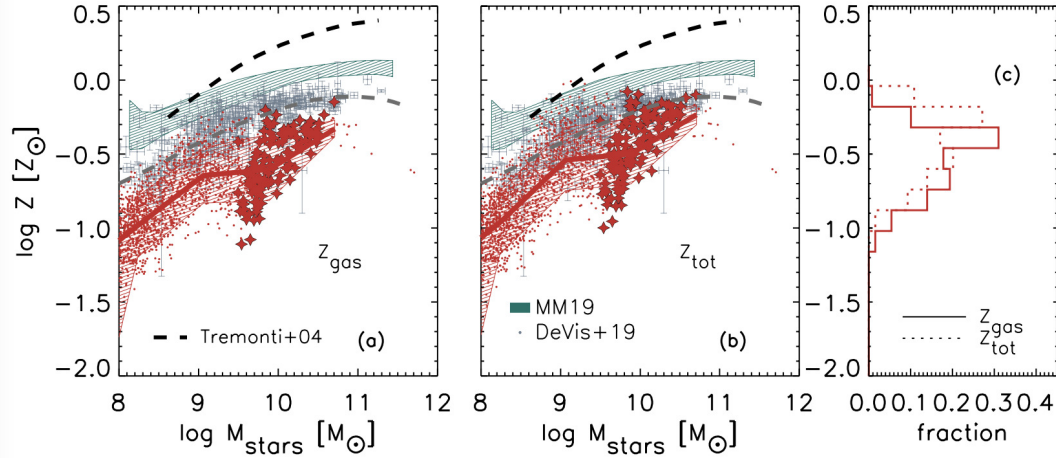


FIGURE 4.8: Mass-Metallicity relation for our simulated galaxies at $z = 0.0$ (MWHM galaxies are marked with a star symbol). We report both the gas metallicity ($Z_{\text{gas}} = M_{\text{metals,gas}} / M_{\text{gas}}$, panel a) and the total ISM metallicity $Z_{\text{tot}} = (M_{\text{metals,gas}} + M_{\text{metals,dust}}) / M_{\text{gas}}$, panel b), e.g. including also the metals locked in dust grains. Some determinations from literature are shown: Tremonti et al. (2004, black dashed line), Maiolino & Mannucci (2019, green shaded region), and De Vis et al. (2019, gray points and dashed line). De Vis et al. (2019) data refer to the DUSTPEDIA sample, with their reference (PG16S, their Section 3.2) calibration for metallicities and stellar masses derived by Nersesian et al. (2019). In panel (c) the distribution of both Z_{gas} and Z_{tot} is shown for MWHM galaxies. The solid line marks the median of all galaxies, while the shaded region encloses the 25-75th percentiles.

results and with those from other simulations (see for instance figure 3 in [Tacchella et al., 2019](#), and references therein). However, the details depend on the different methods used to derive B/T, as discussed in Section 3.2 of the latter paper.

Figure 4.7 shows 1D and 2D distributions of the gas fraction $f_{\text{gas}} = M_{\text{gas,MP}} / (M_{\text{gas,MP}} + M_{\text{stars}})$ ⁸ as a function of the stellar mass and of B/T. The median gas fraction of MWHM galaxies is 9.3, with a tendency for lower values at larger B/T, as expected. In particular, later type galaxies feature f_{gas} values somewhat larger than those found in nearby late type galaxies (e.g. [Saintonge & Catinella, 2022](#)).

Finally, we report gas phase metallicity Z_{gas} and total ISM metallicity $Z_{\text{tot}} = (M_{\text{metals,gas}} + M_{\text{metals,dust}}) / M_{\text{gas}}$ ⁹ in Figure 4.8. The slope and dispersion of the stellar mass-metallicity relation reasonably well matches the observed ones. As for the normalization, which is still uncertain by a factor ~ 3 ([Maiolino & Mannucci, 2019](#)), we are possibly low by a factor $\gtrsim 2$. It is worth pointing out that most previous model determinations not including dust evolution, neglected the fact that a significant fraction of metals $\gtrsim 50\%$ is depleted to dust (e.g. Figure 4.11), while this is not the case in the present work. To better illustrate this point, the central panel of this figure shows Z_{tot} .

To sum up this Section, we showed that MWHM galaxies in our simulated boxes have a morphological distribution in reasonable agreement with observations, a possibly somewhat high gas fractions, and metallicities likely low by a factor ~ 2 . The latter two issues may partly come from an overabundance of non-processed gas in the galactic region. However, alternative solutions for the low metallicity problem include adopting a more top-heavy IMF or increasing stellar yields¹⁰.

Finally, the stellar masses produced by the selected halos are low by a factor about 3 with respect to expectations. Indeed (see Figure 4.6) even halos whose total mass is three times that of the MW, produce galaxies whose stellar mass is similar to that estimated for the MW $\simeq 5 \cdot 10^{10} M_{\odot}$ by [Cautun et al. \(2020\)](#). This problem is largely inherited from the adopted MUPPI setup ([Valentini et al., 2020](#)) which results in a galaxy whose mass is about 60% that of the MW (see table 5 in the latter work) in a DM halo (dubbed AqC, [Springel et al., 2008](#)) almost twice as massive as the MW halo $M_{200} \sim 1.8 \cdot 10^{12} M_{\odot}$.

4.4 Dust inside galaxies

Let us now analyse the properties of dust within galaxies of our simulated boxes, namely the DMF and some scaling relations involving dust, predominantly at $z = 0$.

4.4.1 Dust Mass Function

The simulation DMF is shown in Figure 4.9 at different redshifts. Local observations are in excellent agreement with our results, while we heavily under-predict the abundance of dust rich galaxies ($M_{\text{dust}} \gtrsim 10^8 M_{\odot}$) at $z = 1.25$ and 2.25 . Comparing with other hydrodynamic simulations, a similar problem has been found by [McKinnon et al. \(2017\)](#) (when calibrated to match the local DMF) and, to a lesser extent, by [Li et al. \(2019\)](#), while the simulations by

⁸Here MP refers to multiphase gas. The fraction is computed excluding hot non-MP particles, since observations typically refer to the cold gas component of galaxies. Note also that MP particles are dominated in mass by its cold component.

⁹In this work we assume $Z_{\odot} = 0.0134$ following [Asplund et al. \(2009\)](#).

¹⁰For an extensive analysis of different IMFs and stellar yields in zoom-in simulations of MW-like galaxies using MUPPI, refer to [Valentini et al. \(2019\)](#).

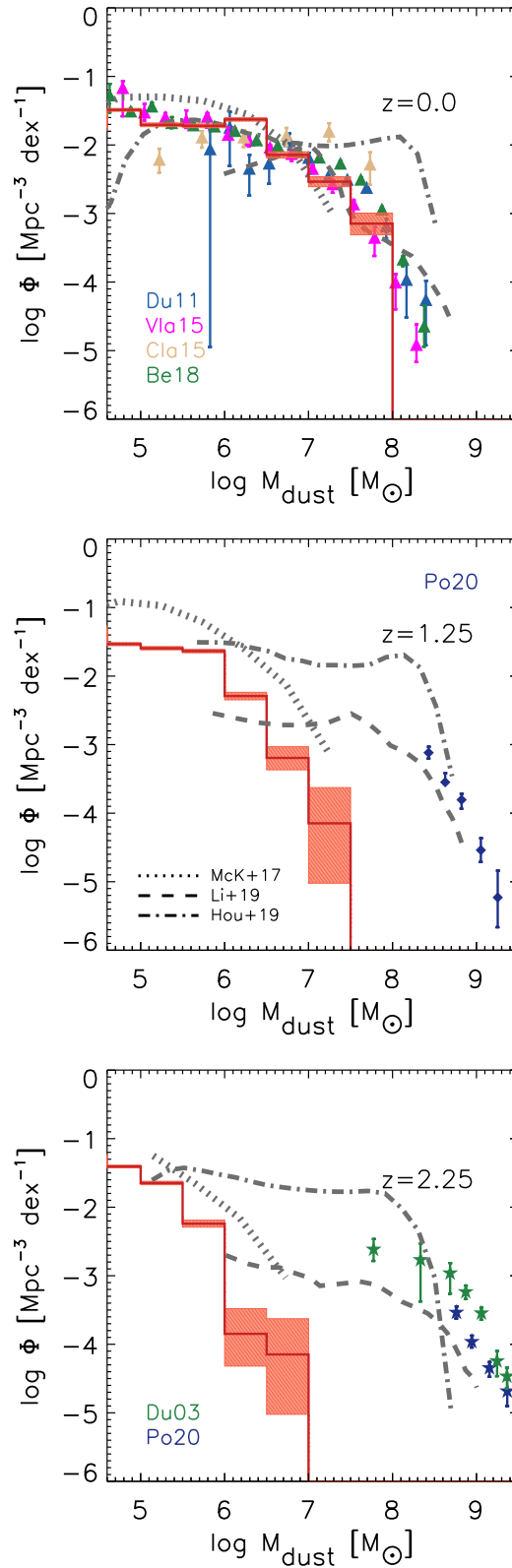


FIGURE 4.9: Dust Mass Function of the set of fiducial runs at different redshifts; the shaded area is the Poissonian error. We show observations from Dunne et al. (2011), Vlahakis et al. (2005), Clark et al. (2015), (Beeston et al., 2018, $z = 0$), (Pozzi et al., 2020, $z = 1.25$ and $z = 2.25$) and (Dunne et al., 2003, $z = 2.25$). Results from other cosmological simulations including dust at similar redshifts are shown as well: (McKinnon et al., 2017, $z = 0.0$, $z = 1.0$, $z = 2.5$), (Li et al., 2019, $z = 0.0$, $z = 1.0$, $z = 2.0$), and (Hou et al., 2019, $z = 0.0$, $z = 1.0$, $z = 2.0$).

| Run | Condensation Efficiency | | | Accretion |
|--|-------------------------|------------------------|-----------------------|-----------------------------|
| | δ_{SNII} | δ_{SNIa} | δ_{AGB} | τ_{acc} |
| condG21-accG21 | 0.8 | 0.8 | 1.0 | τ_{G21} |
| condG21-acc0.2 | 0.8 | 0.8 | 1.0 | $5 \cdot \tau_{\text{G21}}$ |
| COND0.1-accG21 | 0.1 | – | 0.1 | τ_{G21} |
| COND0.1-acc0.2 (fiducial this work) | 0.1 | – | 0.1 | $5 \cdot \tau_{\text{G21}}$ |

TABLE 4.1: Dust parameters adopted in runs of Figure 4.12. The condensation efficiencies for all the stellar channels are shown (they are the same for both carbonaceous and silicate grains), as well as the accretion timescale with respect to Granato et al. (2021) choices. Refer to Sections 3.4.1 and 3.4.3 for the definition of these parameters.

Hou et al. (2019) over-predict the number of very dusty system at $z = 0$, and under-predict them at $z = 2.5$. In conclusion, most current hydrodynamic cosmological simulations do not reproduce well the observed DMF over cosmic time. Identifying the reasons behind the differences between cosmological simulations is complex and outside the scope of the present work. We only point out that, while the dust processes included are the same, their implementation differs in several aspects. I refer to Section 3.3.2 for a deeper comparison of the DMF (and DMD) predicted by various hydrodynamic and SAM-based cosmological simulations.

4.4.2 Dust, Stellar Mass and SFR

Figure 4.10 illustrates the correlation between dust mass M_{dust} and stellar mass M_{stars} , where colors indicate the specific star formation rate (sSFR = $\text{SFR}/M_{\text{stars}}$) of each simulated galaxy. Our findings are compared with various observational datasets. Dust content shows an almost linear increase with stellar mass, and galaxies with higher sSFR at a given stellar mass tend to contain more dust.

Similarly, recent determinations by De Vis et al. (2019) show a linear increase of dust mass with stellar mass, akin to our simulations, while older estimates suggest a gentler growth.

4.4.3 Dust and Metallicity

While both the gas phase and dust metals originate from evolved stars, their relative abundances are strongly influenced by dust evolutionary processes in the ISM. We illustrate in Figure 4.11 the DTM (bottom panel) and DTG (top panel) ratios as functions of metallicity at $z = 0$. Simulated galaxies populate these diagrams across three distinct regimes, as previously identified by various studies (e.g., Hirashita, 2013, and Section 3.3.2).

Firstly, a regime at low metallicity where dust content is determined by direct production from stars. Secondly, an intermediate metallicity regime characterized by a steep increase in the DTG ratio with metallicity due to enhanced accretion. Lastly, a high metallicity regime, often referred to as the *saturation limit*, where the growth of the DTG ratio slows down as the availability of metals that contribute to the dust budget becomes nearly depleted. The influence of grain accretion on shaping these relationships is highlighted by the fraction of cold gas in each galaxy, as color-coded in Figure 4.11. Grain growth predominantly occurs in the cold and dense phases of the ISM; hence, galaxies with higher fractions of cold gas at a given metallicity tend to exhibit larger DTG and DTM ratios.

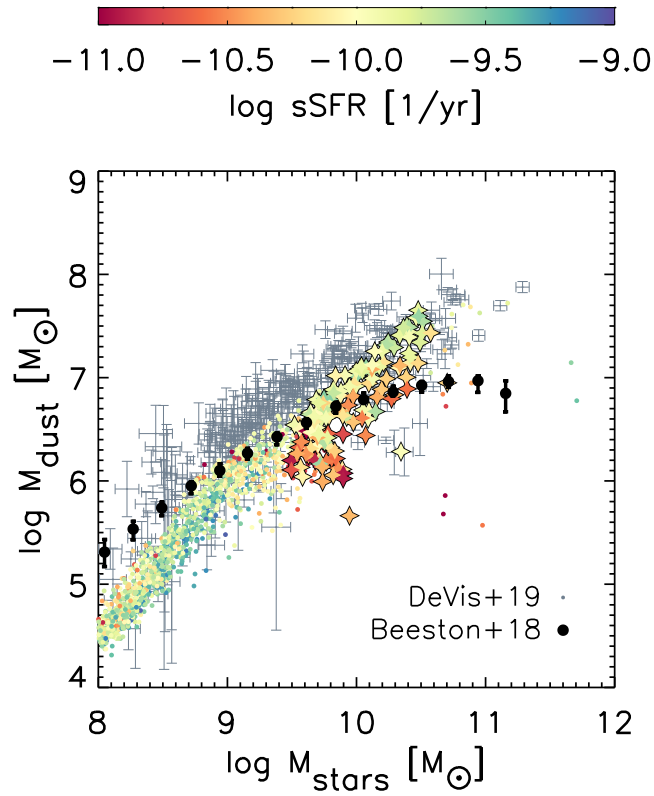


FIGURE 4.10: Dust mass as a function of the stellar mass of our simulated galaxies at $z = 0$, while the specific SFR is shown as color code. Star symbols are the MWM galaxies in our sample. Data from [De Vis et al. \(2019\)](#), [Beeston et al. \(2018\)](#). [De Vis et al. \(2019\)](#) data refer to the DUSTPEDIA sample, with their reference (PG16S, their Section 3.2) calibration for metallicities and stellar masses derived by [Nersesian et al. \(2019\)](#).

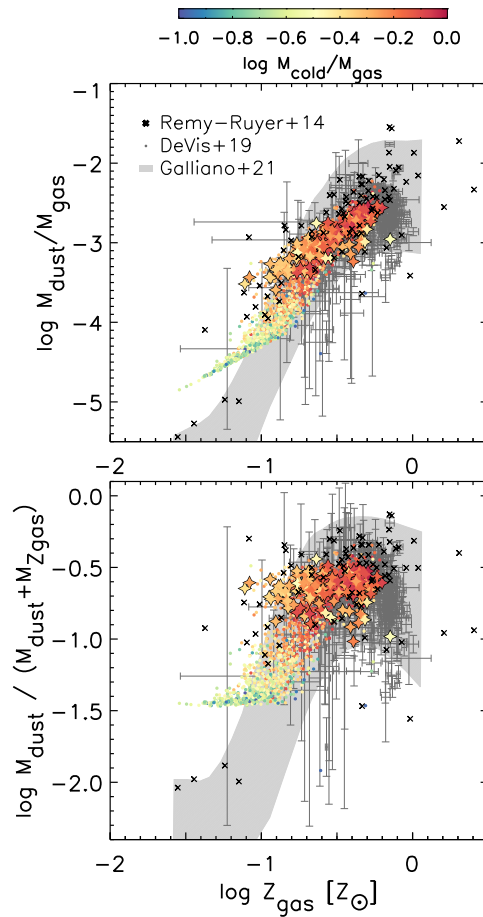


FIGURE 4.11: Dust-to-Gas (*top panel*) and Dust-to-Metals (*bottom panel*) ratio as a function of the ISM gas phase metallicity Z for simulated galaxies at $z = 0$ (MWHM galaxies are star symbols). The compilations of observational data are by Rémy-Ruyer et al. (2014) (black cross) and De Vis et al. (2019) (dots). We also report the fit derived by Galliano et al. (2021) (grey shaded area, which contains the 98% of their observations). The color code shows the cold fraction of the total gas content of each galaxy.

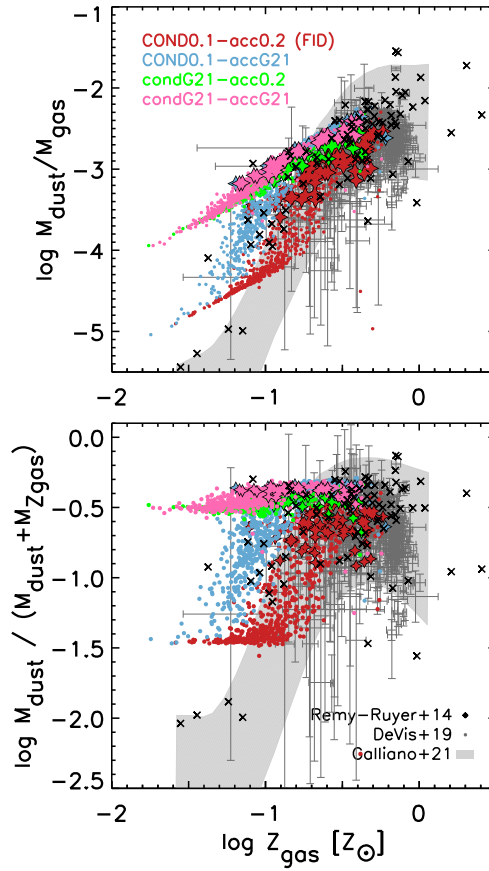


FIGURE 4.12: Same as Figure 4.11, but for different assumptions on the dust condensation and/or accretion efficiencies (see Section 4.4.3 and Table 4.1).

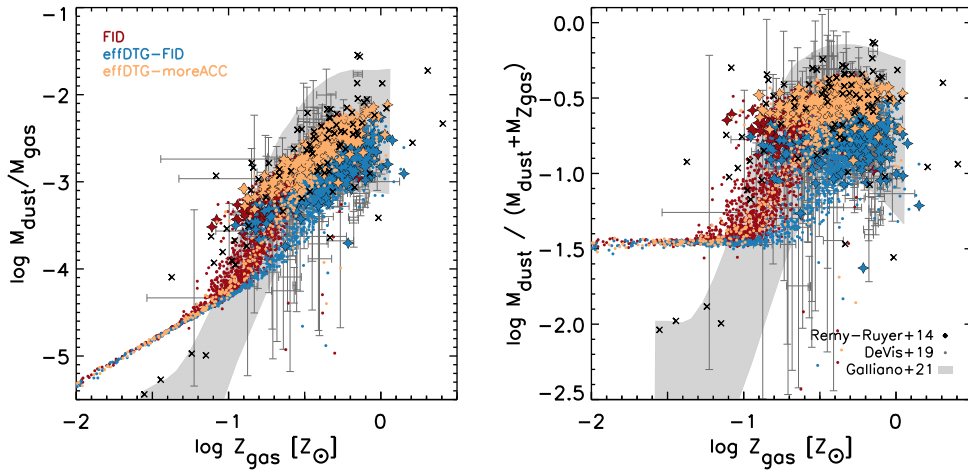


FIGURE 4.13: Dust-to-Gas (left panel) and Dust-to-Metals (right panel) ratio as a function of the ISM gas phase metallicity Z for simulated galaxies at $z = 0$ (MWHM galaxies are star symbols). We report results from our fiducial run (red) compared to the effDTG-FID (blue) and effDTG-moreACC (yellow) model, with DTG dependent star formation efficiency (see text).

The compilations of observational data is the same as in Figure 4.12.

A few model assumptions largely determine the precise locations of the three regimes mentioned earlier. This dependency becomes evident when examining Figure 4.12, where we present results not only from our current fiducial model but also from simulations using different dust parameter values, as detailed in Table 4.1, most of which coming from Granato et al. (2021) choices.

The vertical position of the low metallicity branch depends on the dust condensation efficiencies assumed for ejecta from evolved stars. The transition between the low and intermediate metallicity regimes is influenced by the adopted accretion efficiency, while the vertical placement of the saturation limit is dictated by the maximum availability of metals, which is closely linked to the chosen IMF and stellar yields. To better align with observational data from nearby galaxies, we found it necessary to significantly reduce both efficiencies compared to those originally proposed by Granato et al. (2021)¹¹.

Figure 4.11 displays a fairly good agreement between the fiducial model and the available data. However, the three regimes are much less evident in the data, possibly due to their significant uncertainties.

Before concluding this Section, we note that if we adopt the alternative effDTG model proposed in Section 4.2.4, which results in galaxies having a lower amount of gas available for efficient accretion, a higher accretion efficiency would be required. This efficiency would need to be closer to the value used in Granato et al. (2021) to align with this dataset.

This is shown in Figure 4.13, where we report two renditions of the effDTG model. The run effDTG-FID has dust parameters identical to the fiducial run, while in the effDTG-moreACC the accretion efficiency has been enhanced by a factor 2.5. These modified models produce galaxies featuring a factor ~ 3 lower gas fraction than the fiducial one. An even higher decrease, by a factor ~ 4 , occurs in the molecular gas fraction. As a result, the predicted molecular mass in MWHM galaxies in the effDTG runs turns out to be less than $\sim 1.5\%$ of the baryonic mass. Consequently, in the effDTG-FID model, the accretion process is less productive than in the fiducial one, and the *critical* metallicity (that above which accretion becomes relevant) shifts to larger values. When increasing the accretion efficiency (effDTG-moreACC; still a timescale twice as large as that used by Granato et al. 2021), the tension with observations reduce. Considering this and the fact that the effDTG models require some future adjustment to increase the predicted molecular mass, the conclusion that the accretion timescale adopted in the latter work needs a downward revision appears to be robust.

4.4.4 Size and chemical composition of grains

Our dust model tracks the formation and evolution of four distinct grain species, tracking their chemical compositions and, to a limited extent, size distributions of grains. Figure 4.14 includes two panels illustrating the Small-to-Large grains mass ratio (S-to-L), respectively plotted against the *total* ISM metallicity Z_{tot} (including both metals in gas and dust grains) and the stellar mass at $z = 0$. As in previous plots, larger symbols denote MWHM galaxies. This figure allows for a direct comparison with Figure 6 of Hou et al. (2019), who conducted cosmological simulations in a (larger) cosmological volume, modeling dust enrichment through a two-size approximation without accounting for dust chemical composition.

Our findings generally align with those reported in their study. However, discrepancies arise due to our local galaxy sample covering a narrower range of Z_{tot} . At the high Z_{tot} (or M_{stars}) end, this discrepancy may arise from their use of the more top-heavy IMF by Chabrier (2003). Conversely, at the low M_{stars} and Z_{tot} end, subtle differences in their modeling resulted

¹¹By running a couple of zoom-in simulations of MW-like galaxies, we verified that these adjustments do not substantially alter the conclusions drawn in their study.

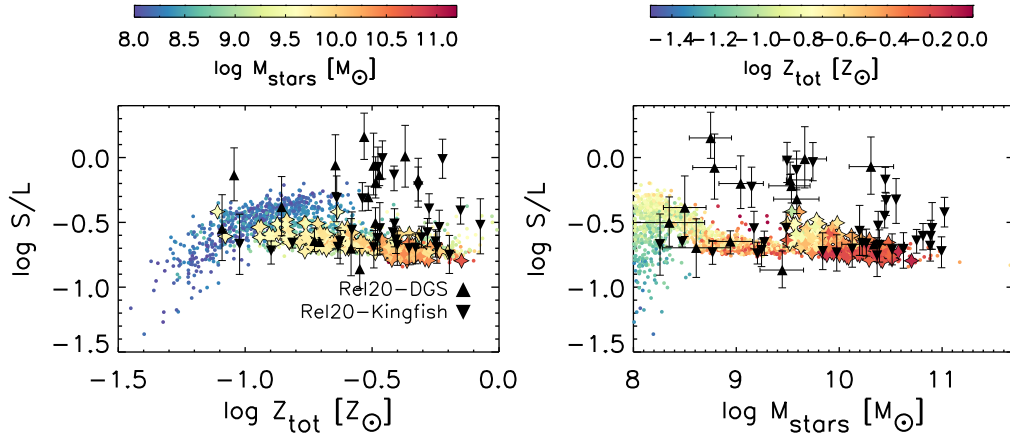


FIGURE 4.14: Small-to-Large grains ratio at $z = 0.0$ as a function of total ISM metallicity Z_{tot} and stellar mass. Star symbols represent MWHM galaxies. Local observations from [Relaño et al. \(2020\)](#) are shown for comparison (upward triangles for the DSG sample, downward triangles for Kingfish galaxies).

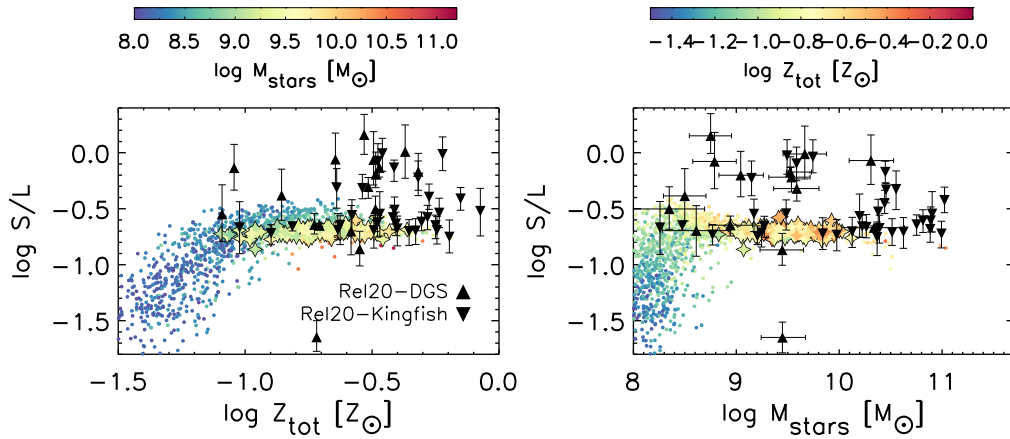


FIGURE 4.15: Same as Figure 4.14 at $z = 1.25$. Star symbols refer to MWHM progenitors. Local data from [Relaño et al. \(2020\)](#) are also shown for reference.

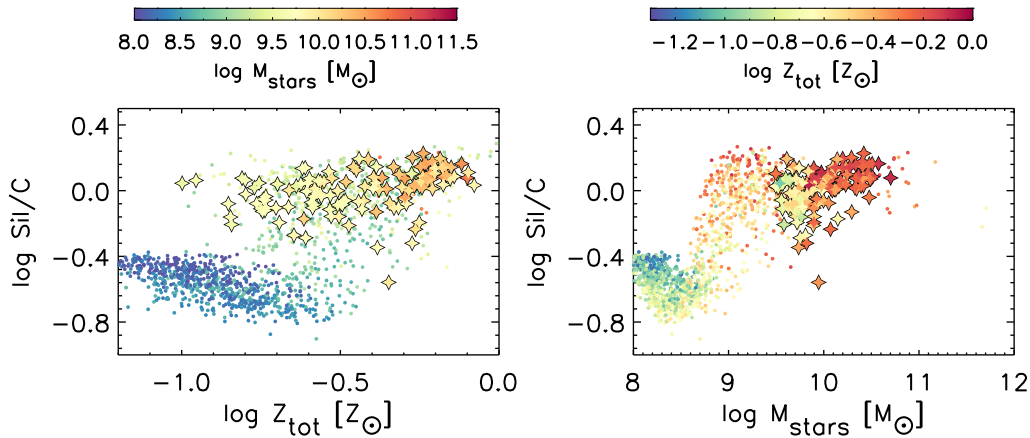


FIGURE 4.16: Same as Figure 4.14, but the Silicate-to-Carbon grains ratio is shown.

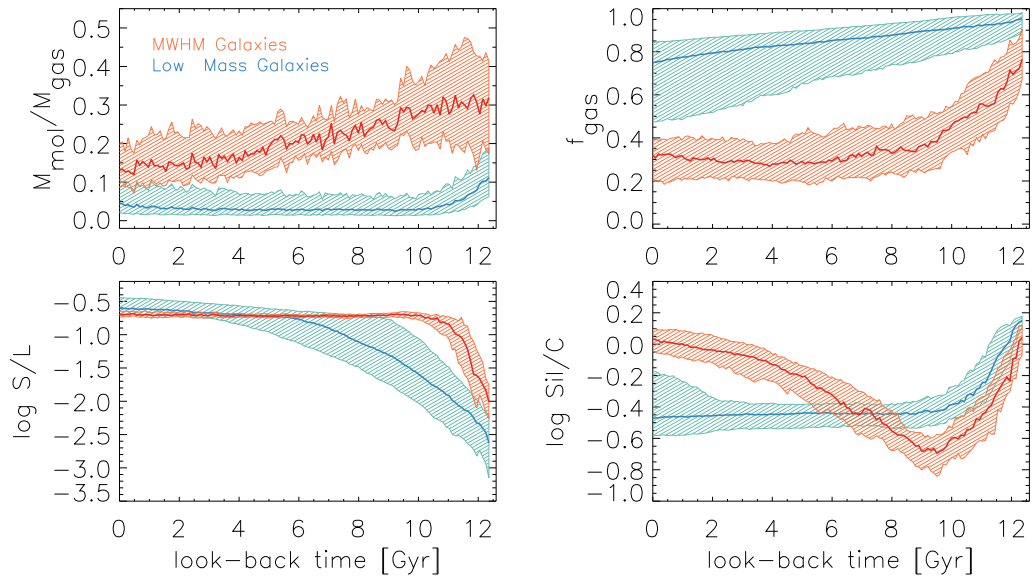


FIGURE 4.17: Evolution in time of the median and 25-75% percentiles of molecular fraction, gas fraction, Small-to-Large grains ratio and Silicate-to-Carbon grains ratio. MWHM galaxies are depicted in red while in blue we show the behaviour of galaxies with $M_{200} < 3 \cdot 10^{11} M_{\odot}$.

in significantly lower metallicities, as evident when comparing their Figure 2 with our Figure 4.14. Notably, our results in this mass range are more consistent with observational data.

The behavior of our model in the very low metallicity regime can be explored at earlier times, as it is done in Figure 4.15 for $z = 1.25$. Together, these figures support the conclusions drawn by Hou et al. (2019): in small galaxies with high gas fractions and low metallicities, the predominance of relatively large grains formed by stellar ejecta contributes to the relatively modest dust content. As metallicity increases, and consequently mass, the production of small grains through shattering and accretion becomes increasingly significant, leading to a rapid rise in the S-to-L grains mass ratio with Z_{tot} . However, beyond a certain threshold, approximately $\log Z_{\text{tot}} \sim -1$ or $\log Z_{\text{gas}} \sim -1.5$, further increases in metallicity do not correspondingly increase the S-to-L ratio, because in the saturation regime the mass increase of small grains due to accretion turns out to be balanced by their coagulation into large ones.

We compare our model predictions with the determination of the S-to-L reported in Relaño et al. (2020), where the authors analyzed the integrated spectral energy distributions (SEDs) from the KINGFISH and DSG surveys. Our model results, varying with stellar mass and metallicity, generally agree with observational data, except for the absence of simulated galaxies showing a log S-to-L ratio $\gtrsim -0.2$. Additionally, observations appear to confirm a flat relationship between S-to-L ratio and M_{stars} up to large stellar masses. In contrast, Hou et al. (2019) predicted a sharp decrease in this ratio at high stellar masses, which Relaño et al. (2020) tentatively attributed to the influence of AGN feedback in their simulations (refer to Section 4 of Relaño et al. (2020) for detailed discussion).

Similarly, Figure 4.16 illustrates the variation of the Silicate-to-Carbon dust mass ratio (Sil-to-C) at $z = 0$ as a function of total metallicity and stellar mass. Interestingly, within $\log Z_{\text{tot}} \in [-0.9, -0.6]$, galaxies exhibit a diverse range of Sil-to-C ratios, displaying a somewhat dichotomous distribution. Less massive galaxies with $M_{\text{stars}} \lesssim 3 \cdot 10^8 M_{\odot}$ typically feature a ratio approximately three times smaller than MWHM galaxies at the same Z_{tot} . These less massive galaxies also show Sil-to-C ratios similar to those observed in galaxies

with lower metallicities within the same stellar mass range.

The distinct behaviors observed in the two stellar mass regimes can be understood by examining Figure 4.17, where we present the evolution of some key quantities for galaxies in two representative mass regimes. These include the gas molecular fraction $M_{\text{mol}}/M_{\text{gas}}$, the gas mass fraction $f_{\text{gas}} = M_{\text{gas}}/(M_{\text{gas}} + M_{\text{stars}})$, and the S-to-L and Sil-to-C ratios.

At very early times, all galaxies in our simulations tend to exhibit a relatively high Sil-to-C ratio because dust predominantly consists of grains produced by SNI. Subsequently, this ratio decreases rapidly due to the substantial production of carbonaceous dust by AGB stars. If dust accretion becomes significant, the ratio begins to increase again, albeit slowly, as the growth of silicate dust is constrained by the availability of key elements.

Lower mass galaxies encounter greater difficulty in reaching the regime dominated by dust accretion compared to their more massive counterparts at the same metallicity. This challenge arises because lower mass galaxies typically possess a smaller fraction of dense gas, where efficient accretion processes occur. In the low mass bin, the gas mass fraction remains consistently higher by a factor of several, while the fraction of molecular gas is lower by an order of magnitude or more throughout much of cosmic history (top panels of Figure 4.17). Consequently, the dust accretion process never becomes sufficiently robust to increase the Sil/C ratio in low mass galaxies.

Finally, we remark that the typical values obtained here for both the Large-to-Small and Sil-to-C ratios for MWHM galaxies at $z = 0$ are not far from those adopted in most dust mixture models derived for the MW dust. For instance, model 4 in Weingartner & Draine (2001) has S-to-L ≈ 0.21 and Sil-to-C ≈ 2.5 . However, the variations predicted in different galaxies at $z = 0$, and even more at higher redshift, would be significant when computing dust radiative effects (see also Section 3.1 in Granato et al., 2021).

4.5 Dust outside galaxies

Observations have detected dust beyond the galactic region (Holwerda et al., 2009; Ménard et al., 2010; Roussel et al., 2010; Hodges-Kluck & Bregman, 2014; Peek et al., 2015; Ruoyi & Haibo, 2020). This has been found also in several cosmological simulations (McKinnon et al., 2017; Aoyama et al., 2018). Exploring this issue is crucial for providing a more comprehensive description of the cosmic cycle of dust and metals, constraining the cooling capacity of the CGM, and characterizing the opacity of the Universe on intergalactic scales. Dust produced and reprocessed within galactic environments can be expelled from the ISM through mechanisms such as galactic winds and radiative pressure (see e.g. Bianchi & Ferrara, 2005; Hirashita & Inoue, 2019).

In our simulation, only galactic winds acting on gas particles are considered. Additionally, our model assumes dust is dynamically coupled with gas. This assumption, which might impact the quantity and nature of ejected dust, has generally been validated as a good approximation due to the strong coupling between these two components in most situations (see e.g. McKinnon et al., 2018, who explicitly address the dynamical forces acting on dust particles).

In the following sections, we analyze our simulation to investigate the quantity and properties of dust surrounding our simulated galaxies at various epochs.

4.5.1 Dust profile around galaxies

To quantify the amount of dust beyond galactic scales, we compute the dust surface density profiles. Observationally, Ménard et al. (2010) examined the reddening caused by dust in

the halos of massive galaxies (i.e., on extra-galactic scales). Their data come from a sample of $\sim 85,000$ quasars at $z \gtrsim 1$ and a massive sample of $2 \cdot 10^7$ galaxies at $z \simeq 0.3$. By cross-correlating the colors of the quasars with the (projected) overdensity of galaxies, they were able to constrain the reddening caused by dust grains outside galactic regions. Their findings suggest that the dust associated with an extra-galactic diffuse component is at least comparable to that observed in the ISM of galaxies and that the dust profile extends up to ~ 10 Mpc from the centers of galaxies. Subsequent studies (e.g. Peek et al., 2015) have confirmed the presence of significant amounts of dust beyond galactic radii.

To compare our simulation results with the observational estimates by Ménard et al. (2010), we compute the dust surface density for galaxies at $z \simeq 0.3$ with $M_{\text{stars}} > 10^{10} M_{\odot}$. This mass range is broadly similar to the masses of the galaxies studied by Ménard et al. (2010, see e.g. Aoyama et al. 2018). Although this mass range is slightly larger than that of our MWHM galaxies progenitors at $z = 0.3$, using MWHM progenitors as in the rest of the paper would only slightly alter the profile, without affecting our conclusions.

The results are presented in Figure 4.18, where we show the median dust profile¹² compared with Ménard et al. (2010). We also plot the median dust profile excluding MP particles and the gas metals profile.

The slope of our dust profile is somewhat steeper than that derived by Ménard et al. (2010), and its normalization is slightly lower than the observational data, although this discrepancy is reduced when considering the overall dispersion. It is important to note that the dust density derived from reddening by Ménard et al. (2010) also depends on the dust model adopted. They assume a Small Magellanic Cloud dust type, but the properties of dust on extragalactic scales at $z = 0.3$ may differ from those inferred in local galaxies (see the following discussion).

To understand the extent to which this profile originates from the diffuse dust component outside galaxies, we also plot in Figure 4.18 the median dust profile obtained excluding MP particles, which trace the dusty galactic environments in our simulations. The contribution of non-MP particles to the total profile is minor within $r \lesssim 10$ kpc (the galactic region where star formation occurs), but outside this region, it accounts for about 90% of the total. Therefore, on extra-galactic scales, the dust budget in the simulations is dominated by a diffuse dust component in galactic halos. Satellites and overlapping galaxies play a minor role, consistent with the conclusions of Ménard et al. (2010).

Finally, we compare our profile with results from two other cosmological simulations that include dust evolution, those by McKinnon et al. (2017) and Aoyama et al. (2018). Despite the different sub-grid modeling prescriptions for dust evolution, all three simulations show a similar slope for Σ_{dust} on extra-galactic scales. Notably, our profile normalization is quite close to that of McKinnon et al. (2017). We note that factors beyond dust-related prescriptions, such as feedback and galactic winds recipes, are also expected to substantially impact these results.

4.5.2 Redshift evolution of dust profiles

In Figure 4.19, we present the redshift evolution of the median profiles for the S-to-L and Sil-to-C dust mass ratios, as well as for the DTG and DTM. This analysis considers the MWHM galaxies and their main progenitors at $z = 0.5, 1.0$, and 2.0 . The radial coordinate is

¹²Radial profiles are obtained by considering a randomly oriented cylinder centered on each selected galaxy. Gas particles are grouped into 20 logarithmic bins along the cylinder radius, and the surface density is calculated by summing the contributions of all particles in each annulus. The vertical axis coincides with the z axis of our simulation box. The cylindrical region has a radius of 4 cMpc/h and a half-height of 500 ckpc/h; we verified that our results are not critically dependent on these parameters.

normalized to the R_{200} of each halo at the corresponding redshift. Both the DTG and DTM profiles show a continuous increase over time, reflecting the ongoing production and ejection of dust from galaxies.

Large grains dominate both inside and outside ($r > 0.1 R_{200}$) galaxies at any redshift. At $z \gtrsim 2$, the S-to-L grains ratio is significantly smaller outside, but this difference decreases over time, nearly disappearing by $z = 0$. This is due to the rapid increase of this ratio in the galactic region at early times (look-back time $\gtrsim 10$ Gyr) for massive galaxies (see the red band in the lower left panel of Figure 4.17). Dust is primarily produced in the galactic region and then transported outside, taking some time to pollute the surrounding area. Therefore, the dust properties in these outer regions reflect the dust properties of the galactic region at earlier times.

At low redshift, the ratio tends to increase up to $\log r/R_{200} \simeq -1.2$. This is likely due to the radial decrease in specific star formation, which increases the relative importance of small grain production by accretion compared to large grain production by stellar injection. Additionally, the balance between shattering and coagulation shifts in favor of shattering, as a result of a decrease of the fraction of dense, star forming, ISM which promotes dust coagulation.

At larger radii, the ratio decreases because the gas temperature suddenly reaches a few 10^5 K, where sputtering, which is ten times more efficient for small grains, begins to be non-negligible, progressively with time (see Figure 4.20).

As for the contribution of Silicates and Carbon to the dust budget, Figure 4.19 (top right panel) confirms the trend discussed in Section 4.4.4. The abundance of silicate grains increases with cosmic time at $z \lesssim 2$ (look-back time $\lesssim 10$ Gyr) in sufficiently massive galaxies. This evolution occurs both in the galactic region (see also Figure 4.17, bottom right panel) and outside it. This trend arises because of the delay in Silicate accretion caused by the limited availability of key elements at early times. A striking feature of the profile evolution is the reversal of the slope over time, shifting from an increasing Sil/C ratio with radius at high redshift to a decreasing ratio at low redshift. This can be understood by considering that the dust mixture outside galaxies is influenced by the dust conditions inside galaxies at an earlier time, with some reprocessing. Figure 4.17 shows that the Sil/C ratio rapidly decreases over time at $z \gtrsim 2$ (look-back time $\gtrsim 10$ Gyr) to a minimum and then begins to increase slowly in massive galaxies.

We compare our results with a few available observations at $z = 0$. Relaño et al. (2020) used spatially resolved observations of three local disc galaxies (M101, M33, and NGC628) to study the shape of the S-to-L, DTG, and DTM radial profiles¹³. Since only disc galaxies were considered in their work, we also show the profile of simulated MWHM galaxies with $B\text{-to-T} < 0.6$ at $z = 0.0$ (grey lines and shaded areas). The simulation reasonably reproduces the observed profiles. The DTG and DTM profiles are underestimated by a modest factor of $\simeq 1.6$, but the discrepancy reduces for the $B\text{-to-T} < 0.6$ sample. Two of the three observed S-to-L profiles have large uncertainties and show a fairly constant profile with $\log \text{S-to-L} \simeq -0.7$, similar to our simulated $z = 0.0$ galaxies. The S-to-L profile of M33 is a factor of $\simeq 1.6$ below our results.

¹³They express the radius in units of R_{25} , the radius where the B-band surface brightness falls to $25, \text{magarcsec}^{-2}$. To translate their profiles to our R_{200} normalization of the radius, we first assumed $R_{25} = 4R_d$, where R_d is the disc-scale length obtained by fitting the simulated stellar surface density profile with an exponential function $\Sigma(r) = \Sigma_0 \exp(-r/R_d)$. Then we used the mean R_{25}/R_{200} for our MWHM disc-like galaxies (those with $B\text{-to-T} < 0.6$) at $z = 0.0$, which turns out to be $\simeq 0.07$.

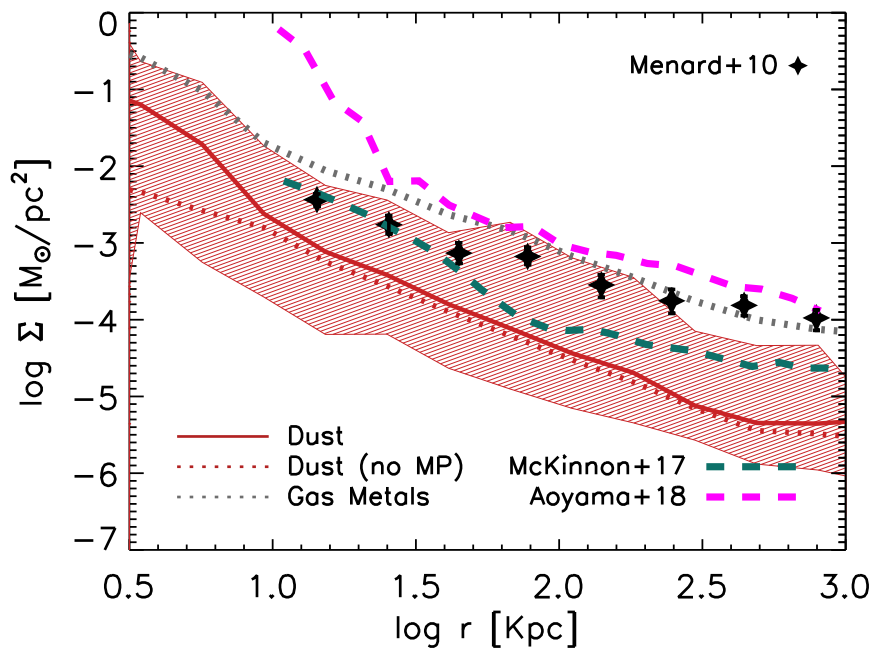


FIGURE 4.18: Median dust surface density profile (solid line) around galaxies with $M_{\text{stars}} > 10^{10} M_{\odot}$ at $z = 0.3$, with the shaded area indicating the full dispersion of the profiles distribution. The profile excluding MP gas particles is also shown as a red dotted line, as well as the gas metals profile (grey dotted line). Filled star points data refer to observations by Ménard et al. (2010). We also overplot results from McKinnon et al. (2017) (green dashed line) and Aoyama et al. (2018) (magenta dashed line).

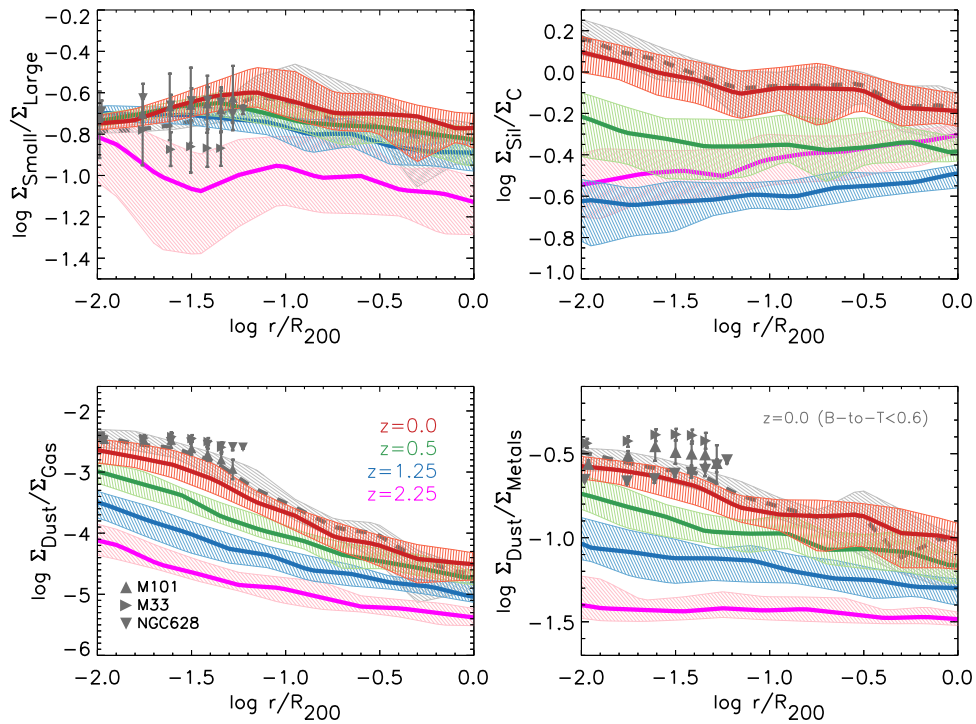


FIGURE 4.19: Median radial profiles ratio of Small-to-Large (top left), Silicate-to-Carbon (top right), Dust-to-Gas (bottom left) and Dust-to-Metals (bottom right) for MWHM galaxies ($z = 0.0$) and their progenitors ($z = 0.5$, $z = 1.25$, and $z = 2.0$). The radial coordinate has been normalized to the R_{200} of each galaxy. We show the 25-75th percentile dispersions. We over plot the profiles reported by [Relaño et al. \(2020\)](#) derived from the spatially resolved observations of three local disc galaxies (M101, M33, NGC628). For the sake of a more meaningful comparison, we also show the profiles obtained considering only $z = 0.0$ simulated disc galaxies ($B\text{-to-}T < 0.6$, grey line and shaded region).

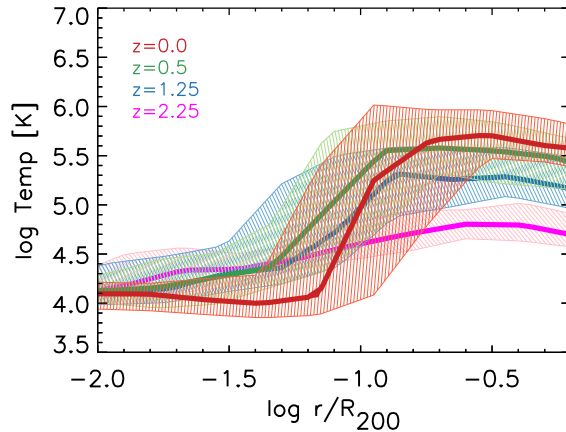


FIGURE 4.20: Median gas temperature profile of MWHM galaxies and their progenitors at $z = 0.5$, $z = 1.25$, and $z = 2.25$. Shaded regions are the 25th-75th percentiles dispersion.

4.6 Summary and Discussion

In this Chapter, we presented and discussed hydrodynamic simulations performed with a state-of-the-art dust model to predict the formation and evolution of grains, taking into account its chemical composition and, to a minimal level, the size distribution. The production of grains by stellar sources and the subsequent evolution of grains in the galactic ISM via different processes are considered. As for the star formation and feedback modelling, we adopted the MUPPI formalism, here in the specific version presented by [Valentini et al. \(2020\)](#), without any tuning of its parameters. Nevertheless, we proposed a couple of possible directions to relieve the tensions with some properties of the galaxy population.

We mainly focused on the dust properties of MW-like galaxies since MUPPI has been calibrated to reproduce the properties of these objects. More precisely, we devoted particular attention to galaxies formed in DM halos having a mass M_{200} within a factor 3 that estimated for the MW, dubbed Milky Way Halo Mass galaxies (MWHM). Dust-independent properties, such as the morphology, the gas fraction and the metal content of our sample of simulated MWHM galaxies, are in acceptable agreement with local observations. However, we identified clear tensions between our results and observational data when considering the entire simulated galaxy population. Specifically, the predicted cosmic SFRD is lower than observed, and there is a deficit of quenched galaxies in the local Universe. Although we propose steps to address these discrepancies, we have chosen to retain the setup carefully calibrated by [Valentini et al. \(2020\)](#) on zoom-in simulations, postponing a thorough analysis of the issue for future work.

Instead, we adjusted the dust parameters from [Granato et al. \(2021\)](#), specifically the condensation efficiency in stellar ejecta and the accretion timescale. We studied the influence of these parameters in shaping the relation between dust and metallicity in local galaxies (DTG-Z and DTM-Z, Figures 4.11 and 4.12). Specifically, the accretion timescale primarily determines the transition metallicity where accretion becomes dominant. Meanwhile, a lower condensation efficiency allows for matching the DTG ratio of objects with the lowest metallicities. Following these adjustments, all simulated scaling relations involving dust, stars, and metal content appear consistent with available observations.

Our dust model also predicts the relative abundance of small and large grains and their chemical composition (silicates and carbonaceous). Interestingly, these properties are interconnected. Low-mass galaxies, where dust content is primarily driven by stellar production, are dominated by large, carbonaceous grains. Silicates, which in our model have a olivine-like chemical composition, are dominant when accretion onto small grains becomes significant (galaxies with $M_* \gtrsim 10^{8.5} M_\odot$, $\log Z/Z_\odot \gtrsim -0.8$). In this transition regime, the Small/Large grains mass ratio peaks but is suppressed in larger galaxies due to the contribution of coagulation. At $z = 0.0$, MWHM galaxies appear rich in silicates and large grains. Dust evolution in these objects indicates that silicate growth becomes prominent at $z \lesssim 2$, contrasting with low-mass galaxies where the molecular gas mass fraction remains approximately an order of magnitude lower throughout cosmic time, causing a low accretion efficiency. For MWHM galaxies, the final S/L and Sil/C values broadly align with those typical of widely used dust extinction models. However, a more detailed analysis, such as studying depletion patterns, would be necessary to validate our chemical predictions, which are also influenced by assumptions on the assumed silicate composition and the adopted IMF.

Surface density profiles around massive galaxies exhibit reasonable agreement with the few available observations, supporting indications from the literature of a significant dust presence beyond galactic regions. Furthermore, the redshift evolution of the S/L and Sil/C profiles indicates that halo dust characteristics reflect those of galactic dust at earlier epochs, with this effect more pronounced at higher redshifts.

The issues discussed here underscore the need for future developments and improvements. It is clear that our sub-resolution model, MUPPI, requires further investigation to achieve accurate statistical properties for the entire galaxy population across cosmic time, while maintaining its strong performance in zoom-in simulations of disc galaxies. Additionally, since we adjusted the dust parameters based on local observations, it would be important to assess the model ability to reproduce dust properties at high redshift once a more robust galaxy evolution framework is in place. A step in this direction was recently taken by [Ragone-Figueroa et al. \(2024\)](#), where we *(i)* improved the physical model by incorporating molecular hydrogen formation on dust grain surfaces, *(ii)* linked the SFR to the H₂ content, and *(iii)* reformulated other sub-resolution physics to better align with the properties of the observed galaxy population, significantly enhancing the model predictive capabilities. Although this resulted in substantial improvements, further testing in larger cosmological volumes than the 26 Mpc box used is required to better capture the high-mass regime.

5

The $z \lesssim 1$ drop of cosmic dust abundance

Given the relevance of dust in our Universe, a detailed understanding of the build-up of dust in galaxies across cosmic time would be highly advantageous. The total budget of dust in our Universe is commonly given in terms of $\Omega_{\text{dust}} = \rho_{\text{dust}}/\rho_{\text{c},0}$ ¹, and can be thought as the sum of a galactic and an extra-galactic component (in this Chapter $\Omega_{\text{dust}}^{\text{ISM}}$ and $\Omega_{\text{dust}}^{\text{CGM}}$ respectively). Understanding the evolution of this quantity is one of the major tasks of cosmological galaxy evolution models which include dust (Section 3.3.2).

In this Chapter, we² will study the cosmic evolution of Ω_{dust} from a theoretical, semi-analytical perspective. The strategy of the Chapter is as follows. First, we will introduce the observations which allow for an estimate of Ω_{dust} in Section 5.1, as well as the shortcomings of current simulations. Then, Section 5.2 is devoted to detailing the adopted SAM. Some basic results concerning the whole galaxy population are presented in Section 5.3, while predictions about dust properties are in Section 5.4. Finally, Section 5.5 contains our predictions of the galactic and extra-galactic dust abundance, as well as their comparisons with observations. The main conclusions are summarised in Section 5.6.

CONTENTS

| | |
|---|-----|
| 5.1 Observing the cosmic dust abundance | 93 |
| 5.2 The SAM simulations | 94 |
| 5.3 General Properties of the Galaxy Population | 98 |
| 5.4 Dust properties | 103 |
| 5.5 The Cosmic Dust Abundance | 107 |
| 5.6 Conclusions | 117 |

5.1 Observing the cosmic dust abundance

From observations, the cosmic abundance of galactic dust ($\Omega_{\text{dust}}^{\text{ISM}}$) can be estimated by deriving the dust mass of a galaxy sample through SED fitting, then constructing a DMF and integrating it. Several examples exist in the literature. Dunne et al. (2011) used a sample of ~ 2000 sources from the *Herschel*-ATLAS survey, each with a reliable counterpart from the SDSS,

¹Here ρ_{dust} is the comoving dust mass density, and $\rho_{\text{c},0} = 2.775 h^2 \times 10^{11} M_{\odot}/\text{Mpc}^3$ is the critical density of the Universe today. Note the common *bad practice* in this definition, which is at odds with the standard meaning of the density parameters Ω in cosmology, where densities are normalized to the critical density at a given redshift $\Omega(z) = \frac{\rho(z)}{\rho_{\text{crit}}(z)}$.

²This Chapter is based on a published work done in collaboration with Cinthia Ragone-Figueroa, Gian Luigi Granato, and Andrea Lapi (Parente et al., 2023).

to examine the DMF evolution at $z < 0.5$. They found that high-redshift massive galaxies contain more dust than local galaxies, and $\Omega_{\text{dust}}^{\text{ISM}}$ decreases with decreasing redshift. [Driver et al. \(2018\)](#) estimated dust masses for $\sim 570,000$ sources from the GAMA, G10-COSMOS, and 3D-HST catalogues over a wide redshift range ($0 < z \lesssim 2$), also finding a smooth decline in $\Omega_{\text{dust}}^{\text{ISM}}$ at $z \lesssim 1$. More recently, [Pozzi et al. \(2020\)](#) greatly enhanced our understanding of the DMF cosmic evolution, studying it up to $z \simeq 2.5$. Their results confirmed earlier findings, showing a broad peak of $\Omega_{\text{dust}}^{\text{ISM}}$ at $z \sim 1$, followed by a decline towards the local Universe. Also $z \sim 0$ determinations of the DMF are available today, and are consistent with the findings highlighted above. To mention one representative work, [Beeston et al. \(2018\)](#) studied the DMF of a $z < 0.1$ galaxy sample from the Herschel-ATLAS and GAMA surveys, providing precise constraints on $\Omega_{\text{dust}}^{\text{ISM}}(z \simeq 0)$.

Conversely, measuring the amount of extra-galactic dust ($\Omega_{\text{dust}}^{\text{CGM}}$) is more challenging and thus more uncertain. Notably, [Ménard et al. \(2010\)](#), also [Ménard & Fukugita 2012](#); [Peek et al. 2015](#)) estimated dust in galactic halos³ by examining the reddening of distant quasars by foreground absorbers, showing a significant amount of dust beyond galaxies.

The combined result of these observations (e.g., [Péroux & Howk 2020](#), their Figure 12) indicates that the dust abundance in galaxies has decreased by a factor of about 2-3 over the last ~ 8 Gyr. This trend remains unclear from a theoretical perspective. The relatively recent inclusion of dust in some SAMs ([Popping et al. 2017](#); [Vijayan et al. 2019](#); [Triani et al. 2020](#)) and hydrodynamic cosmological simulations ([McKinnon et al. 2017](#); [Aoyama et al. 2018](#); [Hou et al. 2019](#); [Li et al. 2019](#); [Graziani et al. 2020](#); [Parente et al. 2022](#)) of galaxy evolution has allowed the study of the DMF build-up across cosmic epochs, investigating the roles of various processes in dust evolution in a cosmological context. However, most of these studies do not reproduce the observed peak of $\Omega_{\text{dust}}^{\text{ISM}}$. Notable exceptions are the hydrodynamic simulations by [Aoyama et al. \(2018\)](#) and [Li et al. \(2019\)](#). The former group reproduces a decline in $\Omega_{\text{dust}}^{\text{ISM}}$ at $z < 1$, attributing it to astration, though their normalization is about six times too high at $z = 0$. The latter group provides an excellent fit to the observed galactic $\Omega_{\text{dust}}^{\text{ISM}}$ across cosmic time but does not discuss the origin of this behavior.

Motivated by this issue, [Ferrara & Peroux \(2021\)](#) tried to constrain the efficiency of dust destruction processes, assuming these processes overcome⁴ the processes responsible for dust growth at $z < 1$. However, their straightforward calculation only considers the efficiency of dust processes for $z < 1$, neglecting the impact of these processes on the earlier evolution of Ω_{dust} .

The goal of this Chapter is to address the shortcomings of current simulations and discuss a model that can reproduce the observed cosmic dust abundance. Additionally, we aim to discuss the reasons behind the decline in cosmic dust abundance at $z \lesssim 1$ from a theoretical perspective.

5.2 The SAM simulations

In this Chapter we make use of the L-GALAXIES SAM ([Henriques et al., 2020](#), see also Section 2.3), which has been extended with the dust model adopted in this Thesis ([Parente et al., 2023](#), and Section 3.4).

³However, some of the absorbers selected by [Ménard & Fukugita \(2012\)](#) feature equivalent widths which are associated with column density typical of neutral gas, thus ISM (see §4.2 of [Péroux & Howk 2020](#)).

⁴This assumption is necessary to obtain a decline in Ω_{dust} , as they consider both galactic and extra-galactic dust.

The model is run on the MILLENNIUM merger trees, (original box size $500/h$, 2160^3 particles) adopting a *Planck* cosmology⁵ (Planck Collaboration et al. 2014) with $h = 0.673$, $\Omega_m = 0.315$, $\Omega_b = 0.0487$, $\sigma_8 = 0.829$. We adopt a Chabrier (2003) IMF.

5.2.1 A new treatment for Disc Instabilities

Alongside with the dust model, the L-GALAXIES SAM adopted in this Thesis has been extended with a new model for the treatment of Disc Instabilities (DIs). The original treatment of this process in the SAM is based on the Efstathiou et al. (1982) criterion (see Section 2.3.5). This prescription determines when a disc becomes unstable to bar formation due to its self-gravity, causing a redistribution of disc material that eventually funnels disc stars into a bulge-like structure (e.g. Debattista et al. 2006). Due to its appealing simplicity, this criterion has been widely adopted, often with minor modifications, within the SAM community (e.g. De Lucia et al. 2011; Lacey et al. 2016; Lagos et al. 2018), although not without criticism (Athanassoula 2008; Devergne et al. 2020; Romeo et al. 2022). This secular process is crucial for producing a sufficient number of intermediate mass spheroids (e.g. Huřko et al. 2022) and may also significantly influence BH growth at high redshift (Bournaud et al. 2011).

Our implementation is inspired by Irodou et al. (2019), with some key differences. Unlike Irodou et al. (2019), we do not differentiate between classical bulges (formed during mergers) and pseudo-bulges (originating from disc instabilities). Another significant difference is our division of discs into rings within the SAM we use. While we determine if a disc is unstable based on its global properties, a ring-by-ring evaluation of instability could also be an interesting approach (see e.g. Stevens et al. 2016). We extend the instability criterion to include the contribution of the gaseous disc to the overall stability of the disc (gas+stars), unlike Henriques et al. (2020), which considers only stars. To achieve this, we evaluate the stability of the galactic disc using the parameter ϵ_{tot} :

$$M_{\text{disc,tot}}\epsilon_{\text{tot}} = M_{\text{disc,stars}}\epsilon_{\text{stars}} + M_{\text{disc,gas}}\epsilon_{\text{gas}}, \quad (5.1)$$

where

$$\epsilon_i = c_i \left(\frac{GM_{\text{disc},i}}{V_c^2 R_{\text{disc},i}} \right)^{0.5}, \quad (5.2)$$

with $i = \{\text{stars, gas}\}$.

In this formula, V_c is the circular velocity of the host halo, M_i is the mass of the i component of the disc, R_i the scale length, and c_{stars} , c_{gas} are parameters of order of 1 (Efstathiou et al. 1982; Christodoulou et al. 1995). In our fiducial model we set $c_{\text{stars}} = c_{\text{gas}} = 1$.

If $\epsilon_{\text{tot}} > 1$ the disc is unstable. Unstable gas is allowed to form stars and to accrete the central SMBH, while stars are transferred from the disc to the bulge, until stability is restored. This is done by iterating over rings, from the innermost to the outermost one, and for each of them:

- if gas $M_{\text{gas}}^{\text{ring}}$ is present in the ring, some of it forms disc stars and accretes the central SMBH. In a single time-step dt , we assume that the mass available for the former processes is $M_{\text{gas,unst}}^{\text{ring}} = (dt/\tau) \cdot M_{\text{gas}}^{\text{ring}}$, where τ is proportional to the free fall timescale

⁵The original MILLENNIUM cosmology has been scaled according to Angulo & White (2010) and Angulo & Hilbert (2015).

of each ring, i.e.

$$\tau = \sqrt{\frac{1}{G\rho}}, \quad (5.3)$$

where ρ is evaluated as in Equation 3.20.

A fraction $f_{\text{BH,unst}}$ of the mass $M_{\text{gas,unst}}$ accretes onto the central SMBH. This fraction is evaluated following almost the same prescription adopted by the SAM when dealing with BH growth in galaxy mergers⁶, namely

$$f_{\text{BH,unst}} = \frac{f_{\text{BH}}}{1 + \left(\frac{V_{\text{BH,DI}}}{V_{\text{vir}}}\right)^2}, \quad (5.4)$$

where f_{BH} controls the accretion efficiency and the $(V_{\text{BH,DI}}/V_{\text{vir}})^2$ term introduces a dependence on the binding energy of the system since we expect that less gas concentrates in the center of low mass systems.

This prescription was initially introduced by [Kauffmann & Haehnelt \(2000\)](#) to model SMBH gas accretion during major mergers. This *phenomenological* recipe has been widely adopted by the SAM community (e.g., [Croton et al. 2016](#); [Lagos et al. 2018](#); [Izquierdo-Villalba et al. 2020](#)) for both galaxy mergers and disc instabilities, where gas is funneled toward the galaxy center, triggering starburst episodes. We adopt the same approach. Specifically, in our fiducial model, we assume $f_{\text{BH}} = 0.066$ during disc instabilities, as in mergers, but use a $V_{\text{BH,DI}}$, the virial velocity at which accretion saturates, that is six times larger than that used during mergers (700 km s^{-1}). This increase is necessary to prevent excessive SMBH growth and the subsequent quenching of intermediate mass galaxies.

Once the fraction of the unstable mass accreting the BH has been determined, the residual fraction $1 - f_{\text{BH,unst}}$ form stars.

- If a stellar mass $M_{\text{stars}}^{\text{ring}}$ is in the disc ring, it is moved to the bulge. In a single time-step dt , we perform a sub-iteration of N_{steps} , removing at each sub-step a mass $M_{\text{stars}}^{\text{ring}}/N_{\text{steps}}$ and re-evaluating the stability of the disc each time. This procedure avoids removing the whole stellar mass from a single ring when just a fraction of it would be sufficient to restore stability. We adopt $N_{\text{steps}} = 20$, and we verified any value $N_{\text{steps}} \gtrsim 10$ yields similar results.

We perform the steps above for each ring until the stability of the whole disc is restored.

5.2.2 Bulge sizes

Also the size of bulges formed/grown as a result of both mergers and disc instabilities is determined taking inspiration from [Irodou et al. \(2019\)](#).

- **Major Mergers**

In major mergers, all the pre-existing stars and those formed during the merger are added to the bulge of the descendant galaxy, following the collisional starburst formulation

⁶Equation S27 of the supplementary material of [Henriques et al. 2020](#), setting $M_{\text{sat}}/M_{\text{cen}} = 1$.

by [Somerville et al. \(2001\)](#). Its half-mass radius $R_{\text{fin, bulge}}$ is computed from energy conservation arguments (see also [Tonini et al. 2016](#)):

$$\frac{(M_{*,1} + M_{*,2} + M_{*,\text{burst}})^2}{R_{\text{fin, bulge}}} = \left(\frac{M_1^2}{R_1} + \frac{M_2^2}{R_2} \right) (1 + k_{\text{rad}}) + \left(\frac{M_1 M_2}{R_1 + R_2} \right). \quad (5.5)$$

In this equation, M_i are the total baryonic mass of the progenitors, $M_{*,i}$ their total stellar mass, R_i their stellar half-mass radii, and $M_{*,\text{burst}}$ the stellar produced in the burst. The term k_{rad} includes energy dissipation by gas due to radiative losses, and it is computed as:

$$k_{\text{rad}} = C_{\text{rad}} \left(\frac{M_{\text{gas},1} + M_{\text{gas},2}}{M_1 + M_2} \right), \quad (5.6)$$

being $M_{\text{gas},i}$ the gas mass of the progenitors, and C_{rad} is a parameter of order $\simeq 1$ ([Covington et al., 2008](#)) quantifying the efficiency of radiative losses. Here set to $= 1$.

- **Minor Mergers**

In minor mergers the disc of the larger progenitor survives and will host the smaller progenitor's cold gas and the stars formed during the merger-driven starburst. Instead, the bulge of the larger galaxy accretes the stars of the second progenitor. Its size $R_{\text{fin, bulge}}$ is computed according to:

$$\frac{(M_{\text{bulge},1} + M_{*,2})^2}{R_{\text{fin, bulge}}} = \left(\frac{M_{\text{bulge},1}^2}{R_{\text{bulge},1}} + \frac{M_{*,2}^2}{R_2} \right) (1 + k_{\text{rad}}) + \left(\frac{M_{\text{bulge},1} M_{*,2}}{R_{\text{bulge},1} + R_2} \right). \quad (5.7)$$

In the above expression, $M_{\text{bulge},1}$ and $R_{\text{bulge},1}$ are the mass and half-mass radius of the bulge of the first progenitor *before* the merger, $M_{*,2}$ and $R_{*,2}$ the mass and half-mass radius of the stellar component of the smaller progenitor. The k_{rad} term is computed as in Equation 5.6.

- **Disc instabilities**

If the galaxy already has a bulge with mass M_{in} and half-mass radius R_{in} , the bulge size R_{fin} after a disc instability event leading to a final bulge mass M_{fin} is given by:

$$\frac{M_{\text{fin}}^2}{R_{\text{fin}}} = \frac{M_{\text{in}}^2}{R_{\text{in}}} + \frac{M_{\text{unst}}^2}{R_{\text{unst}}} + \frac{\alpha}{C} \frac{M_{\text{in}} M_{\text{unst}}}{R_{\text{in}} + R_{\text{unst}}}, \quad (5.8)$$

with $\frac{\alpha}{C} = 1.5$ (C is a structural parameter and α regulates the energy dissipation; [Boylan-Kolchin et al. 2005](#)). In the above expression, M_{unst} is the mass of the material transferred from disc to bulge as a result of the instability, and R_{unst} its half-mass radius⁷.

When a galaxy does not possess a bulge before a disc instability event ($M_{\text{in}} = 0$), we simply assume $R_{\text{fin}} = R_{\text{unst}}$.

A couple of results demonstrating the improvements due to these new prescriptions are illustrated and briefly discussed in Section 5.3.3. However, these have no relevant effect in determining the major result discussed in this Chapter, that is the evolution of the cosmic dust abundance.

⁷Note that, since the unstable material is already in rings, we can trivially compute the half mass radius of the unstable mass.

5.3 General Properties of the Galaxy Population

This Section examines model predictions related to general, non-dust-related properties of the galaxy population. This analysis is necessary to understand the impact of the newly introduced prescriptions for DIs detailed in Sections 5.2.1 and 5.2.2. Importantly, none of the model parameters related to the physical processes originally included in the SAM (Section 2.3) has been modified.

5.3.1 Mass Functions and Cosmic SFRD

As an initial benchmark for our model, we discuss its results for the SMF, HI Mass Function (HIMF), and H₂ Mass Function (H₂MF) at $z = 0.0$ (Figure 5.1), as well as the cosmic SFRD (Figure 5.2). In our fiducial model, the SMF and HIMF show slight deviations from the results obtained using the original instability criterion of Henriques et al. (2020, dubbed *oldInsta*). While the fiducial SMF remains consistent with observational data, the HIMF slightly underpredicts observations at high masses. This discrepancy persists regardless of the uncertainty associated with the neutral gas fraction of the cold phase in a galaxy, here assumed to be $f_{\text{neu}} = 1/1.3$ (Fu et al. 2010). Even in the extreme case where $f_{\text{neu}} = 1$, the HIMF still appears under-abundant at high masses. In contrast, both the H₂MF and the cosmic SFRD align well with observations when our fiducial model is used. Notably, the H₂MF shows significant improvement compared to recent determinations by Andreani et al. (2020) and Fletcher et al. (2020), as the *oldInsta* model tends to overestimate H₂ in the most massive galaxies, as previously discussed in Henriques et al. (2020).

We anticipate the reason for the differences outlined above: our model allows SMBHs to grow during disc instabilities, leading to accelerated SMBH growth rates, followed by quicker quenching through cooling suppression via radio mode feedback. This results in lower gas contents (and then H₂ and star formation) when disc instabilities occur.

In summary, our fiducial model yields a plausible galaxy population at $z = 0.0$ and a cosmic SFRD that aligns well with observational data. This outcome holds true despite adjustments made to the physics within the SAM framework, without requiring parameter re-tuning.

5.3.2 Galaxy morphology and star formation

We now move to analyse the morphology of the model galaxies, quantified by the Bulge-to-Total stellar mass ratio (B-to-T). Figure 5.3a shows the relative fraction of disc-dominated (B-to-T < 0.3) and spheroid-dominated galaxies (B-to-T > 0.3) as a function of stellar mass for our fiducial model and the model without the new implementation of disc instabilities (*oldInsta*). The same figure also includes results from the Galaxy And Mass Assembly survey (GAMA; Moffett et al. 2016). In their local sample of observed galaxies, these authors analyzed the contribution of different morphological types to the total galaxy SMF. They found that the *transition mass* where spheroidal galaxies (E, S0-Sa, LBS⁸) types begin to dominate over disc-dominated galaxies (Sd-Irr, Sab-Scd types) occurs at $M_{\text{stars}} \simeq 10^{10} M_{\odot}$. This finding aligns well with our model predictions.

The updated DI recipe is essential to produce a reasonable number of bulge-dominated systems, as the *oldInsta* model predicts a transition mass that is too high. Disc instabilities are crucial for bulge formation in the $10^{10} - 10^{11} M_{\odot}$ stellar mass range, where bulge growth via

⁸We include Little Blue Spheroids (LBS) in spheroid-dominated galaxies, unlike Moffett et al. (2016). LBS are often associated with pseudo-bulges (Sérsic index $n \leq 2$). Since we do not explicitly distinguish between classical and pseudo-bulges, we include LBS in spheroid-dominated galaxies. However, their contribution is significant only at $M_{\text{stars}} \lesssim 10^{9.5} M_{\odot}$.

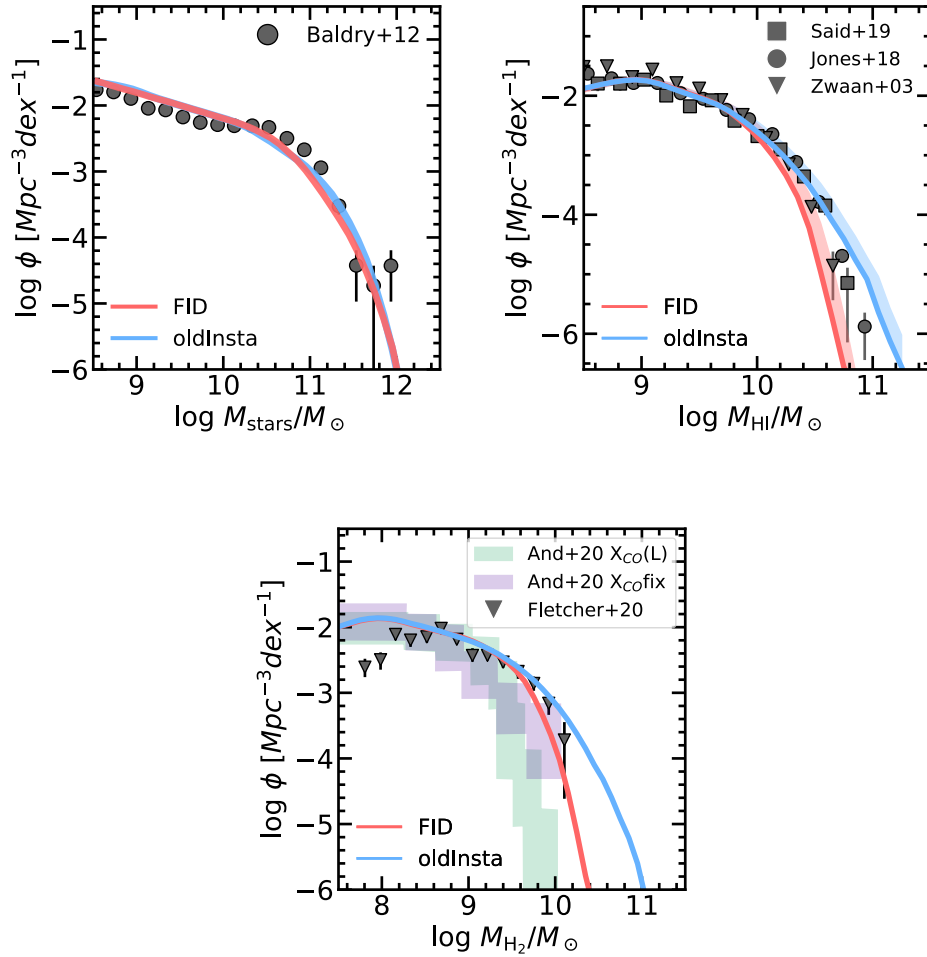


FIGURE 5.1: Mass functions at $z = 0.0$ of our fiducial model (*FID*; red) and the model without updated treatment of disc instabilities (*oldInsta*; blue). Top left panel: SMF compared with observations by [Baldry et al. \(2012\)](#). Top right panel: neutral hydrogen mass function (HIMF) compared with data from [Zwaan et al. \(2003\)](#), [Jones et al. \(2018\)](#), and [Said et al. \(2019\)](#). The dispersion obtained assuming the neutral fraction to be 1/1.3 or 1 is shown. Bottom panel: molecular mass function compared with observations by [Fletcher et al. \(2020\)](#) and [Andreani et al. \(2020\)](#). As for the latter work, results obtained assuming either a constant (purple) and luminosity-dependent (green) CO conversion factor are shown.

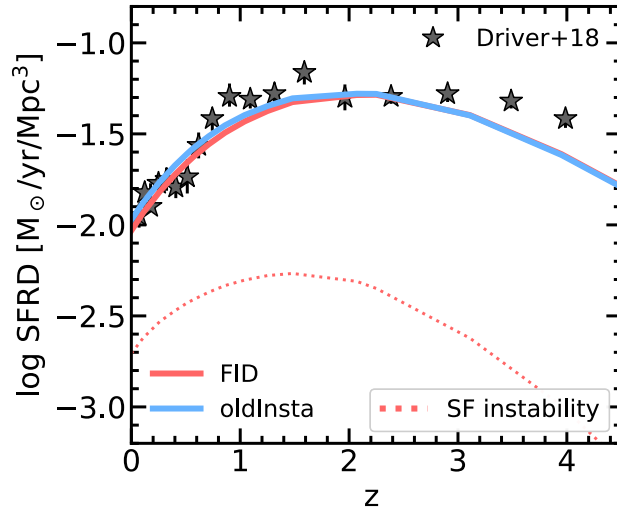


FIGURE 5.2: Cosmic evolution of the Star Formation Rate Density in our fiducial model (*FID*; red) and in the model without the new implementation of disc instabilities (*oldInsta*; blue). As for our *FID* model, we also show the star formation triggered by disc instability episodes (SF instability; dotted line). Data from [Driver et al. \(2018\)](#) are also shown for comparison.

mergers is insufficient (see the detailed discussion in [Irodotou et al. 2019](#) in the context of L-GALAXIES 2015, and in [Huško et al. 2022](#)), and in the mass range ($3 \cdot 10^9 < M_*/M_\odot < 3 \cdot 10^{10}$) where pseudobulges are observed to dominate ([Fisher & Drory, 2011](#)).

After verifying that our model reproduces the number of spheroidal galaxies observed in the local Universe, we now analyze their star formation properties. The relationship between galactic morphology and galaxy properties has been well studied (e.g., [Roberts & Haynes 1994](#)), with early-type galaxies typically being redder and less star-forming than late-type ones (see e.g., the recent work by [Dimauro et al. 2022](#)). While a solid theoretical explanation for this is still lacking, many SAMs, including ours, produce passive, elliptical galaxies as a result of mergers that trigger bulge formation and BH growth. The subsequent BH radio mode feedback prevents the cooling of hot gas, thereby halting star formation (e.g., [Croton et al. 2006](#)). In our model, we introduce a new BH growth channel, i.e. gas accretion during DIs, which indirectly modifies the original quenching mechanism.

It is thus interesting to examine the star formation properties of our simulated galaxies. Figure 5.3b shows the $z = 0$ distribution of our galaxies in the specific SFR (sSFR = $\text{SFR}/M_{\text{stars}}$) vs. M_{stars} plane, colored by the mean B-to-T ratio in each bin. We also plot the observed star formation main sequence fit by [Elbaz et al. \(2007\)](#). Our simulated galaxies follow this relation up to $\log M_{\text{stars}}/M_\odot \lesssim 10^{10.5}$. Galaxies that align with the observed main sequence are mainly disc-like (B-to-T $\lesssim 0.4$). As stellar mass increases, the passive population becomes dominant, typically featuring a bulge-dominated structure (B-to-T $\gtrsim 0.7$). Our model thus shows a qualitative correlation between B-to-T and the position in the sSFR - M_{stars} plane, consistent with observations (e.g., [Dimauro et al. 2022](#)). However, a detailed analysis of the interplay between morphology and quenching is beyond the scope of this work. For a thorough investigation of this topic in a SAM, see [Koutsouridou & Cattaneo \(2022\)](#).

A deeper analysis of the impact of the new DI prescription on the star formation properties of our simulated galaxies is shown in Figure 5.4. This figure reports the specific SFR distribution across different stellar mass bins for both the *FID* and *oldInsta* models, compared

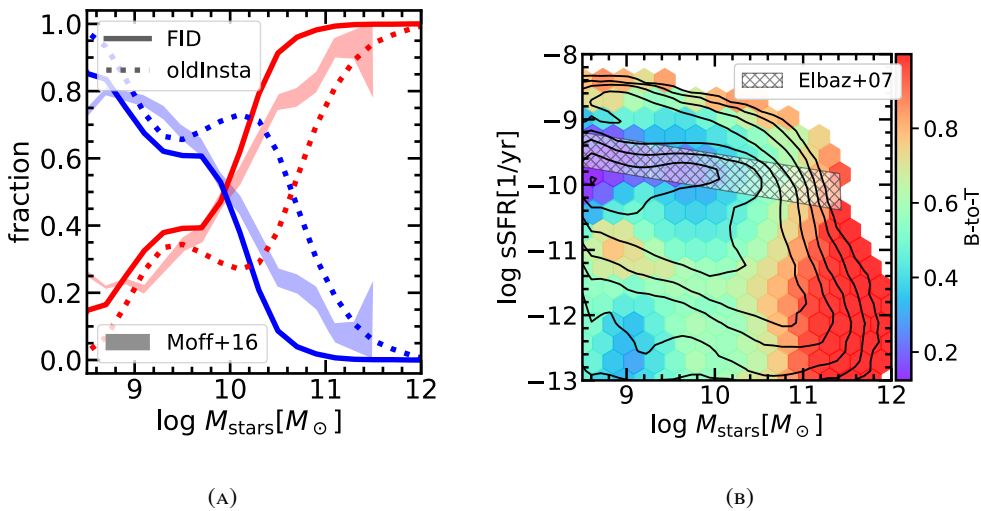


FIGURE 5.3: Left panel: fraction of disc-dominated galaxies ($B\text{-to-T} < 0.3$, blue) and spheroid-dominated galaxies ($B\text{-to-T} > 0.3$, red) for our fiducial model (*FID*; solid line) and the model without the updated disc instability model (*oldInsta*; dotted line). We compare with observations of Moffett et al. (2016) (coloured regions). Right panel: Specific SFR as a function of stellar mass at $z = 0.0$ for our fiducial model. The bins of the 2D histogram are coloured according to the mean $B\text{-to-T}$, while log-spaced density contours are shown as black lines to give a qualitative idea of the distribution of galaxies in this plane. We overplot the Elbaz et al. (2007) star forming main sequence as a gray hatched region.

with SDSS-DR7 data (Katsianis et al. 2020). The two models perform similarly for $\log M_{\text{stars}}/M_{\odot} < 10.5$, but at higher stellar masses, the *FID* model generally exhibits lower sSFRs and less bimodality. Our fiducial model matches the shape of the observed distribution in the highest stellar mass bin, though with a lower normalization. In contrast, the *oldInsta* model predicts too many star-forming objects in the same mass bin, likely due to their excessive molecular gas content (see bottom panel of Figure 5.1).

The differences in star formation between these two models are attributed to the enhanced SMBH growth during DIs. In galaxies in which DI occurs, BHs grow faster and, through radio feedback, prevent cooling, leading to more rapid quenching. This mechanism prevents the formation of massive, gas-rich, star-forming galaxies at $z = 0.0$. However, the discussion above suggests that the current BH-driven quenching likely needs further revision to match SDSS data for $\log M_{*}/M_{\odot} > 11$, where our model normalization is too low.

5.3.3 Bulge sizes and Bulge-BH relation

The DI model introduced here also impacts the bulge size of galaxies and the mass of the central SMBH. Although these are not the main focus of this Chapter, we present some results regarding these predictions as a consistency check.

In Figure 5.5 we present the stellar half-mass radius R_{HM} for disc-dominated ($B\text{-to-T} < 0.5$) and spheroid-dominated ($B\text{-to-T} > 0.5$) galaxies, comparing our results with observations from Lange et al. (2015) and Zhang & Yang (2019). Overall, our trends broadly agree with the observational data. However, our fiducial model predicts a median stellar half-mass radius for disc-dominated galaxies that is approximately half the observed value. This discrepancy is only slightly influenced by the new implementation of DIs, as a similar

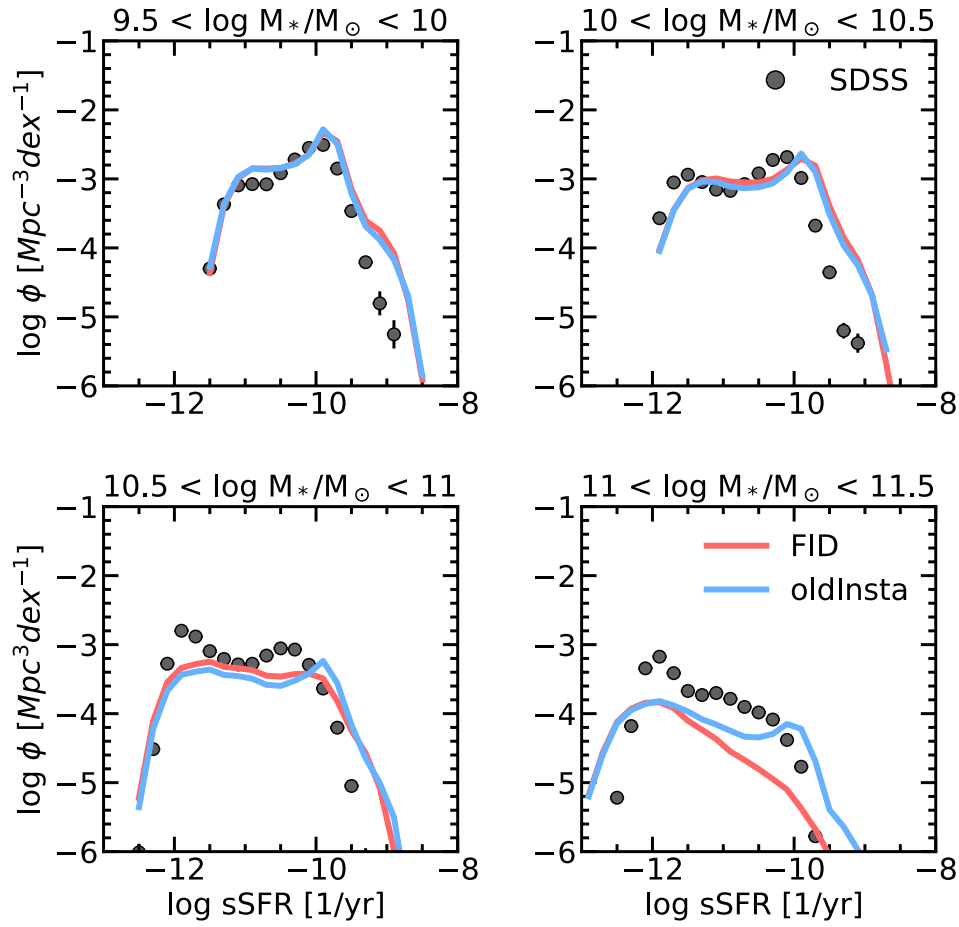


FIGURE 5.4: Specific SFR distribution for our $z = 0.0$ sample of galaxies with $\log \text{SFR} > 10^{-1.5} M_{\odot}/\text{yr}$ in stellar mass bins of width $\Delta \log M_*/M_{\odot} = 0.5$. Our model (*FID*; red) is compared with the model without the updated implementation of disc instabilities (*oldInsta*; blue). Data from SDSS-DR7 (Katsianis et al. 2020) are shown in each panel as filled circles.

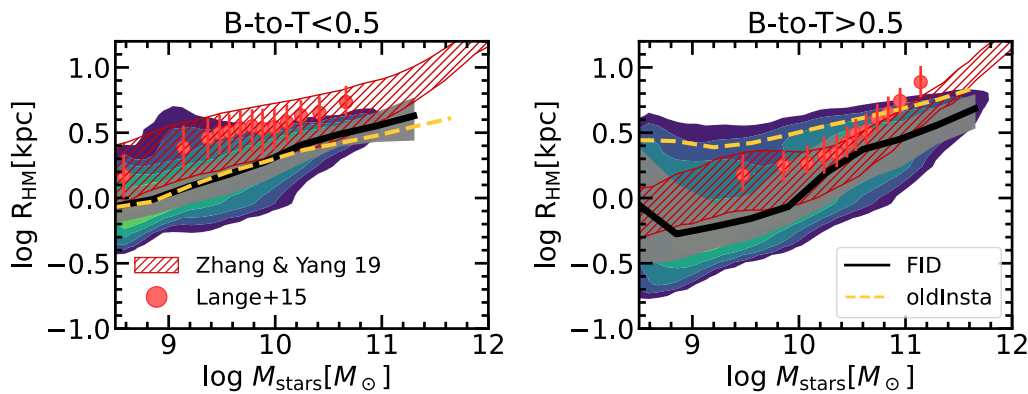


FIGURE 5.5: Stellar half-mass radius as a function of stellar mass for disc-dominated (left panel, $B\text{-to-}T < 0.5$) and bulge-dominated (right panel, $B\text{-to-}T > 0.5$). The black line and gray shaded area represent the median and 16 – 84th percentiles dispersion of our fiducial model results, while log-spaced density contours are shown in background. The median relation obtained by the *oldInsta* model is shown as a gold dashed line. We compare with observations of [Lange et al. \(2015\)](#) (red circles; we use their classification of disc and bulge dominated galaxies according to the Sérsic index) and [Zhang & Yang \(2019\)](#) (hashed red regions, corresponding to the 16 – 84th percentiles of the observed dispersion).

pattern is found in the context of the *oldInsta* model. For bulge-dominated galaxies, the new computation of bulge sizes detailed in Section 5.2.2 improves the fiducial model predictions, resulting in lower stellar half-mass radii that are more consistent with observations.

The BH-bulge mass relation at $z = 0$ is illustrated in Figure 5.6 for both the *FID* and *oldInsta* models. The new implementation of BH growth during disc instabilities results in slightly larger BH masses, but these values still align with the observations by [McConnell & Ma \(2013\)](#).

5.4 Dust properties

To validate our dust implementation within the SAM, we now discuss some model predictions related to dust at various redshifts. In this Section, we consider only galactic dust, which corresponds to the dust in the cold gas of galaxies. Our primary focus is on global galaxy properties, so we limit our analysis to these quantities.

5.4.1 Dust Mass Function

Figure 5.7 shows the DMF at $z = 0.0$, $z = 1.0$, and $z = 2.25$, alongside several observational determinations. The local DMF predicted by our fiducial model aligns excellently with observations ([Vlahakis et al. 2005](#); [Dunne et al. 2011](#); [Beeston et al. 2018](#)), whereas the *oldInsta* model overpredicts the high-mass end. This discrepancy is closely linked to the HI and H_2 mass abundance of the most massive galaxies discussed in Section 5.3, as well as the number of massive star-forming objects shown in Figure 5.4. The faster quenching due to disc instabilities in the *FID* model prevents the presence of very dust-rich galaxies, which are not observed at $z = 0$ but are predicted by other models (see Section 3.3.2).

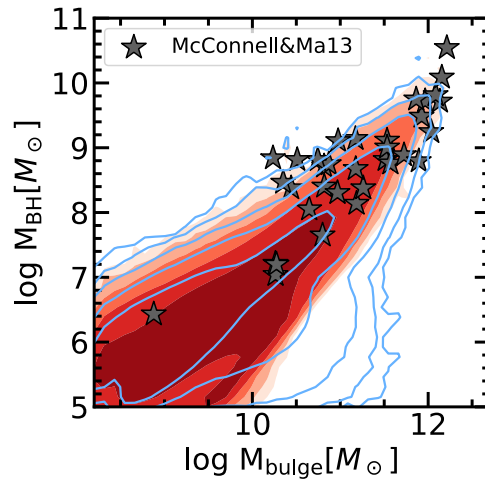


FIGURE 5.6: BH-bulge mass relation at $z = 0$ for our fiducial model (log spaced filled red contours of the density of galaxies in this plane) and for the *oldInsta* model (blue contours) compared with observations by [McConnell & Ma \(2013\)](#).

For $z > 0$ bins, we compare our results with those by [Pozzi et al. \(2020\)](#), who derived the DMF up to $z \approx 2.5$ and found an increasing characteristic dust mass with redshift. Our model also predicts more dust-rich galaxies at $z > 0$ compared to $z = 0$. However, we slightly underestimate the abundance of high- z galaxies with $\log M_{\text{dust}}/M_{\odot} \gtrsim 9$.

Finally, given that the new model for DIs has improved the predictions for the morphological types of simulated galaxies (Section 5.3.2), it is interesting to examine the relationship between dust content and morphology. [Beeston et al. \(2018\)](#) combined their dust mass measurements with the morphological classification of GAMA galaxies ([Driver et al. 2012](#); [Moffett et al. 2016](#)) and derived the local DMF for elliptical and non-elliptical galaxies. We present their results in Figure 5.8, compared with our model predictions. Consistent with the data, our elliptical galaxies are more dust-poor than non-elliptical ones in both the *FID* and *oldInsta* models. Specifically, the update of DIs significantly improves the match for non-elliptical galaxies at the high mass end. In contrast, the DMF for elliptical galaxies is less affected by the DI prescription. Both models slightly overestimate the high mass end of the observed DMF for elliptical galaxies.

5.4.2 Dust, stars and metallicity

Figure 5.9 shows the relationship between dust and stellar masses in our fiducial model at $z = 0.0$, $z = 1.0$, and $z = 2.25$, compared with observations from [Beeston et al. \(2018\)](#), [De Vis et al. \(2019\)](#) (DustPedia), and [Santini et al. \(2014\)](#). Overall, our predictions align well with all data points. The relation observed in the $z > 0$ redshift bins is reproduced up to $M_{\text{dust}} \sim 10^8 - 10^{8.5} M_{\odot}$. As mentioned in the previous Section, galaxies with such high dust masses are not observed in the local Universe. At $z = 0$, the observed $M_{\text{stars}} - M_{\text{dust}}$ relation flattens towards larger stellar masses ([Beeston et al. 2018](#), binned data), trend successfully captured by our model as well.

Such a drop of $M_{\text{dust}}/M_{\text{stars}}$ towards large stellar masses has been previously observed in literature and linked to various processes that regulate the ISM dust content (e.g. [Cortese et al., 2012](#); [Hunt et al., 2014](#); [Calura et al., 2017](#)). Here we utilize our detailed modeling and tracking of these processes to investigate the cause of the decline in $M_{\text{dust}}/M_{\text{stars}}$ at large stellar

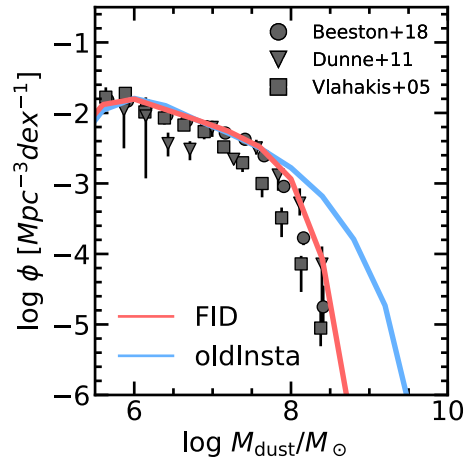
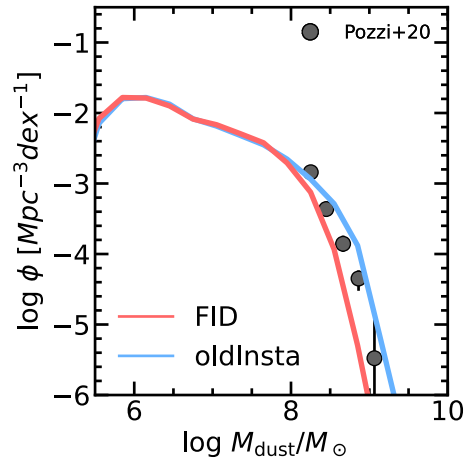
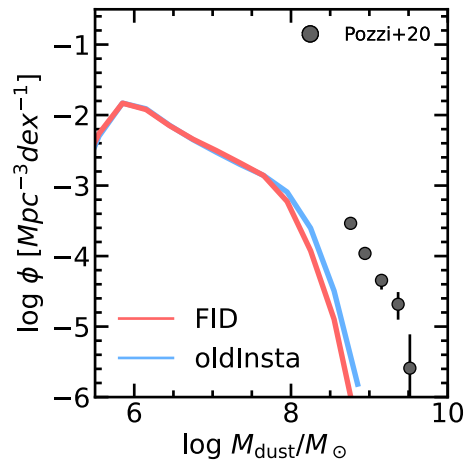
(A) $z = 0.0$ (B) $z = 1.0$ (C) $z = 2.25$

FIGURE 5.7: Dust Mass Functions of the fiducial model (*FID*; red solid line) and the model without updated disc instability recipe (*oldInsta*; solid line) at $z = 0.0, 1.0$, and 2.25 (top, middle, and bottom panel, respectively). We also report observations by [Beeston et al. \(2018\)](#), [Dunne et al. \(2011\)](#) and [Vlahakis et al. \(2005\)](#) at $z = 0.0$, and by [Pozzi et al. \(2020\)](#) at higher redshift.

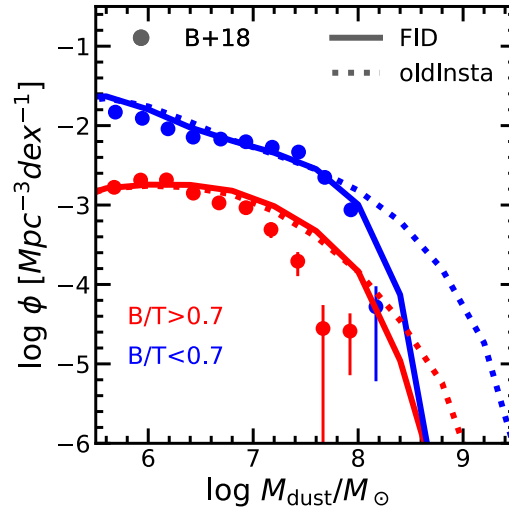


FIGURE 5.8: Dust Mass Function at $z = 0$ for elliptical (B-to-T > 0.7 ; red) and non-elliptical (B-to-T < 0.7 ; blue) galaxies. Results from both the *FID* and *oldInsta* model are shown (solid and dotted lines). We compare with the observations of [Beeston et al. \(2018\)](#).

masses. The left panel of Figure 5.10 presents the evolution of $M_{\text{dust}}/M_{\text{stars}}$ for galaxies with $z = 0$ stellar masses of $\approx 10^{9.5}$, 10^{10} , $10^{10.5}$, $10^{11} M_{\odot}$. The peak value of $M_{\text{dust}}/M_{\text{stars}}$ during their evolution has a weak dependence on the final stellar mass (it is within a factor of $\lesssim 2$ for all the galaxies samples). However, more massive galaxies feature a lower dust-to-stellar mass ratio today due to their earlier evolutionary history. In these galaxies, the (molecular) gas budget and star formation drop earlier, causing the ISM dust destruction processes (SN shock destruction, astration, and ejection) to dominate over dust growth processes (stellar production and accretion). This is explicitly shown in the right panel of Figure 5.10, where the ratio of dust *production* to *destruction* rates is plotted over time. More massive galaxies reach an equilibrium between these processes earlier, and since this equilibrium is skewed towards destruction, their dust mass continues to decrease over time, leading to a lower $M_{\text{dust}}/M_{\text{stars}}$ by $z = 0$.

In concluding this analysis, it is worth mentioning the work by [Calura et al. \(2023\)](#), who used a chemical evolution model to study the dust abundance and distribution in M74. Their findings also indicate that dust accretion and destruction reach equilibrium at recent times. However, they highlight potential model degeneracies, as different models with different equilibrium values can still produce similar dust profiles.

Another critical relation is that between the ISM DTG and the metallicity, since the accretion process links these two quantities (e.g. [Hirashita 2013](#)). Figure 5.11 illustrates this relationship at various redshifts. Observations ([Rémy-Ruyer et al. 2014](#); [De Vis et al. 2019](#); [Popping & Péroux 2022](#)) indicate a positive correlation between DTG and gas metallicity, with a nearly non-evolving trend over cosmic time (see the discussion in [Popping & Péroux 2022](#)). Our fiducial model successfully reproduces this scenario, particularly at $z = 0.0$, where this relation is well constrained by observations. The model also aligns well with data at $z > 0$, although it slightly overpredicts DTG in the $2 < z < 3$ redshift bin.

5.4.3 Grain sizes

Our dust model accounts for two distinct dust grain sizes: small and large grains (Section 3.4). The relative abundance of grains with different sizes can be estimated in observations through SED fitting. This estimation has been conducted for a sample of local galaxies in two recent studies by [Relaño et al. \(2020\)](#) and [Relaño et al. \(2022\)](#). Figure 5.12 shows their results alongside our model predictions. We caution the reader about this comparison. In our model, the transition from small to large grains occurs at $0.03 \mu\text{m}$, whereas it occurs at $0.015 \mu\text{m}$ in the model used by [Relaño et al. \(2020\)](#) and [Relaño et al. \(2022\)](#)⁹. Additionally, [Relaño et al. \(2020\)](#) and [Relaño et al. \(2022\)](#) assume carbonaceous properties for small grains, whereas our model also considers a silicate composition for small grains.

The relation between the observed Small-to-Large grain mass ratio (S-to-L) and stellar mass (top panel) shows a nearly flat trend with a median value of S-to-L $\sim 0.2 - 0.3$ and a dispersion of ~ 0.7 dex. However, the more recent work by [Relaño et al. \(2022\)](#), which used a significantly larger sample of galaxies with respect to [Relaño et al. \(2020\)](#), suggests a slowly decreasing trend of S-to-L with M_{stars} . The relationship between S-to-L and ISM metallicity (bottom panel) exhibits a similar qualitative behavior. While our model matches the median S-to-L, it fails to reproduce the decrease toward high M_{stars} and Z . Other cosmological simulations that use the two size approximation ([Hou et al. 2019](#); [Parente et al. 2022](#)) attribute this behavior to the dominance of coagulation over accretion and shattering. In our model, high S-to-L galaxies with large M_{stars} or Z typically have low molecular gas fractions, making coagulation of small grains less effective. We conclude that, although our model can reproduce the S-to-L ratio for most observations, some improvements in the treatment of shattering and coagulation are necessary to avoid over-predicting the abundance of small grains in massive galaxies.

5.4.4 Dust profiles

Adopting a non-constant $n_{\text{gas}}(r)$ in Equation 3.30 (according to Equation 3.20) has a negligible impact on the integrated grain size properties. However, it is relevant when looking at the S-to-L radial profile of galaxies, as shown in Figure 5.13. The S-to-L profile is too high in the outer regions of the galaxies when assuming $n_{\text{gas}} = 1$ or 10 cm^{-3} because these values are too high for the outer rings. In contrast, calculating n_{gas} from $\Sigma_{\text{cold gas}}$ ensures a progressively lower efficiency of shattering with increasing radial distance, which is necessary to match the observational results of local disc galaxies ([Relaño et al. 2020](#)).

5.5 The Cosmic Dust Abundance

In this Section we present and discuss the main result of this Chapter, that is the cosmic evolution of the galactic, extra-galactic and total dust budget across cosmic time.

5.5.1 Galactic dust budget

The galactic dust mass density $\Omega_{\text{dust}}^{\text{ISM}}$ as a function of redshift for the two models discussed above is shown in Figure 5.14, along with observational determinations and predictions from some other cosmological models. We also present results from a model where $f_{\text{BH, unst}} = 0$ (Equation 5.4), meaning BH growth during DIs is not allowed. Observations from [Vlahakis](#)

⁹The adopted cosmic dust model by [Desert et al. \(1990\)](#) includes polycyclic aromatic hydrocarbons (PAHs), very small grains (VSGs), and big grains (BGs). The former two are considered small grains, while the latter component is the only constituent of large grains.

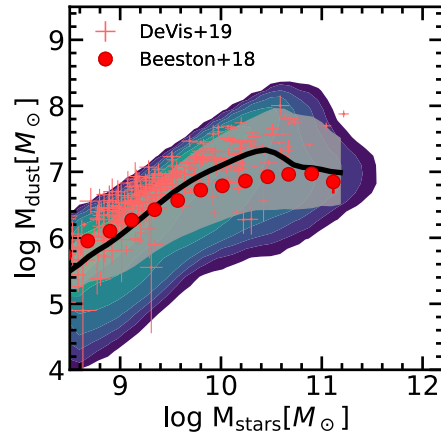
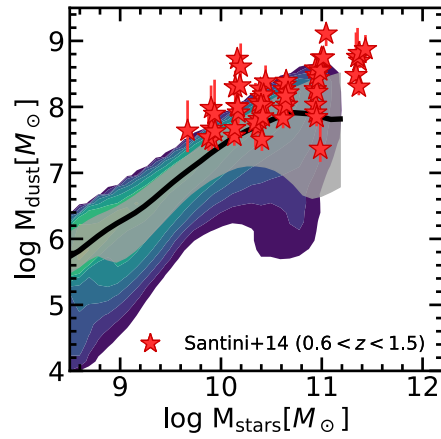
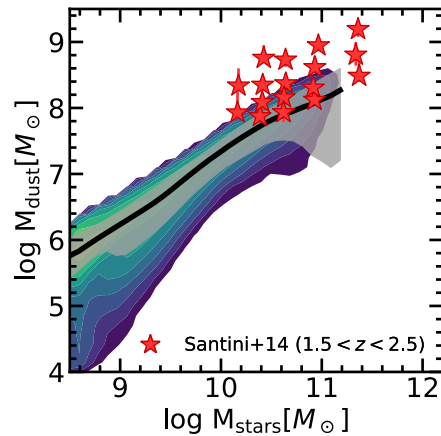
(A) $z = 0.0$ (B) $z = 1.0$ (C) $z = 2.25$

FIGURE 5.9: $M_{\text{dust}} - M_{\text{stars}}$ relation for our fiducial model at $z = 0.0$, $z = 1.0$, and $z = 2.25$ (top, middle, and bottom panel, respectively). The median relation is shown as black line, while the gray shaded region refers to the 16 – 84th percentile dispersion. We show in background log-spaced density contours of our galaxies in this plane. Data from [Beeston et al. \(2018\)](#), [De Vis et al. \(2019\)](#), and [Santini et al. \(2014\)](#) are shown for comparison.

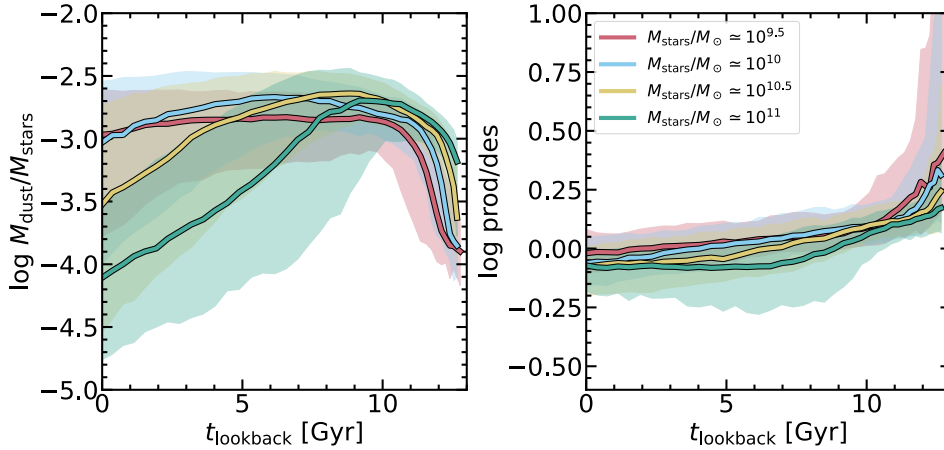


FIGURE 5.10: Evolution of $M_{\text{stars}}/M_{\text{dust}}$ (left panel) and the ratio between ISM dust production and destruction rates (right panel) for galaxies with different stellar mass at $z = 0$, namely $M_{\text{stars}}/M_{\odot} \simeq 10^{9.5}$, 10^{10} , $10^{10.5}$ and 10^{11} . The processes contributing to dust *production* are stellar production and ISM grains accretion, while *destruction* processes are astration, ejection and destruction in SNe shocks. Solid lines and shaded areas refer to the median trend and 16 – 84th percentile dispersion.

et al. (2005), Dunne et al. (2011), Beeston et al. (2018), Driver et al. (2018), Dudzevičiūtė et al. (2020), and Pozzi et al. (2020), which are based on integrating the observed DMF, are included for comparison.

Both the *FID* and *oldInsta* models align with the data within a factor of ~ 2 . While the *oldInsta* model better matches the $z \gtrsim 1$ data, our fiducial model performs better at lower redshifts, particularly in drop of $\Omega_{\text{dust}}^{\text{ISM}}$. This is due to the influence of BH accretion during DIs and its effect on quenching. This is further confirmed by the $f_{\text{BH,unst}} = 0$ model, which behaves similarly to the *oldInsta* model and fails to reproduce the desired decline of $\Omega_{\text{dust}}^{\text{ISM}}(z)$ toward $z = 0$.

Figure 5.14 illustrates that most other cosmological simulations (SAM or hydrodynamic) published so far struggle to accurately reproduce the observed $\Omega_{\text{dust}}^{\text{ISM}}(z)$, often overpredicting the data and showing only a mild, if any, decrease from $z \sim 1$ to $z = 0$ (see also Section 3.3.2 for a more updated comparison). The exception is the SIMBA simulation (Li et al. 2019), which exhibits an $\Omega_{\text{dust}}^{\text{ISM}}$ evolution very similar to our fiducial model.

We now investigate *why* and *how* galactic dust decreases from $z \sim 1$ to $z = 0$ in our fiducial model. To do this, we examine the rates of various processes that affect the abundance of dust in the cold gas of our model galaxies: production by stars, accretion, dust transfer from hot to cold gas by cooling, destruction by SNe, ejection from cold gas, and astration. These rates are shown in Figure 5.15 as a function of redshift, along with the sum of those contributing to a decrease (increase) of $\rho_{\text{dust,cold}}$.

Except for dust cooled (i.e., dust transferred from the hot to cold gas during cooling), all other rates roughly follow the shape of the SFRD with some delay. This result is expected since they all depend directly (dust produced by stars, astration) or indirectly (destruction by SN, ejection from cold gas due to stellar feedback, grain growth) on star formation. Among the processes contributing to the increase of dust, accretion is by far the dominant one (accounting for $\gtrsim 80 - 90\%$, at least for $z \lesssim 4$, where our focus lies). Conversely, all destruction/ejection processes significantly contribute to the decrease of ISM dust (destruction by SN $\sim 45\%$, ejection $\sim 35\%$, and astration about $\sim 20\%$ at $z = 0$).

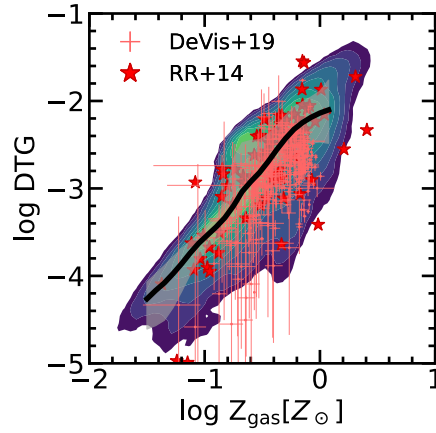
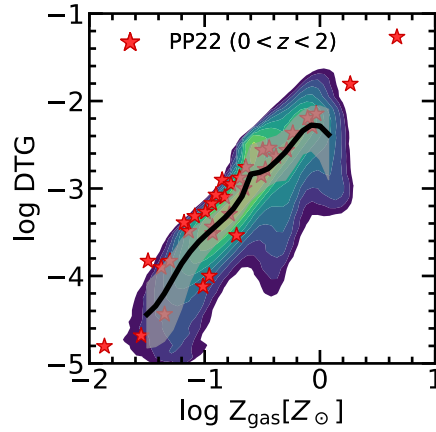
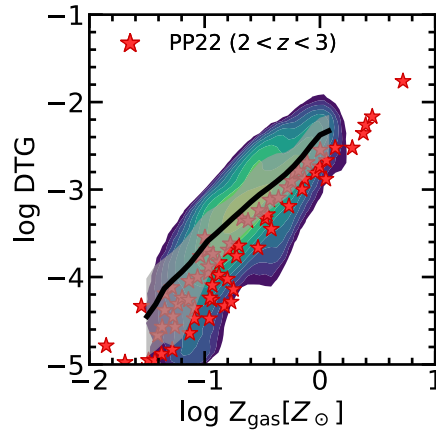
(A) $z = 0.0$ (B) $z = 1.0$ (C) $z = 2.25$

FIGURE 5.11: DTG– Z_{gas} relation for our fiducial model at $z = 0.0$, $z = 1.0$, and $z = 2.25$ (top, middle, and bottom panel, respectively). The median relation is shown as black line, while the gray shaded region refers to the 16 – 84th percentile dispersion. We show in background log-spaced density contours of our galaxies in this plane. We compare with observations by Rémy-Ruyer et al. (2014), De Vis et al. (2019), and Popping & Péroux (2022).

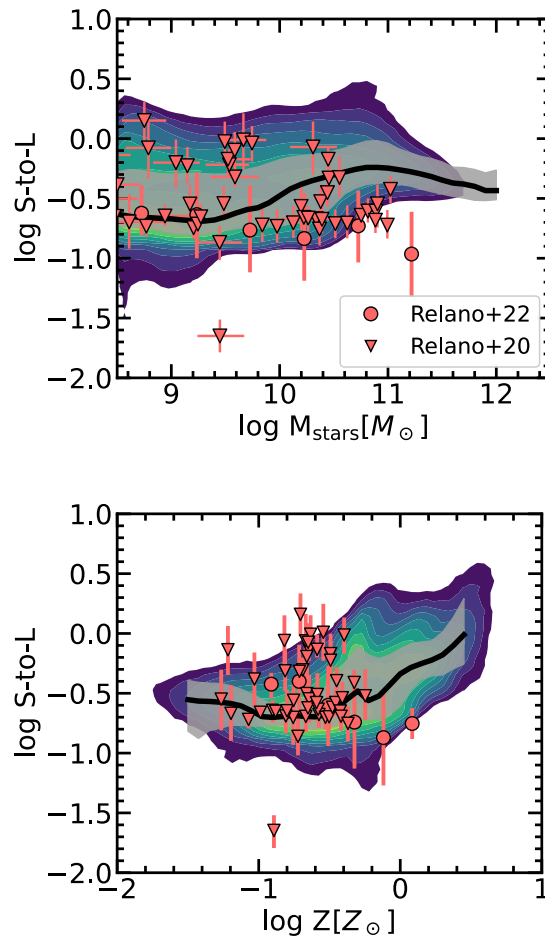


FIGURE 5.12: Small-to-Large grains mass ratio as a function of stellar mass (top panel) and ISM total metallicity (bottom panel) for our fiducial model (density contours) at $z = 0.0$. The median relation is shown as black line, while the gray shaded region refers to the 16 – 84th percentile dispersion. We show in background log-spaced density contours of our galaxies in this plane. The SAM results are compared with observations by [Relaño et al. \(2020\)](#) (red triangles; both DSG and KINGFISH data), and [Relaño et al. \(2022\)](#) (red circles; binned data).

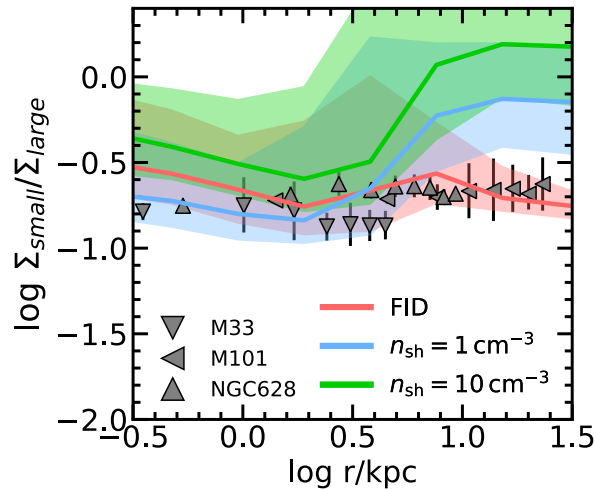


FIGURE 5.13: S-to-L median profile (solid lines) and associated 16 – 84th percentile dispersion (shaded regions) for $z = 0$ disc (B-to-T < 0.3) galaxies with $10^9 < M_*/M_\odot < 10^{10.5}$. We show results for our fiducial model, and two models where the number density in Equation 3.30 is assumed to be fixed ($n_{\text{gas}} = 1$ and 10 cm^{-3}). Results for three local disc galaxies derived by [Relaño et al. \(2020\)](#) are shown as triangles.

An interesting exercise is to examine the impact on $\Omega_{\text{dust}}^{\text{ISM}}$ when the processes of destruction/ejection (astration, ejection from cold gas, and SN destruction) are alternatively turned off. Figure 5.16 illustrates the results of this experiment.

When neglecting dust destruction by SNe (*noSNdes*), the predicted $\Omega_{\text{dust}}^{\text{ISM}}$ closely resembles that of our fiducial model, albeit with a slight increase, particularly at higher redshifts. This pattern emerges because in the *FID* model, most of the gas phase metals produced by SN destruction are rapidly incorporated into dust grains via the accretion process. In contrast, in the *noSNdes* model, this mechanism does not occur, and accretion is also reduced compared to the *FID* model. Consequently, the final $\Omega_{\text{dust}}^{\text{ISM}}$ does not deviate significantly from the fiducial result. Thus, the decline of $\Omega_{\text{dust}}^{\text{ISM}}$ is evident even in this model without SN destruction.

Regarding the importance of SN destruction, [Ferrara & Peroux \(2021\)](#) recently proposed that the observed drop in Ω_{dust} from $z \sim 1$ to $z \sim 0$ may imply that each SN destroys approximately $M_{\text{des,SN}} \simeq 0.45 M_\odot$ of dust, which is much lower than the commonly assumed value of $M_{\text{des,SN}} \simeq 4.3 M_\odot$. [Ferrara & Peroux \(2021\)](#) derived this lower destruction mass assuming a solar DTG of ~ 0.006 . In our calculations, we find $M_{\text{des,SN}} \simeq 2.5 M_\odot$ for galaxies with $\text{DTG} \simeq \text{DTG}_\odot$, but when considering the entire galaxy population, we obtain a median $M_{\text{des,SN}} \simeq 0.71(0.47) M_\odot$ at $z = 0(1)$, which aligns closely with the estimate by [Ferrara & Peroux \(2021\)](#). We also confirm that $M_{\text{des,SN}} \simeq 4.3 M_\odot$ would not be acceptable. This higher median value would require increasing the efficiency of SN destruction by a factor of $\sim 6 - 10$, yet it would still under-predict $\Omega_{\text{dust}}^{\text{ISM}}$ at all redshifts by a factor of $\sim 1.5 - 2.5$. This discrepancy arises because the accretion process is not sufficiently effective in re-incorporating all the metals destroyed by SNe back into dust grains.

As for the other destruction/ejection processes, a similar decline of $\Omega_{\text{dust}}^{\text{ISM}}$ occurs when astration and ejection from cold gas are switched off, but for the normalization, which is higher than in the fiducial model, since we are shutting down channels able to remove dust grains and the metals locked in them from the cold gas. Note that this is intrinsically different from what SNe destruction does. Indeed, the latter process transfers dust metals to gas metals, still leaving them available for new accretion processes in the cold phase.

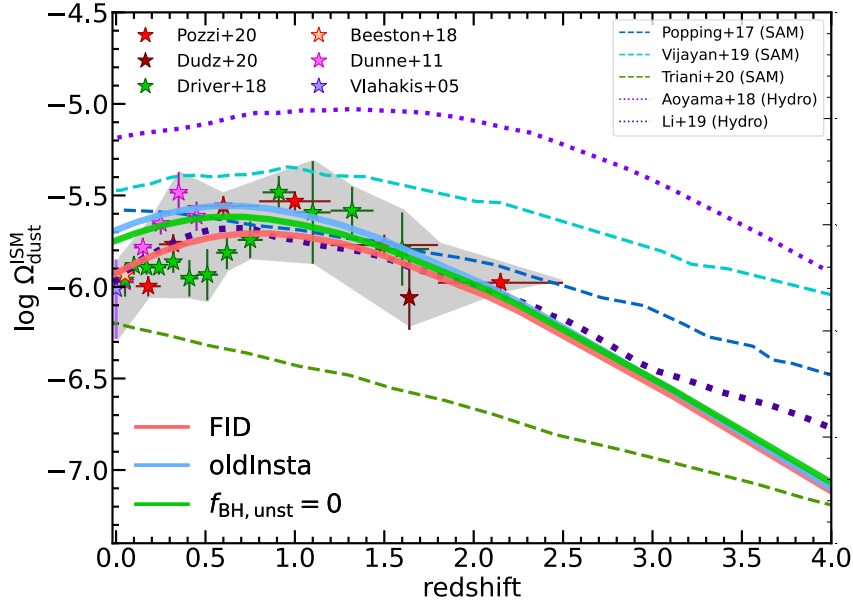


FIGURE 5.14: Cosmic ISM dust abundance across cosmic time. We show the dust abundance in cold gas for: (i) our fiducial model (*FID*; red solid line); (ii) a model without the new implementation of disc instabilities discussed in this work (*oldInsta*; blue solid line); (iii) a model without BH accretion during disc instabilities ($f_{\text{BH,unst}} = 0$ in Equation 5.4; green solid line). Results derived from the integration of the DMF at various redshifts are shown as stars: Vlahakis et al. (2005) (purple), Dunne et al. (2011) (pink), Beeston et al. (2018) (orange), Driver et al. (2018) (green), Dudzevičiūtė et al. (2020) (brown), and Pozzi et al. (2020) (red). A shaded grey region shows the global behaviour of these data. Results from other groups are shown as dashed (SAMs; Popping et al. 2017 in blue, Vijayan et al. 2019 in light cyan, Triani et al. 2020 in green) and dotted (hydrodynamic simulations; Aoyama et al. 2018 in purple, Li et al. 2019 in dark blue) lines.

In concluding this Section, the processes included in our model provide a good normalization of $\Omega_{\text{dust}}^{\text{ISM}}$, and we have shown that none is the only one responsible for its decline. The cosmic evolution of galactic $\Omega_{\text{dust}}^{\text{ISM}}$ is intrinsically linked to the star formation history, since all processes depend on it to some degree. The new treatment of DIs and the associated SMBH growth reduces the star formation, gas, and dust content of massive local galaxies, sharpening the $\Omega_{\text{dust}}^{\text{ISM}}$ drop towards $z = 0$, which improves the match with low redshift data.

5.5.2 Extra-galactic dust budget

This Section presents the predictions of our model concerning the quantity of extra-galactic dust. As mentioned earlier in Section 5.1, there are only a few observational estimates of dust located beyond the ISM of galaxies, notably those derived by Ménard et al. (2010) and Ménard & Fukugita (2012). In Figure 5.17, we compare their determinations of $\Omega_{\text{dust}}^{\text{CGM}}$ with the dust present in the hot halos of our model galaxies, which can broadly be associated with the CGM of galaxies. However, within the framework of our SAM, there exists another component of extragalactic dust, namely the ejected reservoir. This component represents a reservoir of hot gas that cannot cool (unlike the *hot gas*), but its physical interpretation remains ambiguous. For this reason, we also present the extreme scenario where CGM dust is considered to reside in both the hot gas and the ejected reservoir.

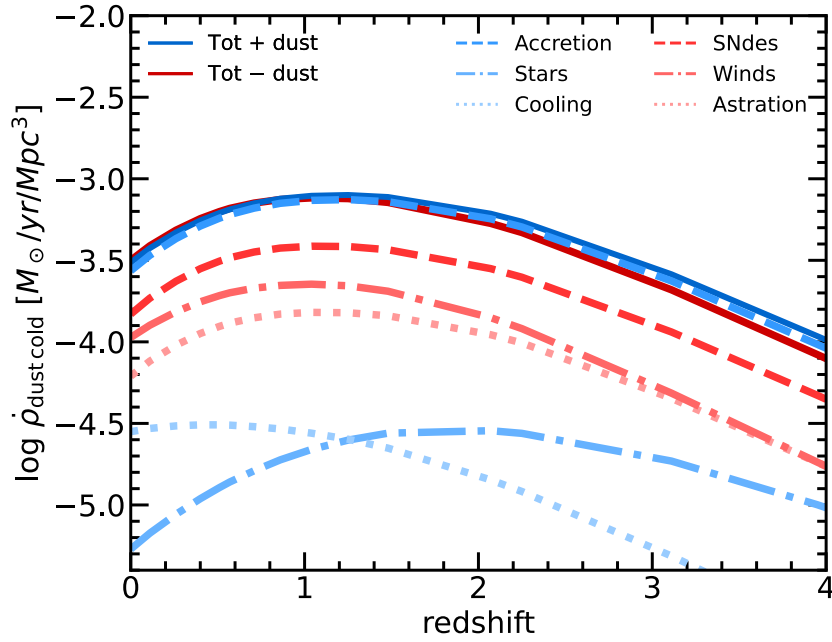


FIGURE 5.15: Cosmic evolution of the rates of the processes contributing to the overall abundance of dust in the cold gas of galaxies in our fiducial model: stellar production (blue dot-dashed), accretion (blue dashed), dust transferred from hot to cold gas by cooling (blue dotted), destruction by SN (red dashed), dust ejected from cold by stellar driven winds (red dot-dashed), and astration (red dotted). The total rate of the processes leading to an increase(decrease) of dust in the cold gas is shown as a solid blue(red) line.

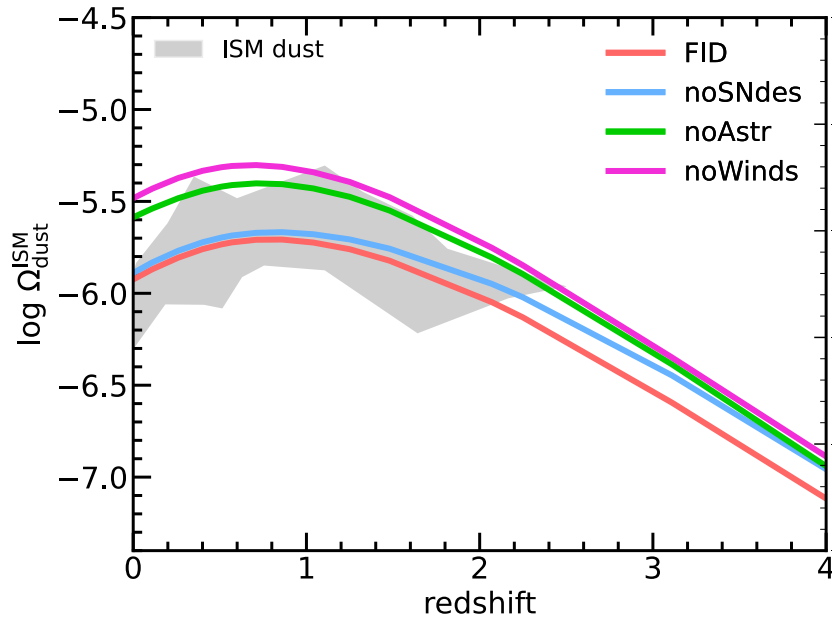


FIGURE 5.16: Cosmic evolution of galactic dust obtained by switching off one at a time the processes responsible for the dust destruction/removal in the cold gas: destruction by SNaE (*noSNdes*; blue), astration (*noAstr*; green), ejection from cold gas (*noWinds*; pink). We also report for comparison our fiducial (*FID*; red) model and the compilation of observations introduced in Section 5.5.1 (gray shaded region).

It is important to note that in our fiducial model, we adopt a sputtering efficiency that is reduced by a factor of 10 compared to the efficiency originally proposed by [Tsai & Mathews \(1995\)](#), as we discussed in Section 3.4.5. This adjustment is consistent with findings from studies by [Gjergo et al. \(2018\)](#) and [Vogelsberger et al. \(2019\)](#), who conducted simulations of dust evolution in galaxy clusters and found that the [Tsai & Mathews \(1995\)](#) sputtering efficiency results in an insufficient amount of dust in the Intracluster Medium (ICM) compared to recent observations based on Planck data ([Planck Collaboration \(XLIII\) et al., 2016](#)). In this Section, we provide further support for the lower sputtering efficiency by presenting results from a model labeled $\tau_{\text{sput}} \times 0.1$, which employs the original [Tsai & Mathews \(1995\)](#) sputtering efficiency.

When considering only hot dust, the $\tau_{\text{sput}} \times 0.1$ model consistently underestimates observations across all cosmic epochs, typically by a factor of 3 – 10, with the discrepancy diminishing towards lower redshifts. On the other hand, the model incorporating both hot and ejected dust aligns better with observations at lower redshifts, yet it still exhibits a tension of approximately a factor of 5 around $z \sim 2$. Conversely, adopting a longer sputtering timescale as in our fiducial model helps to match the abundance of CGM dust more closely to observations, especially when considering both hot and ejected dust components. It is noteworthy that available observations do not indicate a significant decline in the abundance of extragalactic dust at $z \lesssim 1$, unlike what is observed for ISM dust. Instead, observations suggest a nearly constant trend with redshift, which contrasts with our model steeper decline. This discrepancy may imply that our model lacks some crucial physics. While sputtering is the primary process directly influencing the amount of dust in the hot gas and ejected reservoir, its quantity also depends on various physical mechanisms incorporated in our SAM. For instance, SN-driven winds play a crucial role in enriching the hot gas with dust. Moreover, assumptions regarding the composition of ejected material with respect to cold gas DTG and the inclusion of AGN-driven outflows, which are currently not accounted for in our model, could potentially impact our findings.

The agreement observed at low z with a reduced sputtering efficiency is confirmed by comparison with the work of [Peek et al. \(2015\)](#). These authors examined the CGM reddening of low z galaxies, deriving typical CGM dust masses of $\sim 6 \cdot 10^7 M_{\odot}$ and a weak dependence on stellar mass for $0.1L_* - L_*$ galaxies. Their results are shown in Figure 5.18 alongside our predictions for both the fiducial and the $\tau_{\text{sput}} \times 0.1$ models. The *FID* model successfully captures the CGM dust values reported by [Peek et al. \(2015\)](#), and we note that including both hot gas and the ejected reservoir as CGM dust improves the comparison with the observed, nearly flat slope of this relation. From the comparison of the *FID* and $\tau_{\text{sput}} \times 0.1$ models, it is evident that sputtering is significant only above a stellar mass of $M_{\text{stars}} \gtrsim 10^{10} M_{\odot}$, where virial temperatures are high enough to make this process efficient. Additionally, in both models, ejected dust contributes notably only below this critical mass threshold, beyond which SN-driven winds are less effective at expelling gas (and dust) from the hot halo. These qualitative findings align with those discussed by [Popping et al. \(2017\)](#) and [Triani et al. \(2020\)](#), though within different SAM frameworks. Finally, we note that above $M_{\text{stars}} \gtrsim 10^{11} M_{\odot}$, the amount of hot phase dust increases since $T_{\text{vir}} \gtrsim T_{\text{sput},0}$, the temperature above which sputtering efficiency saturates (see Equation 3.28).

To conclude this section, we note that the limited information on the extra-galactic dust budget suggests a reduction in the thermal sputtering efficiency, as previously observed by [Gjergo et al. \(2018\)](#) and [Vogelsberger et al. \(2019\)](#) in hydrodynamic simulations of galaxy clusters. However, we advise caution with these comparisons, as CGM dust within a SAM framework is not well defined.

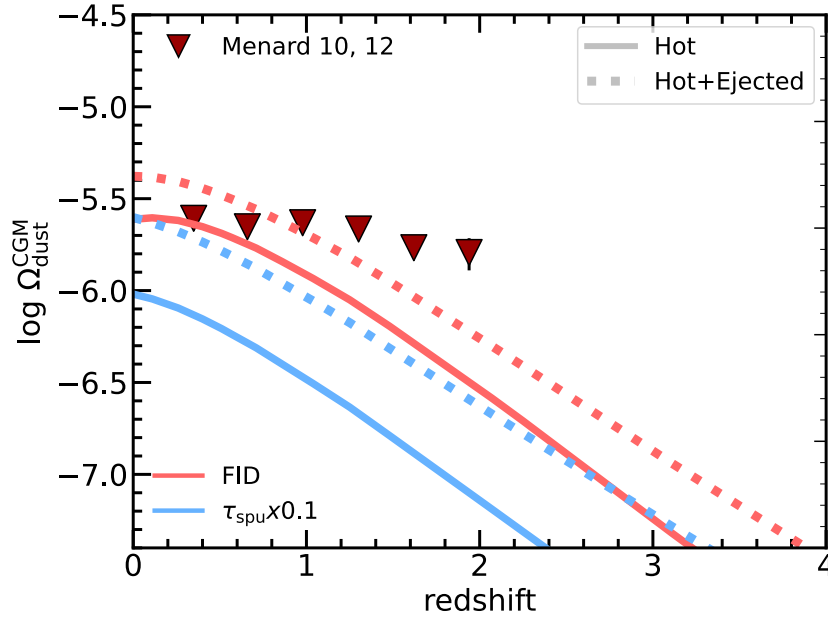


FIGURE 5.17: Cosmic evolution of dust in hot gas (solid line) and both hot gas and ejected reservoir (dotted line). The fiducial model is shown as red lines, while a model with a sputtering efficiency enhanced by a factor 10 (i.e. adopting the timescale originally introduced by Tsai & Mathews 1995) is shown as blue lines. We report observations by Ménard et al. (2010) (the lowest redshift point) and Ménard & Fukugita (2012), corresponding to CGM dust.

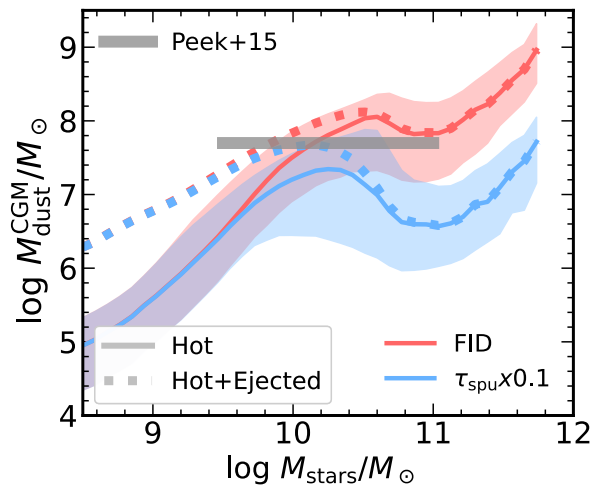


FIGURE 5.18: CGM dust as a function of stellar mass when considering dust in the hot gas (solid, with 16 – 84th percentiles dispersion) and both hot and ejected gas (dotted). The fiducial model is shown as red lines, while a model with a sputtering efficiency reduced by a factor of 10 is shown as blue lines. We report results by Peek et al. (2015) as a gray line.

5.5.3 Total dust budget

Finally, we put together the results concerning the amount of galactic and extra-galactic dust and thus discuss the cosmic evolution of the total amount of dust in our simulation. Deriving an accurate observational estimate of this quantity is a challenging task, so we consider two different estimates. The first one is simply the sum of the galactic ISM ($\Omega_{\text{dust}}^{\text{ISM}}$, that is the compilation of observations introduced in Section 5.5.1) and CGM contribution¹⁰ ($\Omega_{\text{dust}}^{\text{CGM}}$, Ménard et al. 2010 and Ménard & Fukugita 2012 data, Section 5.5.2). The second one is the result of Thacker et al. (2013), obtained with the observation of FIR background. This technique should capture the thermal emission of the whole population of dust grains in our Universe. Both these determinations are shown in Figure 5.19, together with our model predictions. Moreover, we show results considering the CGM made either by hot gas only or hot plus ejected gas.

First, we note that our naive derivation of the total amount of dust and Thacker et al. (2013) results agree remarkably well, but at $z \lesssim 0.2$, where FIR background observations predict a weak decline of Ω_{dust} . However, we stress that our Ω_{dust} derivation is based on an extrapolation of CGM observations down to $z = 0$; this may constitute a source of tension. Second, our model predictions broadly reproduce observations within a factor ~ 2 , even better when considering the CGM made of hot+ejected gas (as already highlighted in Section 5.5.2). Our model does not reproduce any drop in the total dust budget towards $z = 0$. However, this drop is evident only for ISM data. Thacker et al. (2013) observations only constrain the whole population of (typically cold) grains responsible for the emission; a hot dust component may be thus missed. On the other hand, CGM observations, which trace the absorption of grains in typically hot environments, do not show any sign of drop up to $z \approx 0.3$. We thus conclude that, given the available observations, our model reasonably reproduces the cosmic evolution of the total amount of dust. Future observations may better constrain its behaviour, especially for the hot, extra-galactic counterpart.

5.6 Conclusions

In this Chapter, we investigated the $z \lesssim 1$ drop of galactic cosmic dust from a SAM perspective. The integration of observationally derived DMFs at $0 < z \lesssim 2.5$ suggests that the total dust content in galaxies has decreased by a factor of $\sim 2 - 3$ over the last ~ 8 Gyr. However, the reasons for this decline remain unclear.

We utilized the latest public version of the L-GALAXIES SAM (Henriques et al., 2020), incorporating a state-of-the-art dust model and new prescriptions for disc instability. The dust model is based on the two-size approximation and includes dust production by type II SNe and AGB stars, grain accretion in molecular clouds, destruction in SNe shocks, sputtering in the hot phase, and the shattering and coagulation of grains. Additionally, we updated the original model disc instability recipe to account for the gaseous disc contribution to the overall disc stability and to allow for star formation and SMBH growth when the instability criterion is met.

This new prescription for disc instability significantly impacts galaxy evolution. Firstly, it enhances the efficiency of stellar bulge growth, resulting in a better match with the observed number of local bulge-dominated galaxies. Secondly, it promotes SMBH growth, which indirectly promotes quenching according to the radio-mode feedback scheme used in the SAM. Key quantities predicted by our model, such as the local SMF, HIMF, cosmic SFRD, and the local BH-bulge mass relation, show good agreement with observations. Additionally,

¹⁰To take into account the contribution of CGM observations, we perform a linear fit extrapolated down to $z = 0$. We have no reasons to assume something more complex than this.

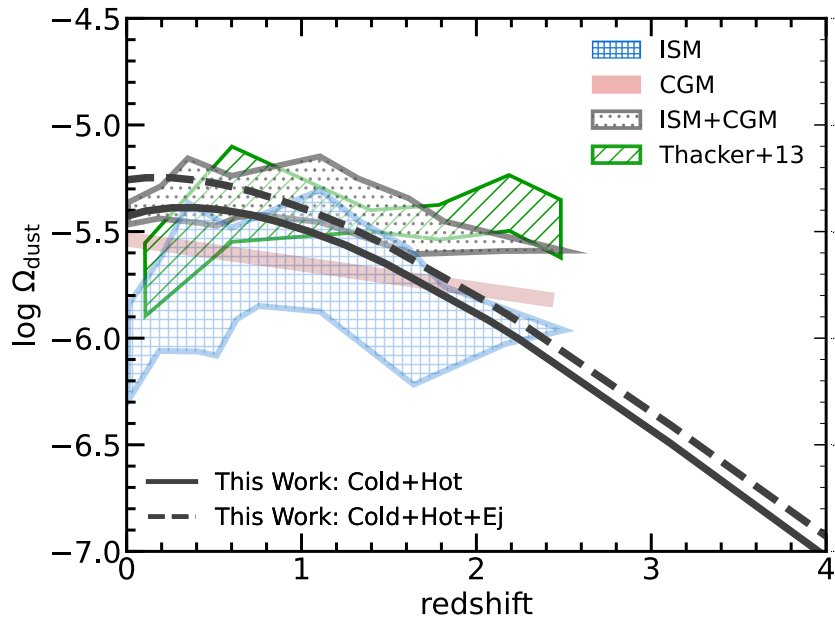


FIGURE 5.19: Cosmic evolution of the total dust budget (Cold+Hot, black solid line, and Cold+Hot+Ej, black dashed line) as predicted by our fiducial model. Shaded and hatched regions correspond to different sets of observations. ISM dust (blue hatched region) refers to the compilation of observations shown in Section 5.5.1. CGM dust (red shaded region) is obtained by performing a linear fit, extrapolated down to $z = 0$, of [Ménard et al. \(2010\)](#) and [Ménard & Fukugita \(2012\)](#) data (Section 5.5.2). Summing the above components (ISM+CGM) we obtain an estimate of the total dust content (gray hatched region). Results obtained by [Thacker et al. \(2013\)](#) are shown as a green hatched region.

the H_2 mass function (H2MF), which was previously slightly overestimated, now aligns well with the observed one.

The enhanced SMBH growth also (indirectly) influences the dust properties of our simulated galaxies. While it has only a modest effect on the DMF at $z > 0$, it significantly improves the match with observations by suppressing the high mass end of the local DMF. Additionally, several scaling relations involving dust, such as $M_{\text{dust}} - M_{\text{stars}}$ and $\text{DTG} - Z$, show good agreement with observations at $0 < z \lesssim 2.5$. The reproduced median small-to-large grains mass ratio at $z = 0$ also aligns well with observations. However, our model tends to overproduce the mass of small grains in galaxies with large M_{stars} (and ISM metallicity Z), indicating that an improved treatment of shattering and coagulation processes may be necessary.

Our model provides insights into the behavior of the cosmic dust density, particularly the galactic component, which is the primary focus of this Chapter. We successfully reproduce the observed evolution of the galactic cosmic dust density, a challenging task for cosmological galaxy evolution models. Specifically, incorporating the new treatment of disc instabilities results in a more pronounced decrease in the amount of dust in galaxies from $z \sim 1$ to $z = 0$. Among the processes contributing to the increase of galactic dust, accretion in molecular clouds is dominant. Regarding the processes responsible for the destruction or ejection of galactic dust – astration, destruction in SNe shocks, and ejection in winds – all play significant roles. In the fiducial model, their contributions to the total destruction rate of dust in cold gas at $z = 0$ are approximately 45%, 35%, and 20%, respectively. Notably, Ω_{dust} only slightly increases when SNe shock destruction is turned off, as the metals returned to the gas phase are rapidly re-incorporated into grains via grain growth. Conversely, turning off astration or dust ejection from cold gas results in a factor of $\sim 2 - 3$ increase in Ω_{dust} .

The amount of extra-galactic dust in our model continuously grows with time. It broadly reproduces the few available observations but with a steeper redshift evolution, especially when considering both hot gas and the ejected reservoir as CGM. This achievement has been made possible by adopting a sputtering efficiency which is a factor of 10 lower than the canonical one. This result confirms the claim of hydrodynamic cosmological simulations (Gjergo et al. 2018; Vogelsberger et al. 2019). The total cosmic dust budget also grows with time, and we argue that more observations of extra-galactic dust, especially at $z \sim 0$, are needed to constrain this quantity better.

The main conclusion of the work presented in this Chapter is that the observed decrease of the galactic dust budget at $z \lesssim 1$ may be reproduced assuming canonical prescriptions for dust production and evolution. This drop is enhanced by the new treatment of disc instabilities and SMBH growth, which promotes the suppression of highly star forming, dust-rich galaxies at $z = 0$, providing a better match of the observed local galactic dust abundance. However, although we presented a reasonable model of SMBH growth during disc instabilities, we also speculate that a comparable result could be obtained with different prescriptions. Indeed, many processes may affect the gas content of these galaxies. For instance, SMBH feedback may cause AGN-driven outflows, while in the present model it only brakes gas cooling.

6

Star Formation and Dust in the Cosmic Web

Galaxy evolution is shaped not only by the physical processes occurring *within* galaxies, but also by the external interactions with the surrounding environment. It is well established that galaxy local environment ($\lesssim 5$ Mpc) strongly affects their star formation activity, colors and morphology (e.g. Dressler, 1980). These works show that galaxies tend to be less star forming, redder and more elliptical as local density increases. On the other hand, galaxies define a large scale cosmic web structure, ranging from vast low-density regions known as cosmic voids to higher-density regions such as walls, filaments, groups, and galaxy clusters. This has been demonstrated by extensive redshift galaxy surveys, and reproduced by cosmological simulations. The latter helped to understand how the cosmic web results from the gravity-driven evolution of primordial density perturbations. As a result, galaxies and their local environments are embedded in different large-scale environments ($\gtrsim 10 - 100$ Mpc) of the cosmic web. However, the role of such environments on galaxy formation and evolution remains a matter of debate (e.g. Alfaro et al., 2022; Rodríguez-Medrano et al., 2023; Wang et al., 2023).

In this Chapter, we¹ study the dependence on the large-scale environment of the star formation and, for the first time, the dust content of local galaxies. We use a galaxy catalog obtained from the SAM discussed in this Thesis (Sections 2.3 and 5.2), and different methods are adopted to identify cosmic environments, namely voids, walls, filaments, and nodes. Adopting multiple methods to define environments enhances the reliability of our results and mitigates the inherent arbitrariness in defining large-scale structures.

Our results have been compared with observations. We use the Sloan Sky Digital Survey (SDSS-DR16) for environmental classification, stellar mass, and star formation rates. At the same time, for a subset of galaxies, we utilised dust mass measurements from the GAMA and *H-ATLAS* surveys. Our *qualitative* comparison yields highly encouraging results, highlighting the significance of the in situ supermassive black hole (SMBH) growth mechanism, specifically secular accretion during disc instabilities (DIs) in our case. This work underscores the importance of investigating galaxy evolution in diverse environments as a possible way to assess the relative significance of in situ and ex situ processes.

The chapter is organised as follows. Section 6.1 recaps some results from literature concerning galaxy properties across the cosmic web from both simulations and observations. In Sections 6.2 and 6.3 we present the simulated and observed galaxy sample adopted here, as well as the techniques adopted to identify cosmic web environments. Section 6.4 discusses the properties of galaxies in different environments as predicted by the theoretical model,

¹This Chapter is based on a published work done in collaboration with C. Ragone-Figueroa, P. López, H. J. Martínez, A. N. Ruiz, L. Ceccarelli, V. Coenda, F. Rodríguez, G. L. Granato, A. Lapi, and R. van de Weygaert (Parente et al., 2024a).

while Section 6.5 compares these results with observations. Finally, results are summarised and discussed in Section 6.6.

CONTENTS

| | |
|--|-----|
| 6.1 Galaxies in the Cosmic Web: Observations and Models so far | 122 |
| 6.2 The simulated and observed samples | 123 |
| 6.3 Identifying Cosmic Web Environments | 124 |
| 6.4 Properties of galaxies across cosmic environments | 126 |
| 6.5 Comparison with observations | 136 |
| 6.6 Summary and Conclusions | 141 |

6.1 Galaxies in the Cosmic Web: Observations and Models so far

Both observations and theoretical studies indicate that different large-scale regions of the Universe host distinct galaxy populations. The densest regions of the cosmic web are nodes and filaments. The most massive nodes host galaxy clusters, which represent the largest entities in the Universe that exist in a state of quasi-virial equilibrium. They feature a deep gravitational potential well permeated by an intra-cluster medium (ICM) of hot ionized gas. In this dense and possibly hostile environment, multiple mechanisms influence galaxy evolution. Some of them, such as ram pressure stripping, strangulation and tidal stripping, trigger gas depletion, leading to the quenching of star formation (see e.g. Abadi et al. 1999; Vijayaraghavan & Ricker 2015; Steinhauser et al. 2016; Peng et al. 2015; Gnedin 2003). Due to these processes and frequent interactions, clusters of galaxies host galaxies, often characterised by red colours and elliptical morphologies (e.g. Dressler, 1980; Whitmore et al., 1993; Domínguez et al., 2001; Bamford et al., 2009; Paulino-Afonso et al., 2019).

Nodes are connected by filaments, elongated structures which have undergone gravitational collapse along two principal axes. They represent a kind of *bridges* along which matter flows to accrete into nodes. Filaments are the predominant visual features within the cosmic web and host galaxies, which tend to exhibit a larger mass, a redder colour, and earlier-type morphologies compared to their counterparts in less dense environments (Chen et al., 2017; Kuutma et al., 2017; Laigle et al., 2018; Kraljic et al., 2018).

In contrast to high-density regions, large voids represent the extremely low-density environment characterized by reduced galaxy mergers and interactions compared to the field or groups. Cosmic voids represent a unique and pristine environment where galaxies are unaffected by the transformation processes typical of over-dense galaxy systems, like clusters and groups. Thus, they allow us to study the evolution of the galaxy as a result of nature alone, without nurture. Numerous studies have focused on galaxies in cosmic voids and found that they appear to have significantly different properties than field galaxies. The luminosity function of galaxies in voids (e.g. Hoyle et al. 2005) shows a fainter characteristic magnitude. However, the relative importance of faint galaxies is similar to that found in the field. The spectroscopic and photometric properties of void galaxies have also been studied in detail (Rojas et al., 2005; Hoyle et al., 2005, 2012; Kreckel et al., 2012). These results indicate that galaxies inside voids have higher star formation rates and bluer colours than galaxies in denser regions and are still forming stars at a rate relatively closer to the past one. Statistical studies using observational data report that void galaxies are smaller, bluer, later-type morphology and more star forming than those in average density environment (Grogin & Geller, 2000; Rojas et al., 2004; Hoyle et al., 2005; Patiri et al., 2006; Park et al., 2007; Wegner & Grogin, 2008; Kreckel et al., 2011; Liu et al., 2015; Tavasoli et al., 2015; Moorman et al., 2016; Beygu

et al., 2017; Ceccarelli et al., 2021; Jian et al., 2022). Finally, we mention the relevant result recently presented by Domínguez-Gómez et al. (2023), within the context of the CAVITY project. The authors of the latter work performed a spectral analysis on a sample of nearby galaxies in voids, filaments and walls, and clusters. They find a clear correlation between the density of the large-scale environment and the star formation history (SFH), namely galaxies in less dense environments feature a slower SFH, that is, void galaxies assemble their stellar mass slower.

On the theoretical side, both hydrodynamic simulations and SAMs have been used to shed light on the influence of the large-scale environment on galaxy evolution. Kreckel et al. (2011) identified higher star formation rates and younger stellar ages in void galaxies through their hydrodynamic simulation. Rieder et al. (2013) studied the formation of (sub)structures in the halo distribution in voids, within the context of the COSMOGRID simulation. Habouzit et al. (2020) employed the Horizon-AGN simulation (Dubois et al., 2014), coupled to the VIDE void finder (Sutter et al., 2015), in order to investigate the black hole population within cosmic voids. They reported no significant variations in black hole growth in voids compared to more dense environments. Rosas-Guevara et al. (2022) studied central galaxies located within and near voids using the EAGLE simulation (Schaye et al., 2015) and the spherical voids catalog by Paillas et al. (2017). They analysed in detail the star formation, metallicity, morphology, and assembly history of galaxies as a function of their stellar mass and environment. Alfaro et al. (2020, 2021) studied the Halo Occupation Distribution (HOD) in cosmic voids and Future Virialized Structures (FVS). Making use of the semi-analytic catalog MDPL2-SAG (Knebe et al., 2018; Cora et al., 2018) and the hydrodynamic simulation TNG300 (Pillepich et al., 2018), they found a lower(higher) than average HOD and formation redshift in voids. Finally, Jaber et al. (2023) exploited the SAGE SAM (Croton et al., 2016) and the Spine-Web algorithm (Aragón-Calvo et al., 2010) to study the large-scale dependence of the metallicity and stellar-to-halo mass ratio. Their results indicate the presence of a threshold mass (respectively, $M_{\text{halo}} \approx 10^{12} M_{\odot}/h$ and $M_{\text{stars}} \approx 10^{10} M_{\odot}/h$) below which the stellar-to-halo ratio and metallicity are enhanced in dense environments.

Despite the substantial achievements of these studies, we still need a complete understanding of how galaxy properties correlate with the large-scale environment. The distinct underlying physical models within different simulations and the lack of a single clear definition for large-scale environments hinder a direct comparison of results. Furthermore, such complexities make it challenging to establish the relative impact of different physical mechanisms on galaxy evolution in distinct environments.

6.2 The simulated and observed samples

6.2.1 The SAM catalog

The galaxies catalog adopted for this work to study large-scale dependencies of galaxy properties have been obtained exploiting the SAM discussed in this Thesis. This is an updated version of the public L-GALAXIES SAM (Henriques et al., 2020) which includes a state-of-the-art dust model and an updated treatment of disc instabilities. I refer to Sections 2.3 (general features), 3.4 (dust model), and 5.2 (disc instability) for an extensive description of the model. The catalog here adopted has been obtained by running the SAM on the MILLENNIUM merger trees (Springel et al. 2005b, box size 500Mpc/h, adopting a Planck Collaboration et al. (2016) cosmology ($h = 0.673$, $\Omega_{\text{m}} = 0.315$, $\Omega_{\text{b}} = 0.0487$, $\sigma_8 = 0.829$) and a Chabrier (2003) IMF. For this analysis, we consider galaxies with a stellar mass content

of at least $\log(M_{\text{stars}}/M_{\odot}) \geq 9$, which approximately corresponds to the resolution limit of the underlying DM simulation (e.g. Guo et al., 2011).

6.2.2 Observational data

We use different data sets to test our model predictions on the star formation and dust content of galaxies in various environments. We use the SDSS Data Release DR16 (Ahumada et al., 2020) to identify cosmic environments. We use galaxies with r -band apparent magnitudes $r < 17.77$ (completeness limit) and in the redshift range $0.02 < z < 0.1$. We take stellar masses and star formation rates from the MPA-JHU catalog (Kauffmann et al., 2003).

As for dust masses, we exploit the results presented in Beeston et al. (2018), who studied the local ($z < 0.1$) dust mass function for galaxies in the GAMA/H-ATLAS surveys. Specifically, the physical properties of these galaxies (including dust mass) were obtained by Driver et al. (2018) using a SED fitting procedure.

6.3 Identifying Cosmic Web Environments

In this Chapter different methods are employed to identify cosmic environments within the simulated and observed large-scale structures. Environments are categorized in two fundamental ways: one involves employing a single and homogeneous method, NEXUS+, to segment the cosmic web into voids, walls, filaments and nodes. The other approach, which will be often dubbed as R19+T23+FOF, utilizes multiple independent methods for identifying specific environments (voids and walls, filaments, and groups). The former is exclusively applied to the simulation, while the latter is employed in both the observed and simulated galaxy catalogs. It is important to stress that no tuning of their parameters has been made to match environments extracted from NEXUS+ to those extracted with the R19+T23+FOF approach. As can be appreciated in Figure 6.1, there are various differences between these two approaches, the most important one being the number of galaxies detected as belonging to a given environment. While NEXUS+ associates *every* galaxy in our simulation to a given environment, this is not true for the R19+T23+FOF method. However, although there is a discrete visual match between the environments detected by the two approaches, we stress that the aim of our study is not to compare the performances of different identification algorithms. Instead, our focus is on examining the consistency and reliability of our results concerning the influence of the environment on galaxy properties, regardless of the method used to identify the different environments.

In the following sections, we introduce each specific environment we focus on and a comprehensive overview of each identification method adopted.

6.3.1 Cosmic web segmentation: NEXUS+

For the segmentation of the simulated cosmic web into its distinct structural environments we use the Multiscale Morphology Filter (MMF)/NEXUS pipeline, specifically its NEXUS+ version (Cautun et al., 2013; Cautun et al., 2014). It is the highest dynamic range version of the library of routines for pattern classification based on the MMF/NEXUS formalism (Aragón-Calvo et al., 2007, 2010; Cautun et al., 2013; Cautun et al., 2014; Aragon-Calvo et al., 2014, see also Libeskind et al. 2018 for a short review). This formalism represents a scale adaptive framework that classifies the matter distribution on the basis of local spatial variations in either the density field, velocity field or gravity field. Subsequently, a set of morphological filters is used to classify the spatial matter distribution into three basic components, the clusters, filaments and walls that constitute the cosmic web. The remaining

volume elements are classified as part of voids. The end product of the pipeline is a map in which for each location in the analyzed volume the morphological identity is specified.

In practice, NEXUS+ takes as input a regularly sampled density field, which we obtain by projecting the halo distribution to a regular grid using the cloud-in-cell interpolation scheme. In a first step, the input field is Gaussian smoothed using a Log-density filter that is applied over a set of scales from 1 to $11h^{-1}\text{Mpc}$. It results in a map of 1024^3 cells, corresponding to a cellsize of $0.472h^{-1}\text{Mpc}$. Then, for each smoothing scale, the resulting density is used to calculate the Hessian matrix and its corresponding eigenvalues, whose values and signs determine the environment response at each location, i.e. grid cell. In the last step, NEXUS+ combines the environmental signature of all the scales to obtain a scale-independent value. In this work, roughly 79.3% of the total volume of the box corresponds to cells located in voids, 14.5% is classified as belonging to walls, 6.0% as located in filaments and only 0.2% correspond to nodes. Assigning to each halo the environment of its hosting cell, we find that, out of the total DM mass within the box, 9.5% resides in voids, 16.9% in walls, 34.5% in filaments and 39.1% in the cluster nodes of the cosmic web.

6.3.2 Spherical voids identification

We use the spherical void finder algorithm presented in Ruiz et al. (2015, 2019) as an alternative method to construct our voids catalog. This method aims at identifying the largest and non-overlapping spherical regions that satisfy that the number density of tracers inside them is less than 10 percent of the mean:

$$\Delta(r_{\text{void}}) \leq -0.9, \quad (6.1)$$

where $\Delta(r)$ is the integrated density contrast at scale r and r_{void} is the void radius.

We use the DM halos as structure tracers when applying this algorithm to our SAM galaxies. We adopt $M_{\text{halo}} \geq 10^{12}h^{-1}M_{\odot}$ as halo mass cut, obtaining 2729 voids. After constructing the voids catalog, we define void galaxies as those residing within $r/r_{\text{void}} \leq 1$ and void wall galaxies as those located immediately outside the voids with $1 < r/r_{\text{void}} \leq 1.2$. These void galaxies are predominantly found in NEXUS+ voids ($\sim 64\%$), while galaxies in the voids shells are more homogeneously distributed among NEXUS+ voids, walls and filaments (respectively, $\sim 31\%$, 34% , 32%).

The same algorithm is adopted to identify voids on top of the observational catalog. Details about the algorithm application to observational samples are provided in Ruiz et al. (2019). Specifically, in this work the void identification is the same as in Rodríguez-Medrano et al. (2023, see their Section 2.1). Voids are identified in a volume complete sample with limiting redshift $z = 0.1$ and maximum absolute magnitude in the r band $M_r - 5\log h = -20$ extracted from the main SDSS region. In our analysis, we have discarded voids close to the edge of the catalog, namely, void centers at distances smaller than $1.8r_{\text{void}}$. Starting from this voids catalog we then define void ($r/r_{\text{void}} \leq 1$) and void wall galaxies ($1 < r/r_{\text{void}} \leq 1.2$).

6.3.3 Filaments and groups identification

As for the more dense environments, we also identify galaxy groups and filaments with an alternative approach. Galaxy groups are identified with FOF haloes in our SAM catalog. As for observed galaxies, we utilize the groups catalog presented by Rodríguez et al. (2022), which is derived from the SDSS-DR16 using the algorithm introduced in Rodríguez & Merchán (2020). This method initially applies the FOF algorithm to identify galaxy systems that are gravitationally bound and have at least one bright galaxy with an r-band absolute magnitude brighter than -19.5 . Subsequently, a halo-based algorithm (Yang et al.,

| | Number of objects [10^5] | |
|------------------------|------------------------------|-------------|
| | NEXUS+ | R19+T23+FOF |
| Voids | 33.6 | 9.3 |
| Walls | 38.4 | 19.0 |
| Filaments | 49.9 | 8.6 |
| Nodes / Massive groups | 30.1 | 11.0 |

TABLE 6.1: Number of galaxies in our simulated catalog categorized based on environmental classification via the two approaches employed in this work, namely NEXUS+ and R19+T23+FOF (Section 6.3).

2005, 2007) is applied. A three-dimensional density contrast is calculated in redshift space using a characteristic luminosity calculated with the potential FOF galaxy members. The estimation procedure considers the incompleteness caused by the observational catalog limiting magnitude. Next, by abundance matching on luminosity, the mass of each group is assigned. Assuming that galaxies populate the DM halos following a Navarro, Frenk & White (1997) profile and using the assigned mass, the three-dimensional density contrast is calculated to associate galaxies to the groups. With this last assignment of members, the procedure recalculates the characteristic luminosity and iterates until it converges. This algorithm showed excellent results in purity and completeness (Rodríguez & Merchán, 2020).

Once galaxy groups are identified, they are used to build a catalog of filaments in the large scale structure. They are cylinders linking groups of galaxies. Our approach is similar to the filament identification carried out by Taverna et al. (2023), which, in turn, is based on the original algorithm by Martínez et al. (2016). Starting from the group sample, we search for all pairs of groups more massive than a selected mass cut-off M_{\min} that are separated (in redshift space in the case of the observations) by a comoving distance smaller than a given threshold Δ_{\max} . For each pair of groups thus selected, we compute the numerical overdensity of galaxies in a cylinder of radius R that extends between the two groups. The overdensity in this volume is obtained by the ratio between the number of galaxies that lie in the cylinder, and the number of points within the same cylinder from an unclustered homogeneous distribution of points. This homogeneous distribution of points mimics the selection function of galaxies while being 100 times denser in order to reduce shot noise in the overdensity computation. We require the numerical overdensity of galaxies in the cylinder to be greater than unity in order to consider a pair of groups are linked by a filament. Galaxies in these cylindrical regions are considered to be galaxies in filaments.

In this work we use $M_{\min} = 10^{13.5} M_{\odot}$, $\Delta_{\max} = 20$ Mpc, which is the correlation length of groups more massive than M_{\min} according to Zandivarez et al. (2003), and $R = 2.2$ Mpc (see Taverna et al. 2023). Galaxies identified in cylindrical filaments belong mainly to NEXUS+ filaments ($\sim 55\%$), walls ($\sim 25\%$), and nodes ($\sim 19\%$), while galaxies in massive groups almost uniquely belong to NEXUS+ nodes ($\sim 95\%$). For the SDSS-DR16 groups and galaxies, our unclustered homogeneous distribution of points mimics the selection function of SDSS-DR16 galaxies regarding angular coverage and redshift distribution.

6.4 Properties of galaxies across cosmic environments

This Section examines various physical properties of our simulated galaxies in different environments. First, we look at the stellar mass distribution and the central/satellite galaxies relative fraction in each environment. Then we look at the star formation and dust content,

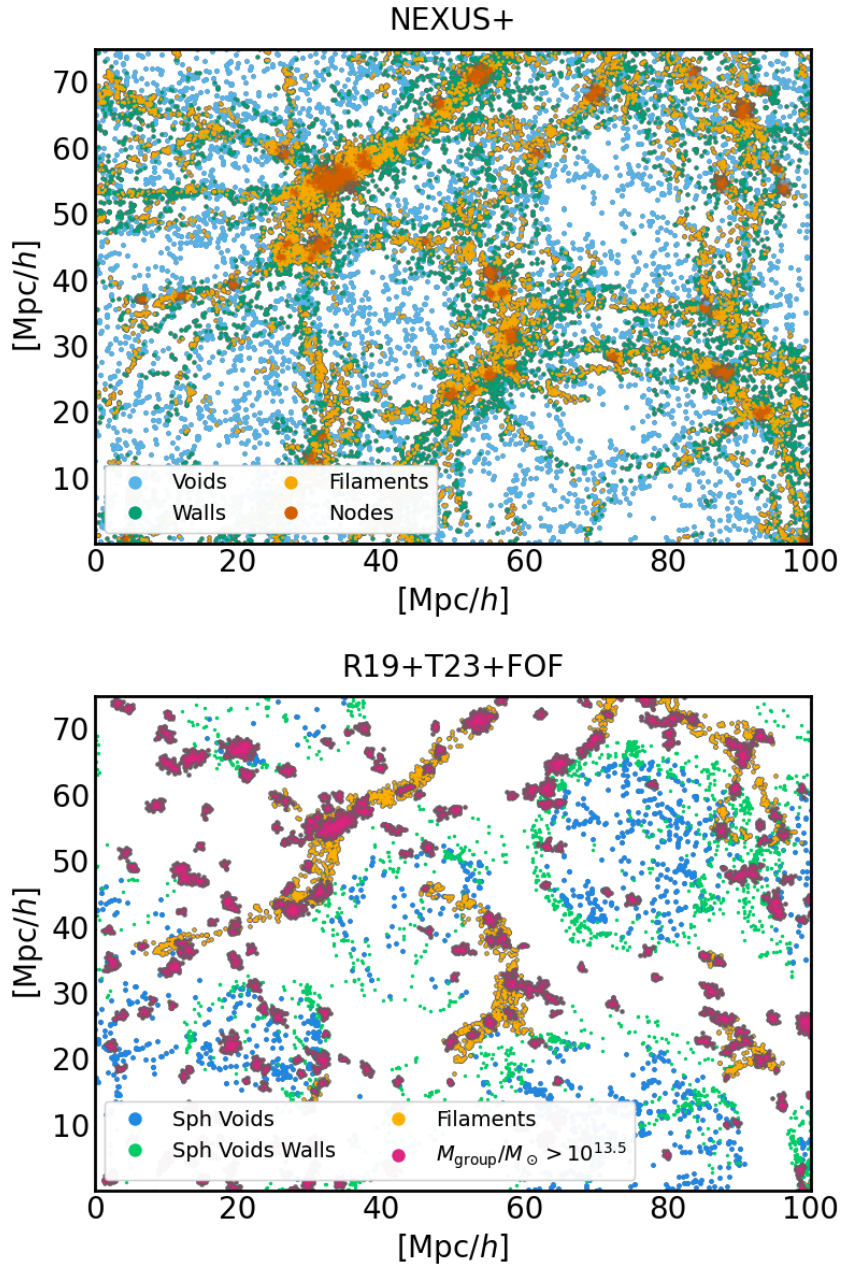


FIGURE 6.1: A $25 \text{ Mpc}/h$ slice of our simulation box showing the outcome of the environment identification processes. Each point represents a DM halo, and is color-coded according to the assigned environment. The left panel shows the results obtained by NEXUS+, which categorizes *each* DM halo of the simulation as belonging to a void, wall, filament, or node. On the right panel we show the combination of the specific identifiers for distinct environments (R19+T23+FOF), i.e. spherical voids and their walls, cylindrical filaments, and massive groups ($M_{\text{group}} > 10^{13.5} M_{\odot}$). It is important to note that while NEXUS+ assigns every DM halo to an environment, this is not necessarily the case for the R19+T23+FOF approach, where a galaxy might not be classified as belonging to any specific environment.

as well as dust properties such as the DTG ratio, the size and chemical composition of dust grains.

In the following analysis, we show the results for the NEXUS+ environments (voids,

walls, filaments, and nodes), as well as for the other environments definitions adopted in this work, namely spherical voids and their associated walls, cylindrical filaments and massive groups ($M_{\text{group}} > 10^{13.5} M_{\odot}$). A visual representation of the environments identification in our simulated box can be appreciated in Figure 6.1 for both the aforementioned methods, and we report the number of objects identified in each environment in Table 6.1.

6.4.1 Environments Stellar Mass Function and satellites fraction

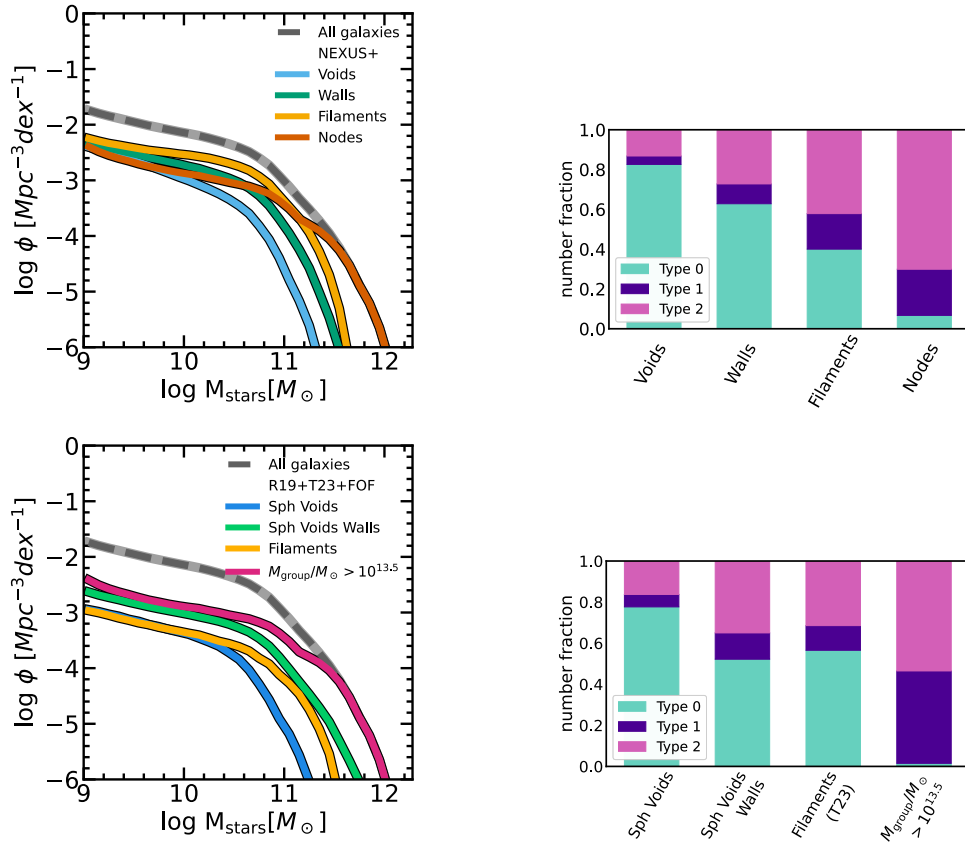


FIGURE 6.2: Stellar Mass Function (*left panels*) and number fraction of simulated galaxies of type 0 (centrals, green), type 1 (satellites, purple), and type 2 (orphans, pink) (*right panels*) at $z = 0.0$ for different environments. The *top panels* shows the predictions for environments as identified by NEXUS+ (voids, walls, filaments and nodes), while the *bottom panels* report the other environments definitions adopted in this work, namely spherical voids and their walls, cylindrical filaments and massive groups (R19+T23+FOF). The SMF of the whole sample of galaxies is also shown as a dashed gray line for reference.

Here we present the SMF and the number abundance of type 0, 1, and 2 galaxies (respectively centrals, satellites and orphans² in the L-GALAXIES framework) for different cosmic environments at $z = 0$. We report the cosmic environments we focus on in the paper: voids, walls, filaments and nodes as identified by NEXUS+, as well as spherical voids and their associated walls, cylindrical filaments and massive groups (R19+T23+FOF). Results are shown in Figure 6.2. We also perform a fit of the SMFs with a Schechter function (Schechter, 1976):

²Orphan galaxies are objects that have already lost their DM halo, but still have a baryonic component (see Section 2.3.7).

| Environment | $\log M_*/M_\odot$ | Environment | $\log M_*/M_\odot$ |
|-------------|--------------------|-----------------|--------------------|
| Voids | 10.66 | Sph Voids | 10.59 |
| Walls | 10.84 | Sph Voids Walls | 11.02 |
| Filaments | 10.92 | Filaments (T23) | 11.02 |
| Nodes | 11.64 | Massive groups | 11.67 |

TABLE 6.2: Characteristic mass, derived with a Schechter fit, for the SMFs of the different environments discussed in the main text. SMFs are shown in Figure 6.2.

$$\phi(m)dm = \ln(10)\phi^*10^{(m-m^*)(1+\alpha)}\exp(-10^{m-m^*})dm, \quad (6.2)$$

where $m = \log M_{\text{stars}}/M_\odot$ and $m^* = \log M_*/M_\odot$. The latter is a parameter often referred to as *characteristic mass*. We report this parameter of the SMFs of different environments in Table 6.2.

As for the NEXUS+ SMF, the *denser* is the environment, the larger is the number of massive galaxies (the same is observed for the HMF; see e.g. Figure 17 of Cautun et al. 2013). The characteristic mass M_* of the SMF as well increases with the density of the environment (Table 6.2). The Nodes SMF exhibits a feature at $\log M_{\text{stars}}/M_\odot \simeq 11.5$. This is due to one of the parameters required by NEXUS+, that is the minimum mass for a cell to be classified as a node ($M_{\text{vir}} \geq 2 \cdot 10^{14} M_\odot$ here, about $M_{\text{stars}} \gtrsim 2.5 \cdot 10^{11} M_\odot$). For this reason, every cell containing objects which meet this criterion will automatically be classified as a node.

Also, the relative fraction of central, satellites and orphan galaxies is sensitive to the environment (top right panel of Figure 6.2). The denser is the environment, the smaller is the number of central (type 0) galaxies. More dense environments, particularly nodes, typically host more groups and clusters of galaxies, and this explains the progressively larger number of satellite (and orphan) galaxies.

A similar pattern is observed when comparing R19+T23+FOF environments (bottom panels). We note that in this case walls galaxies are typically more massive than filaments, and also host a lower fraction of central (type 0) galaxies.

6.4.2 Star Formation and Dust

Since the environment selection introduces a mass bias, namely, more massive galaxies are associated with more clustered environments, in this Section we analyze galaxy properties in different environments at fixed stellar mass.

Figure 6.3 reports the sSFR and dust mass as a function of stellar mass. In the range $9 \leq \log M_{\text{stars}}/M_\odot \lesssim 10.8$ we observe a clear trend with the environment, regardless of the definitions adopted. Namely, at fixed stellar mass, the *less dense* is the environment, the more star forming and dust-rich are the galaxies. Above this stellar mass value, we observe no clear trend with the environment for the sSFR. As for the dust mass, differences among environments are strongly reduced. This result suggests that the environmental dependence of dust and star formation properties is suppressed in galaxies above the stellar mass threshold. We will discuss this point at length in the following.

We note that our finding of higher star formation in voids is in keeping with some observational results which pointed out that void galaxies are typically more SF and gas-rich than non-void ones (e.g. Rojas et al. 2005; von Benda-Beckmann & Müller 2008; Kreckel et al. 2014; Beygu et al. 2016; Moorman et al. 2016; Florez et al. 2021). The same has also

been found in numerical simulations (e.g. Cen 2011; but see also Rosas-Guevara et al. 2022, who found different environmental trends in different stellar mass regimes). Our findings are also consistent with Martínez et al. (2016) particularly in relation to the sSFR of filament galaxies. These rates are intermediate falling between those observed in groups and those in less dense environments. These authors additionally find indications that variations among environments are less pronounced when considering high mass galaxies.

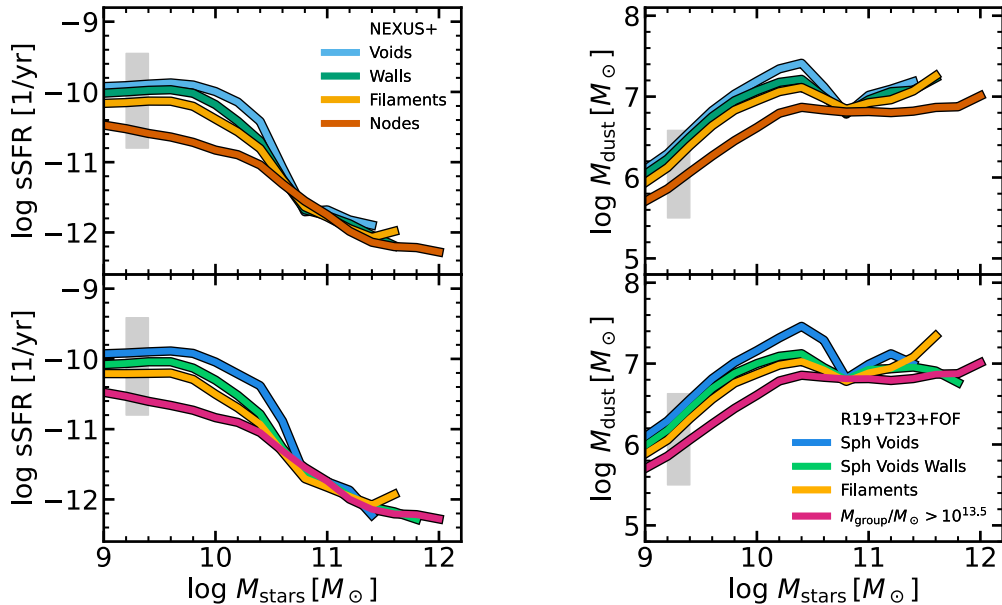


FIGURE 6.3: Specific SFR (*left panel*) and dust mass (*right panel*) as a function of stellar mass for simulated galaxies in different environments. We report the results for NEXUS+ environments (voids, walls, filaments and nodes, *top panels*), as well as for the other environments definitions adopted in this work, namely spherical voids and their walls, cylindrical filaments and massive groups (R19+T23+FOF, *bottom panels*). Solid lines represent median trends, with the typical 16 – 84th percentile dispersion shown as a gray shaded area.

6.4.3 Galaxy evolution across environments

The scenario depicted above, mainly in Section 6.4.2, may be understood if galaxies undergo a *slower* evolutionary process in *less dense* environments. This idea is corroborated by the mass-weighted age of stellar populations, displayed in Figure 6.4, which suggests the existence of a relationship between age and environment for $M_{\text{stars}} \lesssim 10^{10.8} M_{\odot}$. Voids galaxies are the youngest and nodes (or massive groups) galaxies exhibit the oldest ages. Walls and filaments galaxies fall in between, with filament galaxies systematically displaying older ages compared to wall galaxies. We devote this Section to further investigation of this point. In particular, we aim to understand the differences in the evolution of galaxies with equal stellar mass at $z = 0$, but residing in different environments.

We thus inspect the stellar mass³, SFR, and dust mass evolution for galaxies with $M_{\text{stars}}^{z=0}/M_{\odot} \simeq 10^9$, 10^{10} , $10^{10.5}$, and 10^{11} in Figure 6.5. The figures indicate that the *denser* is the environment, the *faster* is the evolution for $M_{\text{stars}}^{z=0} \leq 10^{10.5} M_{\odot}$, in the sense that the SFR peaks at earlier epochs, and consequently the evolution of the stellar mass is more rapid. This

³Normalized to the $z = 0$ value.

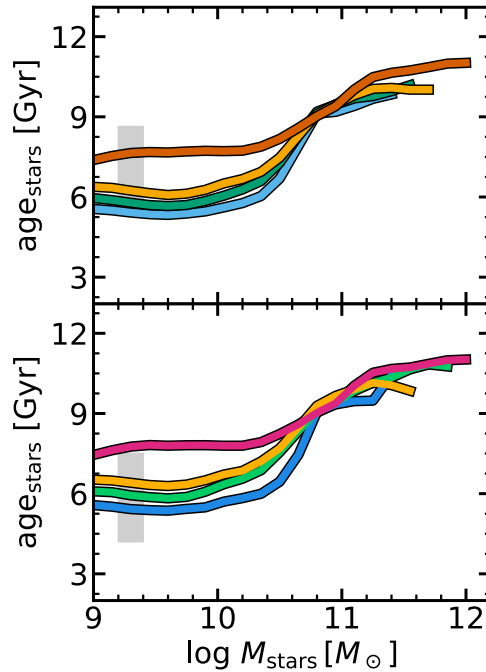


FIGURE 6.4: Mass-weighted stellar populations age as a function of stellar mass for simulated galaxies in different environments, as detailed in Figure 6.3.

holds true irrespective of the chosen environments definition. As for the dust mass evolution, it reaches a maximum more recently than the SFR, suggesting that the time of the maximum dust content of a galaxy does not correspond to the time of the maximum of its star formation activity. We argue that this is due to the fact that the dust budget is determined not only by the production of dust by stars but also by its evolution, and by grains accretion in particular⁴. We also note that the peak of the dust abundance occurs later in lower density environments *and* in lower $M_{\text{stars}}^{z=0}$ objects. This maximum has yet to be reached in voids and wall galaxies of the less massive $M_{\text{stars}}^{z=0}$ bin. This is consistent with the slower evolution of galaxies in lower density environments.

The slower stellar assembly in less dense environments has already been pointed out by other works based on hydrodynamical simulations (Artale et al., 2018; Alfaro et al., 2020; Habouzit et al., 2020; Rosas-Guevara et al., 2022), and recently confirmed through observations by Domínguez-Gómez et al. (2023).

As for the most massive stellar bin under examination, galaxies with $M_{\text{stars}}^{z=0} \simeq 10^{11} M_{\odot}$ show no notable differences across diverse environments. The lack of differences in the evolution of these high-mass galaxies aligns with the findings discussed in Section 6.4.2, which suggest the existence of a certain stellar mass threshold ($\simeq 10^{10.8} M_{\odot}$) above which the influence of the large-scale environments becomes less relevant.

The same conclusions may be drawn from an analysis of t_{70} , the look-back time at which the stellar mass of a given galaxy is 70% of its present day value. In Figure 6.6, t_{70} is shown as a function of stellar mass and for different environments. First, we note that t_{70} tends to increase with stellar mass for voids, walls, filaments and, more weakly, nodes and massive groups. The last is due to the significant impact of old satellite galaxies, mainly dominating

⁴The efficiency of the accretion process is delayed with respect to the dust production by stars also on a cosmic scale, as can be appreciated in Figure 5.15.

the population of these dense environments at $\log M_{\text{stars}}/M_{\odot} \lesssim 10.5$. Secondly, we observe that for $\log M_{\text{stars}}/M_{\odot} \lesssim 10.5 - 11$, at a fixed stellar mass, the time of assembly for the stellar mass is delayed in less dense environments. This delay is reflected in t_{70} , which is typically smaller for galaxies in less dense environments. Above the mentioned mass, there is no clear dependence on the environments, as already pointed out earlier.

Notably, the observational study by Domínguez-Gómez et al. (2023) also revealed minimal changes in the assembly time of high-mass galaxies ($\log M_{\text{stars}}/M_{\odot} \approx 10.5 - 11$) across various environments, contrasting with galaxies of smaller masses ($9 < M_{\text{stars}}/M_{\odot} \lesssim 10.5 - 11$, refer to their Figure 4a and 4d). They hypothesized that the evolution of these high-mass galaxies might be more influenced by local interactions or their massive DM halos than by large-scale environments. In our model, we anticipate that, regardless of galaxy interactions, the in-situ growth of SMBHs in galaxies is crucial for understanding this behavior. Likewise, Domínguez-Gómez et al. (2023) observed similar assembly times for galaxies in their lowest stellar mass bin ($\log M_{\text{stars}}/M_{\odot} < 9$), suggesting a strong impact of the small-scale environment on objects of these masses, which are predominantly satellites. Since our analysis is limited to galaxies with $\log M_{\text{stars}}/M_{\odot} \geq 9$, we cannot determine if this behavior is also present in our model.

6.4.4 The impact of in situ SMBH growth on isolated galaxies evolution

The latter result(s) is quite interesting. It suggests that the environmental dependence of galaxy evolution is important up to some characteristic mass ($\log M_{\text{stars}}/M_{\odot} \approx 10.8$ in our model). Above this *threshold*, galaxies in different large-scale environments and the same stellar mass feature very similar properties.

This outcome is due to the treatment of SMBH growth and feedback, the main channel of massive galaxies quenching in the adopted SAM. More in detail, SMBHs can grow during mergers, by hot gas accretion, and during disc instabilities (see Sections 2.3.6 and 5.2.1). In massive galaxies, the contribution of the latter process⁵ is typically less relevant than mergers in terms of mass. However, this channel is crucial in isolated systems, where (in absence of mergers) it is the only available channel for starting the SMBH growth, which will eventually quench the galaxy. Thus it has a profound impact on the results discussed in this work.

We demonstrate this by comparing the results obtained by our fiducial (FID) SAM and a version in which the SMBH growth in DIs is switched off ($f_{\text{BH,DI}} = 0$; similarly to what has been done in Section 5.5.1). In particular, Figure 6.7 displays the number of mergers experienced up to $z = 0$ and the fraction of stellar mass assembled ex situ (i.e. in mergers) for galaxies in distinct environments for both models. In the $f_{\text{BH,DI}} = 0$ model there are evident differences across environments for $\log M_{\text{stars}}/M_{\odot} \gtrsim 10.8$, namely the denser the environment, the larger the number of mergers experienced at $z = 0$, and consequently the fraction of stellar mass assembled ex situ. However, these differences are not present in the FID model. At first glance, this is quite surprising since we would expect the number of mergers to be independent of the baryonic physics implemented within the model, as it is determined by the adopted DM halos merger tree⁶.

⁵It has been introduced in this Thesis work, while the other two SMBH growth channels are left as in the public L-GALAXIES release (Henriques et al., 2020).

⁶Actually, the number of mergers experienced by a galaxy up to a certain redshift also depends on the time a galaxy need to merge once its associated DM subhalo merged. In the adopted SAM, such a *merging time* is estimated with the dynamical friction timescale (Binney & Tremaine, 1987), as detailed in Section S1.16.1 of the supplementary material of Henriques et al. (2020).

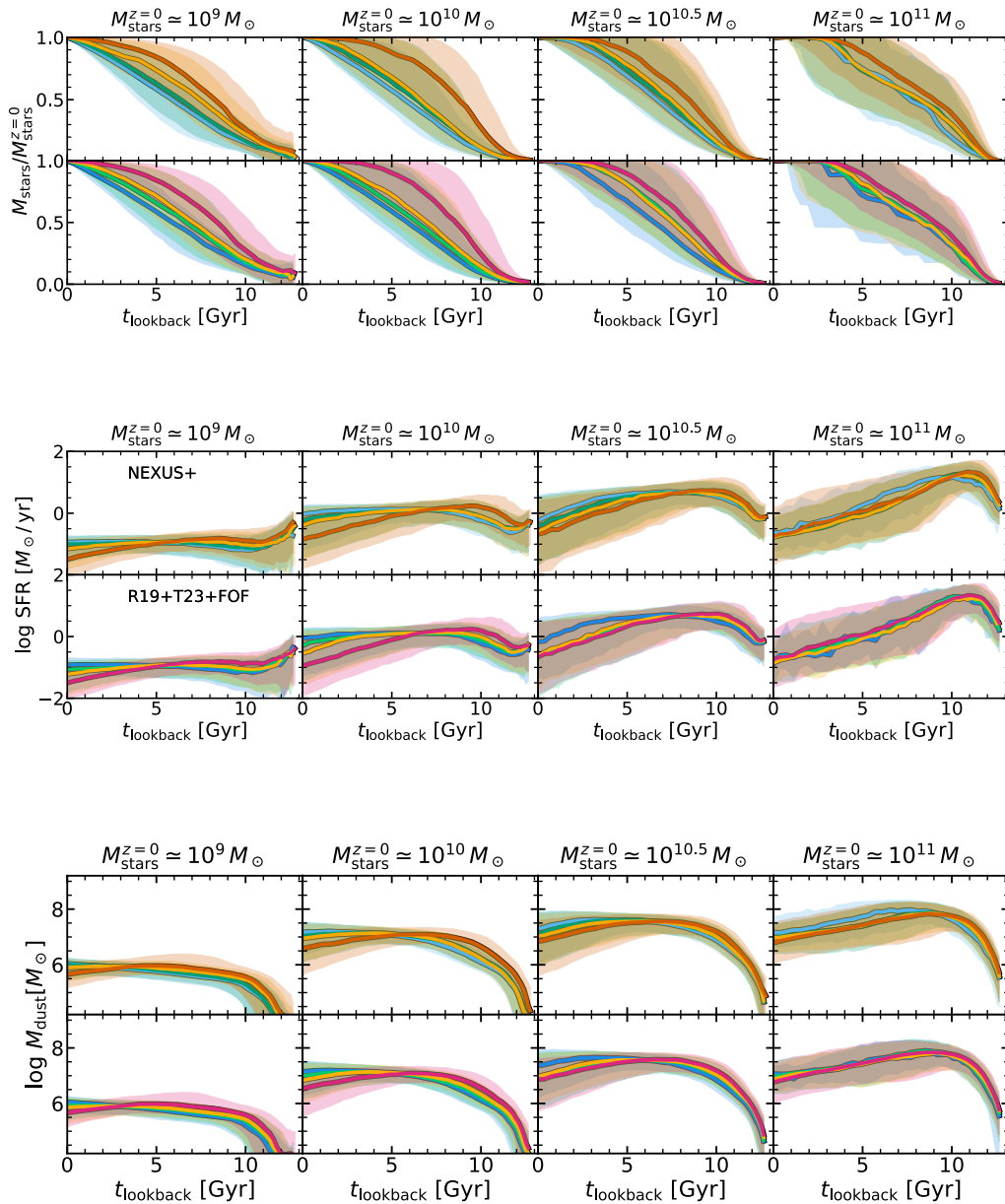


FIGURE 6.5: Stellar mass (*top panels*), SFR (*middle panels*), and dust mass (*bottom panels*) evolution for galaxies with different values of the present-day stellar mass, namely (from left to right) $M_{\text{stars}}^{z=0}/M_{\odot} \approx 10^9$, 10^{10} , $10^{10.5}$, and 10^{11} . For each quantity, we report the results for galaxies residing at $z = 0$ in different NEXUS+ environments (voids, walls, filaments and nodes), as well as for the other environments definitions adopted in this work, namely spherical voids and their walls, cylindrical filaments and massive groups (R19+T23+FOF). Colors are as in previous figures. For each environment, we randomly selected $\sim 10^3$ objects with $M_{\text{stars}}^{z=0}$ in a narrow range (0.1 dex) around the reported value, and traced their evolutionary paths along the merger tree back in time. Solid lines represent median trends, with the 16 – 84th percentile dispersion shown as a shaded area.

The reason why the novel⁷ in situ SMBH growth channel produces such differences may

⁷It is worth clarify that the SMBH growth during DIs is not a novelty in the panorama of SAMs, since it has been adopted by the community for a long time (e.g. Croton et al., 2016; Lacey et al., 2016; Lagos et al., 2018),

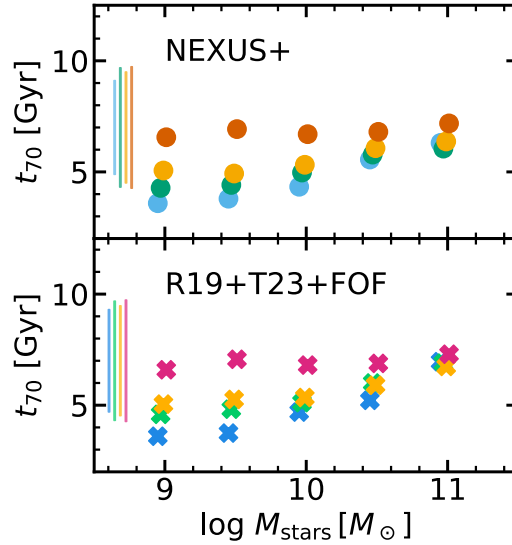


FIGURE 6.6: Assembly time of the stellar mass for galaxies in different environments and different $z = 0$ stellar mass bins. The time is expressed as t_{70} , the look-back time when the galaxy reached the 70% of the present stellar mass. Crosses and circles refer to median values, while the typical 16 – 84th percentile dispersion is reported as lines on the left side of each panel. Colors and environments are as in Figure 6.3.

be understood in the following picture. The DI-driven SMBH growth enhances the quenching of the most massive objects, thus only galaxies that can accumulate a significant mass fraction through mergers are capable of reaching large stellar masses ($\log M_{\text{stars}}/M_{\odot} \gtrsim 10.8$), since the in situ star formation is suppressed by the instability-driven SMBH growth. This effect is particularly pronounced in galaxies located in less dense environments, which generally undergo fewer merger events. This is the reason why also the fraction of stellar mass formed through mergers, i.e. acquired ex situ, is influenced by our DI model (Figure 6.7).

In other words, according to our fiducial SAM, *only galaxies which acquire a substantial stellar mass from mergers can reach large M_{stars} ($\gtrsim 10^{10.8} M_{\odot}$).*

Concluding this Section, it is worth remarking that the adopted DI model significantly modifies the in situ evolution of galaxies⁸, particularly impacting the environmental dependence of certain properties. This is not surprising, considering the prominent role of mergers in shaping galaxy evolution within SAM frameworks. Consequently, we speculate that a thorough (also observational) study of galaxy properties in different cosmic environments could serve as an effective test bench for assessing the relative significance of the in situ and ex situ processes implemented within SAMs. We perform a step in this direction in Section 6.5, where we compare the specific SFR and dust content for the FID and $f_{\text{BH,DI}} = 0$ models across different large-scale environments with observations.

Finally, it should be noted that Jaber et al. (2023), using the SAGE SAM, observed a significant increase in metallicities for galaxies located in the densest environments compared

also in the context of the same L-GALAXIES model (Irodotou et al., 2019; Izquierdo-Villalba et al., 2020). The wording *novel* adopted here has to be intended as *novel with respect to the public release* of the L-GALAXIES SAM (Henriques et al., 2020).

⁸Nonetheless, we note that our model still reproduces many crucial properties of the galaxy population, including the Stellar Mass Function, which is only mildly affected by the DI model (Section 5.3).

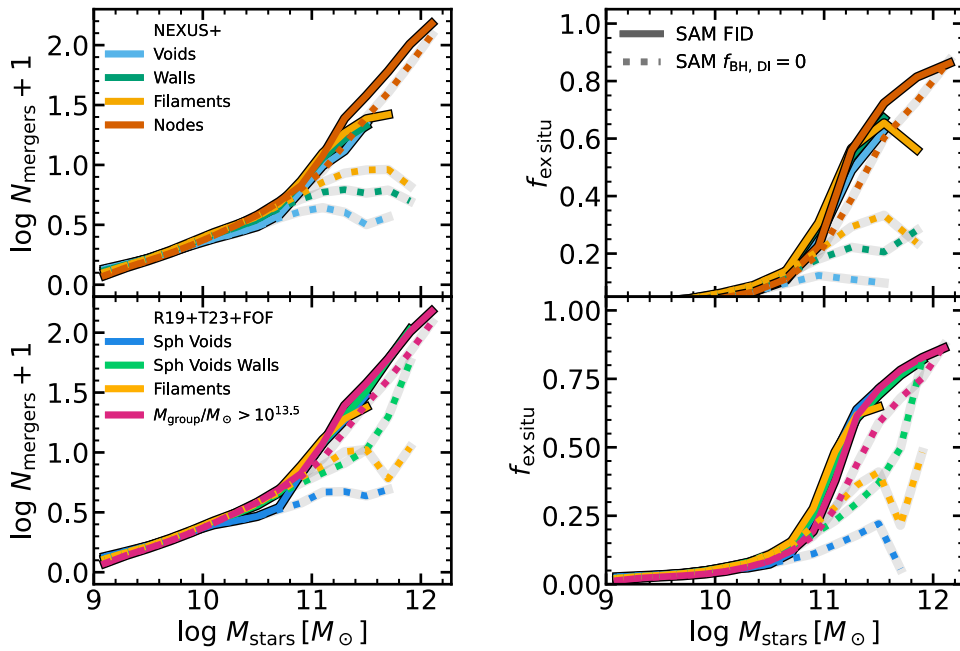


FIGURE 6.7: Mean number of mergers (*left panel*) and ex situ fraction of the total stellar mass (*right panel*) as a function of stellar mass for simulated galaxies. We report the results for galaxies residing at $z = 0$ in different NEXUS+ environments (voids, walls, filaments and nodes, *top panels*), as well as for the other environments definitions adopted in this work, namely spherical voids and their walls, cylindrical filaments and massive groups (R19+T23+FOF, *bottom panels*). Results from both the fiducial (*solid*) and $f_{\text{BH, DI}} = 0$ (*dotted*) SAM are shown.

to the entire sample. However, similar to our findings, the influence of the environment disappears for galaxies with stellar masses exceeding $\approx 10^{10} M_{\odot}/h$. It is notable that their model also utilizes unstable cold gas to fuel the growth of central black holes, although they do not attribute the observed result to this mechanism.

6.4.5 Convergence mass and SMBH growth

Based on the previous discussion, it becomes clear that there is a stellar mass threshold beyond which no noticeable distinctions exist among galaxies in various environments, given a constant stellar mass. In our reference model, this *convergence mass* may exhibit slight variations depending on the property under consideration and the method used to identify the different environments. However, it is approximately $M_{\text{conv}} \approx 10^{10.8} M_{\odot}$ for both the sSFR and dust mass (Figure 6.3). In Section 6.4.4 we have shown that this behaviour is due to the DI-driven SMBH growth channel. This process is regulated by the parameter $f_{\text{BH, DI}}$, representing the fraction of unstable gas that undergoes accretion onto the BH during episodes of DIs ($f_{\text{BH, unst}}$ in Equation 5.4). Here we assess the stability of the *convergence mass* to changes in $f_{\text{BH, DI}}$ when using different environments identifiers: NEXUS+ on one hand; or specific identifiers for distinct environments – spherical voids, cylindrical filaments and massive halos – on the other hand (R19+T23+FOF).

To this aim, we operationally define the *convergence mass* as follows. We calculate the median trends of the $M_{\text{stars}} - \text{sSFR}$ relation⁹ for all the environments, as reported in Figure 6.3. We employ stellar mass bins of 0.1 dex. The *convergence mass* M_{conv} is identified as

⁹A similar approach can be applied to the $M_{\text{stars}} - M_{\text{dust}}$ relation.

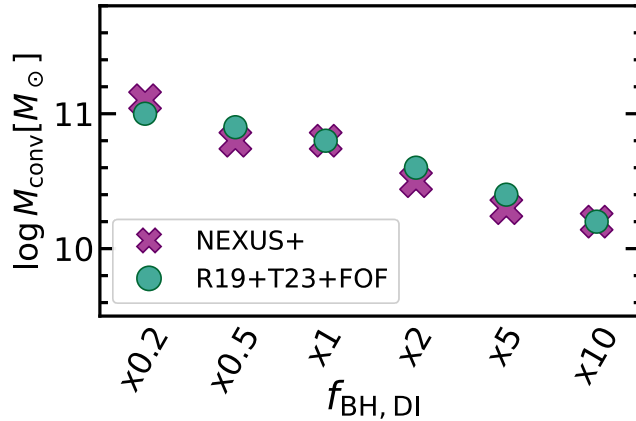


FIGURE 6.8: Convergence mass for different runs where the parameter ruling the DI-driven SMBH growth ($f_{\text{BH,DI}}$) is modified by a constant factor, specifically $f_{\text{BH,DI}} \times 0.2, 0.5, 2, 5,$ and 10 . The convergence mass is the stellar mass above which the $M_{\text{stars}} - \text{sSFR}$ relation show no discernible differences among galaxies belonging to different environments, at fixed stellar mass. We report the results obtained with NEXUS+ environments (*purple crosses*) as well as for the other environments definitions adopted in this work, namely spherical voids and their walls, cylindrical filaments and massive FOF groups (*green circles*, R19+T23+FOF).

the smallest M_{stars} value where the median sSFR for all environments falls within a range of 0.2 dex. We compute M_{conv} for different runs in which we modify only the $f_{\text{BH,DI}}$ parameter by a constant factor¹⁰, specifically $f_{\text{BH,DI}} \times 0.2, 0.5, 2, 5,$ and 10 . The results for the *convergence mass* obtained in these experiments are reported in Figure 6.8.

The general trend suggests that, regardless of the environment classification process, the *convergence mass* decreases as the efficiency of the DI-driven SMBH growth increases. This is because higher values of $f_{\text{BH,DI}}$ lead to more efficient and rapid SMBH growth, enabling these objects and their associated feedback to be relevant in less massive systems. A departure of a factor of 2 from the fiducial $\times 1$ value implies a variation of approximately 0.2 dex in M_{conv} .

It is important to note that the parameters defining $f_{\text{BH,DI}}$ allow our model to reproduce the local SMF and the fractions of quenched galaxies at different masses (Sections 5.3) and were not further adjusted in the present work. Interestingly, as will be seen in Section 6.5, the *convergence mass* also manifests in observed galaxy samples. However, we prefer to use the results in this Section as an experiment to improve the understanding of our model’s physics rather than using it for direct model refinement.

6.5 Comparison with observations

In this Section, we compare observations with our SAM predictions. As for our simulated galaxies, in order to highlight the importance of the in situ, DI-driven, SMBH growth channel, we compare the predictions obtained from our fiducial version of the SAM with the aforementioned scenario where SMBH accretion during DIs is switched off ($f_{\text{BH,DI}} = 0$).

Our goal is to compare the environments identified in the simulated and observed samples as fairly as possible, exploiting the identification methods detailed in Section 6.3. Specifically, here we focus on four different environments, ranging from low to high large-scale density:

¹⁰But maintaining its functional dependence on the halo virial velocity.

| Environment | Algorithm | Criterion | Number of galaxies | |
|----------------|----------------------------|--|--------------------|---------------------------|
| | | | SDSS catalog | GAMA H-ATLAS sample |
| Voids | Ruiz et al. (2015, 2019) | $r/r_{\text{void}} \leq 1$ | 9367 | 95 |
| Walls | Ruiz et al. (2015, 2019) | $1 < r/r_{\text{void}} \leq 1.2$ | 16863 | 138 |
| Filaments | Taverna et al. (2023) | $M_{\text{nodes}} \geq 10^{13.5} M_{\odot}$ | 12556 | 395 |
| Massive groups | Rodríguez & Merchán (2020) | $M_{\text{groups}} \geq 10^{13.5} M_{\odot}$ | 35161 | 380 |

TABLE 6.3: Details on the environment identification performed on the SDSS-DR16 catalog (see Section 6.3). For each environment (voids, walls, filaments, and massive groups), we report the identification method adopted and the number of galaxies identified in the SDSS catalog and GAMA/H-ATLAS sample. Note that the number of galaxies in our simulated sample is much larger (Table 6.1).

- **Voids** In both the observed and simulated catalogs we take galaxies residing within the spherical voids as identified by the Ruiz et al. (2015, 2019) algorithm (Section 6.3.2).
- **Walls** This category includes galaxies in the proximity ($1 < r/r_{\text{void}} \leq 1.2$) of the aforementioned spherical voids.
- **Filaments** Galaxies within filaments are identified using the Taverna et al. (2023) algorithm, as applied to both the observed and simulated galaxy samples (Section 6.3.3).
- **Massive groups** These are galaxies belonging to groups more massive than $M_{\text{group}} > 10^{13.5} M_{\odot}$. In the observational catalog the group mass is estimated by the Rodríguez & Merchán (2020) algorithm, while in our SAM we take the virial mass of the FOF halo (Section 6.3.3). We take these galaxies as representative of the densest regions of the large-scale structure.

The criteria employed and the number of objects identified in each environment within the observed galaxies catalog are summarized in Table 6.3.

We emphasize that our purpose is not to conduct a one-to-one comparison between environments in observations and simulations. Instead, our main interest is comparing trends among the environments of the two samples.

6.5.1 Star formation

In Figure 6.9 we show the sSFR distributions for galaxies in different stellar mass bins and cosmic web environments. As widely discussed in literature (e.g. Katsianis et al., 2020), this distribution typically features a bimodal behaviour, which corresponds to the superposition of a star forming (sSFR $\approx 10^{-10} \text{ yr}^{-1}$) and a passive population (sSFR $\approx 10^{-12} \text{ yr}^{-1}$) at $z = 0$.

From the reported observations it is clear that the larger the stellar mass is, the larger is the prevalence of the passive population *in each environment*. This pattern is even more evident when examining the fraction of passive galaxies f_{passive} (defined as those featuring sSFR $< 10^{-11} \text{ yr}^{-1}$) and the sSFR as a function of stellar mass, both displayed in Figure 6.10. The observed f_{passive} (sSFR) increases(decreases) with the density of the environment *at fixed stellar mass* for $M_{\text{stars}} \lesssim 10^{11} M_{\odot}$.

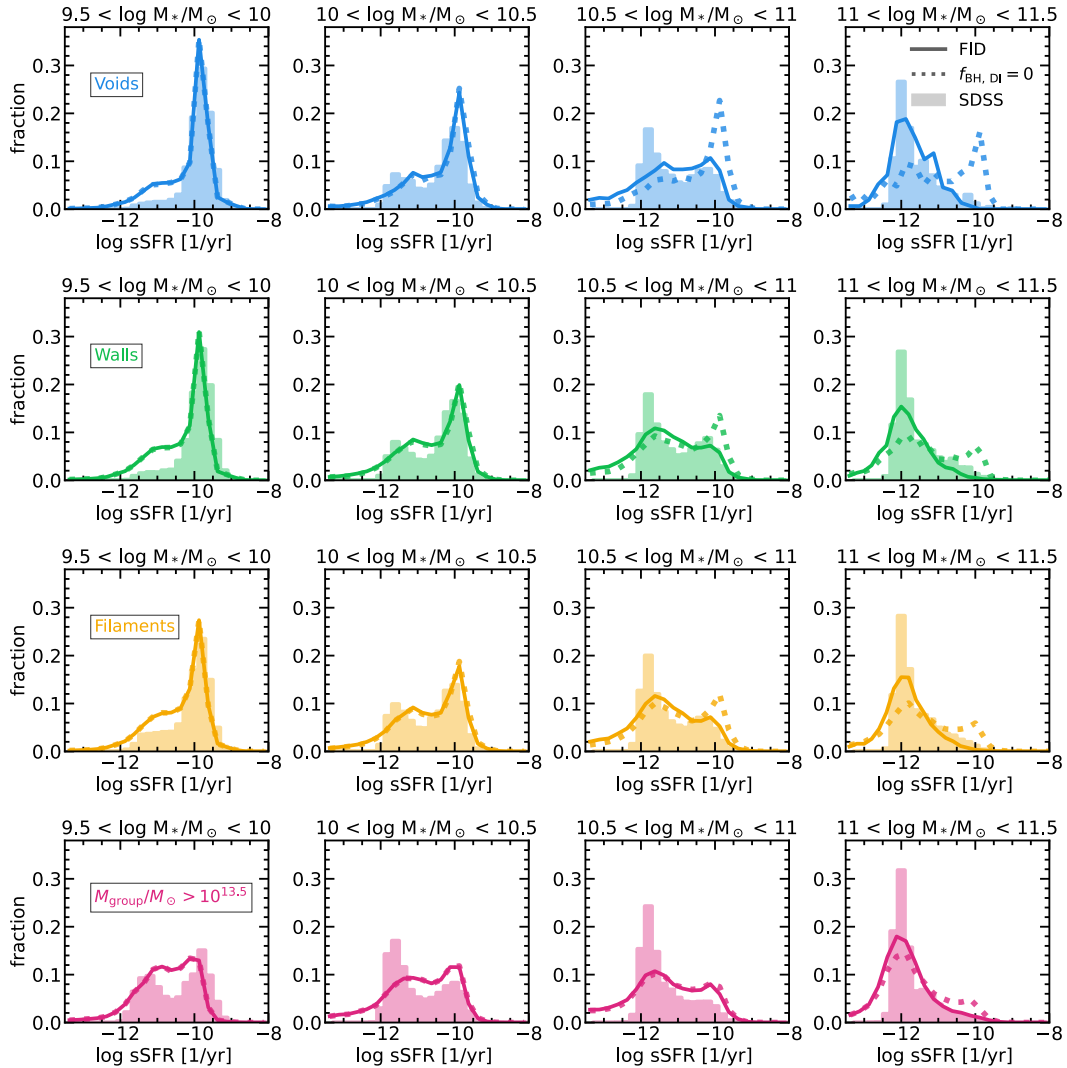


FIGURE 6.9: Specific star formation rate distributions for galaxies in different stellar mass bins, namely (from left to right) $\log M_{\text{stars}}/M_{\odot} \in (9.5 - 10)$, $(10 - 10.5)$, $(10.5 - 11)$, $(11 - 11.5)$. Results for different cosmic environments are shown, namely (from top to bottom): voids in blue, walls in green, filaments in orange, and massive groups ($M_{\text{group}} > 10^{13.5} M_{\odot}$) in magenta. We report our model predictions obtained with both the fiducial (FID) and $f_{\text{BH,DI}} = 0$ version of our SAM (respectively solid and dotted lines). In each panel we compare with SDSS data, shown as filled histograms. Environmental classification in both the observed and simulated catalog is performed as detailed in Section 6.5 (see also Table 6.3).

Our fiducial model displays similar trends, that is an increase of f_{passive} and a decrease of the sSFR with stellar mass and, for $M_{\text{stars}} \lesssim 10^{10.8} - 10^{11} M_{\odot}$, with the density of the environment. Differences between the FID and $f_{\text{BH,DI}} = 0$ results are particularly evident at large M_{stars} and for low density environments. In the two most massive stellar mass bins reported in Figure 6.9, the $f_{\text{BH,DI}} = 0$ model tends to predict more star forming galaxies than the FID one in both voids and walls. The same holds true when inspecting Figure 6.10. Voids galaxies in the $f_{\text{BH,DI}} = 0$ model exhibit a too large (small) sSFR (f_{passive}) with respect to observations at large M_{stars} . Instead, the FID model aligns well with SDSS observations in this mass regime. Thus the impact of the SMBH growth during DIs is particularly relevant for star formation quenching in such isolated galaxies.

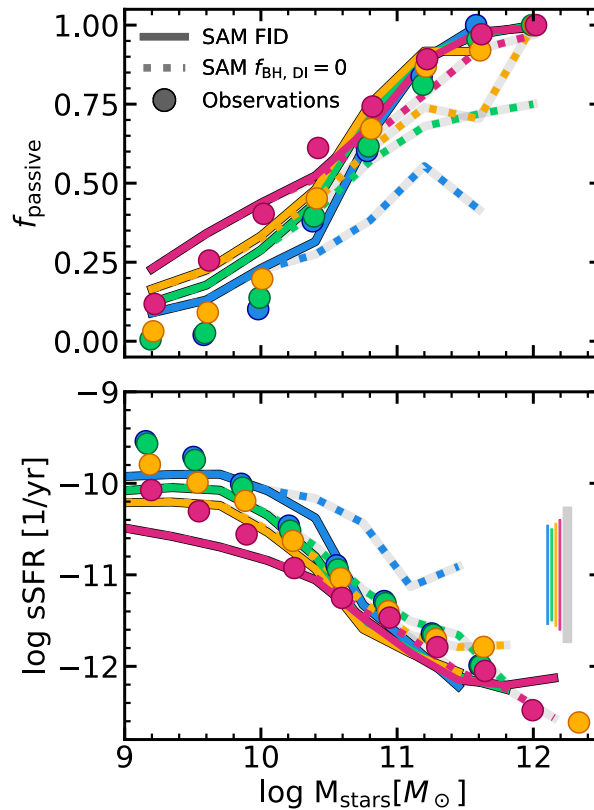


FIGURE 6.10: Fraction of passive galaxies ($\text{sSFR} < 10^{-11} \text{ yr}^{-1}$; *top panel*) and sSFR (*bottom panel*) as a function of stellar mass in voids, walls, filaments and massive groups ($M_{\text{group}} > 10^{13.5} M_{\odot}$). Colors are as in Figure 6.9. We report our model predictions obtained with both the fiducial (FID) and $f_{\text{BH, DI}} = 0$ version of our SAM (respectively solid and dotted lines). Filled circles refer to observations (SDSS data). We also report the typical 14-86th dispersion of observations (vertical lines) and of our model (grey shaded rectangle) in the right side of the bottom panel.

Also, the passive fraction (and the sSFR , to some extent) of the $f_{\text{BH, DI}} = 0$ model exhibits a clear trend with the environment at *any stellar mass*. This behaviour contrasts with observations, where the environmental trend is observed only up to $M_{\text{stars}} \lesssim 10^{11} M_{\odot}$. Conversely, the fiducial model predicts a lack of environmental dependence at large $M_{\text{stars}} (\gtrsim 10^{10.8} - 10^{11} M_{\odot})$, in keeping with the observed pattern.

We conclude that the SMBH growth mechanism adopted by the $f_{\text{BH, DI}} = 0$ model is not sufficient to shut down the star formation in massive, isolated galaxies.

6.5.2 Dust mass

Figure 6.11 compares model predictions on dust masses in local galaxies, as a function of stellar mass and environment, to available observations. The data reported in this Section are obtained by matching the SDSS-DR16 catalog and the GAMA/H-ATLAS sample, thus the final number of objects is much smaller than the number of SDSS objects shown in the previous Section (see Table 6.3). We focus on the mean trends of data, which feature a large dispersion, keeping in mind the limited sample size.

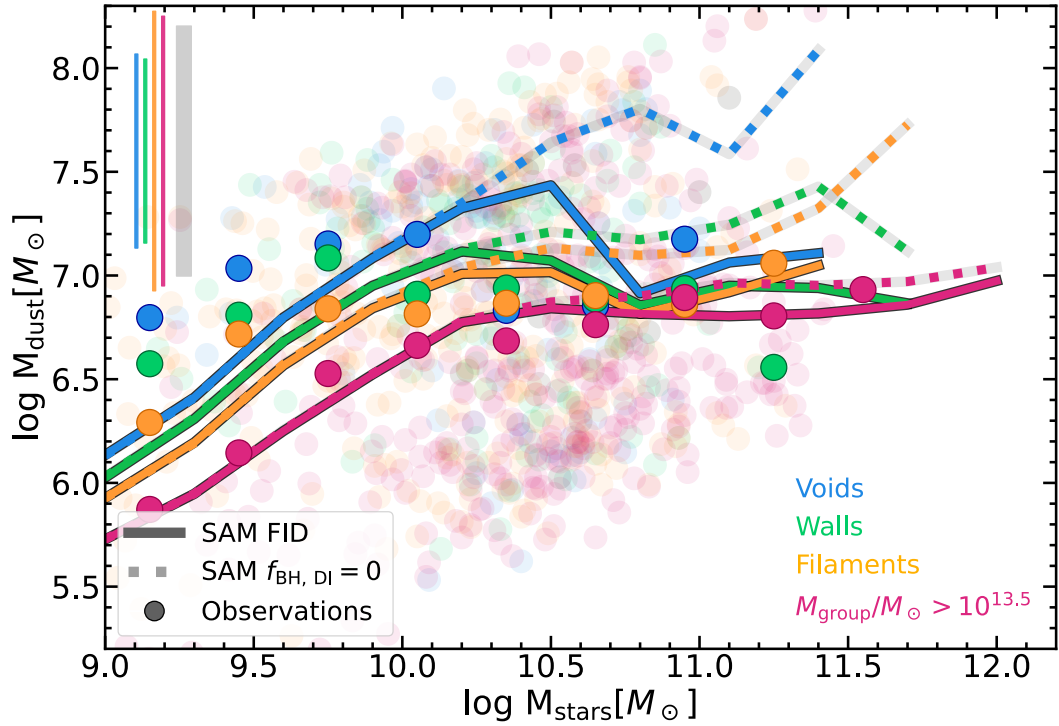


FIGURE 6.11: Dust – stellar mass relation in different large scale environments: voids in blue, walls in green, filaments in orange, and massive groups ($M_{\text{group}} > 10^{13.5} M_{\odot}$) in magenta. The results obtained from our SAM are shown as lines, which refer to medians, while the typical 14-86th dispersion is shown as a grey shaded rectangle in the upper left of the plot. Solid lines refer to our fiducial SAM, while results from the $f_{\text{BH, DI}} = 0$ model are shown as dotted lines. Observations from the GAMA/H-ATLAS sample (Beeston et al., 2018) are shown as filled points which represent the mean dust mass in stellar mass bins of 0.3 dex width, while the whole sample of observations is shown in the background as low opacity circles. We also report the typical 14-86th dispersion associated with each environment as vertical lines in the upper left side of the figure. Environments and groups in this figure are identified as detailed at the beginning of Section 6.5 (see also Table 6.3).

For $M_{\text{stars}} \lesssim 10^{10.5} M_{\odot}$, observations suggest that at fixed stellar mass galaxies are generally more dust rich in less dense environments, with void galaxies featuring a mean dust content 5 – 10 times larger than massive groups objects. The median trends and the environmental differences in this mass range predicted by the FID run of our SAM are consistent with observations.

At larger stellar masses ($M_{\text{stars}} \gtrsim 10^{10.5} M_{\odot}$ in observations and $M_{\text{stars}} \gtrsim 10^{10.8} M_{\odot}$ in our model) dust masses appear to be nearly environment-independent both in observations and in the FID model. By converse, in the $f_{\text{BH,DI}} = 0$ model, the objects residing in low density environments feature a far too large median M_{dust} . This is consistent with the discussion in Section 6.5.1, according to which the fraction of highly star forming massive galaxies (likely gas and dust rich) is suppressed in low density environments by the in situ SMBH growth.

Although a direct comparison between the *convergence mass* (Section 6.4.5) in the SAM and observations is not straightforward¹¹, we note that for observed M_{dust} curves, convergence occurs around $\log M_{\text{stars}}/M_{\odot} \sim 10.5 - 11$, which is in nice agreement with the results obtained from SAM galaxies.

6.6 Summary and conclusions

In this Chapter, we studied the dependence of local galaxy properties, mainly sSFR and dust, on the large-scale environment, at fixed stellar mass. We adopt the simulated galaxy catalog produced by the SAM discussed in this Thesis (Sections 2.3, 3.4 and 5.2; also Parente et al. 2023), which is an extension of the L-GALAXIES SAM (Henriques et al., 2020). This version includes a state of the art model of dust production and evolution in galaxies, as well as an updated treatment of the bulge and SMBH growth during disc instabilities (DIs). We identify cosmic web environments from the underlying DM simulation exploiting different methods. We employ NEXUS+ (Cautun et al., 2013) as a comprehensive method to dissect the cosmic web into voids, walls, filaments, and nodes. This approach provides us with a unified framework to identify different cosmic environments. In contrast, we also utilize specific algorithms tailored for distinct environments: the method introduced by Ruiz et al. (2015, 2019) for identifying spherical voids and associated walls, the approach outlined in Taverna et al. (2023) for detecting cylindrical filaments, and the well-known FOF halo finder to pinpoint massive groups ($M_{\text{group}} > 10^{13.5} M_{\odot}$), representing the most dense environments.

First, we study galaxy properties as a function of M_{stars} to highlight the role of the environments (Section 6.4.2). For galaxies with $M_{\text{stars}} \lesssim 10^{10.8} M_{\odot}$ we find a clear and systematic trend: at fixed stellar mass, galaxies in less dense environments feature a larger specific SFR and dust abundance. Contrarily, differences among environments are much less evident in more massive objects.

We interpret these results in light of the evolution of galaxies with the same $z = 0$ stellar mass, but residing in different environments (Section 6.4.3). At $M_{\text{stars}}^{z=0} \leq 10^{10.5} M_{\odot}$, the less dense is the environment, the slower is the stellar mass evolution. At a given $M_{\text{stars}}^{z=0}$, galaxies in less dense environments feature a SFR peak at more recent times, ending up with a larger SFR and dust content. Contrarily, galaxies in more dense environments are in the declining phase of their star formation activity. Thus void galaxies host, on average, younger stellar populations, are more star forming and dust rich with respect to galaxies located in other environments with the same $M_{\text{stars}}^{z=0}$. Relevant differences in the stellar mass assembly are not

¹¹This would need to identify environments in mock catalogues from the simulated galaxy sample in the same way as we do in the observed sample. Also, due to the lower number of objects in the observed catalog the accuracy of its calculation in observations is somewhat unreliable.

observed instead for more massive galaxies ($M_{\text{stars}}^{z=0} \gtrsim 10^{10.8} M_{\odot}$), and this is in keeping with the environment-insensitivity of star formation and dust for massive objects already discussed. This finding is remarkably robust, irrespective of the variety of methods for environments identification adopted in this work.

The picture resulting from our model suggests that galaxy properties are affected by the large-scale environment up to a certain *threshold* mass. The key to interpreting this finding stands in the supermassive black hole (SMBH) growth channel during DIs, which is adopted in our model. This channel enables the growth of SMBHs even in isolated galaxies, allowing them to halt star formation through AGN radio mode feedback. In the absence of this channel, the growth of SMBHs in isolated objects is significantly discouraged, as the other prominent growth channel in our SAM occurs during merger events. This *in situ* SMBH growth tends to erase differences among galaxies that exceed a specific stellar mass ($M_{\text{stars}} \approx 10^{10.8} M_{\odot}$, mass above which the SMBH driven quenching becomes relevant in our model) residing in different environments.

Finally, we test our results against observations (Section 6.5). We identify different environments in the SDSS-DR16, namely spherical voids, their associated walls, cylindrical filaments, and massive groups ($M_{\text{group}} \gtrsim 10^{13.5} M_{\odot}$) using the algorithms by Ruiz et al. (2015), Taverna et al. (2023), and Rodriguez & Merchán (2020). This is conceptually similar to the identification process in our SAM catalog, allowing us to compare the results. The fraction of passive galaxies ($\text{sSFR} < 10^{-11} \text{yr}^{-1}$) with $M_{\text{stars}} \lesssim 10^{10.5} - 10^{11} M_{\odot}$ increases with the increasing density of the environment, in both the SAM and SDSS catalog. As for the most massive objects ($M_{\text{stars}} \gtrsim 10^{10.5} - 10^{11} M_{\odot}$), in both our model and observations, we do not find any sign of a prominent star forming population in any environment. This is a direct consequence of the DI-driven SMBH growth adopted in our model. Without this channel ($f_{\text{BH,DI}} = 0$), our model would produce a star forming population among massive voids galaxies, and this is not present in the observed sample (Figures 6.9 and 6.10).

We perform a similar comparison between our model and observations (combining the SDSS-DR16 and GAMA/H-ATLAS surveys) in the $M_{\text{stars}} - M_{\text{dust}}$ plot (Figure 6.11). We find a good match, namely the less dense is the environment, the larger is the dust content of galaxies with $M_{\text{stars}} \lesssim 10^{10.5} M_{\odot}$ in observations ($M_{\text{stars}} \lesssim 10^{10.8} M_{\odot}$ in our model). The $\sim 0.5 - 1$ dex difference in the mean dust mass of voids and massive groups galaxies is not observed above this mass. Again, this confirms the importance of the SMBH growth channel in DIs, without which too dust-rich void galaxies would be predicted.

We draw two main conclusions from this work. First, we confirm the relevance of the secular process of SMBH growth during DIs in our SAM, since it causes quenching of galaxies in isolated environments. The importance of this growth channel has been pointed out also by recent observational and simulation-based investigations, whose claim is that secular processes dominate over mergers in growing the central SMBH (e.g. Martin et al., 2018; Smethurst et al., 2019). The second conclusion concerns our approach more than our results. Investigating the properties of galaxies in different large-scale environments may be a useful tool for constraining the relevance of in situ and ex situ processes in shaping galaxy evolution.

The method outlined here can be improved in various ways, for example, by striving for a more accurate match between the environments identified in simulations and observations. A possible way to achieve this may be to identify environments from mock catalogs derived from the SAM (or from hydrodynamical simulations as well) to mimic the identification process performed on the observed catalog as closely as possible.

In any case, besides any possible improvement, the role of future observational surveys such as Euclid (Laureijs et al., 2011), DESI (DESI Collaboration et al., 2016) and LSST

(Ivezić et al., 2019), is crucial. They will substantially advance our knowledge of the large-scale structure and, concomitantly, deepen our insight into the evolution of galaxies within distinct cosmic environments.

7

Dust sub-mm emission in Green Valley galaxies

The "Green Valley" (GV; Wyder et al. 2007) in galaxy evolution refers to the transitional region on a color-magnitude (or color-mass) diagram that lies between the blue cloud (BC) of star-forming galaxies and the red sequence (RS) of passive galaxies. This valley is believed to result from the relatively rapid transition of galaxies from the star-forming state to a passive one, making it crucial for understanding galaxy quenching processes (see Salim 2014 for a review). However, some inactive galaxies can experience "rejuvenation," a phase where they undergo a new burst of star formation after a period of minimal activity. This rejuvenation can move galaxies in the red sequence back into the GV, and in some cases, even into the blue cloud (e.g., Graham et al. 2017; Rowlands et al. 2018; Chauke et al. 2019).

In this Chapter, we¹ focus on the sub-mm emission of galaxies within the GV. As highlighted by Eales et al. (2018) using *Herschel* data, GV galaxies display notably strong sub-mm emission compared to galaxies with either bluer or redder colors. We explore this characteristic using a galaxy catalog generated from the SAM discussed in this Thesis, which includes a self-consistent model of dust formation and evolution. By applying a radiative transfer (RT) approach, we derive observable properties that account for both stellar emission and the absorption and re-emission by dust grains. After defining GV galaxies with a new criterion applicable to any dataset, we find that the number of 250 μm emitters in the GV is comparable to that found in the BC, in keeping with local observations. This is because, despite a decline in sSFR and the resulting green optical colors, the dust content remains high during the GV phase, fueling the sub-mm emission. The differences in the evolution of sSFR and dust content make sub-mm emission a potential indicator for identifying rejuvenating galaxies, which transition to bluer optical colors while still exhibiting low sub-mm fluxes.

The Chapter is organized as follows. We introduce our simulated galaxy catalog in Section 7.1, and in particular the pipeline to obtain observable properties from it (Section 7.1.2), while the observational data we compare with are presented in Section 7.2. After inspecting the color-mass diagram predicted by our simulation in Section 7.3, we present our new definition of GV in Section 7.4, which is applied to both the simulated and observed sample of galaxies. We then move to analyse dust attenuation in GV galaxies in Section 7.5, while Section 7.6 and 7.7 focus on dust 250 μm emission. Such emission in systems undergoing rejuvenation is discussed in Section 7.8. Finally, we summarise our results and highlight the main conclusions in Section 7.9.

¹This Chapter is based on a work (submitted, under revision) done in collaboration with C. Ragone-Figueroa, G. L. Granato, L. Silva, V. Coenda, H. J. Martinez, H. Muriel, and A. Lapi Parente et al. (2024b).

CONTENTS

| | |
|--|-----|
| 7.1 The simulated catalog | 146 |
| 7.2 Observational data | 148 |
| 7.3 The color-mass diagram | 148 |
| 7.4 Defining the GV | 149 |
| 7.5 The impact of dust attenuation | 153 |
| 7.6 The sub-mm 250 μm emission | 154 |
| 7.7 Evolution in the color- $S_{250\mu\text{m}}$ diagram | 158 |
| 7.8 Rejuvenating systems | 163 |
| 7.9 Summary and Conclusions | 163 |

7.1 The simulated catalog

7.1.1 The SAM catalog

The simulated catalog adopted in this analysis is derived from the SAM extensively discussed in this Thesis, which is an updated version of the public L-GALAXIES SAM (Henriques et al., 2020, Section 2.3). This version incorporates a state-of-the-art dust model (Section 3.4) and an improved treatment of disc instabilities (Section 5.2).

While referring to the above mentioned sections for full details on the model, the main feature of the simulation are reported here for convenience. The catalog used in this analysis is obtained by running the SAM on the MILLENNIUM merger trees (Springel et al. 2005b, box size 500Mpc/ h , adopting a Planck Collaboration et al. (2014) cosmology ($h = 0.673$, $\Omega_{\text{m}} = 0.315$, $\Omega_{\text{b}} = 0.0487$, $\sigma_8 = 0.829$) and a Chabrier (2003) IMF. In this work, to keep the analysis within a reasonable computational time, a reduced sample – preserving the same SMF as the full simulation – is post-processed to derive observable properties.

7.1.2 Radiative Transfer with GRASIL

The observable properties of our simulated galaxies are derived using the Radiative Transfer (RT) code GRASIL (Silva et al., 1998; Granato et al., 2000). This code computes the emission from stellar populations and the absorption and thermal emission from dust grains. It utilises the information on SFHs, the geometry of stars and ISM, and the abundance and properties of dust grains for each galaxy as predicted by the SAM, as detailed in the following sections. We refer to the above-mentioned papers for a detailed description of GRASIL.

Stars and ISM geometry

Simulated galaxies are assumed to have a disc-like ISM, while the stellar component is organized into a disc and a bulge. Both the stellar and ISM discs follow a radial and vertical exponential profile, meaning the density of the disc is given by

$$\rho \propto \exp(-r/r_{\text{d}}) \exp(-|z|/z_{\text{d}}), \quad (7.1)$$

where r and z are the radial and vertical coordinate, while r_{d} and z_{d} the respective scale lengths of the exponential profiles. The scale length radii of the stellar and ISM discs are predictions from the SAM (note that these values usually differ). For both cases, we set the scale height to 0.1 of the scale radius. The stellar bulge is assumed to have a King profile, with its core radius derived from the half-mass radius predicted by the SAM.

Stellar emission

The stellar emission of galaxies originates from the populations in the disc and bulge. Both components have an associated SFH², which tracks the time assembly of their stellar mass and metallicity. The SFH is stored in N_{SFH} time bins, with the size of each bin varying with time so that the most recent bins have the highest resolution (see Figure S2 of the [Henriques et al. 2020](#) documentation for a schematic representation). The emission from stellar populations at time t is calculated (for both disc and bulge stars) by summing over the SFH bins:

$$L(t) = \sum_{i=0}^{N_{\text{SFH}}} l_i(t - t_i; Z_i) \cdot \psi_i \Delta t_i, \quad (7.2)$$

where $l_i(t - t_i; Z_i)$ is the emission associated with a unit mass simple stellar population featuring age³ $t - t_i$ and metallicity Z_i ; ψ_i and Δt_i are the SFR and time width associated with the i -th bin.

Radiative Transfer

Radiation emitted from stars propagates into the ISM, where it is extinguished, heats dust grains, and causes their subsequent thermal emission. Modeling these processes requires detailed RT computations, which are performed by GRASIL.

The interaction between starlight and dust grains depends on the abundance and properties of the latter. The mass of dust in each galaxy, as well as the chemical composition and size of the grains, are predictions of the SAM. As detailed in Section 3.4, the model predicts the abundance of four dust species, following two chemical compositions (silicate and carbonaceous) and two sizes with representative radii of $0.05 \mu\text{m}$ and $0.005 \mu\text{m}$ (referred to as large and small). GRASIL uses this information and considers a population of silicate and carbonaceous grains with two different grain size distributions, which are power laws shaped by the ratio of small to large grains. These information are needed to model the absorption and emission of grains.

Dust is assumed to be organized into two phases of the ISM: the dense molecular clouds (MCs) and the diffuse medium. Dust properties are assumed to be the same in the two regions. The fraction of the total dust mass residing in MCs is f_{mol} , which is the fraction of the total ISM gas in molecular form. This parameter is predicted by the SAM, which relies on the [Krumholz et al. \(2009\)](#) prescription.

MCs are assumed to have a mass M_c and a radius r_c , which are parameters of GRASIL. The combination M_c/r_c^2 determines the optical depth of the clouds. Stars are assumed to form in these clouds and progressively escape according to an escape timescale t_{esc} . The escape time t_{esc} is a GRASIL parameter and is set to 3 Myr here. Specifically, the fraction of stars inside MCs decreases with time according to

$$f(t) = \begin{cases} 1 & t \leq t_{\text{esc}}, \\ 2 - t/t_{\text{esc}} & t_{\text{esc}} < t \leq 2t_{\text{esc}}, \\ 0 & t > 2t_{\text{esc}}. \end{cases} \quad (7.3)$$

²The same SFH is adopted within the SAM to compute the chemical enrichment from stars. However, although the SFH in the code is recorded on a ring-by-ring basis, for GRASIL post-processing we use the SFH integrated over the entire stellar disc and bulge.

³Here t_i is the central lookback time of the i -th bin.

Starlight propagation in MCs is simulated using full RT computations (Granato & Danese, 1994) because the high densities of these objects make the self-absorption of IR photons significant.

In contrast, starlight propagation in the diffuse medium (where IR photon self-absorption is negligible) is treated in a simplified manner by introducing an *effective* absorption optical depth, defined as $\tau_{\text{abs,eff}} = \sqrt{\tau_{\text{abs}} (\tau_{\text{abs}} + \tau_{\text{sca}})}$, where τ_{abs} and τ_{sca} are the true absorption and scattering optical depths, respectively.

The outcome of the pipeline described above is that, at each point of the galaxy, stellar radiation is absorbed, the temperature of the grains is calculated (with large grains reaching an equilibrium temperature and small grains experiencing stochastic temperature fluctuations), and the dust emission is modelled as a grey body. This results in a SED from $0.1 \mu\text{m}$ to $1000 \mu\text{m}$ for each galaxy along a given line of sight. The apparent magnitude of the galaxy in a specific band is then obtained by convolving the resulting SED with the appropriate filter⁴.

7.2 Observational data

The observational analysis presented in this work relies on data from the Galaxy And Mass Assembly (GAMA) survey⁵ (Driver et al., 2009; Driver et al., 2011; Liske et al., 2015; Baldry et al., 2018; Driver et al., 2022). This is a spectroscopic, large scale survey covering a total area of $\sim 280 \text{ deg}^2$ across five different regions of the sky. Together with spectroscopic redshifts, this survey provides pancromatic photometry for $\gtrsim 200,000$ galaxies obtained combining data from other surveys operating from the X-ray to the far-IR side of the spectrum. Moreover, many other data products obtained from SED fitting are available, such as stellar masses, SFRs, dust masses.

In this work we exploit the last GAMA Data Release DR4 (Driver et al., 2022). In particular, we use GAMA II⁶ data for the three equatorial survey regions G09, G12 and G15, which all have a limiting Petrosian r -band apparent magnitude of 19.8. We select galaxies with high quality redshift measurements in the range $0.002 < z \leq 0.8$. In our analysis we are interested in the optical colour $u - r$ and the sub-mm $250 \mu\text{m}$ emission of galaxies. GAMA provides both quantities, the former coming from the Sloan Digital Sky Survey (SDSS; Abazajian et al. 2009) and the latter from the H -ATLAS survey (Eales et al., 2010; Valiante et al., 2016). Here we use the matched aperture photometry fluxes obtained from the LAMBDA code (Wright et al., 2016) and select galaxies with a signal-to-noise ratio > 3 . Fluxes are corrected for galactic extinction and k -corrected to $z = 0$ (i.e. they are rest-frame; Loveday et al. 2012). Finally, we select stellar masses obtained from this photometry by SED fitting (Taylor et al., 2011), selecting galaxies with $M_{\text{stars}} \geq 10^9 M_{\odot}$, as in our simulated sample.

7.3 The color-mass diagram

Before analysing any properties of GV galaxies in our catalogs, it is worth looking at the distribution of simulated galaxies in the color-mass diagram. The color ($u - r$) – stellar mass diagram for local galaxies ($z \leq 0.08$) is reported in Figure 7.1. For comparison, we also report observations from the GAMA sample as black contours. The reported colors are k -corrected to $z = 0$ and dust-attenuated, the latter meaning that they are not intrinsic stellar colors.

⁴The technical specifications of the filters are taken from <http://svo2.cab.inta-csic.es/theory/fps/>

⁵<https://www.gama-survey.org/>

⁶The second GAMA surveying phase.

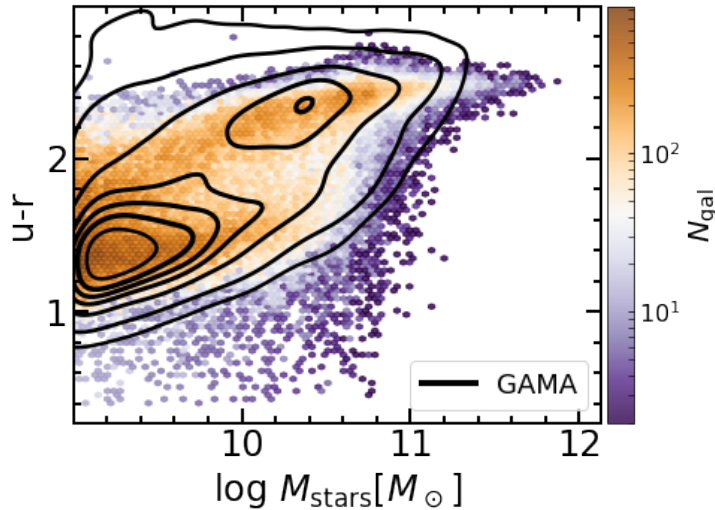


FIGURE 7.1: Color ($u-r$) – stellar mass diagram at $z \leq 0.08$ for our simulated galaxies (2D histogram). Contour lines are 1, 5, 20, 50, 70, 80, 90% of the distribution and refer to the same color-mass relation in the GAMA sample adopted in this work. The $u-r$ color is dust-attenuated and k -corrected to $z = 0$.

Our model produces a clear population of blue galaxies at $M_{\text{stars}} \lesssim 10^{10.5} M_{\odot}$, which well matches the observed BC. As for red galaxies, in our model these are typically more massive than the blue ones, in line with observations. However, our model overproduces the abundance of low mass ($M_{\text{stars}} \lesssim 10^{10} M_{\odot}$) red galaxies. These are mainly satellite systems, and in particular orphan galaxies. This has been noted recently by Harrold et al. (2024) in the context of L-GALAXIES. These authors highlighted the overabundance of orphans in the low mass SMF at $0.5 < z < 3$, and claimed that increasing star formation in these systems could help resolve this problem.

A similar distribution, and similar issues as well, are observed when adopting NUV- r or $g-r$ colors, not shown here for brevity.

7.4 Defining the GV

The GV lacks a universally accepted definition, with its boundaries differing across studies and sometimes being set by subjective empirical limits. Since our work involves defining the GV in both observed and simulated samples, our aim is to establish a clear, objective definition that can be applied automatically, free from subjective criteria.

- **Gaussian fits**

We adopt a Gaussian fitting approach to define the GV, applicable to any color-mass distribution of galaxies. The sample is first divided into N_{bins} mass bins, with only bins containing more than 50 objects being considered. Within each bin, we use the Python class `GaussianMixture` to fit both one and two Gaussians to the color distribution. For the two-Gaussian fit, this class also provides the mixture weights of the resulting Gaussian components, indicating the significance of each component in the overall distribution. Additionally, it computes the Bayesian Information Criterion (BIC) value, which evaluates not only how well the model fits the data but also considers the simplicity of the model.

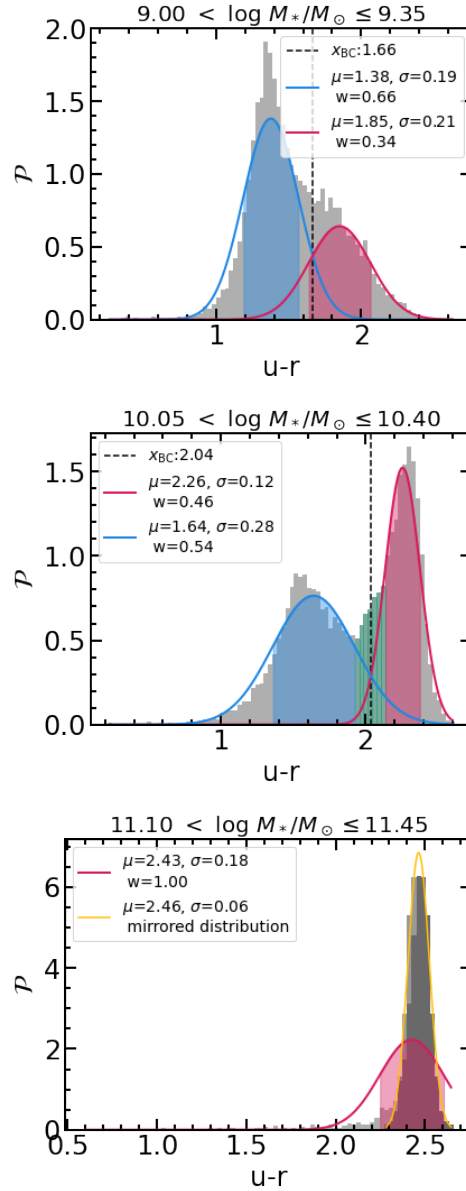


FIGURE 7.2: Examples of the Gaussian fits based algorithm used to identify blue and red populations across different mass bins are shown. The three cases illustrate the color distribution of our simulated sample at $z \leq 0.08$ in three different mass bins, offering a clear demonstration of how our algorithm works (see text for full details). The full color distribution of galaxies in each bin is shown as a grey histogram, and the gaussian fits are reported as curves, with the shaded regions indicating the standard deviation, and the dashed line the intersection between the two curves, where present. The parameters for each Gaussian (mean μ , standard deviation σ , and weight w) are labeled in every panel. In the top and middle panels, our algorithm favours a double Gaussian distribution (blue and red). However, a real GV (green histogram) is identified only in the middle panel, since here the condition in Equation 7.4 is met. In the bottom panel, the algorithm prefers a single Gaussian fit, which is reported as a red curve. In this case, a subsample of the total is extracted to obtain a symmetric distribution centered around the peak of the original sample. This sub-distribution, represented by the dark grey histogram, is fitted by the yellow Gaussian curve. The parameters from this fit better represent the red population in this mass bin and are used in our analysis.

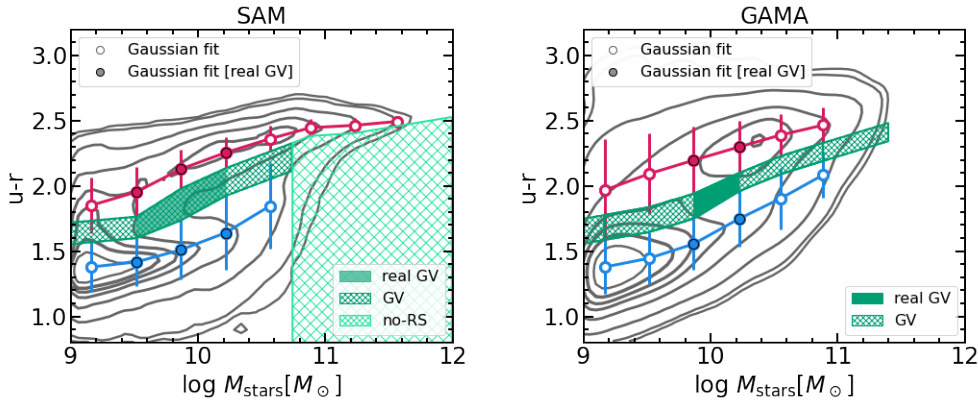


FIGURE 7.3: GV identification in the color-mass diagram of both our simulated and observed sample at $z \leq 0.08$. The distribution of galaxies is shown as contours marking the 1, 5, 20, 50, 70, 80, 90% percentiles of the distribution. The circles and error bars indicate the mean and standard deviation of the Gaussian fits performed by our algorithm in each mass bin for both the blue and red population. Filled circles are associated with bins in which the real GV can be identified (according to Equationn 7.4). This region is depicted as solid green in the plots. The green hatched region represents an extension of this GV, obtained by using information from the Gaussian fits. The light green hatched region in the SAM sample marks the region of the diagram occupied by galaxies identified as *non* belonging to the RS, since a single Gaussian fit is favoured at these mass bins. In the GAMA sample, the GV has been linearly extrapolated in the high stellar mass range where the number of galaxies per bin resulted to be not sufficient to perform a double Gaussian fit (< 50 galaxies).

To determine whether the distribution is better represented by two populations, we apply three criteria.

- (i) The BIC value must favour the two-Gaussian model.
- (ii) None of the obtained weights w must be less than $w_{\min} = 0.2$.
- (ii) The areas within one standard deviation in the two Gaussian curves must not overlap.

When all conditions are met, we determine that the color distribution is described by a two-Gaussian fit. The means μ and standard deviations σ of these Gaussian components are used to help determine the presence of a GV in the distribution. Specifically, denoting x_{BR} as the intersection point of the blue and red Gaussians, we require that

$$\begin{cases} \mu_R - \sigma_R \geq x_{BR}, \\ \mu_B + \sigma_B \leq x_{BR}, \end{cases} \quad (7.4)$$

where the subscripts B and R refer to the blue and red Gaussians, respectively. This approach defines the GV, which we term the real GV, as the region of the color distribution spanning from $\mu_B + \sigma_B$ to $\mu_R - \sigma_R$.

The described conditions at work are explicitly shown in Figure 7.2, in the top and middle panels. In both mass bins, our algorithm prefers a double-Gaussian fit for the distribution. However, in the $9 < \log, M/M_{\odot} \leq 9.35$ mass bin, the two Gaussians do not meet the criterion specified in Equationn 7.4, so a real GV is not identified. In contrast, the Gaussians in the $10.05 < \log, M_*/M_{\odot} \leq 10.40$ bin are well-separated, allowing us to identify a real GV,

represented by the green distribution in the histogram.

When the algorithm favors a single-Gaussian fit, we proceed as follows. We first identify the peak of the entire distribution and isolate the portion extending from this peak to the nearest extreme. This segment is then mirrored to create a symmetric distribution centered on the original peak. We fit this mirrored distribution with a single Gaussian, using its mean and standard deviation as representative of the population.

An example of this process is illustrated in the bottom panel of Figure 7.2. The mirrored distribution, shown in dark grey, is fitted with a Gaussian (yellow curve), in contrast to the red curve used to fit the full distribution (light grey). This mirroring technique effectively removes the tail of the distribution, yielding Gaussian parameters that better represent the bulk of the objects in this region.

• Building the GV

The fitting procedure described above results in the Gaussian function parameters for each mass bin of the distribution. These parameters are then used to split the color-mass diagram into different classes (and in particular to identify a GV), as illustrated in Figure 7.3 for both the simulated and observed samples.

We begin with the real GV, which is identified in the bins where the condition in Equation 7.4 is satisfied. In these cases, the GV directly corresponds to the real GV, represented by the green shaded area in Figure 7.3.

In the mass bins where the algorithm does not identify a real GV but still applies a two-Gaussian fit, we extend the real GV by using the Gaussian parameters and assigning a width based on that of the real GV. Specifically, we select the Gaussian with the highest weight in the double-Gaussian fit. Given the mean and standard deviation of this Gaussian, the extended GV in this mass bin is defined with bounds of $\mu \pm \sigma$ and $\mu \pm (\sigma + \Delta_{\text{real,GV}}^{\text{near}})$, where $\Delta_{\text{real,GV}}^{\text{near}}$ represents the width of the real GV in the nearest mass bin where it has been identified. If two neighboring mass bins have a real GV, the average width is used. The \pm sign is chosen based on the Gaussian fit, with + for blue and – for red. This extended GV is shown as a hatched green region in Figure 7.3. This approach allows us to define a GV in the color-mass diagram for every mass bin where a two-Gaussian fit has been applied.

In cases where a single-Gaussian fit is used, we take a more conservative approach and choose not to define a GV. Instead, we divide the galaxy population into two categories, using $\mu \pm \sigma$ as the boundaries for these groups, with – for a red peak and + for a blue peak. If a red peak is identified, the categories are labeled RS and no-RS. If a blue peak is identified, they are labeled BC and no-BC. This scenario occurs in the most massive bins of our simulated sample, where only the red population is clearly defined, as indicated in light green in Figure 7.3. Conversely, in high-redshift snapshots of our simulation, it is more common to find only a clear blue population in the less massive bins (see Fig. 7.8).

This definition allows us to identify a GV (where possible) for any given distribution in the color-mass diagram. Once the GV is specified, the BC and RS are defined as everything below and above the GV, respectively (except in cases where no-BC or no-RS is identified). It is important to note that our approach is fairly conservative, as we avoid to extrapolate the GV to mass bins where a clear color bimodality is not observed. However, our findings remain largely unaffected by this definition. We have verified that using alternative methods, such as extrapolating the GV where a single Gaussian is preferred or applying two simple linear fits to delimit the GV, would not significantly alter our conclusions.

All analyses presented below use the definition of GV outlined above, specifically the region formed by the real GV and its extensions where a two-Gaussian fit is preferred.

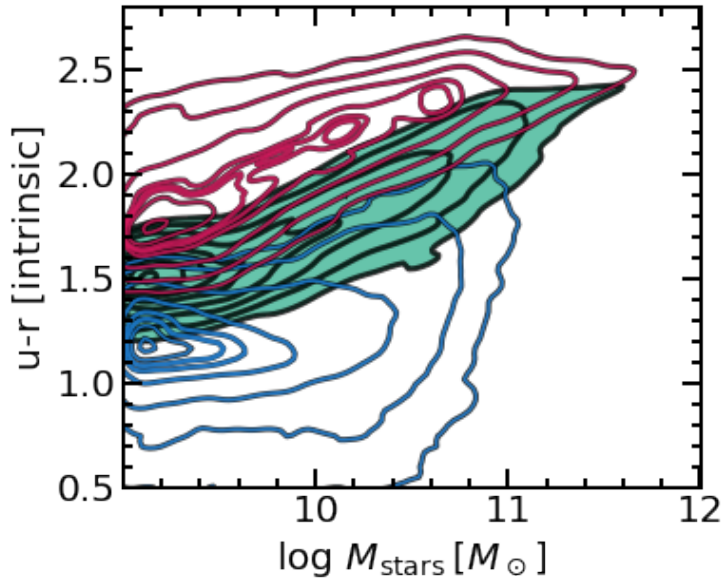


FIGURE 7.4: Intrinsic color ($u - r$)–mass diagram for our sample of simulated galaxies at $z \leq 0.08$. Contour lines represent the 1, 5, 20, 50, 70, 80, 90, 99% of the distribution. Red, green and blue contours refer to galaxies in the RS, GV and BC, respectively, as defined using the dust-attenuated color-mass diagram (Section 7.4 and left panel of Fig. 7.3).

7.5 The impact of dust attenuation

It is well known that dust obscuration reddens the true, *intrinsic* color of galaxies resulting from pure stellar emission. Consequently, some intrinsically blue, star-forming galaxies may appear redder (green or red in our classification). We exploit our simulated sample, for which both dust-attenuated and dust-free colors are available, to explore the impact of dust on shaping the color-mass diagram.

In our model, galaxies in the BC and GV typically have more dust than equal stellar mass galaxies in the RS, which are mainly passive and gas-poor. As a result, dust reddening is more pronounced for galaxies in the BC and GV, where the intrinsic $u - r$ color is reddened by $\sim 0.4 - 0.2$ dex. Attenuation is modest in RS galaxies ($\lesssim 0.2 - 0.1$ dex).

In light of this, when considering intrinsic colors the blue region of the color-mass diagram shifts downward by about $0.2 - 0.3$ dex, while intrinsic colors are nearly identical to dust-attenuated ones for red galaxies. The net effect of the attenuated-to-intrinsic transformation is a shift towards bluer $u - r$ colors, which is more pronounced for blue galaxies. Importantly, in this transformation, GV galaxies are likely to remain GV galaxies: although their color becomes bluer, most dust-attenuated GV galaxies also have intrinsic green colors. In other words, the transition population identified in the dust-attenuated color-mass diagram of Figure 7.1 mainly consists of galaxies with intrinsic intermediate colors. The percentage of significant outliers due to dust attenuation is very low. To give an idea, only $\sim 6.5\%$ of intrinsically blue galaxies move to what would be classified as GV when dust attenuation is considered. As for the transformation of the GV, the $\sim 94\%$ of galaxies belonging to the intrinsic GV are within 0.2 dex of the dust-attenuated GV. These percentages were derived by defining BC, GV, and RS in the intrinsic color-mass diagram using the same procedure detailed in Section 7.4.

Figure 7.4 further illustrates the modest impact of dust on the BC-GV-RS classification. Keeping the categories established in Figure 7.3, we now plot the intrinsic colour of galaxies

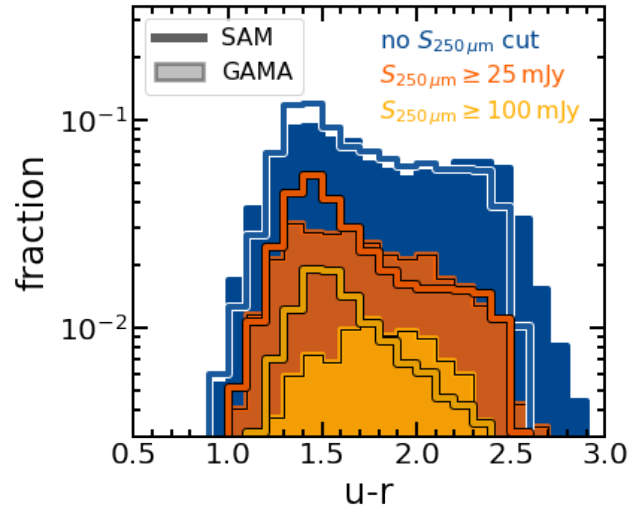


FIGURE 7.5: Color $u - r$ distribution for all the galaxies in both our simulated (solid lines) and observed sample (filled histograms) at $z \leq 0.08$. We report the full color distribution in dark blue, as well as the one obtained when selecting galaxies with a $S_{250\mu\text{m}}$ larger than a given threshold, i.e. 25 and 100 mJy (orange and yellow).

on the y-axis. The overlap of contours illustrates the extent to which colors shift due to dust attenuation. The bulk of the GV population is observed to have intermediate intrinsic colors.

The conclusion of this analysis is that, although dust obscuration plays a role in reddening galaxies, the bulk of the galaxies in a dust-attenuated GV belongs as well to a transition region in the intrinsic color-mass diagram.

7.6 The sub-mm $250\mu\text{m}$ emission

In this Section we analyse the sub-mm $250\mu\text{m}$ emission of both simulated and observed $z \leq 0.08$ galaxies. We start from the $u - r$ color distribution as reported in Figure 7.5, imposing a threshold (25 or 100 mJy) on $S_{250\mu\text{m}}$. The 25 mJy threshold, which will be adopted in the rest of this work, is approximately the flux value of the 14th percentile of the observed $S_{250\mu\text{m}}$ distribution when selecting objects with a signal-to-noise ratio larger than 3. For this reason, we will often refer to the objects satisfying this criterion as sub-mm emitters. In model galaxies, both the $S_{250\mu\text{m}} \geq 25$ mJy and $S_{250\mu\text{m}} \geq 100$ mJy distributions are biased towards the blue peak, indicating that blue galaxies are more likely to have significant sub-mm emissions. This is also the case for the $S_{250\mu\text{m}} \geq 25$ mJy distribution of the GAMA sample. However, when raising the sub-mm emission threshold to 100 mJy, the distribution of observed galaxies peaks at around intermediate colors.

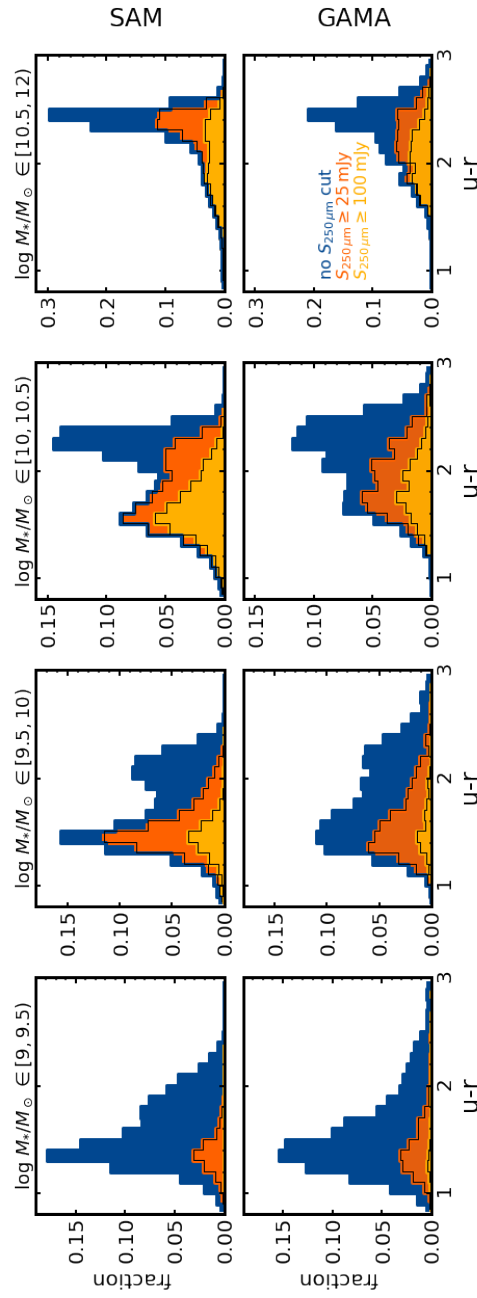


FIGURE 7.6: Color distribution in different stellar mass bins for our model (top panels) and observed (bottom panels) galaxies at $z \leq 0.08$. In each panel we report the total distribution (dark blue histograms), as well as the distribution obtained applying different cuts on the 250 μm flux, namely $S_{250\mu\text{m}} \geq 25$ and 100 mJy (respectively orange and yellow histograms).

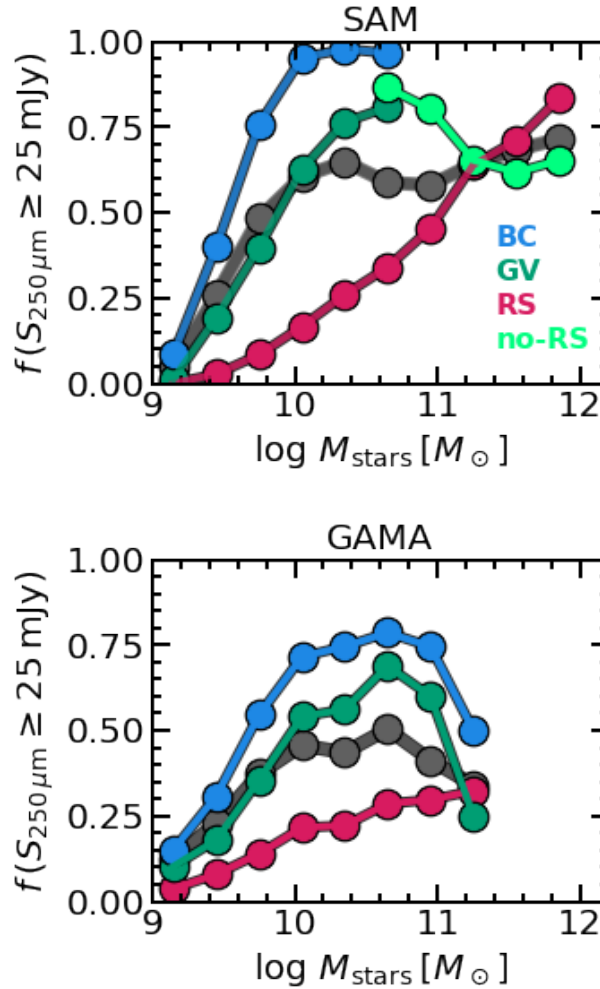


FIGURE 7.7: Fraction of galaxies in the BC (blue), GV (green) and RS (red) with a $S_{250\mu\text{m}}$ flux larger than 25 mJy as a function of stellar mass in both our model (top) and GAMA+ H -ATLAS observations (bottom panel). The top panel sample (SAM) also includes galaxies classified as *not* belonging to the RS in light green (see Section 7.4). Results for the whole samples are reported in grey.

A similar result was previously noted by Eales et al. (2018), based on a similar dataset⁷. They observed that sub-mm detected galaxies (specifically those with $250\mu\text{m}$ emission ≥ 30 mJy from H -ATLAS) are predominantly located in the optical GV (although no explicit GV definition is used in that work). They suggested that this could originate from a continuous, *non*-bimodal distribution of galaxies in the M_{stars} -SFR diagram, attributing the SFR bimodality to an incorrect mapping between colors and SFR (and vice versa). In other words, they interpret the observation of a ‘green mountain’ as an argument against the widely accepted scenario which associate GV galaxies to a transition (in terms of SFR) population. While we stay agnostic regarding this conclusion, we will exploit our model to investigate the substantial sub-mm emission in GV galaxies.

We conduct a more detailed analysis of the above result, noting that in general the color distributions shift towards redder colors with increasing stellar mass (e.g. Figure 7.1). We

⁷We have exploited more recent data products of the GAMA team, in particular matched aperture photometry. Also, our limiting $250\mu\text{m}$ fluxes are different.

perform the same analysis but at various mass bins, as shown in Figure 7.6. At fixed stellar mass, galaxies with bluer colors have a higher fraction of sub-mm emitters. Thus, the analysis reveals that $S_{250\mu\text{m}}$ emission is likely present in galaxies with colors within the blue peak of the $u - r$ distribution, as well as within the GV region between the blue and red peaks. This finding is consistent in both the simulated and observed samples.

This analysis helps to understand the main discrepancy between our model galaxies and the GAMA sample, as noted in Figure 7.5, i.e. the different color distribution of $S_{250\mu\text{m}} \geq 100$ mJy galaxies. Our model produces a non negligible number of blue, $S_{250\mu\text{m}} \geq 100$ mJy galaxies with masses $10 \leq \log M_{\text{stars}}/M_{\odot} < 10.5$, whereas the GAMA sample shows a lower fraction of blue galaxies in this mass range, with the observed population peaking at redder colors compared to our model predictions. We argue that the primary shortcoming of our model is the overproduction of blue galaxies in this mass range, rather than an issue with the sub-mm emission itself. Indeed, when plotting Figure 7.5 for $\log M_{\text{stars}}/M_{\odot} < 10$ galaxies (not shown here for brevity), the distribution of $S_{250\mu\text{m}} \geq 25$ mJy and $S_{250\mu\text{m}} \geq 100$ mJy galaxies peaks on the blue peak in both the observed and simulated sample.

The above considerations do not rely on any specific definition of the GV but are solely derived from the positions of the blue and red peaks in the color distribution. We can further analyze the results using the explicit definitions of BC, GV, and RS. To accomplish this, we categorize galaxies into these three classes (and also no-RS galaxies for the simulated sample) in both the model and observed samples, as detailed in Section 7.4. Figure 7.7 shows the fraction of galaxies with a 250 μ m flux larger than 25 mJy as a function of stellar mass for both our model and observations. Across the whole sample (grey points), the fraction of galaxies with $S_{250\mu\text{m}} \geq 25$ mJy generally increases with stellar mass up to $M_{\text{stars}} \simeq 10^{10} - 10^{11} M_{\odot}$, after which the slope becomes shallower. The 250 μ m emission is strongly correlated with the dust content of galaxies. Indeed, this trend mirrors the $M_{\text{stars}} - M_{\text{dust}}$ relation, which also flattens above a similar stellar mass (e.g., [Beeston et al. 2018](#) for GAMA and [Parente et al. 2023](#) for our model galaxies). This is because galaxies in this stellar mass range have relatively low quantities of gas (and dust) due to the quenching process. In our model, this is regulated by radio-mode AGN feedback.

We also note that the $f(S_{250\mu\text{m}} \geq 25 \text{ mJy})$ fraction is typically higher, by a modest factor, in our model compared to GAMA. This is due to slightly larger dust content in intermediate-mass galaxies in our model sample (see top panel of Figure 5.9), which is linked with the overproduction of blue, intermediate-mass galaxies in our model as noted above.

A more intriguing insight comes from the analysis of $f(S_{250\mu\text{m}} \geq 25 \text{ mJy})$ for the different considered populations. In both the model and observed samples, BC and GV galaxies with $\log M_{\text{stars}}/M_{\odot} \lesssim 10^{11}$ are more likely to have $S_{250\mu\text{m}} \geq 25$ mJy, while the fraction is generally lower for RS galaxies. At large stellar masses ($M_{\text{stars}} \gtrsim 10^{11} M_{\odot}$), the differences among the classes reduce. In our model, this behaviour is due to the large fraction of rejuvenating galaxies found in this mass range. These galaxies are those that were previously passive (i.e. they were in the RS), but now have bluer colors (meaning that they belong to the no-RS class, since a BC is not explicitly identified in this mass range) as a consequence of a rejuvenation event (a starburst). Despite featuring blue-to-green colors, these rejuvenating systems have relatively low 250 μ m emission (see discussion in Section 7.8), lowering the fraction of galaxies with $S_{250\mu\text{m}} \geq 25$ mJy.

To conclude this Section, we highlight that our results are independent of the 25 mJy threshold, as the same qualitative behavior is observed with higher thresholds, such as 50 mJy or 100 mJy. While the adopted GV definition provides a quantitative, albeit approximate, understanding of the sub-mm properties of different populations, we stress that the main result

of this Section is independent of the GV definition. The result is that observed and simulated galaxies in both the blue peak and the transitioning region of the color ($u-r$) distribution exhibit substantial sub-mm emission, in contrast to those in the red peak.

7.7 Evolution in the color- $S_{250\mu\text{m}}$ diagram

This Section is devoted to a careful examination of the sub-mm emission during the evolution of our model galaxies, with particular focus on the GV phase. It might be argued that the substantial sub-mm emission in GV galaxies occurs because these are fundamentally blue galaxies (i.e., star-forming galaxies) with a significant amount of dust, which reddens their optical colors and fuels the sub-mm emission. However, this is not the case, as already indicated in Section 7.5 (Figure 7.4): only $\sim 6.5\%$ of blue galaxies move to the GV as a result of dust attenuation. Model galaxies in the GV (on average) exhibit intermediate sSFR and intrinsic color. Thus, they represent a transitioning population, rather than merely a dust-reddened one.

The reason for the sub-mm emission of GV galaxies is that, while these galaxies experience a rapid quenching that quickly reduces their sSFR and turns their color green, the amount of dust in these objects remains relatively high, enabling a conspicuous $250\mu\text{m}$ emission. We will show this comprehensively in the following sections.

7.7.1 Model GV redshift evolution

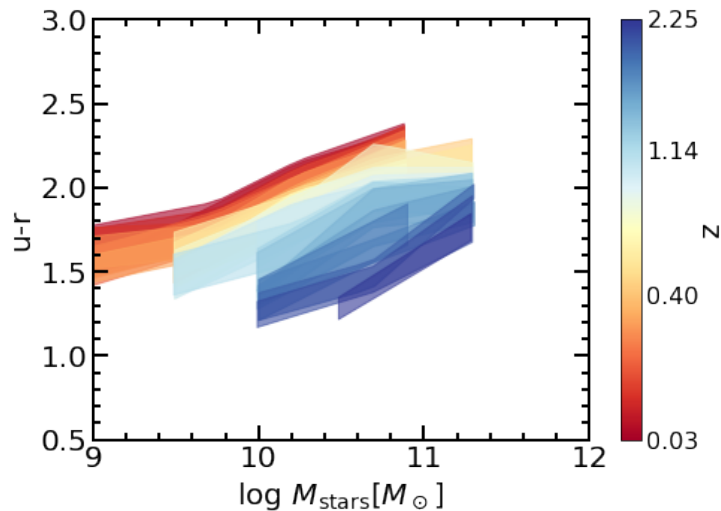


FIGURE 7.8: GV evolution with redshift ($0.03 \leq z \leq 2.25$) as identified in our simulation with the method described in Section 7.4.

Since we are interested in the evolution of the properties of our model galaxies, we need to adopt an evolving definition of the GV, which is expected to vary with redshift. We exploit the definition of GV introduced in Section 7.4 in order to identify it in all the snapshots of our simulations. We only use $z \leq 2.25$ outputs, but this choice does not impact our results given the young age of the Universe at this redshift. The GV(s) are reported as shaded regions with different redshift-dependent colors in Figure 7.8. The two key features to note are the mass and color evolution of these regions. The masses where a GV is identified by our method are generally large at high- z , while they cover nearly the whole range as the redshift decreases. This is because the RS is clearly identified only in the large mass range at high- z . In the low mass range, our method identifies a BC and a no-BC region. Also, we note that the color of

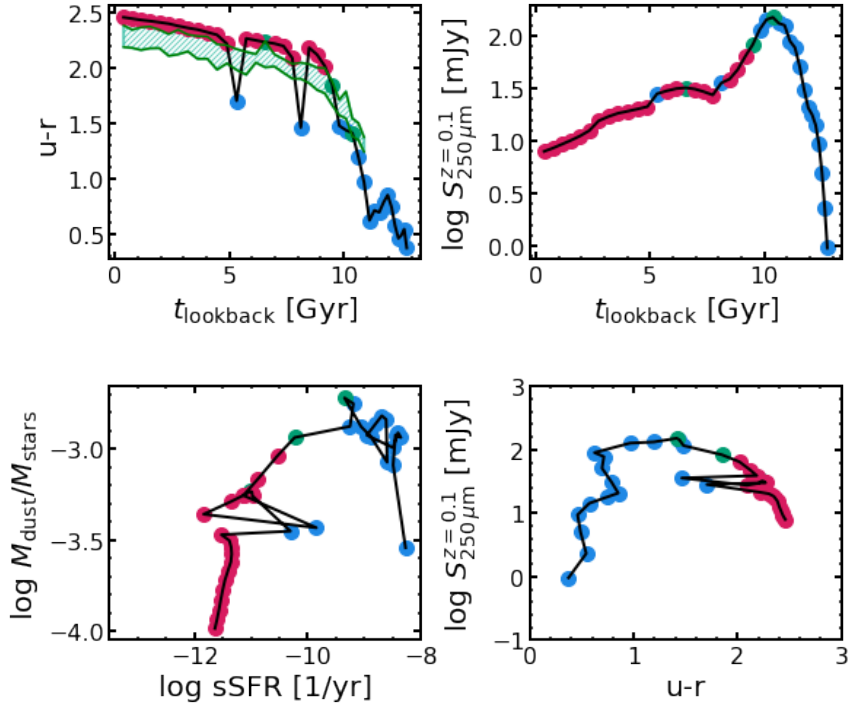


FIGURE 7.9: Evolution of a $z \approx 0$ red sequence galaxy with $M_{\text{stars}}^{z=0} \approx 10^{10.9} M_{\odot}$. The top panels display the rest-frame color ($u - r$) evolution and the $S_{250\mu\text{m}}^{z=0.1}$. The bottom panels illustrate the evolution of the galaxy in the sSFR- $M_{\text{dust}}/M_{\text{stars}}$ and color- $S_{250\mu\text{m}}^{z=0.1}$ diagrams. Each point corresponds to a snapshot of the simulation and is colored accordingly to the galaxy position at that given time in the M_{stars} -color diagram (i.e., blue, green, or red for the BC, GV, or RS, respectively) according to the z -dependent GV definition given in Section 7.7.1. The reference GV evolution is shown in the first panel.

the GV progressively becomes redder as the redshift decreases, mirroring the color evolution of the blue and red populations, both bluer at high- z .

7.7.2 A red galaxy case study

We begin by analyzing the evolution of a red galaxy at $z \approx 0$, with $M_{\text{stars}}^{z=0} \approx 10^{10.9} M_{\odot}$. This is illustrated in Figure 7.9, which shows the evolution of the sSFR, the dust-to-stellar mass ratio ($M_{\text{dust}}/M_{\text{stars}}$), the color ($u - r$), and the 250 μm emission. For the latter, we use $S_{250\mu\text{m}}^{z=0.1}$, which is $S_{250\mu\text{m}}$ calculated assuming the galaxy is at $z = 0.1$ at each time. This particular galaxy was selected because its evolution is relatively smooth in terms of star formation, aside from a few bursty episodes, making it an ideal example for pedagogical purposes. The galaxy is classified as part of the BC, GV or RS, represented by blue, green, and red points, respectively, based on the redshift-dependent definition of the GV outlined in Section 7.7.1.

The sSFR of the galaxy gradually decreases, leading to a reddening of its color. Around $t_{\text{lookback}} \approx 10$ and 9 Gyr, the galaxy transitions into the GV and eventually the RS. The key point to emphasize is that during this transition from the BC to the RS, the galaxy color reddens significantly, while $S_{250\mu\text{m}}^{z=0.1}$, though decreasing, remains comparable to its high levels during the BC phase. In other words, while the $u - r$ color evolves rapidly and consistently towards redder values, the $S_{250\mu\text{m}}^{z=0.1}$ in the transition (GV) region stays relatively high. This results in a semi-circular trajectory in the color- $S_{250\mu\text{m}}^{z=0.1}$ diagram, where the GV region is characterized by intermediate colors and high 250 μm fluxes. This pattern is also reflected in

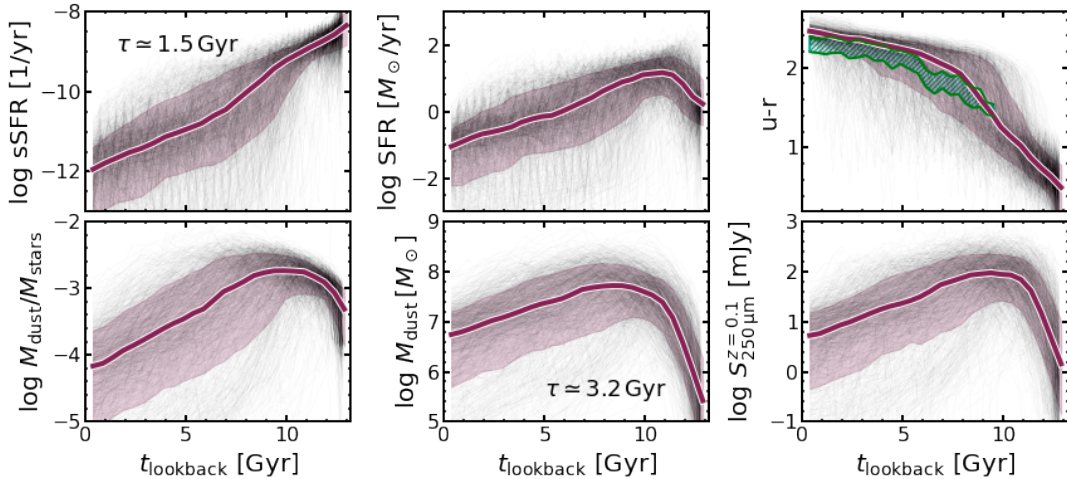


FIGURE 7.10: Time evolution of some key quantities for a sample of $z \sim 0$ red galaxies. In a clockwise order, we show the sSFR, SFR, color $u - r$, $S_{250\mu\text{m}}^{z=0.1}$ flux, dust mass and specific dust mass. An evolving GV (assuming the median mass evolution of the sample) is shown in the $(u - r) - \text{time}$ plot. Tracks of individual galaxies in each diagram are shown in grey lines, while we report the median and 16 – 84th percentiles dispersion of all the tracks in blue. Finally, we report the typical e -folding timescales associated to the (decaying) evolution of the sSFR and dust mass.

other galaxy properties, particularly dust content and SFR, both normalized to stellar mass. Although the sSFR consistently decreases, the specific dust mass in the GV region remains quite high ($M_{\text{dust}}/M_{\text{stars}} \gtrsim 10^{-3}$), comparable to the values observed during the blue phase.

As the galaxy becomes redder, its $S_{250\mu\text{m}}$ continues to decline, along with its specific dust mass. During this phase, two noteworthy events occur at $t_{\text{lookback}} \approx 5$ and 8 Gyr, when the galaxy experiences two bursts of star formation. Each burst temporarily makes the galaxy bluer, moving it from the RS back to the BC for a single snapshot. We refer to galaxies undergoing these events as rejuvenated. However, during these rejuvenation-induced BC phases, the $S_{250\mu\text{m}}$ remains quite low because the dust production has not had sufficient time to accumulate enough mass to produce significant $250\mu\text{m}$ emission. We will discuss some interesting implications of this in Section 7.8 concerning rejuvenating systems.

7.7.3 A red statistical sample

We now turn to the analysis of the evolution of the same key quantities in a large statistical sample of $\sim 2,000$ red galaxies at $z \approx 0$. These are the sSFR, dust mass, $(u - r)$ color, $S_{250\mu\text{m}}^{z=0.1}$, and are shown in Figure 7.10. This analysis, averaged over the entire sample, highlights the key features relevant for interpreting the sub-mm flux during the GV transition.

Both the sSFR and $(u - r)$ color evolve monotonically towards a passive (or red) state. However, this is not the case for the dust content (and specific dust content), which reaches a maximum at $t_{\text{lookback}} \sim 9$ Gyr. Notably, this peak does not coincide with the peak in the SFR, which occurs earlier at $t_{\text{lookback}} \sim 11$ Gyr. This discrepancy is due to two main factors. First, once dust is produced by stars, it remains in the ISM until it is removed by other processes such as astration, galactic outflows, or destruction by SNe. On the contrary, the SFR is an instantaneous quantity, meaning that it keeps track of a relatively short period of the evolution of the galaxy. Second, and more importantly, the dust budget can increase due to grain growth in the ISM, leading to a delay of $\gtrsim 1$ Gyr between the SFR peak and the dust abundance peak.

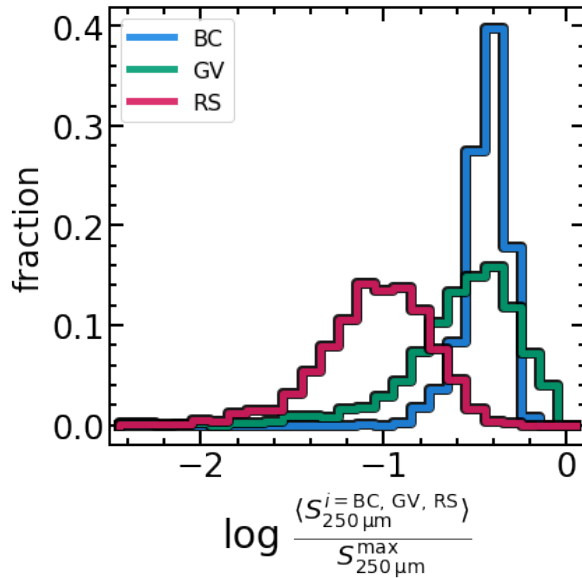


FIGURE 7.11: Time averaged $S_{250\mu\text{m}}^{z=0.1}$ flux normalized to the maximum flux reached during the evolution of each galaxy when it was in the BC, GV, or RS (represented by blue, green, and red histograms, respectively). To construct the histogram, the evolution of the $S_{250\mu\text{m}}^{z=0.1}$ flux was analyzed for each galaxy in a sample of $\sim 2,000$ red galaxies at $z \simeq 0$, and the BC-GV-RS classification was performed according to the redshift evolving GV definition detailed in Section 7.7.1. For each galaxy, a time averaged $S_{250\mu\text{m}}^{z=0.1}$ flux was derived for each phase (BC-GV-RS) and then normalized to the maximum $S_{250\mu\text{m}}^{z=0.1}$ reached.

Another way to examine this is by comparing the e -folding decay timescales of the sSFR and dust abundance, as shown in Figure 7.10. The timescale for dust abundance is roughly twice as long as that for sSFR, indicating a slower decline in dust content.

As a result, the sub-mm $S_{250\mu\text{m}}$ emission remains relatively high throughout the GV transition due to the large dust content. This is clearly illustrated in Figure 7.11, where the time-averaged $S_{250\mu\text{m}}^{z=0.1}$ flux is shown for each of the BC, GV, and RS phases. These values are normalized to the maximum $250\mu\text{m}$ flux achieved during the evolution of each galaxy. The analysis reveals that, on average, the sub-mm flux during the BC and GV phases is close to the peak flux reached by the galaxies. Median values for the BC and GV phases are $\sim 42\%$ and $\sim 40\%$ of the maximum, respectively. In contrast, the mean flux during the red phase is significantly lower, $\lesssim 15\%$ of the maximum.

7.7.4 The color- $S_{250\mu\text{m}}$ diagram

To conclude, we show the color- $S_{250\mu\text{m}}$ diagram for our model galaxies at $z \leq 0.08$ in Figure 7.12. Building on the previous analysis of evolutionary trends, we depict a schematic evolution path in this diagram using a yellow arrow. The key message is that sub-mm emission increases during the BC phase, remains high throughout the GV transition, and then decreases once the galaxy evolves into the RS. Indeed, most red galaxies fall significantly below the 25 mJy threshold used here to select sub-mm emitters.

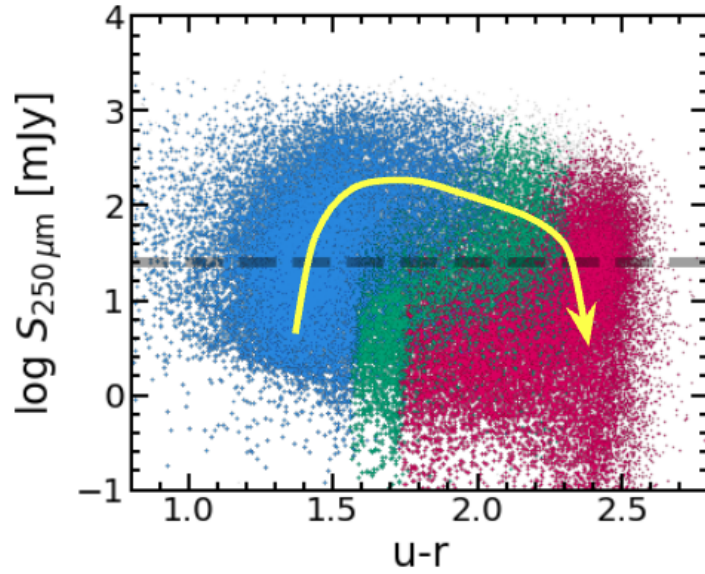


FIGURE 7.12: Color- $S_{250\mu\text{m}}$ diagram for our $z \leq 0.08$ model galaxies in the BC, GV, and RS (represented by blue, green, and red points, respectively). The dashed black line represents the 25 mJy threshold adopted in this work to define sub-mm emitters. The yellow arrow schematically represents the (standard) evolution of a sub-mm bright galaxy in this diagram.

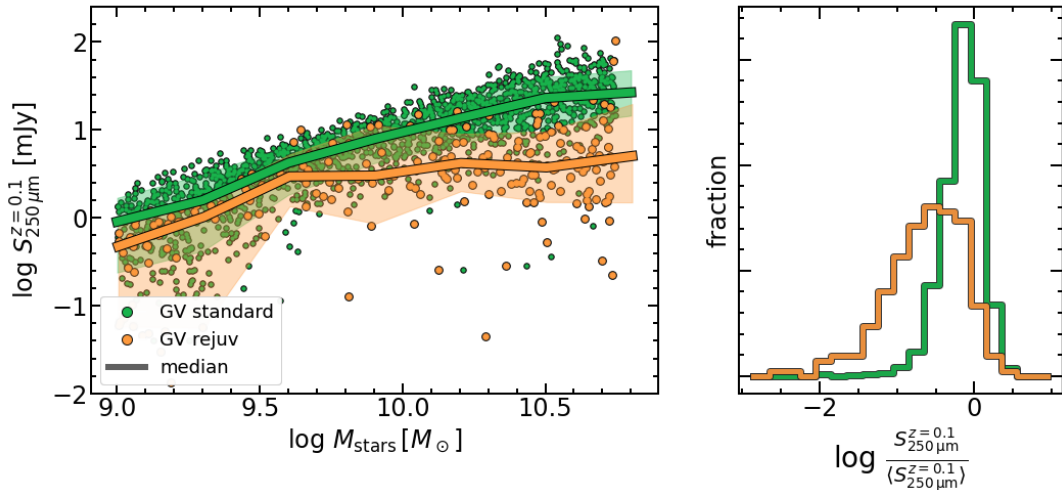


FIGURE 7.13: *Left panel:* $S_{250\mu\text{m}}^{z=0.1}$ as a function of stellar mass for $z \approx 0$ GV galaxies (represented by filled circles). Standard GV galaxies are in green, while rejuvenating systems (transitioning from the RS to the GV) are depicted in orange. Median trends of the two galaxy samples are shown as solid lines, while shaded area refer to the 16 – 84th percentile dispersions. *Right panel:* Distribution of the $250\mu\text{m}$ flux normalized to the $250\mu\text{m}$ flux averaged over the entire galaxy evolution for both standard and rejuvenating GV galaxies (green and orange, respectively).

7.8 Rejuvenating systems

The differential variation in color and sub-mm flux has important implications for rejuvenating systems within the GV. Not all galaxies in the GV come directly from the BC. Some of them are undergoing a rejuvenation process, marked by a reverse quenching scenario in which galaxies shift from a quiescent to a star-forming state, often driven by factors such as increased gas supply, which is frequently the result of mergers in our SAM.

In Figure 7.13 (*left panel*), we show the predicted $S_{250\mu\text{m}}^{z=0.1}$ as a function of stellar mass for $z \simeq 0$ galaxies in the GV. We differentiate between quenching GV galaxies and rejuvenating systems, which are transitioning back from the RS to the GV. Rejuvenating galaxies are operationally defined as those that spent at least 3 out of 5 snapshots in the RS just before moving to the GV. While this definition can be somewhat ambiguous due to the episodic nature of star formation and color evolution, it helps identify galaxies that are not simply transitioning from a star-forming state. However, we have also verified that alternative plausible definitions⁸ of rejuvenating galaxies yield similar results. Typically, rejuvenating systems have $S_{250\mu\text{m}}$ values lower than the GV average. As previously discussed in Section 7.7.2, this occurs because rejuvenating systems experience bursts of star formation that temporarily make their colors bluer, but they maintain relatively low dust masses, leading to lower $250\mu\text{m}$ emission.

In the *right panel* of the same figure, we present the distribution of $S_{250\mu\text{m}}^{z=0.1}$, normalized to the mean $S_{250\mu\text{m}}$ for each galaxy (averaged over its entire evolution). Rejuvenating systems show lower $S_{250\mu\text{m}}^{z=0.1}$ fluxes than standard GV galaxies, typically by a median factor of $\simeq 2$.

In summary, sub-mm emission proves to be a valuable indicator for identifying rejuvenating systems within the GV. Although these systems have green colors similar to other GV galaxies, their sub-mm flux is on average lower, due to their shorter time available to rebuild their dust content.

7.9 Summary and Conclusions

In this work we have studied the $250\mu\text{m}$ sub-mm emission of galaxies during their transition through the GV. We utilized predictions from a SAM of galaxy evolution that incorporates processes for the formation and evolution of dust grains within a galactic context. These predictions were employed to estimate observable properties of galaxies, including sub-mm emission, using the radiative transfer code GRASIL, which simulates both dust attenuation and thermal emission of dust grains.

We concentrate on galaxies at $z \leq 0.08$, whose distribution in the $u-r$ color-mass diagram (Figure 7.1) aligns well with GAMA/ H -ATLAS observations, showing a clear color bimodality, although some tensions are highlighted, especially at low and large stellar masses. To analyze the properties of galaxies in the GV, we introduce a new, precise definition of the GV that can be applied to any color-mass diagram distribution (Section 7.4). This allows us to make consistent comparisons between our simulation results and observational data, although there is no perfect match in terms of absolute colors.

With our new definition, we analyzed various properties of the different galaxy populations identified in the color-mass diagram, mainly the BC, GV and RS. We found that dust-induced attenuation does not significantly alter the distribution of our model galaxies in this diagram (Figure 7.4). Galaxies in the GV, as seen in the dust-attenuated color-mass diagram, are generally also identified as transitioning galaxies in a dust-free (or intrinsic) color-mass diagram.

⁸These include considering galaxies that, just before moving to the GV, have spent (i) at least 5 out of 10 snapshots in the RS, and (ii) 3 consecutive snapshots in the RS.

When examining sub-mm emission across different populations, we observed that both the BC and GV host a substantial number of sub-mm emitters, defined as those with $250\ \mu\text{m}$ emission exceeding 25 mJy. This is true for both our simulated galaxy sample and GAMA observations (Figure 7.7). In contrast, galaxies in the RS exhibit a lower-than-average fraction of sub-mm emitters in both samples. These differences are in place for stellar masses of $\log M_{\text{stars}}/M_{\odot} \lesssim 10^{11}$. At higher stellar masses, the fraction of sub-mm emitters is similar across the various populations. We interpret this finding in the context of the numerous rejuvenating systems outside the RS in this mass range, which have blue colors but relatively low sub-mm emission.

We use our model to further investigate the sub-mm emission of galaxies during the GV phase. The sSFR of galaxies evolves (on average) in a generally monotonic fashion, causing their color to gradually redden. In contrast, $250\ \mu\text{m}$ emission – which is associated with the dust content in galaxies – increases during the BC phase and remains high as galaxies transition toward the RS, making GV galaxies significant sub-mm emitters (Figure 7.9 and 7.10). When averaged over time, the $S_{250\ \mu\text{m}}^{z=0.1}$ emission during a single-galaxy evolution is similar in both the BC and GV phases, being ~ 4 times higher than during the RS phase (Figure 7.11).

Finally, we have highlighted that sub-mm emission can help identifying rejuvenating GV galaxies. Specifically, at a given stellar mass, GV galaxies undergoing a rejuvenation event exhibit median $250\ \mu\text{m}$ emission that is 0.1 – 0.4 dex lower compared to *standard* GV galaxies (Figure 7.13). This lower emission is because rejuvenating galaxies become bluer due to a starburst, not having had sufficient time to accumulate enough dust to produce significant sub-mm emission. Testing this prediction on an observed sample along with other techniques for identifying rejuvenating systems would be extremely interesting.

Part III

Conclusions

8

Closing remarks and perspectives

The results presented in this Thesis cover various aspects of dust in galaxy evolution, including grain properties, cosmic abundance across different epochs, galaxy dust content in different large-scale environments, and the impact of dust on the observability of galaxies. These insights were made possible by exploiting advanced tools such as cosmological simulations – both hydrodynamic and semi-analytic – that are equipped with a state-of-the-art model for dust production and evolution in galactic environments.

Cosmological simulations of galaxy evolution incorporate a wide range of physical processes, enabling us to compare the simulated galaxy populations with observations in order to test the underlying physics thought to drive galaxy evolution. The dust model, integrated into these simulations, can predict the abundance and properties of dust grains throughout the simulation, in a manner that is self-consistent with other processes like star formation, metal enrichment, and outflows. Incorporating a dust model into galaxy evolution simulations is advantageous for two main reasons:

- (i) **enhancing the predictive power of simulations:** this allows for comparison with and interpretation of a broader range of observations;
- (ii) **improving the physical scheme of simulations,** by including dust-related processes which can have an impact on galaxy evolution.

This Thesis mainly addresses the first point by comparing a variety of simulation predictions – such as grain properties, dust abundances inside and outside galaxies, dust content in different regions of the cosmic web, and dust emission – with observational data. The second point, while only marginally explored in this work, is also significant. The simulations are practically ready to incorporate additional physical processes, starting with the predictions made by the dust model, and an example of this will be provided later.

In this Chapter, I summarize the main achievements of this Thesis, along with some other projects carried out with the tools developed here. I also highlight potential future research directions.

8.1 Results summary

- **Dust in hydrodynamic cosmological simulations**

Chapter 4 focuses on dust evolution in hydrodynamic simulations, based on the published work [Parente et al. \(2022\)](#). In that study, we utilized our detailed dust model ([Granato et al., 2021](#)), integrated with the MUPPI star formation and feedback sub-resolution model ([Murante et al., 2010, 2015](#); [Valentini et al., 2020](#)), to explore various properties of the simulated galaxy population. The dust model employed here enables the tracking of grains with different chemical compositions and sizes, allowing us to examine how dust properties vary across different galaxies. The key finding of this study is the predicted evolution of grain

properties over a galaxy lifetime, driven by the dominant role of stellar production at early stages and grain accretion in the dense ISM at later stages. This leads to a clear dichotomy in the chemical composition and size of grains across the galaxy population.

Another key goal of this work was to evaluate the performance of the MUPPI sub-resolution model in cosmological volumes. The model predictions for general galaxy population properties, such as SMFs and the cosmic SFRD, did not align well with observations. This indicates that the MUPPI model, which is optimized for zoom-in simulations of disc-like galaxies, requires modifications when applied to cosmological scales. An initial effort to address this issue was made in [Parente et al. \(2022\)](#), where we explored linking the modeling of star formation with the DTG ratio in gas particle. More recently, in [Ragone-Figueroa et al. \(2024\)](#), we introduced a more physically motivated approach by implementing a model for the formation and evolution of hydrogen molecules (H_2) on grain surfaces. In addition to recalibrating the MUPPI parameters to better match observed galaxy populations with our simulations, this work fully integrates the dust model to incorporate a critical physical process in galaxy evolution. Since molecular clouds are the primary sites of star formation, our self-consistent model allows for a more realistic treatment of this process within the simulations.

• Cosmic dust abundance evolution

The cosmic evolution of dust abundance inside and outside galaxies is the main topic of Chapter 5, which is based on [Parente et al. \(2023\)](#). The study particularly focuses on investigating the causes behind the observed drop in galactic dust abundance at $z \lesssim 1$. This Chapter discusses the integration of the dust model, previously used in hydrodynamic simulations, into the L-GALAXIES SAM ([Henriques et al., 2020](#)). In addition to incorporating the full dust model, the SAM has been enhanced with a new approach for modelling disc instabilities, a secular process that contributes to the growth of both the spheroidal components of galaxies and their central SMBHs.

The scaling relations involving dust show good agreement with observations for $0 \leq z \leq 2.5$, demonstrating the successful implementation of the dust model. However, there is a noticeable scarcity of very dust-rich galaxies at $z \geq 1$ in the simulations compared to the still limited observational data available. This issue is not unique to our model, as it is also a challenge observed in other galaxy formation models. The updated disc instability model also improves predictions related to the morphology of local galaxies. Regarding galactic dust abundance, the model effectively reproduces the observed decline at $z \lesssim 1$. This outcome relies on the disc instability model, which slightly enhances SMBH growth and subsequently increases galaxy quenching through radio-mode feedback, leading to a reduction in both gas and dust content. This result emphasizes that not only dust-related processes but a wide range of physical processes included in these simulations can significantly impact model predictions concerning dust.

As for the extra-galactic dust abundance, it continuously grows with decreasing redshift and does not show clear signs of drops, neither in our simulations nor in observations, although the latter determinations are rather uncertain.

• Dust across the cosmic web

The SAM predictions have been adopted to study also the abundance of dust in the local Universe across different regions of the cosmic web – voids, walls, filaments, and nodes. This has been discussed in Chapter 6, which is based on [Parente et al. \(2024a\)](#). While it is well established that galaxy properties are influenced by the large-scale environment, there has been a lack of studies examining dust abundance in this context. By using various methods

to identify cosmic web environments, we compare the model predictions with observations from SDSS and GAMA data, focusing on star formation and dust mass.

The result is that, at fixed stellar mass, galaxies up to $M_{\text{stars}} \simeq 10^{10} - 10^{11} M_{\odot}$ are more star forming and dust rich in less dense environments, such as voids. This is because these galaxies have experienced delayed evolution (they are younger), as a result of the environmental assembly bias. In contrast, the SFR and dust mass in more massive galaxies are nearly independent of their environment. This result is due to the SMBH-induced quenching, which operates similarly across all environments. Specifically, the in situ SMBH growth driven by disc instabilities is essential to accurately reproduce the observed amount of quenched and dust poor massive galaxies in less dense environments, such as voids and walls. The agreement between our model and observations underscores the significance of in situ SMBH growth in our galaxy evolution paradigm. Specifically, this leads to a more pronounced downsizing effect in less clustered environments, as also shown by the observational analysis of Domínguez-Gómez et al. (2023).

• Dust sub-mm emission in Green Valley galaxies

Including dust in galaxy evolution simulations is important also for predicting the observable SED, which is heavily affected by the absorption and emission of grains. This is possible by coupling model predictions with RT computations able to simulate starlight propagation in a dusty medium. This has been done in Chapter 7, based on Parente et al. (2024b) where SAM predictions are coupled with the RT code GRASIL (Silva et al., 1998). In addition to establishing a pipeline for generating directly observable predictions from our model, the goal of this work was to study the sub-mm emission in galaxies transitioning through the optical Green Valley (GV).

While these galaxies exhibit intermediate optical colors due to their intermediate SFRs, they still feature significant sub-mm emission, as indicated by both our model and observational data. This sub-mm emission results from the relatively high dust content, whose decline is delayed with respect to that of the SFR, which is responsible for their characteristic green optical color. Another interesting finding from this analysis is that rejuvenating systems within the GV are predicted to have relatively low sub-mm emission compared to the whole GV population, offering a potential diagnostic tool for identifying these rejuvenating systems.

8.2 Other projects and perspectives

The tools developed in this Thesis offer valuable and adaptable starting point for various research lines in the field of galaxy evolution. Notably, the SAM introduced in Parente et al. (2023) has received the interest from the observational community, leading to collaborations where model predictions are used to help interpret observational data.

This is the case of Nadolny et al. (2024), where we examined the gas and dust removal timescales in our model for Early Type Galaxies (ETGs) and their progenitors at $0.02 \leq z \leq 0.32$, finding strong agreement with observational data. The main factor driving the reduction in gas and dust is the radio-mode feedback from SMBHs, whose growth is mainly driven by mergers. These are also responsible for the morphological transformations in most of the analyzed ETGs. Interestingly, we found that none of the dust destruction mechanisms in the model – such as astration, ejection, or SN destruction – significantly impact the dust removal timescale.

Another example is Traina et al. (2024), where we derived the DMF and cosmic dust density from the A³COSMOS database on a broad redshift range ($0.5 < z < 6$). When comparing the cosmic dust density with various model predictions, including those from both hydrodynamic simulations and SAMs available in the literature, we found that none of the

existing models successfully reproduce both the high normalization of dust density at $z \gtrsim 1$ and the already discussed drop at $z \lesssim 1$. In particular, in simulations there is a dearth of very dusty galaxies at high redshift. Using the SAM introduced in this Thesis, we investigated this lack of dusty galaxies at high redshift and concluded that the only dust process capable of producing the observed dust amounts is grains accretion in molecular clouds. However, we also noted (as discussed in Chapter 5) that the shortage of dusty galaxies might be related to other limitations of the galaxy evolution model, such as the under representation of highly star forming galaxies.

In addition to continuing these collaborations to use the model for interpreting observational data, I plan to further exploit the model in two main ways. First, I aim to use its predictions, possibly with minor modifications, to study other quantities influenced by dust, including its IR emission through the SAM+GRASIL pipeline.

One ready-to-go project is analyzing the chemical abundance and dust depletion patterns in MW-like and elliptical galaxies, to test the chemical aspect of the dust model. Extending this study to higher redshift, where dust composition is unknown, would be interesting as well. Another natural outcome of the model is investigating sub-mm number counts across a wide range of redshifts, particularly in relation to dust evolution and cosmic dust density.

On the other hand, I aim to extend the SAM by taking advantage of the dust model. Some potential developments, which will require careful implementation, include: *(i)* improving the dust model in terms of grain sizes and chemical composition; *(ii)* incorporating the molecular formation on grain surfaces, as we already done in hydrodynamic simulations (Ragone-Figueroa et al., 2024); and *(iii)* using dust to refine the modeling of galactic outflows (both SN- and AGN-driven), including the effects of dust radiation pressure.

Although these goals are challenging, they are definitely within reach and would offer a more complete understanding of the physical processes taking place in the galaxies that populate our Universe.

Bibliography

- Abadi M. G., Moore B., Bower R. G., 1999, *MNRAS*, 308, 947
- Abazajian K. N., et al., 2009, *ApJS*, 182, 543
- Ahumada R., et al., 2020, *ApJS*, 249, 3
- Alfaro I. G., Rodriguez F., Ruiz A. N., Lambas D. G., 2020, *A&A*, 638, A60
- Alfaro I. G., Ruiz A. N., Luparello H. E., Rodriguez F., Garcia Lambas D., 2021, *A&A*, 654, A62
- Alfaro I. G., Rodriguez F., Ruiz A. N., Luparello H. E., Lambas D. G., 2022, *A&A*, 665, A44
- Andreani P., Miyamoto Y., Kaneko H., Boselli A., Tatematsu K., Sorai K., Vio R., 2020, *Astronomy & Astrophysics*, 643, L11
- Angulo R. E., Hilbert S., 2015, *MNRAS*, 448, 364
- Angulo R. E., White S. D. M., 2010, *MNRAS*
- Aoyama S., Hou K.-C., Shimizu I., Hirashita H., Todoroki K., Choi J.-H., Nagamine K., 2017, *MNRAS*, 466, 105
- Aoyama S., Hou K.-C., Hirashita H., Nagamine K., Shimizu I., 2018, *MNRAS*, 478, 4905
- Aoyama S., Hirashita H., Nagamine K., 2020, *MNRAS*, 491, 3844
- Aragón-Calvo M. A., Jones B. J. T., van de Weygaert R., van der Hulst J. M., 2007, *A&A*, 474, 315
- Aragón-Calvo M. A., Platen E., van de Weygaert R., Szalay A. S., 2010, *ApJ*, 723, 364
- Aragon-Calvo M. A., Neyrinck M. C., Silk J., 2014, *arXiv e-prints*, p. arXiv:1412.1119
- Artale M. C., Zehavi I., Contreras S., Norberg P., 2018, *MNRAS*, 480, 3978
- Asano R. S., Takeuchi T. T., Hirashita H., Inoue A. K., 2013a, *Earth, Planets, and Space*, 65, 213
- Asano R. S., Takeuchi T. T., Hirashita H., Nozawa T., 2013b, *MNRAS*, 432, 637
- Asplund M., Grevesse N., Sauval A. J., Scott P., 2009, *Annual Review of Astronomy and Astrophysics*, 47, 481
- Athanassoula E., 2008, *MNRAS: Letters*, 390, L69
- Baldry I. K., et al., 2012, *MNRAS*, pp no–no
- Baldry I. K., et al., 2018, *MNRAS*, 474, 3875
- Bamford S. P., et al., 2009, *MNRAS*, 393, 1324
- Barlow M. J., 1978, *MNRAS*, 183, 367
- Barnes J., Hut P., 1986, *Nature*, 324, 446
- Beck A. M., et al., 2016, *MNRAS*, 455, 2110
- Beeston R. A., et al., 2018, *MNRAS*, 479, 1077
- Bekki K., 2013, *MNRAS*, 432, 2298
- Bekki K., 2015, *MNRAS*, 449, 1625
- Bernatowicz T., Fraundorf G., Ming T., Anders E., Wopenka B., Zinner E., Fraundorf P., 1987, *Nature*, 330, 728
- Beygu B., Kreckel K., van der Hulst J. M., Jarrett T. H., Peletier R., van de Weygaert R., van Gorkom J. H., Aragon-Calvo M. A., 2016, *MNRAS*, 458, 394
- Beygu B., Peletier R. F., van der Hulst J. M., Jarrett T. H., Kreckel K., van de Weygaert R., van Gorkom J. H., Aragon-Calvo M. A., 2017, *MNRAS*, 464, 666
- Bianchi S., Ferrara A., 2005, *MNRAS*, 358, 379
- Bianchi S., Schneider R., 2007, *MNRAS*, 378, 973

- Bigiel F., Leroy A., Walter F., Brinks E., de Blok W. J. G., Madore B., Thornley M. D., 2008, *AJ*, 136, 2846
- Binney J., Tremaine S., 1987, Galactic dynamics. <https://ui.adsabs.harvard.edu/abs/1987gady.book.....B>
- Blitz L., Rosolowsky E., 2006, *ApJ*, 650, 933
- Bocchio M., Jones A. P., Slavin J. D., 2014, *A&A*, 570, A32
- Bond J. R., Cole S., Efstathiou G., Kaiser N., 1991, *ApJ*, 379, 440
- Bondi H., 1952, *MNRAS*, 112, 195
- Bournaud F., Dekel A., Teyssier R., Cacciato M., Daddi E., Juneau S., Shankar F., 2011, *ApJ*, 741, L33
- Boylan-Kolchin M., Ma C.-P., Quataert E., 2005, *MNRAS*, 362, 184
- Boylan-Kolchin M., Springel V., White S. D. M., Jenkins A., Lemson G., 2009, *MNRAS*, 398, 1150
- Bradamante F., Matteucci F., D’Ercole A., 1998, *A&A*, 337, 338
- Bryan G. L., Norman M. L., 1998, *ApJ*, 495, 80
- Bryan G. L., et al., 2014, *ApJS*, 211, 19
- Bullock J. S., Kolatt T. S., Sigad Y., Somerville R. S., Kravtsov A. V., Klypin A. A., Primack J. R., Dekel A., 2001, *MNRAS*, 321, 559
- Burke J. R., Silk J., 1974, *ApJ*, 190, 1
- Byrne L., Christensen C., Tsekitsidis M., Brooks A., Quinn T., 2019, *ApJ*, 871, 213
- Callingham T. M., et al., 2019, *MNRAS*, 484, 5453
- Calura F., Pipino A., Matteucci F., 2008, *A&A*, 479, 669
- Calura F., Gilli R., Vignali C., Pozzi F., Pipino A., Matteucci F., 2014, *MNRAS*, 438, 2765
- Calura F., et al., 2017, *MNRAS*, 465, 54
- Calura F., et al., 2023, *MNRAS*, 523, 2351
- Casasola V., et al., 2017, *A&A*, 605, A18
- Cautun M., van de Weygaert R., Jones B. J. T., 2013, *MNRAS*, 429, 1286
- Cautun M., van de Weygaert R., Jones B. J. T., Frenk C. S., 2014, *MNRAS*, 441, 2923
- Cautun M., et al., 2020, *MNRAS*, 494, 4291
- Cavaliere A., Fusco-Femiano R., 1976, *A&A*, 49, 137
- Ceccarelli L., Duplancic F., Lambas D. G., 2021, *MNRAS*, 509, 1805
- Cen R., 2011, *ApJ*, 741, 99
- Chabrier G., 2003, *PASP*, 115, 763
- Chauke P., et al., 2019, *ApJ*, 877, 48
- Chen Y.-C., et al., 2017, *MNRAS*, 466, 1880
- Chiang I.-D. et al., 2021, *ApJ*, 907, 29
- Chiappini C., Matteucci F., Romano D., 2001, *ApJ*, 554, 1044
- Choban C. R., Kereš D., Hopkins P. F., Sandstrom K. M., Hayward C. C., Faucher-Giguère C.-A., 2022, *MNRAS*, 514, 4506
- Choban C. R., Salim S., Kereš D., Hayward C. C., Sandstrom K. M., 2024a, *arXiv e-prints*, p. arXiv:2408.08962
- Choban C. R., Kereš D., Sandstrom K. M., Hopkins P. F., Hayward C. C., Faucher-Giguère C.-A., 2024b, *MNRAS*, 529, 2356
- Christodoulou D. M., Shlosman I., Tohline J. E., 1995, *ApJ*, 443, 551
- Clark C. J. R., et al., 2015, *MNRAS*, 452, 397
- Cole S., Aragon-Salamanca A., Frenk C. S., Navarro J. F., Zepf S. E., 1994, *MNRAS*, 271, 781
- Cora S. A., et al., 2018, *MNRAS*, 479, 2

- Cortese L., et al., 2012, *Astronomy & Astrophysics*, 540, A52
- Covington M., Dekel A., Cox T. J., Jonsson P., Primack J. R., 2008, *MNRAS*, 384, 94
- Croton D. J., et al., 2006, *MNRAS*, 365, 11
- Croton D. J., et al., 2016, *ApJ Supplement Series*, 222, 22
- DESI Collaboration et al., 2016, *arXiv e-prints*, p. [arXiv:1611.00036](https://arxiv.org/abs/1611.00036)
- Dalla Vecchia C., Schaye J., 2012, *MNRAS*, 426, 140
- Damiano A., Valentini M., Borgani S., Tornatore L., Murante G., Ragagnin A., Ragone-Figueroa C., Dolag K., 2024, *arXiv e-prints*, p. [arXiv:2403.12600](https://arxiv.org/abs/2403.12600)
- Davé R., Anglés-Alcázar D., Narayanan D., Li Q., Rafieferantsoa M. H., Appleby S., 2019, *MNRAS*, 486, 2827
- Davies L. J. M., et al., 2016, *MNRAS*, 461, 458
- Davis M., Efstathiou G., Frenk C. S., White S. D. M., 1985, *ApJ*, 292, 371
- Dayal P., et al., 2022, *MNRAS*, 512, 989
- De Lucia G., Kauffmann G., White S. D. M., 2004, *MNRAS*, 349, 1101
- De Lucia G., Fontanot F., Wilman D., Monaco P., 2011, *MNRAS*, 414, 1439
- De Vis P., et al., 2017, *MNRAS*, 471, 1743
- De Vis P., et al., 2019, *Astronomy & Astrophysics*, 623, A5
- Debattista V. P., Mayer L., Carollo C. M., Moore B., Wadsley J., Quinn T., 2006, *ApJ*, 645, 209
- Debuhr J., Quataert E., Ma C.-P., 2011, *MNRAS*, 412, 1341
- Dehnen W., Read J. I., 2011, *European Physical Journal Plus*, 126, 55
- Dell’Agli F., García-Hernández D. A., Schneider R., Ventura P., La Franca F., Valiante R., Marini E., Di Criscienzo M., 2017, *MNRAS*, 467, 4431
- Desert F. X., Boulanger F., Puget J. L., 1990, *A&A*, 500, 313
- Devergne T., et al., 2020, *Astronomy & Astrophysics*, 644, A56
- Di Criscienzo M., et al., 2013, *MNRAS*, 433, 313
- Di Matteo T., Springel V., Hernquist L., 2005, *Nature*, 433, 604
- Dimauro P., et al., 2022, *MNRAS*, 513, 256
- Dolag K., Borgani S., Murante G., Springel V., 2009, *MNRAS*, 399, 497
- Domínguez-Gómez J., et al., 2023, *Nature*, 619, 269
- Domínguez M., Muriel H., Lambas D. G., 2001, *AJ*, 121, 1266
- Dressler A., 1980, *ApJ*, 236, 351
- Driver S. P., et al., 2009, *Astronomy and Geophysics*, 50, 5.12
- Driver S. P., et al., 2011, *MNRAS*, 413, 971
- Driver S. P., et al., 2012, *MNRAS*, 427, 3244
- Driver S. P., Robotham A. S. G., Bland-Hawthorn J., Brown M., Hopkins A., Liske J., Phillipps S., Wilkins S., 2013, *MNRAS*, 430, 2622
- Driver S. P., et al., 2018, *MNRAS*, 475, 2891
- Driver S. P., et al., 2022, *MNRAS*, 513, 439
- Dubinski J., Carlberg R. G., 1991, *ApJ*, 378, 496
- Dubois Y., et al., 2014, *MNRAS*, 444, 1453
- Dubois Y., et al., 2024, Galaxies with grains: unraveling dust evolution and extinction curves with hydrodynamical simulations, [doi:10.48550/ARXIV.2402.18515](https://doi.org/10.48550/ARXIV.2402.18515)
- Dudzevičiūtė U., et al., 2020, *MNRAS*, 500, 942
- Dunne L., Eales S. A., Edmunds M. G., 2003, *MNRAS*, 341, 589
- Dunne L., et al., 2011, *MNRAS*, 417, 1510
- Dwek E., 1998, *ApJ*, 501, 643
- Dwek E., Scalo J. M., 1980, *ApJ*, 239, 193

- Dwek E., Werner M. W., 1981, *ApJ*, 248, 138
- Dwek E., Galliano F., Jones A. P., 2007, *ApJ*, 662, 927
- Eales S., Lilly S., Webb T., Dunne L., Gear W., Clements D., Yun M., 2000, *The Astronomical Journal*, 120, 2244
- Eales S., et al., 2010, *PASP*, 122, 499
- Eales S. A., et al., 2018, *MNRAS*, 481, 1183
- Edmunds M., 2001, *MNRAS*, 328, 223
- Efstathiou G., Lake G., Negroponte J., 1982, *MNRAS*, 199, 1069
- Efstathiou G., Frenk C. S., White S. D. M., Davis M., 1988, *MNRAS*, 235, 715
- Elbaz D., et al., 2007, *Astronomy & Astrophysics*, 468, 33
- Fabian A. C., 2012, *ARA&A*, 50, 455
- Feder J., Russell K., Lothe J., Pound G., 1966, *Advances in Physics*, 15, 111
- Feldmann R., 2015, *MNRAS*, 449, 3274
- Ferrara A., Peroux C., 2021, *MNRAS*, 503, 4537
- Ferrarotti A. S., Gail H.-P., 2006, *A&A*, 447, 553
- Fisher D. B., Drory N., 2011, *ApJ*, 733, L47
- Fitzpatrick E. L., Massa D., 2007, *ApJ*, 663, 320
- Fletcher T. J., Saintonge A., Soares P. S., Pontzen A., 2020, *MNRAS*, 501, 411
- Florez J., et al., 2021, *ApJ*, 906, 97
- Fu J., Guo Q., Kauffmann G., Krumholz M. R., 2010, *MNRAS*, 409, 515
- Fu J., et al., 2013, *MNRAS*, 434, 1531
- Gail H.-P., Zhukovska S. V., Hoppe P., Trieloff M., 2009, *ApJ*, 698, 1136
- Galliano F., Dwek E., Chaniel P., 2008, *ApJ*, 672, 214
- Galliano F., et al., 2021, *Astronomy & Astrophysics*, 649, A18
- Gao L., Navarro J. F., Cole S., Frenk C. S., White S. D. M., Springel V., Jenkins A., Neto A. F., 2008, *MNRAS*, 387, 536
- Gehrz R. D., Woolf N. J., 1971, *ApJ*, 165, 285
- Ghigna S., Moore B., Governato F., Lake G., Quinn T., Stadel J., 1998, *MNRAS*, 300, 146
- Gingold R. A., Monaghan J. J., 1977, *MNRAS*, 181, 375
- Ginolfi M., Graziani L., Schneider R., Marassi S., Valiante R., Dell'Agli F., Ventura P., Hunt L. K., 2017, *MNRAS*, 473, 4538
- Gioannini L., Matteucci F., Vladilo G., Calura F., 2017, *MNRAS*, 464, 985
- Gjergo E., Granato G. L., Murante G., Ragone-Figueroa C., Tornatore L., Borgani S., 2018, *MNRAS*, 479, 2588
- Glatzle M., Graziani L., Ciardi B., 2022, *MNRAS*, 510, 1068
- Glover S. C. O., Clark P. C., 2012, *MNRAS*, 421, 9
- Gnedin N. Y., 2000, *ApJ*, 542, 535
- Gnedin O. Y., 2003, *ApJ*, 582, 141
- Graham A. W., Janz J., Penny S. J., Chilingarian I. V., Ciambur B. C., Forbes D. A., Davies R. L., 2017, *ApJ*, 840, 68
- Granato G. L., Danese L., 1994, *MNRAS*, 268, 235
- Granato G. L., Lacey C. G., Silva L., Bressan A., Baugh C. M., Cole S., Frenk C. S., 2000, *ApJ*, 542, 710
- Granato G. L., De Zotti G., Silva L., Bressan A., Danese L., 2004, *ApJ*, 600, 580
- Granato G. L., et al., 2021, *MNRAS*, 503, 511
- Graziani L., Schneider R., Ginolfi M., Hunt L. K., Maio U., Glatzle M., Ciardi B., 2020, *MNRAS*, 494, 1071
- Grogin N. A., Geller M. J., 2000, *AJ*, 119, 32

- Guo Q., et al., 2011, *MNRAS*, **413**, 101
- Haardt F., Madau P., 2001, in Neumann D. M., Tran J. T. V., eds, Clusters of Galaxies and the High Redshift Universe Observed in X-rays. p. 64 (arXiv:astro-ph/0106018), doi:10.48550/arXiv.astro-ph/0106018, <https://ui.adsabs.harvard.edu/abs/2001cghr.confE..64H>
- Haardt F., Madau P., 2012, *ApJ*, 746, 125
- Habouzit M., Pisani A., Goulding A., Dubois Y., Somerville R. S., Greene J. E., 2020, *MNRAS*, 493, 899
- Harrold J. E., Almaini O., Pearce F. R., Yates R. M., 2024, *MNRAS*, **532**, L61
- Henriques B. M. B., Yates R. M., Fu J., Guo Q., Kauffmann G., Srisawat C., Thomas P. A., White S. D. M., 2020, *MNRAS*, 491, 5795
- Hirashita H., 1999a, *A&A*, **344**, L87
- Hirashita H., 1999b, *ApJ*, **510**, L99
- Hirashita H., 2010, *MNRAS: Letters*, 407, L49
- Hirashita H., 2013, in Proceedings of The Life Cycle of Dust in the Universe: Observations. p. 27
- Hirashita H., 2015, *MNRAS*, **447**, 2937
- Hirashita H., 2022, *MNRAS*, 518, 3827
- Hirashita H., 2023, *MNRAS*, 522, 4612
- Hirashita H., Il'in V. B., 2022, *MNRAS*, 509, 5771
- Hirashita H., Inoue A. K., 2019, *MNRAS*, 487, 961
- Hirashita H., Kuo T.-M., 2011, *MNRAS*, **416**, 1340
- Hirashita H., Murga M. S., 2020, *MNRAS*, 492, 3779
- Hirashita H., Voshchinnikov N. V., 2014, *MNRAS*, **437**, 1636
- Hirashita H., Yan H., 2009, *MNRAS*, **394**, 1061
- Hirashita H., Nozawa T., Yan H., Kozasa T., 2010, *MNRAS*
- Hirschmann M., Dolag K., Saro A., Bachmann L., Borgani S., Burkert A., 2014, *MNRAS*, 442, 2304
- Hockney R. W., Eastwood J. W., 1988, Computer simulation using particles. <https://ui.adsabs.harvard.edu/abs/1988csup.book.....H>
- Hodges-Kluck E., Bregman J. N., 2014, *ApJ*, 789, 131
- Holwerda B. W., Keel W. C., Williams B., Dalcanton J. J., de Jong R. S., 2009, *The Astrophysical Journal*, 137, 3000
- Hou K.-C., Hirashita H., Nagamine K., Aoyama S., Shimizu I., 2017, *MNRAS*, **469**, 870
- Hou K.-C., Aoyama S., Hirashita H., Nagamine K., Shimizu I., 2019, *MNRAS*, **485**, 1727
- Hoyle F., Rojas R. R., Vogeley M. S., Brinkmann J., 2005, *ApJ*, 620, 618
- Hoyle F., Vogeley M. S., Pan D., 2012, *MNRAS*, 426, 3041
- Hu C.-Y., Zhukovska S., Somerville R. S., Naab T., 2019, *MNRAS*, 487, 3252
- Hubble E. P., 1925, *ApJ*, 62, 409
- Hunt L. K., et al., 2014, *A&A*, 565, A112
- Huško F., Lacey C. G., Baugh C. M., 2022, *MNRAS*, 518, 5323
- Inoue A. K., 2003, *PASJ*, **55**, 901
- Inoue A. K., 2011, *Earth, Planets, and Space*, **63**, 1027
- Irodoutou D., Thomas P. A., Henriques B. M., Sargent M. T., Hislop J. M., 2019, *MNRAS*
- Issa M. R., MacLaren I., Wolfendale A. W., 1990, *A&A*, **236**, 237
- Ivezić Ž., et al., 2019, *ApJ*, **873**, 111
- Izquierdo-Villalba D., Bonoli S., Dotti M., Sesana A., Rosas-Guevara Y., Spinoso D., 2020, *MNRAS*, 495, 4681

- Jaber M., Peper M., Hellwing W. A., Aragon-Calvo M. A., Valenzuela O., 2023, *arXiv e-prints*, p. [arXiv:2304.14387](https://arxiv.org/abs/2304.14387)
- Jaffe W., 1983, *MNRAS*, 202, 995
- Jenkins E. B., 2009, *ApJ*, 700, 1299
- Jian H.-Y., et al., 2022, *ApJ*, 926, 115
- Jing Y. P., 2000, *ApJ*, 535, 30
- Jones M. G., Haynes M. P., Giovanelli R., Moorman C., 2018, *MNRAS*, 477, 2
- Kannan R., Smith A., Garaldi E., Shen X., Vogelsberger M., Pakmor R., Springel V., Hernquist L., 2022, *MNRAS*, 514, 3857
- Katsianis A., et al., 2020, *MNRAS*, 500, 2036
- Katz N., Weinberg D. H., Hernquist L., 1996, *ApJS*, 105, 19
- Kauffmann G., Haehnelt M., 2000, *MNRAS*, 311, 576
- Kauffmann G., White S. D. M., Guiderdoni B., 1993, *MNRAS*, 264, 201
- Kauffmann G., et al., 2003, *MNRAS*, 341, 33
- Kennicutt Robert C. J., 1998, *ApJ*, 498, 541
- Kim J.-G., Ostriker E. C., Filippova N., 2021, *ApJ*, 911, 128
- Knebe A., et al., 2011, *MNRAS*, 415, 2293
- Knebe A., et al., 2018, *MNRAS*, 474, 5206
- Koutsouridou I., Cattaneo A., 2022, *MNRAS*, 516, 4194
- Kozasa T., Hasegawa H., Nomoto K., 1989, *ApJ*, 344, 325
- Kraljic K., et al., 2018, *MNRAS*, 474, 547
- Kreckel K., Joung M. R., Cen R., 2011, *ApJ*, 735, 132
- Kreckel K., Platen E., Aragón-Calvo M. A., van Gorkom J. H., van de Weygaert R., van der Hulst J. M., Beygu B., 2012, *The Astronomical Journal*, 144, 16
- Kreckel K., van Gorkom J. H., Beygu B., van de Weygaert R., van der Hulst J. M., Aragon-Calvo M. A., Peletier R. F., 2014, *Proceedings of the International Astronomical Union*, 11, 591
- Kroupa P., Tout C. A., Gilmore G., 1993, *MNRAS*, 262, 545
- Krumholz M. R., McKee C. F., Tumlinson J., 2009, *ApJ*, 693, 216
- Krumholz M. R., Leroy A. K., McKee C. F., 2011, *ApJ*, 731, 25
- Kuo T.-M., Hirashita H., Zafar T., 2013, *MNRAS*, 436, 1238
- Kuutma T., Tamm A., Tempel E., 2017, *A&A*, 600, L6
- Lacey C., Cole S., 1994, *MNRAS*, 271, 676
- Lacey C. G., et al., 2016, *MNRAS*, 462, 3854
- Lagos C., Tobar R. J., Robotham A. S. G., Obreschkow D., Mitchell P. D., Power C., Elahi P. J., 2018, *MNRAS*, 481, 3573
- Laigle C., et al., 2018, *MNRAS*, 474, 5437
- Lange R., et al., 2015, *MNRAS*, 447, 2603
- Laureijs R., et al., 2011, *arXiv e-prints*, p. [arXiv:1110.3193](https://arxiv.org/abs/1110.3193)
- Leja J., et al., 2019, *ApJ*, 877, 140
- Lewis R. S., Ming T., Wacker J. F., Anders E., Steel E., 1987, *Nature*, 326, 160
- Li Q., Narayanan D., Davé R., 2019, *MNRAS*, 490, 1425
- Li Q., Narayanan D., Torrey P., Davé R., Vogelsberger M., 2021, *MNRAS*, 507, 548
- Libeskind N. I., et al., 2018, *MNRAS*, 473, 1195
- Liffman K., 1990, *ApJ*, 355, 518
- Liffman K., Clayton D. D., 1989, *ApJ*, 340, 853
- Lilly S. J., Eales S. A., Gear W. K. P., Hammer F., Le Fevre O., Crampton D., Bond J. R., Dunne L., 1999, *ApJ*, 518, 641

- Lisenfeld U., Ferrara A., 1998, *ApJ*, 496, 145
- Liske J., et al., 2015, *MNRAS*, 452, 2087
- Liu C.-X., Pan D. C., Hao L., Hoyle F., Constantin A., Vogeley M. S., 2015, *ApJ*, 810, 165
- Loveday J., et al., 2012, *MNRAS*, 420, 1239
- Lucy L. B., 1977, *AJ*, 82, 1013
- Madau P., Dickinson M., 2014, *Annual Review of Astronomy and Astrophysics*, 52, 415
- Maio U., Dolag K., Ciardi B., Tornatore L., 2007, *MNRAS*, 379, 963
- Maiolino R., Mannucci F., 2019, *The Astronomy and Astrophysics Review*, 27
- Maiolino R., Oliva E., Ghinassi F., Pedani M., Mannucci F., Mujica R., Juarez Y., 2004a, *A&A*, 420, 889
- Maiolino R., Schneider R., Oliva E., Bianchi S., Ferrara A., Mannucci F., Pedani M., Roca Sorb M., 2004b, *Nature*, 431, 533
- Makiya R., Hirashita H., 2022, *MNRAS*, 517, 2076
- Mancini M., Schneider R., Graziani L., Valiante R., Dayal P., Maio U., Ciardi B., Hunt L. K., 2015, *MNRAS: Letters*, 451, L70
- Martin G., et al., 2018, *MNRAS*, 476, 2801
- Martínez H. J., Muriel H., Coenda V., 2016, *MNRAS*, 455, 127
- Matsuura M., et al., 2011, *Science*, 333, 1258
- Matteucci F., 2003, *The chemical evolution of the galaxy*. Kluwer Academic Publishers
- Matteucci F., Tornambe A., 1987, *A&A*, 185, 51
- Mattsson L., 2016, *Planet. Space Sci.*, 133, 107
- Mattsson L., Andersen A. C., 2012, *MNRAS*, 423, 38
- McConnell N. J., Ma C.-P., 2013, *ApJ*, 764, 184
- McKee C., 1989, in Allamandola L. J., Tielens A. G. G. M., eds, *IAU Symposium Vol. 135, Interstellar Dust*. p. 431
- McKee C. F., Krumholz M. R., 2010, *ApJ*, 709, 308
- McKinnon R., Torrey P., Vogelsberger M., 2016, *MNRAS*, 457, 3775
- McKinnon R., Torrey P., Vogelsberger M., Hayward C. C., Marinacci F., 2017, *MNRAS*, 468, 1505
- McKinnon R., Vogelsberger M., Torrey P., Marinacci F., Kannan R., 2018, *MNRAS*, 478, 2851
- Melzer A., 2019, *Physics of Dusty Plasmas: An Introduction*. Springer International Publishing, doi:10.1007/978-3-030-20260-6
- Ménard B., Fukugita M., 2012, *ApJ*, 754, 116
- Ménard B., Scranton R., Fukugita M., Richards G., 2010, *MNRAS*, 405, 1025
- Moffett A. J., et al., 2016, *MNRAS*, 462, 4336
- Monaco P., Benson A. J., De Lucia G., Fontanot F., Borgani S., Boylan-Kolchin M., 2014, *MNRAS*, 441, 2058
- Monaghan J. J., 1992, *ARA&A*, 30, 543
- Montier L. A., Giard M., 2004, *A&A*, 417, 401
- Moorman C. M., Moreno J., White A., Vogeley M. S., Hoyle F., Giovanelli R., Haynes M. P., 2016, *ApJ*, 831, 118
- Moseley S. H., Dwek E., Glaccum W., Graham J. R., Loewenstein R. F., Silverberg R. F., 1989, *Nature*, 340, 697
- Murante G., Monaco P., Giovalli M., Borgani S., Diaferio A., 2010, *MNRAS*, 405, 1491
- Murante G., Monaco P., Borgani S., Tornatore L., Dolag K., Goz D., 2015, *MNRAS*, 447, 178
- Murray N., Quataert E., Thompson T. A., 2005, *ApJ*, 618, 569

- Murray S. G., Power C., Robotham A. S. G., 2013, *Astronomy and Computing*, 3, 23
- Nadolny J., et al., 2024, *arXiv e-prints*, p. arXiv:2406.16533
- Nanni A., Bressan A., Marigo P., Girardi L., 2013, *MNRAS*, 434, 2390
- Nanni A., Bressan A., Marigo P., Girardi L., 2014, *MNRAS*, 438, 2328
- Nanni A., Burgarella D., Theulé P., Côté B., Hirashita H., 2020, *A&A*, 641, A168
- Nanni A., Cristallo S., Donevski D., Michałowski M. J., Romano M., Sawant P., 2024, *A&A*, 684, A163
- Navarro J. F., Frenk C. S., White S. D. M., 1996, *ApJ*, 462, 563
- Navarro J. F., Frenk C. S., White S. D. M., 1997, *ApJ*, 490, 493
- Nersesian A., et al., 2019, *A&A*, 624, A80
- Nozawa T., Kozasa T., Umeda H., Maeda K., Nomoto K., 2003, *ApJ*, 598, 785
- Nozawa T., Kozasa T., Habe A., 2006, *ApJ*, 648, 435
- Nozawa T., Kozasa T., Habe A., Dwek E., Umeda H., Tominaga N., Maeda K., Nomoto K., 2007, *ApJ*, 666, 955
- Ormel C. W., Paszun D., Dominik C., Tielens A. G. G. M., 2009, *A&A*, 502, 845
- O'Donnell J. E., Mathis J. S., 1997, *ApJ*, 479, 806
- Paillas E., Lagos C. D. P., Padilla N., Tissera P., Helly J., Schaller M., 2017, *MNRAS*, 470, 4434
- Parente M., Ragone-Figueroa C., Granato G. L., Borgani S., Murante G., Valentini M., Bressan A., Lapi A., 2022, *MNRAS*, 515, 2053
- Parente M., Ragone-Figueroa C., Granato G. L., Lapi A., 2023, *MNRAS*, 521, 6105
- Parente M., et al., 2024a, *ApJ*, 966, 154
- Parente M., Ragone-Figueroa C., Granato G. L., Silva L., Coenda V., Martínez H. J., Muriel H., Lapi A., 2024b, arXiv:2410.05385
- Park C., Choi Y.-Y., Vogeley M. S., Gott J. Richard I., Blanton M. R., SDSS Collaboration 2007, *ApJ*, 658, 898
- Parkinson H., Cole S., Helly J., 2008, *MNRAS*, 383, 557
- Patiri S. G., Prada F., Holtzman J., Klypin A., Betancort-Rijo J., 2006, *MNRAS*, 372, 1710
- Paulino-Afonso A., et al., 2019, *A&A*, 630, A57
- Peek J. E. G., Ménard B., Corrales L., 2015, *ApJ*, 813, 7
- Peng Y., Maiolino R., Cochrane R., 2015, *Nature*, 521, 192
- Percival W. J., et al., 2001, *MNRAS*, 327, 1297
- Péroux C., Howk J. C., 2020, *Annual Review of Astronomy and Astrophysics*, 58, 363
- Pillepich A., et al., 2018, *MNRAS*, 473, 4077
- Planck Collaboration (XLIII) et al., 2016, *A&A*, 596, A104
- Planck Collaboration et al., 2014, *A&A*, 571, A16
- Planck Collaboration et al., 2016, *A&A*, 594, A13
- Popping G., Péroux C., 2022, *MNRAS*, 513, 1531
- Popping G., Somerville R. S., Galametz M., 2017, *MNRAS*, 471, 3152
- Portinari L., Sommer-Larsen J., Tantalo R., 2004, *MNRAS*, 347, 691
- Pozzi F., Calura F., Zamorani G., Delvecchio I., Gruppioni C., Santini P., 2020, *MNRAS*, 491, 5073
- Press W. H., Schechter P., 1974, *ApJ*, 187, 425
- Price D. J., et al., 2017, PHANTOM: Smoothed particle hydrodynamics and magnetohydrodynamics code, Astrophysics Source Code Library, record ascl:1709.002, <https://ui.adsabs.harvard.edu/abs/2017ascl.soft09002P>
- Ragone-Figueroa C., Granato G. L., Parente M., Murante G., Valentini M., Borgani S., Maio U., 2024, *arXiv e-prints*, p. arXiv:2407.06269

- Relaño M., Lisenfeld U., Hou K. C., De Looze I., Vílchez J. M., Kennicutt R. C., 2020, *A&A*, **636**, A18
- Relaño M., et al., 2022, *MNRAS*, **515**, 5306
- Rémy-Ruyer A., et al., 2014, *A&A*, **563**, A31
- Renzini A., Peng Y.-j., 2015, *ApJ*, **801**, L29
- Rieder S., van de Weygaert R., Cautun M., Beygu B., Portegies Zwart S., 2013, *MNRAS*, **435**, 222
- Roberts M. S., Haynes M. P., 1994, *Annual Review of Astronomy and Astrophysics*, **32**, 115
- Rodríguez F., Merchán M., 2020, *A&A*, **636**, A61
- Rodríguez-Medrano A. M., Paz D. J., Stasyszyn F. A., Rodríguez F., Ruiz A. N., Merchán M., 2023, *MNRAS*, **521**, 916
- Rodríguez-Puebla A., Calette A. R., Avila-Reese V., Rodríguez-Gomez V., Huertas-Company M., 2020, *PASA*, **37**, e024
- Rodríguez F., Merchán M., Artale M. C., 2022, *MNRAS*, **514**, 1077
- Rojas R. R., Vogeley M. S., Hoyle F., Brinkmann J., 2004, *ApJ*, **617**, 50
- Rojas R. R., Vogeley M. S., Hoyle F., Brinkmann J., 2005, *ApJ*, **624**, 571
- Romano L. E. C., Nagamine K., Hirashita H., 2022, *MNRAS*, **514**, 1441
- Romeo A. B., Agertz O., Renaud F., 2022, *MNRAS*, **518**, 1002
- Rosas-Guevara Y. M., et al., 2015, *MNRAS*, **454**, 1038
- Rosas-Guevara Y., Tissera P., del P Lagos C., Paillas E., Padilla N., 2022, *MNRAS*, **517**, 712
- Roussel H., et al., 2010, *Astronomy and Astrophysics*, **518**, L66
- Rowlands K., Gomez H. L., Dunne L., Aragón-Salamanca A., Dye S., Maddox S., da Cunha E., van der Werf P., 2014, *MNRAS*, **441**, 1040
- Rowlands K., et al., 2018, *MNRAS*, **473**, 1168
- Ruiz A. N., Paz D. J., Lares M., Luparello H. E., Ceccarelli L., Lambas D. G., 2015, *MNRAS*, **448**, 1471
- Ruiz A. N., Alfaro I. G., Garcia Lambas D., 2019, *MNRAS*, **483**, 4070
- Ruoyi Z., Haibo Y., 2020, *ApJ Letters*, **905**, L20
- Said K., Kraan-Korteweg R. C., Staveley-Smith L., 2019, *MNRAS*, **486**, 1796
- Saintonge A., Catinella B., 2022, arXiv e-prints, p. [arXiv:2202.00690](https://arxiv.org/abs/2202.00690)
- Salim S., 2014, *Serbian Astronomical Journal*, **189**, 1
- Salpeter E. E., 1955, *ApJ*, **121**, 161
- Santini P., et al., 2014, *Astronomy & Astrophysics*, **562**, A30
- Schaye J., et al., 2015, *MNRAS*, **446**, 521
- Schechter P., 1976, *ApJ*, **203**, 297
- Schmidt M., 1959, *ApJ*, **129**, 243
- Schmidt K. H., Boller T., 1993, *Astronomische Nachrichten*, **314**, 361
- Schneider R., Hunt L., Valiante R., 2016, *MNRAS*, **457**, 1842
- Shamshiri S., Thomas P. A., Henriques B. M., Tojeiro R., Lemson G., Oliver S. J., Wilkins S., 2015, *MNRAS*, **451**, 2681
- Shen X., Vogelsberger M., Nelson D., Tacchella S., Hernquist L., Springel V., Marinacci F., Torrey P., 2022, *MNRAS*, **510**, 5560
- Sheth R. K., Mo H. J., Tormen G., 2001, *MNRAS*, **323**, 1
- Sijacki D., Springel V., Di Matteo T., Hernquist L., 2007, *MNRAS*, **380**, 877
- Silva L., Granato G. L., Bressan A., Danese L., 1998, *ApJ*, **509**, 103
- Smethurst R. J., Simmons B. D., Lintott C. J., Shanahan J., 2019, *MNRAS*, **489**, 4016
- Somerville R. S., Davé R., 2015, *ARA&A*, **53**, 51
- Somerville R. S., Primack J. R., Faber S. M., 2001, *MNRAS*, **320**, 504

- Somerville R. S., Hopkins P. F., Cox T. J., Robertson B. E., Hernquist L., 2008, *MNRAS*, 391, 481
- Springel V., 2005, *MNRAS*, 364, 1105
- Springel V., 2010, *MNRAS*, 401, 791
- Springel V., Hernquist L., 2003, *MNRAS*, 339, 289
- Springel V., White S. D. M., Tormen G., Kauffmann G., 2001, *MNRAS*, 328, 726
- Springel V., Di Matteo T., Hernquist L., 2005a, *MNRAS*, 361, 776
- Springel V., et al., 2005b, *Nature*, 435, 629
- Springel V., et al., 2008, *MNRAS*, 391, 1685
- Steinhauser D., Schindler S., Springel V., 2016, *A&A*, 591, A51
- Stevens A. R. H., Croton D. J., Mutch S. J., 2016, *MNRAS*, 461, 859
- Stinson G., Seth A., Katz N., Wadsley J., Governato F., Quinn T., 2006, *MNRAS*, 373, 1074
- Stone J. M., Norman M. L., 1992, *ApJS*, 80, 753
- Sutherland R. S., Dopita M. A., 1993, *ApJS*, 88, 253
- Sutter P. M., et al., 2015, *Astronomy and Computing*, 9, 1
- Tacchella S., et al., 2019, *MNRAS*, 487, 5416
- Tavasoli S., Rahmani H., Khosroshahi H. G., Vasei K., Lehnert M. D., 2015, *ApJ*, 803, L13
- Taverna A., Salerno J. M., Daza-Perilla I. V., Díaz-Giménez E., Zandivarez A., Martínez H. J., Ruiz A. N., 2023, *MNRAS*, 520, 6367
- Taylor E. N., et al., 2011, *MNRAS*, 418, 1587
- Teyssier R., 2002, *A&A*, 385, 337
- Thacker C., et al., 2013, *ApJ*, 768, 58
- Tielens A. G. G. M., McKee C. F., Seab C. G., Hollenbach D. J., 1994, *ApJ*, 431, 321
- Tinsley B. M., 1980, *Fund. Cosmic Phys.*, 5, 287
- Todini P., Ferrara A., 2001, *MNRAS*, 325, 726
- Tomczak A. R., et al., 2014, *ApJ*, 783, 85
- Tonini C., Mutch S. J., Croton D. J., Wyithe J. S. B., 2016, *MNRAS*, 459, 4109
- Tornatore L., Borgani S., Dolag K., Matteucci F., 2007, *MNRAS*, 382, 1050
- Traina A., et al., 2024, *arXiv e-prints*, p. arXiv:2407.09607
- Tremmel M., Governato F., Volonteri M., Quinn T. R., 2015, *MNRAS*, 451, 1868
- Tremonti C. A., et al., 2004, *ApJ*, 613, 898
- Triani D. P., Sinha M., Croton D. J., Pacifici C., Dwek E., 2020, *MNRAS*, 493, 2490
- Triani D. P., Croton D. J., Sinha M., Taylor E. N., Pacifici C., Dwek E., 2023, *MNRAS*, 519, 2500
- Trumpler R. J., 1930, *PASP*, 42, 214
- Tsai J. C., Mathews W. G., 1995, *ApJ*, 448, 84
- Valentini M., Murante G., Borgani S., Monaco P., Bressan A., Beck A. M., 2017, *MNRAS*, 470, 3167
- Valentini M., Borgani S., Bressan A., Murante G., Tornatore L., Monaco P., 2019, *MNRAS*, 485, 1384
- Valentini M., et al., 2020, *MNRAS*, 491, 2779
- Valiante R., Schneider R., Bianchi S., Andersen A. C., 2009, *MNRAS*, 397, 1661
- Valiante R., Schneider R., Salvadori S., Bianchi S., 2011, *MNRAS*, 416, 1916
- Valiante E., et al., 2016, *MNRAS*, 462, 3146
- Ventura P., et al., 2012, *MNRAS*, 424, 2345
- Vijayan A. P., Clay S. J., Thomas P. A., Yates R. M., Wilkins S. M., Henriques B. M., 2019, *MNRAS*, 489, 4072

- Vijayan A. P., Lovell C. C., Wilkins S. M., Thomas P. A., Barnes D. J., Irodotou D., Kuusisto J., Roper W. J., 2021, *MNRAS*, 501, 3289
- Vijayaraghavan R., Ricker P. M., 2015, *MNRAS*, 449, 2312
- Vlahakis C., Dunne L., Eales S., 2005, *MNRAS*, 364, 1253
- Vogelsberger M., McKinnon R., O’Neil S., Marinacci F., Torrey P., Kannan R., 2019, *MNRAS*, 487, 4870
- Volonteri M., 2010, *A&A Rev.*, 18, 279
- Wadsley J. W., Stadel J., Quinn T., 2004, *New A*, 9, 137
- Wadsley J. W., Keller B. W., Quinn T. R., 2017, *MNRAS*, 471, 2357
- Wakelam V., et al., 2017, *Molecular Astrophysics*, 9, 1
- Wang B., 1991, *ApJ*, 374, 456
- Wang K., Avestruz C., Guo H., Wang W., Wang P., 2023, *arXiv e-prints*, p. arXiv:2309.15306
- Wegner G., Grogin N. A., 2008, *AJ*, 136, 1
- Weingartner J. C., Draine B. T., 2001, *ApJ*, 548, 296
- White S. D. M., Frenk C. S., 1991, *ApJ*, 379, 52
- Whitmore B. C., Gilmore D. M., Jones C., 1993, *ApJ*, 407, 489
- Wiersma R. P. C., Schaye J., Smith B. D., 2009, *MNRAS*, 393, 99
- Winters J. M., Fleischer A. J., Le Bertre T., Sedlmayr E., 1997, *A&A*, 326, 305
- Wooden D. H., Rank D. M., Bregman J. D., Witteborn F. C., Tielens A. G. G. M., Cohen M., Pinto P. A., Axelrod T. S., 1993, *ApJ Supplement Series*, 88, 477
- Wright A. H., et al., 2016, *MNRAS*, 460, 765
- Wyder T. K., et al., 2007, *ApJS*, 173, 293
- Yamasawa D., Habe A., Kozasa T., Nozawa T., Hirashita H., Umeda H., Nomoto K., 2011, *ApJ*, 735, 44
- Yan H., Lazarian A., Draine B. T., 2004, *ApJ*, 616, 895
- Yang X., Mo H. J., van den Bosch F. C., Jing Y. P., 2005, *MNRAS*, 356, 1293
- Yang X., Mo H. J., van den Bosch F. C., Pasquali A., Li C., Barden M., 2007, *ApJ*, 671, 153
- Yates R. M., Henriques B., Thomas P. A., Kauffmann G., Johansson J., White S. D. M., 2013, *MNRAS*, 435, 3500
- Yates R. M., Hendriks D., Vijayan A. P., Izzard R. G., Thomas P. A., Das P., 2024, *MNRAS*, 527, 6292
- Yu H., Wang F. Y., 2016, *ApJ*, 820, 114
- Zandivarez A., Merchán M. E., Padilla N. D., 2003, *MNRAS*, 344, 247
- Zentner A. R., 2007, *International Journal of Modern Physics D*, 16, 763
- Zhang Y.-C., Yang X.-H., 2019, *Research in Astronomy and Astrophysics*, 19, 006
- Zhukovska S., 2014, *A&A*, 562, A76
- Zhukovska S., Gail H.-P., Tieloff M., 2008, *A&A*, 479, 453
- Zhukovska S., Henning T., Dobbs C., 2018, *ApJ*, 857, 94
- Zwaan M. A., et al., 2003, *The Astronomical Journal*, 125, 2842
- de Bernardis P., et al., 2000, *Nature*, 404, 955
- von Benda-Beckmann A. M., Müller V., 2008, *MNRAS*, 384, 1189